A FINITE-ELEMENT-BASED APPROACH TO MODELING CRACKING & REPAIRS FOR DISTORTION-INDUCED FATIGUE IN STEEL BRIDGES

By

Hao Liu

Submitted to the graduate degree program in Civil Engineering
and the Graduate Faculty of the University of Kansas
in partial fulfillment of the requirements for the degree of
Doctor of Philosophy.

Committee Chair _____
Dr. Caroline Bennett

Committee Members _____
Dr. Adolfo Matamoros

_____
Dr. Stanley Rolfe

_____
Dr. Jian Li

_____
Dr. Douglas Ward

Date Defended: _____

The Dissertation Committee for Hao Liu certifies
that this is the approved version of the following dissertation:

A FINITE-ELEMENT-BASED APPROACH TO MODELING CRACKING & REPAIRS FOR DISTORTION-INDUCED FATIGUE IN STEEL BRIDGES

Committee Chair

_____
Dr. Caroline Bennett

Committee Members

_____
Dr. Adolfo Matamoros

_____
Dr. Stanley Rolfe

_____
Dr. Jian Li

_____
Dr. Douglas Ward

Date Approved: _____

EXECUTIVE SUMMARY

Distortion-induced fatigue damage is a common problem in steel girder bridges built prior to the mid-1980s.The University of Kansas has studied and developed several retrofit techniques with an aim to determine the efficacy of different retrofit measures to mitigate the effects of distortion-induced fatigue and stop fatigue crack growth or slow the rate of crack propagation. One simple and commonly-used retrofit technique is the practice of drilling crack-arrest holes at the tips of cracks to smooth out the sharp crack tip, reducing the stress concentration and halting fatigue crack propagation. The practice of hole-drilling has existed for decades, but its application to distortion-induced fatigue cracking has not been adequately studied. Another technique discussed in this thesis, called the angles-with-plate retrofit, requires two angles providing attachment between the connection plate and girder web with a plate placed on the other side of the web to distribute out-of-plane forces. An appealing aspect of the angles-with-plate retrofit is the minimal traffic disruption required during retrofit application. Girder subassemblies were chosen for study to evaluate for the effectiveness of various retrofits using both analytical approach and experimental testing.

This dissertation is divided into five parts and appendices. The first part is the introduction for the dissertation. The second part is analytical and experimental investigations of repairing fatigue damage in steel plate with adhesively bonded carbon fiber reinforced polymer (CFRP) overlays under tension loading. Parts 3 and 4 are analytical and experimental investigations of evaluating the uses of crack-arrest holes and angles-with-plate retrofit to effectively repair distortion-induced fatigue cracking on 3-m (9-ft) steel girder specimens under fatigue loading. Part 5 is the recommendations and synthesis. Part 2, Part 3 and Part 4 within the

document contain particular formatting associated with published or expected publishing requirements.

Part 1: Introduction

Part 2: Use of CFRP Overlays to Repair Fatigue Damage in Steel Plates under Tension Loading

Part 3: Effectiveness of Crack-Arrest Holes under Distortion-Induced Fatigue Loading

Part 4: Evaluation of Three Computational Techniques for Quantifying Distortion-Induced Fatigue Crack Propensity Using Finite Element Analysis

Part 5: Recommendations and Synthesis

Part 2 was published in the Journal of Composites for Construction, American Society of Civil Engineers (ASCE), 2014.18. Part 3 was presented at the ASCE 2014 Structures Congress in April 2014 in Boston, Massachusetts. This research has been accepted for presentation and potential proceedings publication for the 16th European Bridge Conference in June 2015 in Edinburgh, United Kingdom. Part4is intended for future publication.

ACKNOWLEDGEMENTS

First of all, I would like to thank all of those at the University of Kansas that made this dissertation possible. Without the guidance, support, and expertise of Drs. Caroline Bennett, Adolfo Matamoros, and Stanley Rolfe, this research and completed dissertation would not have been possible. Additionally, I would like to thank Drs. Jian Li, Douglas Ward and Ron Barrett-Gonzalez for their contributions to my research and education. Finally, I would like to thank all those graduate students who contributed to this work including James Zhou, Say Hak Bun, Gary G. Simmons, Jack C. Przywara, Temple I. Overman, Fatih Alemdar, Regan Gangel, and Amanda Hartman.

I would like to gratefully acknowledge funding support from the Kansas Department of Transportation (KDOT), University of Kansas Transportation Research Institute (KU TRI), and Transportation Pooled Fund Study TPF 5(189) participants.

Lastly, I would like to thank my family for their continuous support and encouragement throughout all of my education.

TABLE OF CONTENTS

LIST OF FIGURES ..... **IX**

LIST OF TABLES ..... **XIX**

PART 1 ..... **- 1 -**

INTRODUCTION ..... **- 2 -**

PART 2 ..... **- 5 -**

USE OF CFRP OVERLAYS TO REPAIR FATIGUE DAMAGE IN STEEL PLATES UNDER TENSION LOADING ..... **- 6 -**

ABSTRACT ..... - 6 -

INTRODUCTION ..... - 7 -

BACKGROUND ..... - 8 -

OBJECTIVE AND SCOPE ..... - 10 -

FINITE ELEMENT SIMULATIONS ..... - 12 -

Modeling Methodology ..... *- 12 -*

Effect of the Modulus of Elasticity of the CFRP ..... *- 15 -*

Effect of the Thickness of the CFRP Overlay ..... *- 16 -*

RATIO OF OVERLAY AXIAL STIFFNESS TO STEEL AXIAL STIFFNESS ..... *- 16 -*

EFFECT OF THICKNESS OF BOND LAYER ..... *- 18 -*

EXPERIMENTAL PROGRAM ..... - 21 -

STEEL SPECIMEN DIMENSIONS ..... *- 22 -*

FABRICATION AND ATTACHMENT OF THE MULTI-LAYERED CFRP OVERLAYS ..... *- 23 -*

TEST PROCEDURE ..... *- 25 -*

EXPERIMENTAL RESULTS ..... - 29 -

EFFECT OF STIFFNESS RATIO ..... *- 31 -*

SPECIMEN DEBOND BEHAVIOR ..... *- 36 -*

CONCLUSIONS ..... - 37 -

REFERENCES ..... - 38 -

PART 3 ..... **- 41 -**

EFFECTIVENESS OF CRACK-ARREST HOLES UNDER DISTORTION-INDUCED FATIGUE LOADING ..... **- 42 -**

ABSTRACT ..... - 42 -
INTRODUCTION AND BACKGROUND ..... - 43 -
OBJECTIVE AND SCOPE ..... - 49 -
RESEARCH APPROACH ..... - 50 -
Modeling Methodology ..... *- 50 -*
Modeling of Cracks, Crack-Arrest Holes, and Computing Stresses ..... *- 52 -*
Mesh Convergence Study ..... *- 56 -*
Model Validation ..... *- 57 -*
Model Including Plate Washer & Tensioned Bolt ..... *- 65 -*
RESULTS AND DISCUSSION ..... - 66 -
Effect of Crack-Arrest Holes for Diagonal Crack ..... *- 75 -*
Effect of Crack-Arrest Holes for Horseshoe-Shaped Crack ..... *- 76 -*
Effect of Crack-Arrest Holes for a Simultaneously-Occuring Horseshoe-Shaped & Web-To-Flange Crack ..... *- 76 -*
Effect of Crack-Arrest Holes for Web-To-Flange Crack ..... *- 77 -*
Large-Hole Retrofit ..... *- 78 -*
Effect of Including Pretensioned Bolt with Plate Washer ..... *- 78 -*
CONCLUSIONS ..... - 83 -
REFERENCES ..... - 85 -

PART 4 ..... **- 87 -**

EVALUATIONOF THREE COMPUTATIONAL TECHNIQUES FOR QUANTIFYING DISTORTION-INDUCED FATIGUE CRACK PROPENSITY USING FINITE ELEMENT ANALYSIS **88**

ABSTRACT 88
INTRODUCTION 89
OBJECTIVE AND SCOPE 90
FINITE ELEMENT MODELS 91
Modeling Methodology *91*
Extended Finite Element Method (XFEM) *94*
FINITE ELEMENT ANALYSIS TECHNIQUES 97
Hot Spot Stresses *97*

J-Integrals *99*
Stress Intensity Factors *101*
Fatigue Crack Propagation Theory *105*
RESULTS AND DISCUSSION 106
Experimental Results *109*
Hot Spot Stresses *110*
J-Integrals *114*
Stress Intensity Factors *118*
CONCLUSIONS 123
REFERENCES 125

PART 5 128

CONCLUSION 129

APPENDICES 136

APPENDIX A: MAXIMUM PRINCIPAL STRESS AROUND CRACK-ARREST HOLES FOR DIAGONAL CRACK TYPE 137

APPENDIX B: MAXIMUM PRINCIPAL STRESS AROUND CRACK-ARREST HOLES FOR HORSESHOE-SHAPED CRACK TYPE 144

APPENDIX C: MAXIMUM PRINCIPAL STRESS AROUND CRACK-ARREST HOLES FOR HORSESHOE-SHAPED & WEB-TO-FLANGE CRACK TYPE 151

APPENDIX D: MAXIMUM PRINCIPAL STRESS AROUND CRACK-ARREST HOLES FOR WEB-TO-FLANGE CRACK TYPE 157

APPENDIX E: MAXIMUM PRINCIPAL STRESS AROUND CRACK-ARREST HOLES FOR LARGE-HOLE RETROFIT 164

APPENDIX F: LAB NOTES RECORDED DURING TESTING CRACK-ARREST HOLES 166

APPENDIX G: CONVERGENCE STUDY FOR J-INTEGRAL, J-INTEGRAL FORM KS, AND K FACTORS FOR THE UNRETROFITTED MODELS WITH 102-MM (4-IN.) TYPE 1 AND 203-MM (8-IN.) TYPE 2 CRACKS 170

APPENDIX H: MAXIMUM PRINCIPAL STRESS IN THE WEB GAP REGION FOR THE ANGLES-WITH-PLATE RETROFIT MODELS 175

APPENDIX I: DEFORMATION SCREENSHOTS IN THE WEB GAP REGION FOR THE ANGLES-WITH-PLATE RETROFIT MODELS 195

APPENDIX J: BOLT MODELING TECHNIQUES 215

APPENDIX K: FINITE ELEMENT MODELING MESHING TECHNIQUES 219

LIST OF FIGURES

PART 1: INTRODUCTION

N/A

PART 2: USE OF CFRP OVERLAYS TO REPAIR FATIGUE DAMAGE IN STEEL PLATES UNDER TENSION LOADING

FIGURE 1: TENSION SPECIMEN DIMENSIONS (3.2-MM 1/8-IN. THICK SPECIMEN).....12

FIGURE 2: (A) FINITE ELEMENT MODEL MESH (B) MESH IN THE VICINITY OF THE CIRCULAR OPENING FOR AN ELEMENT SIZE AT THE OPENING OF 0.25 MM (0.10 IN.) (C) MESH IN THE VICINITY OF THE CIRCULAR OPENING FOR AN ELEMENT SIZE AT THE OPENING OF 0.12 MM (0.05 IN.) (D) EFFECT OF ELEMENT SIZE AT THE CIRCULAR OPENING ON MAXIMUM PRINCIPAL HSS. 14

FIGURE 3: EFFECT OF STIFFNESS RATIO ON MAXIMUM PRINCIPAL HOT SPOT STRESS IN THE STEEL..... - 17 -

FIGURE 4: PEAK STRESSES ALONG CFRP OVERLAY ON RESIN LAYER END OF HOLE ..... - 19 -

FIGURE 5: PEAK STRESSES DEMAND ON CFRP LAYER AS A FUNCTION OF RESIN LAYER THICKNESS.....20

FIGURE 6: CRACK PROGRESSION IN 3-MM ($^1/_8$-IN.) THICK SPECIMENS. SOLID LINES ARE ADDED FOR COMPARISON AND CORRESPOND TO THEORETICAL CRACK PROGRESSIONS CALCULATED USING EQ. 4 WITH MATERIAL CONSTANTS OF A=3.6X10^{-10} AND M=3 FOR VARIOUS STRESS RANGES IN A SPECIMEN CONFIGURATION WITHOUT OVERLAYS... - 27 -

FIGURE 7: PERCENT CHANGE IN STIFFNESS OF 6-MM ($^1/_4$-IN.) THICK SPECIMENS TESTED AT 221 MPA (32 KSI). ..... - 29 -

FIGURE 8: S-N DIAGRAM FOR PROPAGATION LIFE FOR (A) 3-MM ($^1/_8$-IN.) THICK SPECIMENS AND (B) 6-MM ($^1/_4$-IN.) THICK SPECIMENS 31

FIGURE 9: FATIGUE-CRACK PROPAGATION LIFE FOR ALL SPECIMENS TREATED WITH CFRP OVERLAYS AND AN INITIAL CRACK LENGTH OF 7 MM (0.3 IN.) 32

FIGURE 10: EQUIVALENT APPLIED STRESS OF ALL SPECIMENS TREATED WITH CFRP OVERLAYS AND AN INITIAL CRACK LENGTH OF 7 MM (0.3 IN.) ..... - 36 -

PART 3: EFFECTIVENESS OF CRACK-ARREST HOLES UNDER DISTORTION-INDUCED FATIGUE LOADING

FIGURE 1: ELEVATION VIEW OF GIRDER SECTION AND MODEL GEOMETRY 51

FIGURE 2: GIRDER CROSS-SECTION 51

FIGURE 3: (A) DIMENSION OF THE DIAGONAL CRACK LENGTH; (B) DIMENSION OF THE HORSESHOE-SHAPED AND WEB-TO-FLANGE CRACK LENGTH 54

FIGURE 4: CRACK PLACEMENT AND HOT SPOT STRESS PATHS FOR FE MODELS: (A) DIAGONAL-TYPE CRACK PATTERN; (B) HORSESHOE-SHAPED CRACK; (C) HORSESHOE-SHAPED CRACK AND WEB-TO-FLANGE WELD CRACK; (D) WEB-TO-FLANGE WELD CRACK ..... - 55 -
FIGURE 5: CRACK PLACEMENT AND HOT SPOT STRESS PATHS FOR: (A) 101.6 MM [4.0 IN] HOLE FOR THE MODEL INCLUDING WEB-TO-FLANGE WELD CRACK; (B) 101.6 MM [4.0 IN] HOLE FOR THE MODEL INCLUDING HORSESHOE-SHAPED CRACK ..... - 55 -
FIGURE 6: (A) MESH IN THE VICINITY OF THE CRACK-ARREST HOLES FOR AN ELEMENT SIZE OF 1.80 MM [0.071 IN]; (B) MESH IN THE VICINITY OF THE CRACK-ARREST HOLES FOR AN ELEMENT SIZE OF 0.71 MM [0.028 IN]; (C) EFFECT OF ELEMENT SIZE AROUND THE CRACK-ARREST HOLE PATH ON MAXIMUM PRINCIPAL HSS. ..... - 57 -
FIGURE 7: PROGRESSION OF CRACKING IN PHYSICAL TEST GIRDER; RED LINES INDICATE CRACK LOCATIONS 60
FIGURE 8: FINITE ELEMENT MODEL FOR THE GIRDER INCLUDING ONE PAIR CRACK-ARREST HOLES.....61
FIGURE 9: (A) CRACK-ARREST HOLE AND STRAIN GAGE (CIRCLED) ON THE LEFT SIDE OF THE CONNECTION PLATE; (B) CRACK-ARREST HOLE AND STRAIN GAGE (CIRCLED) ON THE RIGHT SIDE OF THE CONNECTION PLATE; (C) CRACKING FORMING AFTER THE FIRST PAIR OF CRACK-ARREST HOLES HAD BEEN DRILLED AND TESTED ON THE LEFT OF CONNECTION PLATE 62
FIGURE 10: STRAIN DATA FROM LEFT CRACK-ARREST HOLE AND RIGHT CRACK-ARREST HOLE GAGES BOTH MEASURED AT 10 MM (3/8 IN) FROM THE EDGE OF THE HOLE FOR ONE PAIR CRACK-ARREST HOLES.....62
FIGURE 11 : LATERAL DEFLECTION ALONG THE HEIGHT OF THE GIRDER 63
FIGURE 12: FINITE ELEMENT MODEL RESULTS SHOWING TWO PAIRS OF CRACK-ARREST HOLES (THE STRESS CONTOURS ARE PRESENTED WITH LIMITS FROM 0 TO 345 MPA [50 KSI]) 64
FIGURE 13: STRAIN GAGE PLACEMENT AROUND TWO PAIRS OF CRACK-ARREST HOLES IN THE PHYSICAL TESTING: (A) LEFT SIDE OF THE CONNECTION PLATE; (B) RIGHT SIDE OF THE CONNECTION PLATE 64
FIGURE 14: STRAIN DATA FROM LEFT CRACK-ARREST HOLE AND RIGHT CRACK-ARREST HOLE GAGES BOTH MEASURED AT 10 MM (3/8 IN) FROM THE EDGE OF THE HOLE AT THE TOP OF THE SECOND PAIR CRACK-ARREST HOLES ... - 65 -
FIGURE 15: DIAGONAL CRACK MODEL WITH PLATE WASHER & TENSIONED BOLT ..... - 66 -
FIGURE 16: MAXIMUM PRINCIPAL STRESSES FOR (A) DIAGONAL CRACK PATTERN; (B) HORSESHOE-SHAPED CRACK PATTERN; (C) HORSESHOE-SHAPED CRACK AND WEB-TO-FLANGE CRACK PATTERN; (D) WEB-TO-FLANGE CRACK PATTERN (THE DEFLECTION SCALE WAS 1.0, AND THE STRESS CONTOURS ARE PRESENTED WITH LIMITS FROM 0 TO 345 MPA [50 KSI]) ..... - 67 -
FIGURE 17: HSS-1 FOR VARIOUS CRACK PLACEMENTS, LENGTHS, AND HOLE DIAMETERS.....73
FIGURE 18: CHSS-1 FOR VARIOUS CRACK PLACEMENTS, LENGTHS, AND HOLE DIAMETERS 73
FIGURE 19: HSS-2 FOR VARIOUS CRACK PLACEMENTS, LENGTHS, AND HOLE DIAMETERS.....74
FIGURE 20: CHSS-2 FOR VARIOUS CRACK PLACEMENTS, LENGTHS, AND HOLE DIAMETERS 74
FIGURE 21: (A) MAXIMUM PRINCIPAL STRESS FOR DIAGONAL CRACK-ARREST HOLE MODEL WITHOUT PLATE WASHER & PRETENSIONED BOLT; (B) MAXIMUM PRINCIPAL STRESS FOR DIAGONAL CRACK MODEL WITH PLATE WASHER & PRETENSIONED BOLT; (C) MAXIMUM PRINCIPAL STRESS FOR DIAGONAL CRACK MODEL WITH PLATE WASHER & PRETENSIONED BOLT (PLATE WASHER & PRETENSIONED BOLT ARE NOT SHOWN) 80

FIGURE 22: (A) CIRCULAR HSS COMPARISON BETWEEN DIAGONAL CRACK-ARREST HOLE MODEL AND THE MODEL WITH PLATE WASHER & PRETENSIONED BOLT; (B) HSS-1 COMPARISON BETWEEN DIAGONAL CRACK-ARREST HOLE MODEL AND THE MODEL WITH PLATE WASHER & PRETENSIONED BOLT; (C) HSS-2 COMPARISON BETWEEN DIAGONAL CRACK-ARREST HOLE MODEL AND THE MODEL WITH PLATE WASHER & PRETENSIONED BOLT ALONG THE PATH 82

PART 4: EVALUATIONOF THREE COMPUTATIONAL TECHNIQUES FOR QUANTIFYING DISTORTION-INDUCED FATIGUE CRACK PROPENSITY USING FINITE ELEMENT ANALYSIS

FIGURE 1: (A) EXPERIMENTAL GIRDER SUBASSEMBLY AND (B) THE FINITE ELEMENT MODEL OF THE SUBASSEMBLY ...93

FIGURE 2: (A) CRACKS ON THE EXPERIMENTAL GIRDER SUBASSEMBLY AND (B) CRACKS MODELED IN THE FINITE ELEMENT MODEL OF THE SUBASSEMBLY 96

FIGURE 3: AGREEMENT BETWEEN OBSERVED EXPERIMENTAL CRACK LOCATIONS AND PEAK MAXIMUM PRINCIPAL STRESS 99

FIGURE 4: (A) HOT SPOT STRESSES FOR TYPE 1 CRACK ALONG THE PATH FOR 51-MM (2-IN.) HORSESHOE CRACK AND 51-MM (2-IN.) HORIZONTAL CRACK UNRETROFITTED MODEL WITH BLACK BOUNDARY LINES; (B) HOT SPOT STRESSES FOR TYPE 2 CRACK ALONG THE PATH FOR 51-MM (2-IN.) HORSESHOE CRACK AND 51-MM (2-IN.) HORIZONTAL CRACK UNRETROFITTED MODEL WITH BLACK BOUNDARY LINES 99

FIGURE 5: CRACK OPENING (A) MODE I, (B) MODE II, AND (C) MODE III 101

FIGURE 6: EXAMPLE OF HOW CONTOUR INTEGRALS ARE TAKEN IN A FINITE ELEMENT MESH 104

FIGURE 7: EXAMPLE OF CONVERGENCE STUDY FOR J-INTEGRAL AND K FACTORS FOR THE UNRETROFITTED MODELS WITH 102-MM (4-IN.)TYPE 1 AND 203-MM (8-IN.) TYPE 2 CRACKS 104

FIGURE 8: LOGARITHMIC PLOT OF TYPICAL FATIGUE CRACK GROWTH RATE VS. STRESS INTENSITY FACTOR RANGE..105

FIGURE 9: (A) ANGLES-WITH-PLATE RETROFIT APPLIED TO A TEST GIRDER (STIFFENER SIDE), (B) ANGLES-WITH-PLATE RETROFIT APPLIED TO A TEST GIRDER (FASCIA SIDE) AND (C) SKETCH OF THE ANGLES-WITH-PLATE RETROFIT 109

FIGURE 10: (A) HOT SPOT STRESS AT TYPE 1 CRACK WITH NO RETROFIT, F-F RETROFIT, AND S-S RETROFIT; (B) HOT SPOT STRESS AT TYPE 2 CRACK WITH NO RETROFIT, F-F RETROFIT, AND S-S RETROFIT 111

FIGURE 11: (A) HOT SPOT STRESS PERFORMANCE OF EACH RETROFIT COMBINATION AT TYPE 1 CRACK; (B) HOT SPOT STRESS PERFORMANCE OF EACH RETROFIT COMBINATION AT TYPE 2 CRACK 113

FIGURE 12: (A) J-INTEGRALS AT TYPE1 CRACK WITH NO RETROFIT, F-F RETROFIT, AND S-S RETROFIT; (B) J-INTEGRALS AT TYPE 2 CRACK WITH NO RETROFIT, F-FRETROFIT, AND S-S RETROFIT....116

FIGURE 13: (A) EQUIVALENT MODE I STRESS INTENSITY FACTORS AT TYPE 1 CRACK BASED ON J-INTEGRAL COMPUTATION; (B) EQUIVALENT MODE I STRESS INTENSITY FACTORS AT TYPE 2 CRACK BASED ON J-INTEGRAL COMPUTATION 117

FIGURE 14: (A) K1, K2, AND K3 AT TYPE 1 CRACK FOR NO RETROFIT, F-F RETROFIT, AND S-S RETROFIT; (B)K1, K2, AND K3 AT TYPE 2 CRACK FOR NO RETROFIT, F-F RETROFIT, AND S-S RETROFIT 120

FIGURE 15: (A) EQUIVALENT MODE I STRESS INTENSITY FACTORS AT TYPE 1 CRACK BASED ON K1, K2, K3 COMPUTATION; (B) EQUIVALENT MODE I STRESS INTENSITY FACTORS AT TYPE 2 CRACK BASED ON K1, K2, K3 COMPUTATION 122

PART 5: RECOMMENDATIONS AND SYNTHESIS

FIGURE 1: (A) GIRDER SECTION FINITE ELEMENT MODEL GEOMETRY; (B) ANGLES ON THE FRONT SIDE OF THE GIRDER; (C) BACKING PLATE ON THE FASCIA SIDE OF THE GIRDER 131
FIGURE 2: GIRDER CROSS-SECTION 132
FIGURE 3: (A) MAXIMUM PRINCIPAL STRESS FOR ANGLES-WITH-PLATE RETROFIT MODEL; (B) MAXIMUM PRINCIPAL STRESS FOR ANGLES-WITH-PLATE RETROFIT MODEL (ANGLES AND PLATE WERE NOT SHOWN); (C) MAXIMUM PRINCIPAL STRESS FOR CRACK-ARREST HOLE MODEL WITH 13 MM [0.5 IN.] HOLE DIAMETER; (D) MAXIMUM PRINCIPAL STRESS FOR CRACK-ARREST HOLE MODEL WITH 25 MM [1.0 IN.] HOLE DIAMETER; (E) MAXIMUM PRINCIPAL STRESS FOR CRACK-ARREST HOLE MODEL WITH 51 MM [2.0 IN.] HOLE DIAMETER 135

APPENDIX A: MAXIMUM PRINCIPAL STRESS AROUND CRACK-ARREST HOLES FOR DIAGONAL CRACK TYPE

FIGURE A. 1: HOT SPOT STRESS PATHS FOR DIAGONAL CRACK TYPE 137
FIGURE A.2: 70 MM [2.75 IN.] CRACK LENGTH & 13 MM [0.5 IN.] HOLE DIAMETER 138
FIGURE A.3: 70 MM [2.75 IN.] CRACK LENGTH & 25 MM [1.0 IN.] HOLE DIAMETER 138
FIGURE A. 4: 70 MM [2.75 IN.] CRACK LENGTH & 51 MM [2.0 IN.] HOLE DIAMETER 139
FIGURE A. 5: 102MM [4.0 IN.] CRACK LENGTH & 13 MM [0.5 IN.] HOLE DIAMETER 139
FIGURE A. 6: 102MM [4.0 IN.] CRACK LENGTH & 25 MM [1.0 IN.] HOLE DIAMETER 140
FIGURE A. 7: 102MM [4.0 IN.] CRACK LENGTH & 51 MM [2.0 IN.] HOLE DIAMETER 140
FIGURE A. 8: 102MM [4.0 IN.] CRACK LENGTH & 76 MM [3.0 IN.] HOLE DIAMETER 141
FIGURE A. 9: 152 MM [6 IN.] CRACK LENGTH & 13 MM [0.5 IN.] HOLE DIAMETER 141
FIGURE A. 10: 152 MM [6 IN.] CRACK LENGTH & 25 MM [1.0 IN.] HOLE DIAMETER 142
FIGURE A. 11: 152 MM [6 IN.] CRACK LENGTH & 51 MM [2.0 IN.] HOLE DIAMETER 142
FIGURE A. 12: 152 MM [6 IN.] CRACK LENGTH & 76 MM [3.0 IN.] HOLE DIAMETER 143

APPENDIX B: MAXIMUM PRINCIPAL STRESS AROUND CRACK-ARREST HOLES FOR HORSESHOE-SHAPED CRACK TYPE

FIGURE B. 1: HOT SPOT STRESS PATHS FOR HORSESHOE-SHAPED CRACK TYPE 144
FIGURE B. 2: 70 MM [2.75 IN.] CRACK LENGTH & 13 MM [0.5 IN.] HOLE DIAMETER....145

FIGURE B. 3: 70 MM [2.75 IN.] CRACK LENGTH & 25 MM [1.0 IN.] HOLE DIAMETER.....145
FIGURE B. 4: 70 MM [2.75 IN.] CRACK LENGTH & 51 MM [2.0 IN.] HOLE DIAMETER.....146
FIGURE B. 5: 70 MM [2.75 IN.] CRACK LENGTH & 76 MM [3.0 IN.] HOLE DIAMETER.....146
FIGURE B. 6: 102MM [4.0 IN.] CRACK LENGTH & 13 MM [0.5 IN.] HOLE DIAMETER 147
FIGURE B. 7: 102MM [4.0 IN.] CRACK LENGTH & 25 MM [1.0 IN.] HOLE DIAMETER 147
FIGURE B. 8: 102MM [4.0 IN.] CRACK LENGTH & 51 MM [2.0 IN.] HOLE DIAMETER 148
FIGURE B. 9: 102MM [4.0 IN.] CRACK LENGTH & 76 MM [3.0 IN.] HOLE DIAMETER 148
FIGURE B. 10: 152 MM [6 IN.] CRACK LENGTH & 13 MM [0.5 IN.] HOLE DIAMETER.....149
FIGURE B. 11: 152 MM [6 IN.] CRACK LENGTH & 25 MM [1.0 IN.] HOLE DIAMETER.....149
FIGURE B. 12: 152 MM [6 IN.] CRACK LENGTH & 51 MM [2.0 IN.] HOLE DIAMETER.....150
FIGURE B. 13: 152 MM [6 IN.] CRACK LENGTH & 76 MM [3.0 IN.] HOLE DIAMETER.....150

APPENDIX C: MAXIMUM PRINCIPAL STRESS AROUND CRACK-ARREST HOLES FOR HORSESHOE-SHAPED&WEB-TO-FLANGE CRACK TYPE

FIGURE C. 1: HOT SPOT STRESS PATHS FOR HORSESHOE-SHAPED&WEB-TO-FLANGE CRACK TYPE 151
FIGURE C. 2: 70 MM [2.75 IN.] CRACK LENGTH & 13 MM [0.5 IN.] HOLE DIAMETER.....152
FIGURE C. 3: 70 MM [2.75 IN.] CRACK LENGTH & 25 MM [1.0 IN.] HOLE DIAMETER.....152
FIGURE C. 4: 102MM [4.0 IN.] CRACK LENGTH & 13 MM [0.5 IN.] HOLE DIAMETER 153
FIGURE C. 5: 102 MM [4.0 IN.] CRACK LENGTH &25 MM [1.0 IN.] HOLE DIAMETER 153
FIGURE C. 6: 102MM [4.0 IN.] CRACK LENGTH & 51 MM [2.0 IN.] HOLE DIAMETER 154
FIGURE C. 7: 152 MM [6 IN.] CRACK LENGTH & 13 MM [0.5 IN.] HOLE DIAMETER.....154
FIGURE C. 8: 152 MM [6 IN.] CRACK LENGTH & 25 MM [1.0 IN.] HOLE DIAMETER.....155
FIGURE C. 9: 152 MM [6 IN.] CRACK LENGTH & 51 MM [2.0 IN.] HOLE DIAMETER.....155
FIGURE C. 10: 152 MM [6 IN.] CRACK LENGTH & 76 MM [3.0 IN.] HOLE DIAMETER.....156

APPENDIX D: MAXIMUM PRINCIPAL STRESS AROUND CRACK-ARREST HOLES FOR WEB-TO-FLANGE CRACK TYPE

FIGURE D. 1: HOT SPOT STRESS PATHS FOR WEB-TO-FLANGE CRACK TYPE 157
FIGURE D. 2: 140MM [5.5 IN.] CRACK LENGTH & 13 MM [0.5 IN.] HOLE DIAMETER 158
FIGURE D. 3: 140MM [5.5 IN.] CRACK LENGTH & 25 MM [1.0 IN.] HOLE DIAMETER 158
FIGURE D. 4: 140 MM [5.5 IN.] CRACK LENGTH & 51 MM [2.0 IN.] HOLE DIAMETER 159
FIGURE D. 5: 203 MM [8 IN.] CRACK LENGTH & 13 MM [0.5 IN.] HOLE DIAMETER 159
FIGURE D. 6: 203 MM [8 IN.] CRACK LENGTH & 25 MM [1.0 IN.] HOLE DIAMETER 160
FIGURE D. 7: 203 MM [8 IN.] CRACK LENGTH & 51 MM [2.0 IN.] HOLE DIAMETER 160

FIGURE D. 8: 203 MM [8 IN.] CRACK LENGTH & 76 MM [3.0 IN.] HOLE DIAMETER 161
FIGURE D. 9: 305 MM [12 IN.] CRACK LENGTH & 13 MM [0.5 IN.] HOLE DIAMETER 161
FIGURE D. 10: 305 MM [12 IN.] CRACK LENGTH & 25 MM [1.0 IN.] HOLE DIAMETER 162
FIGURE D. 11: 305 MM [12 IN.] CRACK LENGTH & 51 MM [2.0 IN.] HOLE DIAMETER 162
FIGURE D. 12: 305 MM [12 IN.] CRACK LENGTH & 76 MM [3.0 IN.] HOLE DIAMETER 163

APPENDIX E: MAXIMUM PRINCIPAL STRESS AROUND CRACK-ARREST HOLES FOR LARGE-HOLE RETROFIT

FIGURE E. 1: HOT SPOT STRESS PATHS FOR LARGE-HOLE RETROFIT MODEL 164
FIGURE E. 2: WEB-TO-FLANGE CRACK WITH 102 MM [4.0 IN.] HOLE DIAMETER 165
FIGURE E. 3:HORSESHOE-SHAPED CRACK WITH 102 MM [4.0 IN.] HOLE DIAMETER 165

APPENDIX F: LAB NOTES RECORDED DURING TESTING CRACK-ARREST HOLES

N/A

APPENDIX G: CONVERGENCE STUDY FOR J-INTEGRAL, J-INTEGRAL FORM KS, AND K FACTORS FOR THE UNRETROFITTED MODELS WITH 102-MM (4-IN.) TYPE 1 AND 203-MM (8-IN.) TYPE 2 CRACKS

FIGURE G. 1: CONVERGENCE STUDY OF J-INTEGRAL FOR 102-MM (4-IN.) TYPE 1 CRACK 170
FIGURE G. 2: CONVERGENCE STUDY OF J-INTEGRAL FOR 203-MM (8-IN.) TYPE 2 CRACK 170
FIGURE G. 3: CONVERGENCE STUDY OF J-INTEGRAL FROM KS FOR 102-MM (4-IN.) TYPE 1 CRACK 171
FIGURE G. 4: CONVERGENCE STUDY OF J-INTEGRAL FROM KS FOR 203-MM (8-IN.) TYPE 2 CRACK 171
FIGURE G. 5: CONVERGENCE STUDY OF K1 FACTOR FOR 102-MM (4-IN.) TYPE 1 CRACK 172
FIGURE G. 6: CONVERGENCE STUDY OF K1 FACTOR FOR 203-MM (8-IN.) TYPE 2 CRACK 172
FIGURE G. 7: CONVERGENCE STUDY OF K2 FACTOR FOR 102-MM (4-IN.) TYPE 1 CRACK 173
FIGURE G. 8: CONVERGENCE STUDY OF K2 FACTOR FOR 203-MM (8-IN.) TYPE 2 CRACK 173
FIGURE G. 9: CONVERGENCE STUDY OF K3 FACTOR FOR 102-MM (4-IN.) TYPE 1 CRACK 174
FIGURE G. 10: CONVERGENCE STUDY OF K3 FACTOR FOR 203-MM (8-IN.) TYPE 2 CRACK 174

APPENDIX H: MAXIMUM PRINCIPAL STRESS IN THE WEB GAP REGION FOR THE ANGLES-WITH-PLATE RETROFIT MODELS

FIGURE H. 1: 13 MM [1/2 IN.] TYPE 1 CRACK &13 MM [1/2 IN.] TYPE 2 CRACK WITH NO RETROFIT 175
FIGURE H. 2: 13 MM [1/2 IN.] TYPE 1 CRACK & 13 MM [1/2 IN.] TYPE 2 CRACK WITH F-F RETROFIT 175
FIGURE H. 3: 13 MM [1/2 IN.] TYPE 1 CRACK & 13 MM [1/2 IN.] TYPE 2 CRACK WITH F-M RETROFIT 176
FIGURE H. 4: 13 MM [1/2 IN.] TYPE 1 CRACK & 13 MM [1/2 IN.] TYPE 2 CRACK WITH F-S RETROFIT 176
FIGURE H. 5: 13 MM [1/2 IN.] TYPE 1 CRACK & 13 MM [1/2 IN.] TYPE 2 CRACK WITH M-F RETROFIT 177
FIGURE H. 6: 13 MM [1/2 IN.] TYPE 1 CRACK & 13 MM [1/2 IN.] TYPE 2 CRACK WITH M-M RETROFIT 177
FIGURE H. 7: 13 MM [1/2 IN.] TYPE 1 CRACK & 13 MM [1/2 IN.] TYPE 2 CRACK WITH M-S RETROFIT 178
FIGURE H. 8: 13 MM [1/2 IN.] TYPE 1 CRACK & 13 MM [1/2 IN.] TYPE 2 CRACK WITH S-F RETROFIT 178
FIGURE H. 9: 13 MM [1/2 IN.] TYPE 1 CRACK & 13 MM [1/2 IN.] TYPE 2 CRACK WITH S-M RETROFIT 179
FIGURE H. 10: 13 MM [1/2 IN.] TYPE 1 CRACK & 13 MM [1/2 IN.] TYPE 2 CRACK WITH S-S RETROFIT 179
FIGURE H. 11: 25 MM [1 IN.] TYPE 1 CRACK & 25 MM [1 IN.] TYPE 2 CRACK WITH NO RETROFIT 180
FIGURE H. 12: 25 MM [1 IN.] TYPE 1 CRACK & 25 MM [1 IN.] TYPE 2 CRACK WITH F-F RETROFIT 180
FIGURE H. 13: 25 MM [1 IN.] TYPE 1 CRACK & 25 MM [1 IN.] TYPE 2 CRACK WITH F-M RETROFIT 181
FIGURE H. 14: 25 MM [1 IN.] TYPE 1 CRACK & 25 MM [1 IN.] TYPE 2 CRACK WITH F-S RETROFIT 181
FIGURE H. 15: 25 MM [1 IN.] TYPE 1 CRACK & 25 MM [1 IN.] TYPE 2 CRACK WITH M-F RETROFIT 182
FIGURE H. 16: 25 MM [1 IN.] TYPE 1 CRACK & 25 MM [1 IN.] TYPE 2 CRACK WITH M-M RETROFIT 182
FIGURE H. 17: 25 MM [1 IN.] TYPE 1 CRACK & 25 MM [1 IN.] TYPE 2 CRACK WITH M-S RETROFIT 183
FIGURE H. 18: 25 MM [1 IN.] TYPE 1 CRACK & 25 MM [1 IN.] TYPE 2 CRACK WITH S-F RETROFIT 183
FIGURE H. 19: 25 MM [1 IN.] TYPE 1 CRACK & 25 MM [1 IN.] TYPE 2 CRACK WITH S-M RETROFIT 184
FIGURE H. 20: 25 MM [1 IN.] TYPE 1 CRACK & 25 MM [1 IN.] TYPE 2 CRACK WITH S-S RETROFIT 184
FIGURE H. 21: 51 MM [2 IN.] TYPE 1 CRACK & 51 MM [2 IN.] TYPE 2 CRACK WITH NO RETROFIT 185
FIGURE H. 22: 51 MM [2 IN.] TYPE 1 CRACK & 51 MM [2 IN.] TYPE 2 CRACK WITH F-F RETROFIT 185
FIGURE H. 23: 51 MM [2 IN.] TYPE 1 CRACK & 51 MM [2 IN.] TYPE 2 CRACK WITH F-M RETROFIT 186
FIGURE H. 24: 51 MM [2 IN.] TYPE 1 CRACK & 51 MM [2 IN.] TYPE 2 CRACK WITH F-S RETROFIT 186
FIGURE H. 25: 51 MM [2 IN.] TYPE 1 CRACK & 51 MM [2 IN.] TYPE 2 CRACK WITH M-F RETROFIT 187
FIGURE H. 26: 51 MM [2 IN.] TYPE 1 CRACK & 51 MM [2 IN.] TYPE 2 CRACK WITH M-M RETROFIT 187
FIGURE H. 27: 51 MM [2 IN.] TYPE 1 CRACK & 51 MM [2 IN.] TYPE 2 CRACK WITH M-S RETROFIT 188
FIGURE H. 28: 51 MM [2 IN.] TYPE 1 CRACK & 51 MM [2 IN.] TYPE 2 CRACK WITH S-F RETROFIT 188
FIGURE H. 29: 51 MM [2 IN.] TYPE 1 CRACK & 51 MM [2 IN.] TYPE 2 CRACK WITH S-M RETROFIT 189
FIGURE H. 30: 51 MM [2 IN.] TYPE 1 CRACK & 51 MM [2 IN.] TYPE 2 CRACK WITH S-S RETROFIT 189
FIGURE H. 31: 102 MM [4 IN.] TYPE 1 CRACK & 203 MM [8 IN.] TYPE 2 CRACK WITH NO RETROFIT 190
FIGURE H. 32: 102 MM [4 IN.] TYPE 1 CRACK & 203 MM [8 IN.] TYPE 2 CRACK WITH F-F RETROFIT 190
FIGURE H. 33: 102 MM [4 IN.] TYPE 1 CRACK & 203 MM [8 IN.] TYPE 2 CRACK WITH F-M RETROFIT 191
FIGURE H. 34: 102 MM [4 IN.] TYPE 1 CRACK & 203 MM [8 IN.] TYPE 2 CRACK WITH F-S RETROFIT 191
FIGURE H. 35: 102 MM [4 IN.] TYPE 1 CRACK & 203 MM [8 IN.] TYPE 2 CRACK WITH M-F RETROFIT 192
FIGURE H. 36: 102 MM [4 IN.] TYPE 1 CRACK & 203 MM [8 IN.] TYPE 2 CRACK WITH M-M RETROFIT 192

FIGURE H. 37: 102 MM [4 IN.] TYPE 1 CRACK & 203 MM [8 IN.] TYPE 2 CRACK WITH M-S RETROFIT 193
FIGURE H. 38: 102 MM [4 IN.] TYPE 1 CRACK & 203 MM [8 IN.] TYPE 2 CRACK WITH S-F RETROFIT.....193
FIGURE H. 39: 102 MM [4 IN.] TYPE 1 CRACK & 203 MM [8 IN.] TYPE 2 CRACK WITH S-M RETROFIT 194
FIGURE H. 40: 102 MM [4 IN.] TYPE 1 CRACK & 203 MM [8 IN.] TYPE 2 CRACK WITH S-S RETROFIT.....194

APPENDIX I: DEFORMATION SCREENSHOTS IN THE WEB GAP REGION FOR THE ANGLES-WITH-PLATE RETROFIT MODELS

FIGURE I. 1: 13 MM [1/2 IN.] TYPE 1 CRACK & 13 MM [1/2 IN.] TYPE 2 CRACK WITH NO RETROFIT 195
FIGURE I. 2: 13 MM [1/2 IN.] TYPE 1 CRACK & 13 MM [1/2 IN.] TYPE 2 CRACK WITH F-F RETROFIT.....195
FIGURE I. 3: 13 MM [1/2 IN.] TYPE 1 CRACK & 13 MM [1/2 IN.] TYPE 2 CRACK WITH F-M RETROFIT.....196
FIGURE I. 4: 13 MM [1/2 IN.] TYPE 1 CRACK & 13 MM [1/2 IN.] TYPE 2 CRACK WITH F-S RETROFIT.....196
FIGURE I. 5: 13 MM [1/2 IN.] TYPE 1 CRACK & 13 MM [1/2 IN.] TYPE 2 CRACK WITH M-F RETROFIT.....197
FIGURE I. 6: 13 MM [1/2 IN.] TYPE 1 CRACK & 13 MM [1/2 IN.] TYPE 2 CRACK WITH M-M RETROFIT 197
FIGURE I. 7: 13 MM [1/2 IN.] TYPE 1 CRACK & 13 MM [1/2 IN.] TYPE 2 CRACK WITH M-S RETROFIT.....198
FIGURE I. 8: 13 MM [1/2 IN.] TYPE 1 CRACK & 13 MM [1/2 IN.] TYPE 2 CRACK WITH S-F RETROFIT.....198
FIGURE I. 9: 13 MM [1/2 IN.] TYPE 1 CRACK & 13 MM [1/2 IN.] TYPE 2 CRACK WITH S-M RETROFIT.....199
FIGURE I. 10: 13 MM [1/2 IN.] TYPE 1 CRACK & 13 MM [1/2 IN.] TYPE 2 CRACK WITH S-S RETROFIT 199
FIGURE I. 11: 25 MM [1IN.] TYPE 1 CRACK &25 MM [1 IN.] TYPE 2 CRACK WITH NO RETROFIT 200
FIGURE I. 12: 25 MM [1 IN.] TYPE 1 CRACK &25 MM [1 IN.] TYPE 2 CRACK WITH F-F RETROFIT.....200
FIGURE I. 13: 25 MM [1 IN.] TYPE 1 CRACK &25 MM [1 IN.] TYPE 2 CRACK WITH F-M RETROFIT.....201
FIGURE I. 14: 25 MM [1 IN.] TYPE 1 CRACK &25 MM [1 IN.] TYPE 2 CRACK WITH F-S RETROFIT.....201
FIGURE I. 15: 25 MM [1 IN.] TYPE 1 CRACK &25 MM [1 IN.] TYPE 2 CRACK WITH M-F RETROFIT.....202
FIGURE I. 16: 25 MM [1 IN.] TYPE 1 CRACK &25 MM [1 IN.] TYPE 2 CRACK WITH M-M RETROFIT 202
FIGURE I. 17: 25 MM [1 IN.] TYPE 1 CRACK &25 MM [1 IN.] TYPE 2 CRACK WITH M-S RETROFIT.....203
FIGURE I. 18: 25 MM [1 IN.] TYPE 1 CRACK &25 MM [1 IN.] TYPE 2 CRACK WITH S-F RETROFIT.....203
FIGURE I. 19: 25 MM [1 IN.] TYPE 1 CRACK &25 MM [1 IN.] TYPE 2 CRACK WITH S-M RETROFIT.....204
FIGURE I. 20: 25 MM [1 IN.] TYPE 1 CRACK &25 MM [1 IN.] TYPE 2 CRACK WITH S-S RETROFIT.....204
FIGURE I. 21: 51 MM [2 IN.] TYPE 1 CRACK &51 MM [2 IN.] TYPE 2 CRACK WITH NO RETROFIT 205
FIGURE I. 22: 51 MM [2 IN.] TYPE 1 CRACK &51 MM [2 IN.] TYPE 2 CRACK WITH F-F RETROFIT.....205
FIGURE I. 23: 51 MM [2 IN.] TYPE 1 CRACK &51 MM [2 IN.] TYPE 2 CRACK WITH F-M RETROFIT.....206
FIGURE I. 24: 51 MM [2 IN.] TYPE 1 CRACK &51 MM [2 IN.] TYPE 2 CRACK WITH F-S RETROFIT.....206
FIGURE I. 25: 51 MM [2 IN.] TYPE 1 CRACK &51 MM [2 IN.] TYPE 2 CRACK WITH M-F RETROFIT.....207
FIGURE I. 26: 51 MM [2 IN.] TYPE 1 CRACK &51 MM [2 IN.] TYPE 2 CRACK WITH M-M RETROFIT 207
FIGURE I. 27: 51 MM [2 IN.] TYPE 1 CRACK &51 MM [2 IN.] TYPE 2 CRACK WITH M-S RETROFIT.....208

FIGURE I. 28: 51 MM [2 IN.] TYPE 1 CRACK &51 MM [2 IN.] TYPE 2 CRACK WITH S-F RETROFIT 208
FIGURE I. 29: 51 MM [2 IN.] TYPE 1 CRACK &51 MM [2 IN.] TYPE 2 CRACK WITH S-M RETROFIT 209
FIGURE I. 30: 51 MM [2 IN.] TYPE 1 CRACK &51 MM [2 IN.] TYPE 2 CRACK WITH S-S RETROFIT 209
FIGURE I. 31: 102 MM [4 IN.] TYPE 1 CRACK &203 MM [8 IN.] TYPE 2 CRACK WITH NO RETROFIT 210
FIGURE I. 32: 102 MM [4 IN.] TYPE 1 CRACK &203 MM [8 IN.] TYPE 2 CRACK WITH F-F RETROFIT 210
FIGURE I. 33: 102 MM [4 IN.] TYPE 1 CRACK &203 MM [8 IN.] TYPE 2 CRACK WITH F-M RETROFIT 211
FIGURE I. 34: 102 MM [4 IN.] TYPE 1 CRACK &203 MM [8 IN.] TYPE 2 CRACK WITH F-S RETROFIT 211
FIGURE I. 35: 102 MM [4 IN.] TYPE 1 CRACK &203 MM [8 IN.] TYPE 2 CRACK WITH M-F RETROFIT 212
FIGURE I. 36: 102 MM [4 IN.] TYPE 1 CRACK &203 MM [8 IN.] TYPE 2 CRACK WITH M-M RETROFIT 212
FIGURE I. 37: 102 MM [4 IN.] TYPE 1 CRACK &203 MM [8 IN.] TYPE 2 CRACK WITH M-S RETROFIT 213
FIGURE I. 38: 102 MM [4 IN.] TYPE 1 CRACK &203 MM [8 IN.] TYPE 2 CRACK WITH S-F RETROFIT 213
FIGURE I. 39: 102 MM [4 IN.] TYPE 1 CRACK &203 MM [8 IN.] TYPE 2 CRACK WITH S-M RETROFIT 214
FIGURE I. 40: 102 MM [4 IN.] TYPE 1 CRACK &203 MM [8 IN.] TYPE 2 CRACK WITH S-S RETROFIT 214

APPENDIX J: BOLT MODELING TECHNIQUES

FIGURE J. 1: CREATED BOLT PART. 215
FIGURE J. 2: THE BOLT LOAD MUST BE NAMED. THE BOLT LOAD SHOULD BE APPLIED IN THE STEP BEFORE THE LOAD IS APPLIED. 216
FIGURE J. 3: APPLY BOLT LOAD TO THE INTERIOR SURFACE OF THE SHANK. 216
FIGURE J. 4: SELECT A SIDE FOR THE INTERNAL SURFACE DEPENDING ON WHAT COLOR IS SHOWN. IN THIS FIGURE, THE INTERIOR SURFACE IS HIGHLIGHTED BROWN, THEREFORE SELECT BROWN. 217
FIGURE J. 5: SELECT THE DATUM AXIS THAT CORRESPONDS TO THE LONGITUDINAL AXIS OF THE BOLT. IN THIS CASE, THE DATUM AXIS SHOULD BE Z. 217
FIGURE J. 6: ENTER THE BOLT LOAD FOUND IN THE AISC SPECIFICATION. 218
FIGURE J. 7: FIX THE LENGTH OF THE BOLT IN THE STEP WHERE A GLOBAL LOAD IS APPLIED TO THE MODEL. THIS STOPS THE BOLT FROM CONTINUING TO HAVE A PRE-TENSION LOAD. 218

APPENDIX K: FINITE ELEMENT MODELING MESHING TECHNIQUES

FIGURE K. 1: (A) FINITE ELEMENT MODEL MESH;(B) PARTITIONED REGION AROUND THE CIRCULAR OPENING;(C) MESH IN THE VICINITY OF THE CIRCULAR OPENING FOR AN ELEMENT SIZE AT THE OPENING OF 0.25 MM (0.01 IN.); (D) MESH IN THE VICINITY OF THE CIRCULAR OPENING FOR AN ELEMENT SIZE AT THE OPENING OF 0.13 MM (0.005 IN.) 220
FIGURE K. 2: (A) FINITE ELEMENT MODEL MESH;(B) PARTITIONED REGION AROUND THE CRACK-ARREST HOLE FOR THE DIAGONAL CRACK MODEL; (C) MESH IN THE VICINITY OF THE CRACK-ARREST HOLES FOR AN ELEMENT SIZE OF

1.80 MM [0.071 IN]; (D) MESH IN THE VICINITY OF THE CRACK-ARREST HOLES FOR AN ELEMENT SIZE OF 0.71 MM [0.028 IN].....222
FIGURE K. 3: (A) PARTITIONED REGION AROUND THE CRACK-ARREST HOLES FOR THE HORSESHOE-SHAPED CRACK MODEL; (B) MESH IN THE VICINITY OF THE CRACK-ARREST HOLES FOR THE HORSESHOE-SHAPED CRACK MODEL 223
FIGURE K. 4: (A) PARTITIONED REGION AROUND THE CRACK-ARREST HOLES FOR THE HORSESHOE-SHAPED & WEB-TO-FLANGE CRACK MODEL; (B) MESH IN THE VICINITY OF THE CRACK-ARREST HOLES FOR THE HORSESHOE-SHAPED & WEB-TO-FLANGE CRACK MODEL 224
FIGURE K. 5: (A) PARTITIONED REGION AROUND THE CRACK-ARREST HOLES FOR THE WEB-TO-FLANGE CRACK MODEL; (B) MESH IN THE VICINITY OF THE CRACK-ARREST HOLES FOR THE WEB-TO-FLANGE CRACK MODEL 225

LIST OF TABLES

PART 1: INTRODUCTION

N/A

PART 2: USE OF CFRP OVERLAYS TO REPAIR FATIGUE DAMAGE IN STEEL PLATES UNDER TENSION LOADING

TABLE 1: (A) HSS VS. MODULUS OF ELASTICITY OF THE CFRP OVERLAY (E_{CFRP}); (B) HSS VS. THICKNESS OF THE CFRP OVERLAYS (T_{CFRP}) ..... - 16 -
TABLE 2: SPECIMEN TEST MATRIX AND RESULTS 21
TABLE 3: MEASURED MATERIAL PROPERTIES FOR CFRP AND HYSOL RESIN 22
TABLE 4: FABRICATION OF MULTI-LAYERED CFRP OVERLAYS 24
TABLE 5: THEORETICAL FATIGUE LIFE OF UN-RETROFITTED SPECIMEN AND COMPARATIVE INCREASE IN FATIGUE LIFE OF CFRP REPAIRED SPECIMENS 34

PART 3: EFFECTIVENESS OF CRACK-ARREST HOLES UNDER DISTORTION-INDUCED FATIGUE LOADING

TABLE 1: VALUES FOR *C* AND UNITS FOR CRACK -ARREST HOLE EQUATIONS ..... - 48 -
TABLE 2: MODELING TEST MATRIX: SUMMARY OF HOLE DIAMETERS AND CRACK LENGTHS MODELED FOR DIFFERENT CRACK PATTERNS ..... - 67 -
TABLE 3: DIAGONAL CRACK PATTERN STRESSES ..... - 68 -
TABLE 4: HORSESHOE-SHAPED CRACK PATTERN STRESSES ..... - 69 -
TABLE 5: HORSESHOE-SHAPED & WEB-TO-FLANGE CRACK PATTERN STRESSES 70
TABLE 6: WEB-TO-FLANGE CRACK PATTERN STRESSES 71
TABLE 7: 102 MM [4.0 IN.] DIAMETER HOLE STRESSES 72
TABLE 8: OPTIMAL DIAMETER OF CRACK-ARREST HOLE FOR EACH CRACK TYPE WITH DIFFERENT CRACK LENGTH- 72 - 5

PART 4: EVALUATIONOF THREE COMPUTATIONAL TECHNIQUES FOR QUANTIFYING DISTORTION-INDUCED FATIGUE CRACK PROPENSITY USING FINITE ELEMENT ANALYSIS

TABLE 1: NAMING CONVENTION FOR RETROFIT COMBINATIONS USED IN THIS STUDY 107

TABLE 2: SUMMARY OF CRACK COMBINATIONS AND RETROFITS APPLIED 107
TABLE 3: BOTTOM WEB-GAP CRACK GROWTH FOR ANGLES-WITH-PLATE RETROFIT APPLIED TO 2.7-M (9-FT) SUBASSEMBLY 110

PART 5: RECOMMENDATIONS AND SYNTHESIS

TABLE 1: HORSESHOE-SHAPED & WEB-TO-FLANGE CRACK PATTERN STRESSES ..... - 72 -

Part 1

INTRODUCTION

This dissertation is divided into five parts and appendices, and presents investigations into three different techniques for repairing fatigue cracking in steel bridges. The techniques presented and discussed in this dissertation include adhesively bonded carbon fiber reinforced polymer (CFRP) overlays, crack-arrest holes, and a technique developed at the University of Kansas, termed the "angles-with-plate" retrofit. The repair approaches discussed are different from one another in terms of where in a bridge structure they might be applied, level of constructability, cost-effectiveness, and effectiveness in repairing different modes of fatigue. Additionally, the retrofit techniques described are at varying levels of field-readiness.

Part 2of this dissertation presents an investigation into the effectiveness of repairing fatigue damage in steel plate with adhesively bonded carbon fiber reinforced polymer (CFRP) overlays. The CFRP overlays investigated in this portion of the study were developed through analytical and experimental approaches with the aim to repair fatigue cracks propagating under in-plane tensile forces. Of the three retrofit techniques described in this dissertation, this technique is the least field-ready, but presents a framework for parameters which drive the effectiveness of such a retrofit, setting the stage for future work to be performed in which the general framework is extended into applications for various other detail geometries where in-plane fatigue is a concern.

Part 3 of this dissertation describes an investigation that examines the effectiveness of crack-arrest holes of varying diameters, placement, and crack length in a steel girder web subjected to distortion-induced fatigue. Distortion-induced fatigue cracking is much more common in steel bridge infrastructure than in-plane fatigue cracking, and bridge owners often utilize drilled crack-arrest holes in these cases as a "first response" against fatigue cracks

discovered during inspections. The purpose of a crack-arrest hole is to smooth out the sharp crack tip, reducing the stress concentration and halting/delaying crack propagation. Common knowledge has been that large diameter crack-arrest holes are more effective at halting crack propagation under distortion-induced fatigue than small diameter crack-arrest holes. However, drilling large diameter crack-arrest holes can have strength implications for a structure, and may not be desirable; additionally, there is little evidence in the literature that large diameter crack-arrest holes perform better than small diameter crack-arrest holes under distortion-induced fatigue. In relation to the other two retrofit techniques described in Parts 2 and 4, crack-arrest holes are "old technology," and are ubiquitous in application, meaning crack-arrest holes are commonly-applied to a multitude of steel bridges, and used in nearly any cracked detail in which they can be physically drilled. The present study is original in its consideration of their performance under the action of distortion-induced fatigue, which is a subject that has not been rigorously treated in the past.

Part 4 of this dissertation describes an evaluation of three analysis techniques for determining the effectiveness of an "angles-with-plate" retrofit for repairing distortion-induced fatigue. The three analysis techniques studied include: Hot Spot Stress analysis, J-integrals, and Stress Intensity Factors. The angles-with-plate retrofit was recently developed at the University of Kansas for repairing web-gap regions of steel bridge girders that are susceptible to distortion-induced fatigue cracking. This retrofit ranks highly in terms of field-readiness and was developed with constructability as a primary consideration. This study provides new information to the body of knowledge in that it provides guidance to researchers regarding the appropriateness of the three analysis techniques for evaluating distortion-induced fatigue susceptibility. In this regard, the main goal of this investigation was not to conclude the effectiveness of the angles-

with-plate retrofit, but to conclude the best analysis methods for evaluating effectiveness. Therefore, examining variations of the angles-with-plate retrofit provided a means with which to compare computational results across a suite of models. These results were considered in the context of a series of physical tests performed under separate investigation.

Finally, the discussion in Part 5 of this dissertation presents synthesis of the various parts of this work.

Part 2

USE OF CFRP OVERLAYS TO REPAIR FATIGUE DAMAGE IN STEEL PLATES UNDER TENSION LOADING

Fatih Alemdar[1]

Regan Gangel[2]

Adolfo Matamoros[3], A.M. ASCE

Caroline Bennett[4], A.M. ASCE

Ron Barrett-Gonzalez[5]

Stan Rolfe[6], P.E., Hon. M. ASCE

Hao Liu[7]

ABSTRACT

Fiber reinforced polymer (FRP) overlays have been successfully used in the aerospace industry to repair fatigue damage in aluminum plates. With this success there is potential for use of similar FRP overlays to repair fatigue damage in aging steel bridge structures. This study investigated the effectiveness of repairing fatigue damage in steel plate with adhesively bonded carbon fiber reinforced polymer (CFRP) overlays. A total of 15 steel plate specimens with pre-existing fatigue cracks were repaired with varying thicknesses of CFRP overlays to evaluate the effect of the ratio of axial stiffness of the composite to that of the underlying steel, *SR*, on increased fatigue life and decreased applied stress. The results showed that increasing the axial

[1] Fatih Alemdar, Graduate Research Assistant, University of Kansas, 1530 W. 15th St., Lawrence KS, 66045
[2] Regan Gangel, Graduate Research Assistant, University of Kansas, 1530 W. 15th St., Lawrence KS, 66045
[3]Adolfo Matamoros, PhD, Associate Professor, University of Kansas, 1530 W. 15th St., Lawrence KS, 66045
[4]Caroline Bennett, PhD, Assistant Professor, University of Kansas, 1530 W. 15th St., Lawrence KS, 66045
[5]Ron Barrett, PhD, Associate Professor, University of Kansas, 1530 W. 15th St., Lawrence KS, 66045
[6]Stan Rolfe, P.E., PhD, A.P. Learned Professor, University of Kansas, 1530 W. 15th St., Lawrence KS, 66045
[7] Hao Liu, Graduate Research Assistant, University of Kansas, 1530 W. 15th St., Lawrence KS, 66045

stiffness ratio from 0 to 0.4 could increase the fatigue life by a factor of 10 for the most extreme conditions, and with an optimal axial stiffness ratio infinite fatigue life may be reached. Fatigue life of the steel specimens in this study was found to be dependent on both axial stiffness and applied stress range. Results from finite element analyses validated the use of axial stiffness as a design parameter and correlated to the experimental results discussed.

INTRODUCTION

A significant number of aging steel bridge structures experience structural problems due to fatigue cracks. One repair technique that has been used by the Kansas Department of Transportation (KDOT) in cases where fatigue cracks have propagated significantly into girder webs is to retrofit the web with a full-depth bolted steel splice at the location of cracking. The intent of the splice is to provide an alternate load path around the damaged web, and it is designed for the full shear demand at that web location. Attaching full-depth splice plates to the damaged web does reduce the stress in the fatigue sensitive area (Roddis and Zhao 2001), however, this is an expensive repair and there is potential that with a full-depth steel splice plate covering the damaged region of a girder any additional crack propagation may be hidden from view and go unnoticed.

A more localized repair utilizing carbon fiber reinforced polymer (CFRP) materials could result in a more cost-effective and inspectable repair. One potential embodiment of this type of repair is a pair of CFRP overlay elements, one bonded to each face of the steel web over the crack with an epoxy resin layer. The CFRP overlays would not need to extend the full-depth of the web; instead, they could "patch" the region over the crack. However, before the potential of any such specific repair geometry can be effectively investigated, fundamental questions must be

answered concerning the effectiveness of CFRP overlays in extending the fatigue life of steel plate loaded in tension with a pre-existing fatigue crack. The aim of the research described in this article is to provide fundamental information concerning basic proportions (thicknesses) of CFRP overlays relative to the steel to which they are bonded to effectively slow or halt fatigue crack propagation in the steel under various stress demands. The effect of bond thickness and modulus of elasticity of CFRP on the reduction in stress at critical locations was also evaluated.

BACKGROUND

A significant amount of research on the use of composite materials has been carried out in the field of aerospace engineering to address fatigue problems in the fuselages of airplanes (Mall and Conley 2009; Umamaheswar and Singh 1999; Schubbe and Mall 1999; Naboulsi and Mall 1996; Lee and Lee 2004; Liu, Xiao, et al. 2009). The most recent research performed on this topic in the aerospace field has focused on the use of fiber reinforced polymer (FRP) patches to repair fatigue damage in aluminum plates. These studies have shown that FRP plates can reduce stresses in a vulnerable detail significantly if properly proportioned and bonded to the substrate. An experimental study by Mall and Conley (2009) reported that bonding a boron fiber reinforced polymer overlay to only one side of an aluminum specimen increased the fatigue crack propagation life between four and 10 times with respect to the propagation life of an untreated specimen. Wang et al. (2002) also found an increase in fatigue crack propagation life on the order of 10 times in aluminum plates repaired with FRP patches.

In the aerospace field a commonly used parameter for proportioning composite patches for the purpose of repairing fatigue damage is the stiffness ratio:

$$SR = E_{CFRP}t_{CFRP}/\ E_s t_s \quad (1)$$

where *SR* is the stiffness ratio defined as the ratio of axial stiffness of the composite to that of the underlying steel, E_{CFRP} is the modulus of elasticity of the CFRP, t_{CFRP} is the thickness of the CFRP patch, E_s is the modulus of the steel, and t_s is the thickness of the steel plate. The *SR* parameter is used to determine thickness of FRP needed to repair fatigue-damaged steel plates by assuming that the driving force is redistributed in proportion to the relative axial stiffness of the two materials. For aerospace structures the recommended stiffness ratio is 1.0 (Schubbe et al. 2009). Schubbe et al. (1999) performed experimental tests on aluminum plates repaired with a bonded composite patch and found that as the stiffness ratio increased, so did the fatigue life of both thin and thick plates. Stiffness ratios of 1.0 and 1.3 were evaluated in that study.

Although the use of CFRP overlays is not widely implemented in steel structures yet, several studies have investigated their use to repair fatigue-related damage. Tavakkolizadeh and Saadatmanesh (2003) studied the effectiveness of unidirectional CFRP sheets to improve the fatigue strength of S127x4.5 steel girders with pre-existing notch cracks. The authors reported that the fatigue-crack propagation life of the specimens with CFRP sheets was extended by a factor of approximately three compared with that of control specimens. Liu, Al-Mahaidi, et al. (2009) studied the tensile fatigue behavior of notched steel plates strengthened with single-ply CFRP patches. Results showed that single-sided repair extended the fatigue-crack propagation life of the specimen by a factor ranging between 2.2 and 2.7, whereas a double sided repair extended the fatigue-crack propagation life by a factor ranging between 4.7 and 7.9. Roy et al. (2009) performed a study using the same type of materials and procedure used by Liu et al.

(2009), and showed similar increases in fatigue-crack propagation life of steel plates repaired with single-sided CFRP patches as seen in Liu, Al-Mahaidi, et al. (2009). Bocciarelli et al. (2009) studied the use of double-sided CFRP overlays on uncracked steel plates under fatigue loading and found that failure was precipitated by debonding of the overlays. They also found that the fatigue performance of steel plates reinforced with CFRP plates was comparable to that of steel specimens with welded steel plates.

Kaan et al. (2012) studied the behavior of uncracked plate-coverplate connections repaired with CFRP overlays. Results showed that specimen behavior, according to the AASHTO design specifications, could be improved from a fatigue design Category E' detail to fatigue design Category B' or B detail. In this study, increased fatigue crack initiation life was a direct result of maintaining adequate bond.

Analytical modeling of CFRP repairs using the Finite Element (FE) method is also an important technique when developing efficient retrofit schemes for steel structures. Researchers (Liu, Xiao, et al. 2009; Lee and Lee 2004) have shown good agreement between the change in stress demand estimated using FE models and experimentally observed changes in fatigue-crack propagation life. In FE models that include a layer of resin between the CFRP overlay and the underlying metal, the potential for debonding can be assessed by comparing the stress demand in the resin with a limiting value. This approach was also adopted in the FE simulations conducted in this study.

OBJECTIVE AND SCOPE

The overall objective of the research described in this paper was to determine the effectiveness of CFRP overlays to repair existing fatigue damage in steel plate tested under cyclic tensile load.

The scope of study included both physical and computersimulations. First, fifteen steel plate specimens were repaired with CFRP overlays of various thicknesses to evaluate the effect of the axial stiffness ratio, *SR*, on fatigue crack propagation life and effective stress range. Second, relationships between the stiffness of the CFRP overlays and steel substrate were identified such that future CFRP repair techniques can be proportioned to effectively slow or halt fatigue crack propagation in the steel substrate. Third, the effect of bond layer thickness and CFRP overlay thickness on the reduction in Hot Spot Stress (HSS) was evaluated using FE models. In this paper, HSS was defined as the stress at a distance half the thickness of the steel plate away from the point of peak stress, which occurred at the edge of the hole (Marquis and Kaehoenen 1995). HSS was used as an indicator of stress range, and consequently, as a measure of the effectiveness of various composite overlay configurations. This technique has been used in other companion studies aimed at examining fatigue performance and behavior of steel bridges (Hassel 2011; Kaan et al. 2012; Hartman et al 2010). Finally, the effect of overlay stiffness on fatigue performance determined using the FE method was compared with observations from experimental results. FE simulations and experimental testing were performed on using specimens with the configuration shown in Fig 1.

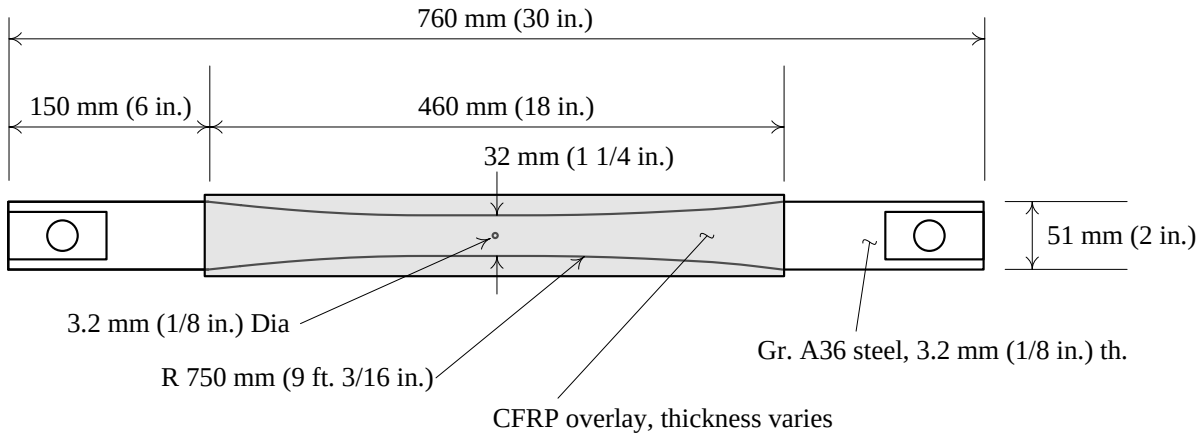

Figure 1: Tension specimen dimensions (3.2-mm 1/8-in. thick specimen)

FINITE ELEMENT SIMULATIONS

There are several parameters that can affect the performance of CFRP overlays as a fatigue repair technique for steel plates. A parametric study was carried out to investigate changes in the stress demand in specimens repaired with varying E_{CFRP} and t_{CFRP}. The effects of bond layer properties on peel and shear stress demands were also evaluated.

MODELING METHODOLOGY

Finite element simulations of the specimens tested during the experimental program (Fig. 1) were carried out using the commercially-available finite element analysis software ABAQUS version 6.8.2 (Simulia 2009). The models consisted of the steel specimen with a modulus of elasticity of 200 GPa (29,000 ksi), overlaid with 6-mm ($^1/_4$-in.) thick, 458-mm (18-in.) long CFRP plates with a modulus of elasticity of 83 GPa (12,000 ksi). The CFRP overlays were attached to each side of the specimen with a 0.6-mm (25-mil) thick resin interface having a

modulus of elasticity of 2 GPa (300 ksi). The study was performed by changing a single parameter while maintaining the remaining parameters constant.

FE models were developed using linear-elastic materials, and meshes were assembled using 8-node brick elements. The mesh configuration for the steel specimen part is shown in Fig. 2 (a). The mesh was configured using several regions with greater mesh density near the circular opening. The mesh configuration near the opening, presented in Figs. 2 (b) and 2(c), consisted of two concentric circular regions, which allowed gradually increasing element size away from the circular opening. Boundaries between the different regions of the mesh are illustrated in Fig. 2 (b).A convergence study was carried out and the results are illustrated in Fig. 2 (d). Because the maximum principal HSS near the circular opening was found to be insensitive to mesh size for the range of mesh densities explored, a mesh with a minimum element size of 0.25 mm (0.01 in.), shown in Fig. 2(b), was used in the study.

(a)

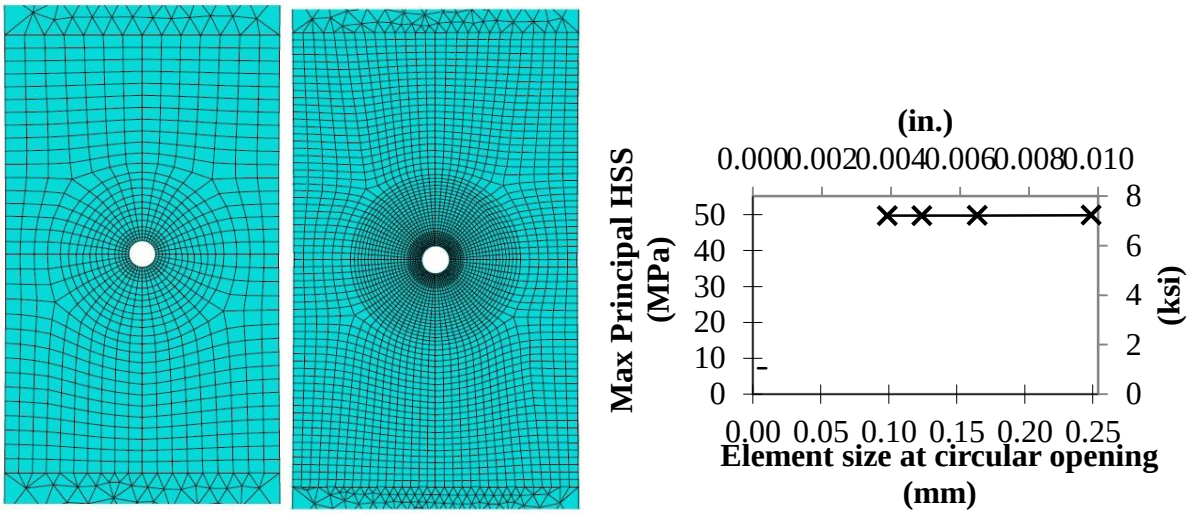

(b) **(c)** **(d)**

Figure 2: (a) Finite element model mesh (b) mesh in the vicinity of the circular opening for an element size at the opening of 0.25 mm (0.01 in.) (c) mesh in the vicinity of the circular opening for an element size at the opening of 0.13 mm (0.005 in.) (d) effect of element size at the circular opening on maximum principal HSS.

Interfaces between the steel, resin, and CFRP parts of the model were defined using tie constraints. Motion was restrained at one end of the model while the other end was free to move only in the vertical direction. Two 10.5-kN (2.35-kip) loads were applied in the vertical direction at the unrestrained end, one on each face of the model, simulating as closely as possible the manner in which the text fixture transferred the load from the testing machine. This load corresponded to a nominal testing stress range of 221 MPa (32 ksi), based on the steel net section area.

It is recognized that there are studies in which FE simulations of composite repairs have been performed using nonlinear constitutive relationships. Given the objective and scope of this study, a simpler modeling approach was adopted with the goal of limiting the effect of modeling assumptions on the computational results and because the consistency between the experimental

findings and simulation results did not warrant increasing the complexity of the computer simulations.

Comparisons of vulnerability to fatigue damage were performed on the basis of the maximum principal Hot Spot Stress (HSS) as defined in the Objective and Scope section of this paper.

EFFECT OF THE MODULUS OF ELASTICITY OF THE CFRP

Six models were developed to investigate the effect of the modulus of elasticity of the CFRP, E_{CFRP}, on stress imposed on the steel specimen. E_{CFRP} was varied between 27 GPa (3,860 ksi) and 138 GPa (20,000 ksi) in increments of 28 GPa (4,000 ksi). The effect of E_{CFRP} on HSS in the steel specimen is shown in Table 1. The relationship was found to be parabolic in nature and inversely proportional, indicating that there was a significant advantage associated with using an overlay, even if E_{CFRP} was relatively low. As Table 1 shows, HSS dropped by 58% with the introduction of an overlay with a very low modulus (26,600 MPa [3,860 ksi]) when compared with the unreinforced case. This data also shows that increasing E_{CFRP} resulted in diminishing returns, which is important to consider when determining optimal configuration of the overlay. Increasing E_{CFRP} by a factor of five, from 26,000 MPa (3,860 ksi) to 138,000 MPa (20,000 ksi), led to a reduction in HSS by a factor of approximately three. If infinite fatigue or propagation life can be achieved with a relatively inexpensive overlay, there is no economic incentive for using stiffer, and often much more expensive, fibers.

Table 1: (a) HSS vs. modulus of elasticity of the CFRP overlay (E_{CFRP}); (b) HSS vs. thickness of the CFRP overlays (t_{CFRP})

E_{CFRP} *MPa (ksi)*	0 (0)	26,600 (3,860)	55,200 (8,000)	82,737 (12,000)	110,300 (16,000)	137,900 (20,000)
HSS *MPa (ksi)*	249 (36)	105 (15)	67 (9.7)	49 (7.2)	39 (5.7)	32 (4.7)

(a)

t_{CFRP} *mm (in.)*	0 (0)	1.6 (1/16)	2.4 (3/32)	3.2 (1/8)	6.4 (1/4)	12.7 (1/2)
HSS *MPa (ksi)*	249 (36)	126 (18)	99 (14)	85 (12.3)	51 (7.4)	28 (4.1)

(b)

EFFECT OF THE THICKNESS OF THE CFRP OVERLAY

The effect of the CFRP overlay thickness, t_{CFRP}, on HSS was evaluated by varying the CFRP overlay thickness on each side of the steel plate using values of 1.6, 2.4, 3.2, 6.4, and 12.7 mm (1/16, 3/32, 1/8, 1/4, and 1/2 in.). Results for these variations are presented in Table 1. The relationship between t_{CFRP} and maximum principal HSS was found to be inversely proportional and parabolic. The addition of the thinnest CFRP tested, 1.6 mm (1/16 in.) decreased the maximum principal HSS by a factor of two when compared to an unreinforced specimen. Similar to the relationship when E_{CFRP} was varied, increasing t_{CFRP} exhibited diminishing returns.

RATIO OF OVERLAY AXIAL STIFFNESS TO STEEL AXIAL STIFFNESS

As discussed in the Introduction Section, one of the design parameters referenced in the literature for proportioning FRP patches is the ratio of axial stiffness of the composite patch to the axial stiffness of the underlying plate (Eq. 1). As Eq. 1 shows, this ratio may be modified by changing

the modulus of elasticity of the FRP, thickness of the FRP, or both. The results presented in Table 1 were used to derive two curves showing the effect of the stiffness ratio *SR* on the maximum principal HSS in the steel substrate (Fig. 2). For each curve, one of the two parameters (E_{CFRP} or t_{CFRP}) was varied while maintaining the other constant. All other parameters were equivalent to that of the base model.

The results presented in Fig. 3 show that changing *SR* by changing E_{CFRP} had similar results than changing *SR* by altering t_{CFRP}. There was a common trend, in that sequential increments in E_{CFRP} and t_{CFRP} resulted in similar reductions of HSS. Therefore, how the axial stiffness parameter was changed did not significantly affect the magnitude of the stress reduction.

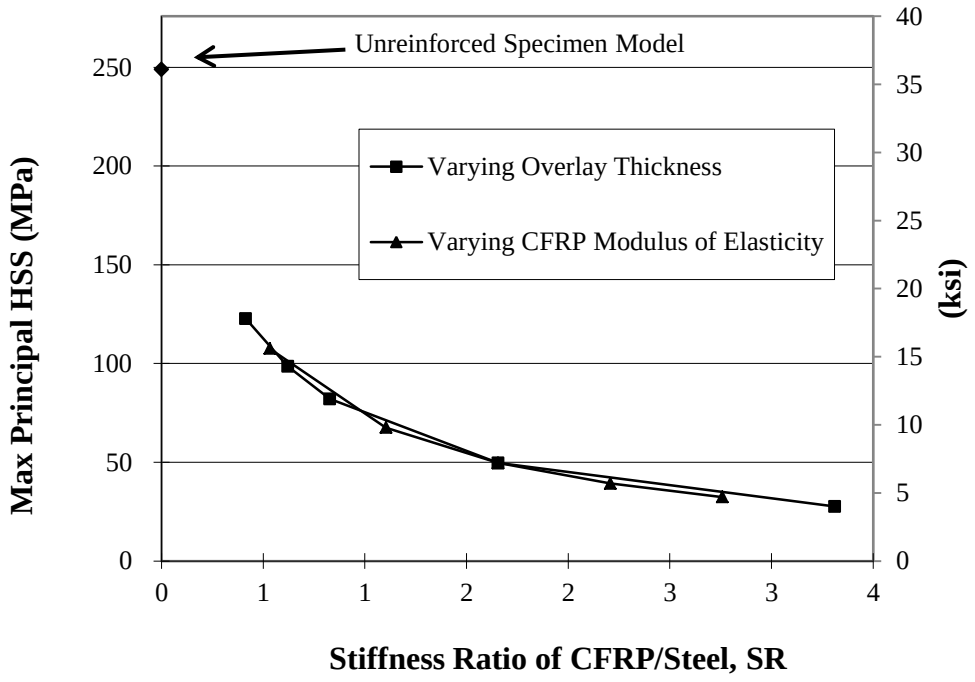

Figure 3: Effect of stiffness ratio on maximum principal Hot Spot Stress in the steel

The parameter that did have a significant effect on the HSS demand was the *SR*. Using an *SR* of approximately 0.41 decreased the maximum principal HSS by a factor of two, when compared with the stress demand in an unreinforced specimen. Increasing the *SR* of the overlay by a factor of 8 to approximately 3.3 had a much smaller effect, decreasing the maximum principal HSS by a factor of 5. The results in Fig. 3 confirm that the effect of the stiffness ratio on HSS decreased with increasing in stiffness ratio, and that the reduction in HSS had dropped significantly at an *SR* of 1.0.For these specimens, modeled with a 221 MPa (32 ksi) testing stress range, it is the opinion of the authors increasing *SR* of the overlay beyond 1.0 has limited benefits.

EFFECT OF THICKNESS OF BOND LAYER

One of the parameters often neglected in FE simulations of retrofit measures with composite overlays is the flexibility inherent to the adhesive resin used to bond the overlay to the metal substrate. It has often been assumed that the thickness of such a layer is very small, and that there is perfect bond between the composite and the substrate (Sabelkin et al. 2006; Liu, Xiao, et al. 2009; Mall and Conley 2009). Explicit modeling of this layer provides an indication of the average shear demand on the resin and the tensile demand on the resin-steel interface, which can be used to gage the potential for debonding. Because the shear and tensile demands on the resin are affected by the thickness of the resin layer, this is an important parameter to consider in terms of fatigue and fatigue crack propagation life.

Five different models were developed to investigate the effect of the thickness of the interface bond layer, t_{resin}, between the CFRP overlay and the steel substrate. The interface layer thickness was varied from 0.6 mm (20 mils) to 5 mm (200 mils). Results discussed by Alemdar

(2011) found that the maximum principal HSS was not significantly affected by t_{resin}. However, another important design consideration is the effect of t_{resin} on the stress demand at the resin layer itself. This is important because maintaining bond between the composite and the steel is critical to the successful performance of the retrofit scheme, and higher stress demands increase the probability of fatigue failure at the interface. Fig. 4 shows the stress demand along the resin layer for a model with t_{resin} = 0.6 mm (20 mil). A closed-form solution for a plate with constant width and without a circular hole presented by Bocciarelli et al. (2009) is also included for reference. Fig. 4shows that as expected based from the closed-form solution, the shear and peel stresses (out-of-plane stress) were relatively low along most of the interface. Stress demands were greatest at ends of the interface, which is the location considered to be the most susceptible to failure.

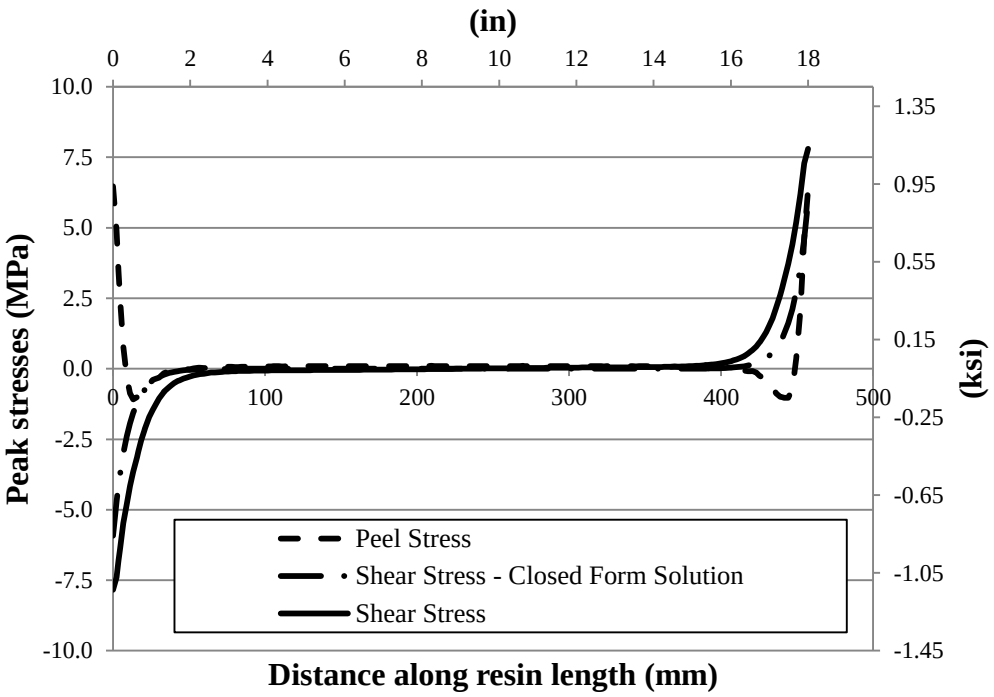

Figure 4: Peak stresses along CFRP overlay on resin layer end of hole

Figure5 presents the variation of peak shear and peel stresses as a function of the t_{resin}. Also in Fig. 5 is the closed-form solution presented by Bocciarelli. The results show that increasing t_{resin} from 0.6 mm (20 mil) to 5.0 mm (200 mil) caused a reduction in peak shear demand by approximately 66%. Figure5 also shows that the same increase in t_{resin} led to a reduction in peak peel stresses by approximately 50%. The trend observed for the peel stress was different from that observed for the shear stress in that the peel stress demand was relatively insensitive to t_{resin} for thicknesses less than 2.5 mm (100 mil), with a significant reduction in stress for t_{resin} greater than that. These data show that although the thickness of the interface layer may not be relevant to fatigue-crack propagation life due to the negligible effect on the stress range, it is a very important parameter in terms of the bond performance of the interface layer under cyclic loading.

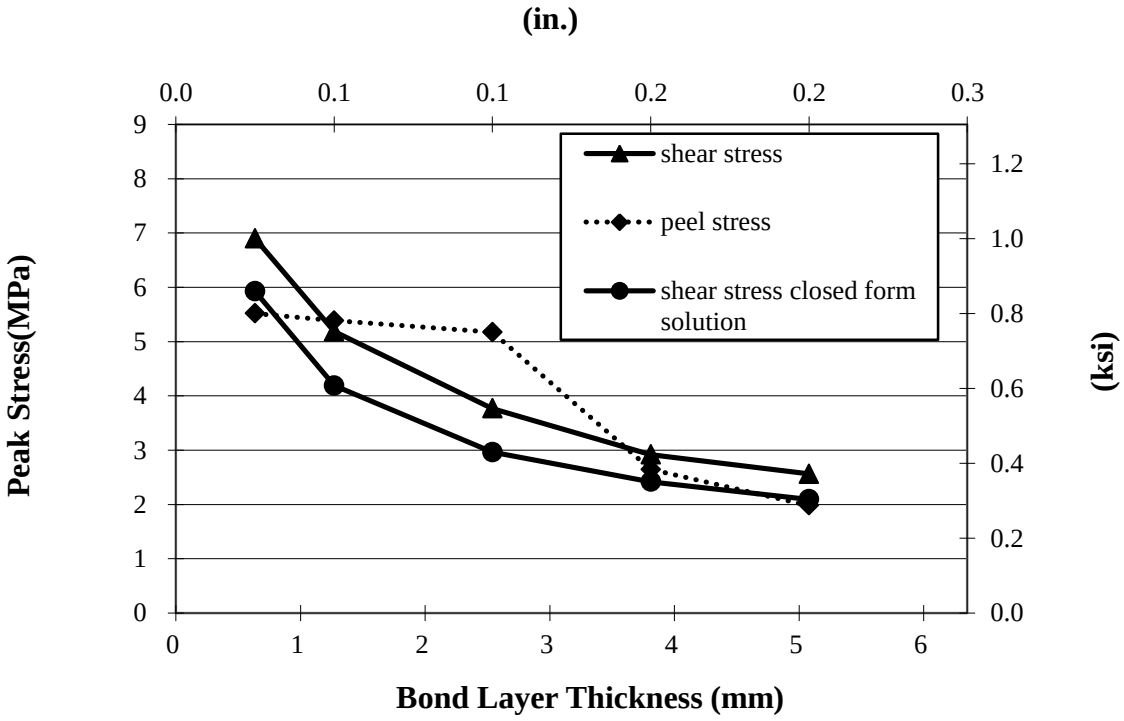

Figure 5: Peak stresses demand on CFRP layer as a function of resin layer thickness

EXPERIMENTAL PROGRAM

The primary goal of the experimental program was to evaluate the effect of stiffness ratio on fatigue crack propagation life of steel specimens with pre-existing fatigue cracks repaired using CFRP overlays. Fatigue cracks were propagated on each side of the drilled and reamed hole at the center of the specimen, shown in Fig.1, until either of the cracks reached a length of approximately 7 mm (0.3 in.). After the initial crack length of 7 mm (0.3 in.) was reached, each specimen was repaired using CFRP overlays. Fifteen specimens were tested, shown in Table 2.

Table 2: Specimen test matrix and results

Specimen Designation	Specimen Thickness mm (in.)	CFRP Overlay Thickness mm (in.)	Stress Range MPa (ksi)	Fatigue Crack Propagation Life
F15	3 ($^1/_8$)	1.6 ($^1/_{16}$)	263 (38)	18,900
F3	3 ($^1/_8$)	1.6 ($^1/_{16}$)	221 (32)	60,000
F6	3 ($^1/_8$)	1.6 ($^1/_{16}$)	166 (24)	340,700
Pick12	3 ($^1/_8$)	2.4 ($^3/_{32}$)	221 (32)	271,100
Pick11	3 ($^1/_8$)	3.2 ($^1/_8$)	263 (38)	95,100
F14	3 ($^1/_8$)	3.2 ($^1/_8$)	221 (32)	313,050
F2	3 ($^1/_8$)	3.2 ($^1/_8$)	166 (24)	1,450,095
Pick10	3 ($^1/_8$)	6.4 ($^1/_4$)	263 (38)	282,550
Pick13	3 ($^1/_8$)	6.4 ($^1/_4$)	221 (32)	Run-Out
Pick7	3 ($^1/_8$)	6.4 ($^1/_4$)	166 (24)	Run-Out
F27	3 ($^1/_8$)	12.8 ($^1/_2$)	221 (32)	Run-Out
F4-25	6 ($^1/_4$)	1.6 ($^1/_{16}$)	221 (32)	15,600
F4-21	6 ($^1/_4$)	3.2 ($^1/_8$)	221 (32)	160,150
F4-23	6 ($^1/_4$)	6.4 ($^1/_4$)	221 (32)	571,650
F4-20	6 ($^1/_4$)	12.8 ($^1/_2$)	221 (32)	Run-Out

Of the four parameters in Eq. 1 that could have been varied to alter the stiffness ratio, two were varied in this study: t_{CFRP} and the thickness of the steel plate, t_s. Testing was conducted at

stress ranges of 166 MPa (24 ksi), 221 MPa (32 ksi) and 263 MPa (38 ksi), to evaluate effect of *SR*at various stress ranges.

Measured material properties are presented in Table 3. Coupon tests (ASTM 2000) from single-layered specimens showed that E_{CFRP} was approximately 83 GPa (12,000 ksi). Liu et al. (2009) observed in their experiments that after the second layer of CFRP the strain demand quickly dropped; therefore, E_{CFRP} used for the computer simulations was selected to be between measured values for one and three layers. The modulus of elasticity of the 9412 Hysol® resin, E_{resin}, was also measured using coupon tests (Table 3) performed as prescribed by ASTM (2000). The measured $E_{resin}$was 2.1 GPa (300 ksi).

Table 3: Measured material properties for CFRP and Hysol resin

Continuous CFRP

No. of Layers in Coupon	No. of Coupons	Avg. Modulus of Elasticity *GPa (ksi)*	Std. Dev. *GPa (ksi)*
1	3	85.8 (12,440)	10.0 (1,450)
3	4	75.3 (10,930)	10.9 (1,580)
5	3	61.7 (8,940)	0.3 (42.0)

9412 Hysol Resin

Coupon Thickness *mm (in.)*	No. of Coupons	Avg. Modulus of Elasticity *GPa (ksi)*	Std. Dev. *GPa (ksi)*
6 (1/4)	6	2.1 (303)	0.2 (25)

STEEL SPECIMEN DIMENSIONS

The specimens were fabricated using grade A36 steel and were either 3-mm ($^1/_8$-in.) or 6-mm ($^1/_4$-in.) thick. For specimens with a thickness of 3 mm ($^1/_8$ in.), the measured average yield

strength was 319 MPa (46 ksi), and the measured tensile strength was 381 MPa (55 ksi). For specimens with a thickness of 6 mm ($^1/_4$ in.), the measured average yield strength was 335 MPa (48 ksi), and the measured tensile strength was 495 MPa (72 ksi) (Crain 2010).

Specimen dimensions for 3-mm ($^1/_8$-in.) thick specimens are shown in Fig. 1. There were three dimensions changed for 6-mm ($^1/_4$-in.) thick specimens with respect to those shown in Fig. 1. First, the width at each end was 63.5 mm (2.5 in.) instead of 60.8 mm (2.0 in.). Second, the width at the reduced net section was 44.5 mm (1.75 in.) instead of 31.8 mm (1.25 in.). Third, the diameter of the drilled and reamed hole at the specimen center was equal to the thickness of the specimen, 6mm ($^1/_4$ in.).

FABRICATION AND ATTACHMENT OF THE MULTI-LAYERED CFRP OVERLAYS

The multi-layered CFRP overlays were pre-fabricated and subsequently attached to the steel specimens. Step-by-step instructions, photographs and diagrams illustrating the fabrication process are presented by Alemdar (2011) and Gangel (2012). Each CFRP overlay consisted of multiple layers of bidirectional pre-impregnated carbon fiber plies. Scotch-Weld Epoxy adhesive (1838 B/A Green) was used between certain layers to ensure that there was a sufficient amount of resin to prevent voids from occurring during the curing process. Table 4 summarizes the number of carbon fiber plies and Scotch Weld Epoxy adhesive layers used in each CFRP overlay.

Table 4: Fabrication of multi-layered CFRP overlays

Overlay Thickness mm (in.)	Single Carbon Fiber Plies	Scotch Weld Epoxy adhesive	Placement of Adhesive
1.6 ($^1/_{16}$)	2	1	After 1st ply
2.4 ($^3/_{32}$)	3	1	After 2rd ply
3.2 ($^1/_8$)	4	2	After 2rd ply
6.4 ($^1/_4$)	8	3	After 3rd and 5th ply
12.8 ($^1/_2$)	16	4	After 4th, 8th, and 12th ply

The overlays were fabricated using a mold consisting of aluminum plates placed between bolted steel plates. Pre-impregnated carbon fiber plies were cut to dimensions of approximately 457 x 152 mm (18 x 6 in.), which was double the size of the overlays. CFRP sheets were placed on the bottom steel plate of the mold, and were added one layer at a time. A single sheet of Scotch-Weld Epoxy adhesive (1838 B/A Green) resin with the same dimensions was added, following the schedule presented in Table 4. The overlay was surrounded by an aluminum spacer with a thickness equal to that of the desired overlay thickness. The top steel plate of the mold was then placed on top of the CFRP stack, and pressure was applied by tightening the bolts around the perimeter of the mold to reach the target thickness. Then, the overlay was placed in a curing oven preheated to a temperature of 175 C (347 *F)*. Overlays were cured inside the mold for three hours, and subsequently allowed to cure at room temperature for 48 hours. After the curing process was completed, the CFRP overlays were taken out of the metal molds and cut to final dimensions of 457 x 64 mm (18 x 2.5 in.) using a diamond saw. Sand paper (grade 400) was used to smooth the edges of the CFRP overlays.

To develop adequate bond, the steel surface was prepared by a process of abrading and cleaning. Abrading consisted of roughening of the surface with a hand grinder to achieve a surface roughness of approximately 0.8 mm (30 mils). After abrading, cleaning of the surface

was performed using acetone and methanol. Overlays were attached to the steel specimens using Hysol® 9412 epoxy resin, which has a nominal shear strength of 28 MPa (4 ksi) (Hysol® 2001). The thickness of the Hysol® layer was 0.6 mm (24 mil), maintained during fabrication by using six spacers evenly distributed throughout the interface. Drafting tape surrounding the steel plate was used to prevent leaking of the Hysol® resin, and pressure was applied to maintain t_{resin} = 0.6 mm (24 mils). After two days of room-temperature curing the interface bond layer, the specimen was cleaned of remnant resin using a chisel and a heat gun.

TEST PROCEDURE

A cyclic tensile load was applied at the ends of the specimen using an MTS closed-loop servo-controlled loading system. The stress range applied to the steel specimen, $\Delta\sigma_{st,}$ was determined based on the following equation:

$$\Delta\sigma_{st} = \frac{F_{actuator}}{A_{net,st}} \quad (2)$$

where $F_{actuator}$is the force or load recorded by the actuator, and $A_{net,st}$ is the nominal net cross sectional area of the steel at the reduced cross-section less the area of the drilled hole. These values, although not representative of the peak stress demand, were adopted to simplify the comparison between various specimens. The ratio of minimum to maximum stress was maintained constant at R = 0.1. The rate of fatigue crack propagation was evaluated at three different stress ranges, 262 MPa (38 ksi), 221 MPa (32 ksi) and 166 MPa (24 ksi).

The propagation life of the steel specimens used in this study was calculated for different stress range demands based on established theoretical expressions. Theoretical crack lengths at a

given number of cycles were determined using the following equation presented by Barsom and Rolfe (1999):

$$\frac{da}{dN} = A(\Delta K)^m \quad (3)$$

where A and m are properties constant for a material, ΔK is the stress intensity factor range, a is crack length, and da is the change in crack length. Material constants of A=3.6 x 10^{-10} and m=3 were adopted, which correspond to values for ferrite-pearlite steel (Barsom and Rolfe, 1999). Because fatigue cracks extended from a round hole on a plate with a finite width, ΔK was calculated using the following equation (Barsom and Rolfe 1999):

$$\Delta K = \Delta\sigma\sqrt{\frac{\pi \times a_{avg}}{Q}} \times f\left(\frac{a}{r}\right) x f\left(\frac{a}{b}\right) \quad (4)$$

where $\Delta\sigma$ is the applied testing stress range, a_{avg} is the average crack length between incremental calculation steps, Q is the flaw-shape parameter (taken as 1.0 in this case), $f(a/r)$ is a function of the radius of the drilled hole to crack length, and $f(a/b)$ is a function of the crack length to finite width of the tensile specimen. Alemdar (2011) showed that good agreement was found between the calculated and measured crack progressions for unretrofitted specimens based Eq. 3 and 4.

A comparison between observed fatigue-crack propagation rate of the specimens with CFRP overlays and the calculated fatigue-crack propagation rate in unreinforced specimens with low stress demands is presented in Fig. 6. As shown in Fig. 6, the crack propagation rate of a specimen repaired with CFRP overlays subjected to a stress range of 166 MPa (24 ksi) was similar to that of an unrepaired specimen subjected to a stress range of 35 MPa (5 ksi) based on

theoretical values. These results indicate that the presence of the overlay resulted in a reduction of approximately 80% in the stress range. The test of the specimen repaired with multi-layered CFRP overlay subjected to a stress range of 166 MPa (24 ksi) was stopped after 4 million cycles, after crack growth started to become noticeable. Had the fatigue crack in this specimen continued to propagate at the theoretical rate for an unreinforced specimen under a stress range of 35 MPa (5 ksi), it would have reached a crack length of 7.6 mm (0.3 in.) at approximately 6 million cycles. A similarly loaded unrepaired steel specimen reached a crack length of 7.6 mm (0.3 in.) at only 50,000 cycles (Alemdar, 2011).

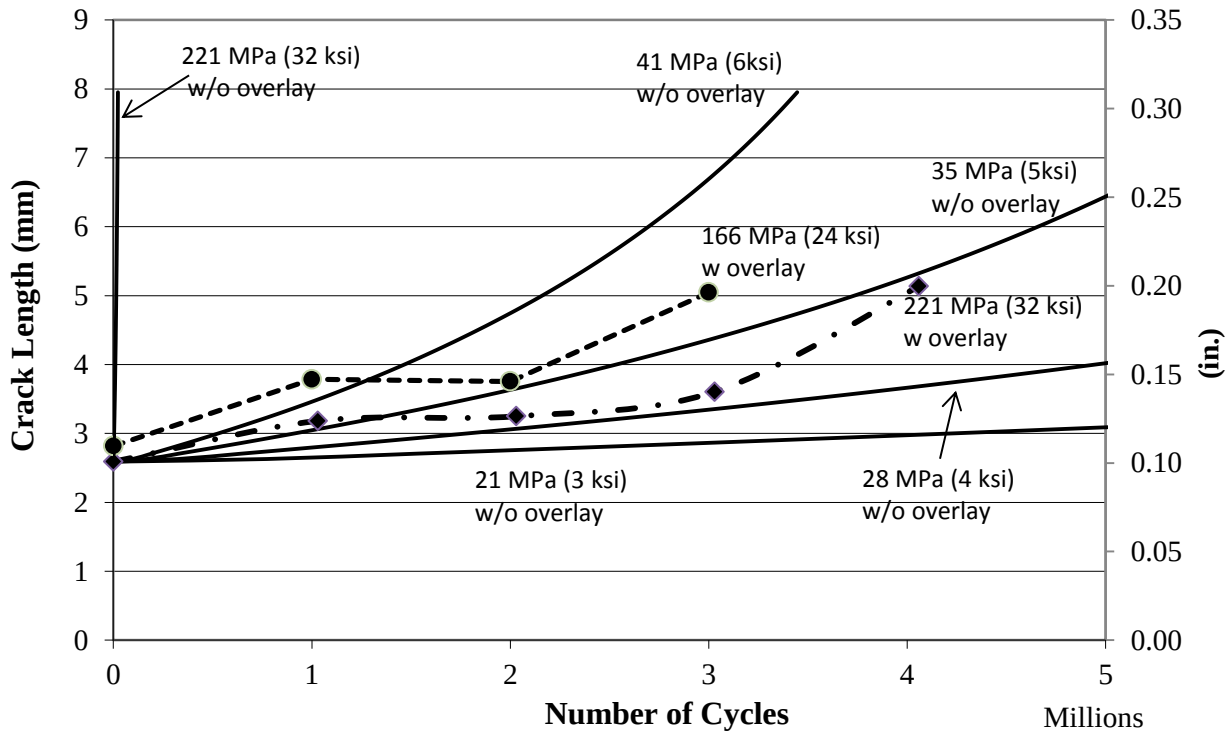

Figure 6: Crack progression in 3-mm ($^1/_8$ in.) thick specimens. Solid lines are added for comparison and correspond to theoretical crack progressions calculated using Eq. 4 with material constants of $A=3.6\text{x}10^{-10}$ and $m=3$ for various stress ranges in a specimen configuration without overlays.

Testing of the remaining specimens with CFRP overlays was carried out without removing the overlays for inspection so that that any cumulative damage to the interface layer and the composite overlay could be directly accounted for in the test results. Each test was terminated after the specimens reached failure or run-out. Failure of these specimens was defined as fatigue crack propagation completely through the width of the steel specimen; however, crack propagation and failure could not be tracked visually due to the bonded overlays. Instead, failure was indicated by a decrease in the percent change in stiffness of the system. The percent change in stiffness was calculated using the following equation:

$$\% \text{ change in } K = [(\delta L/\delta P) - K_{max}] / K_{max} \quad (5)$$

where K is the stiffness of the combined steel and CFRP overlays, δL is the change in load placed on the specimen, δP is the change in position from the testing machine, and K_{max} is the maximum stiffness recorded during testing. Run-out was defined as exceeding the AASHTO S-N curve for a Category A detail at the corresponding nominal stress range (AASHTO 2010).

The relationship between the change in stiffness and the number of cycles for 6-mm ($^1/_4$-in.) thick specimens tested at 221 MPa (32 ksi) are presented in Fig. 7.The relationship between the stiffness and the number of cycles for all the specimens tested in the study is reported by Gangel (2012) and Alemdar (2011).

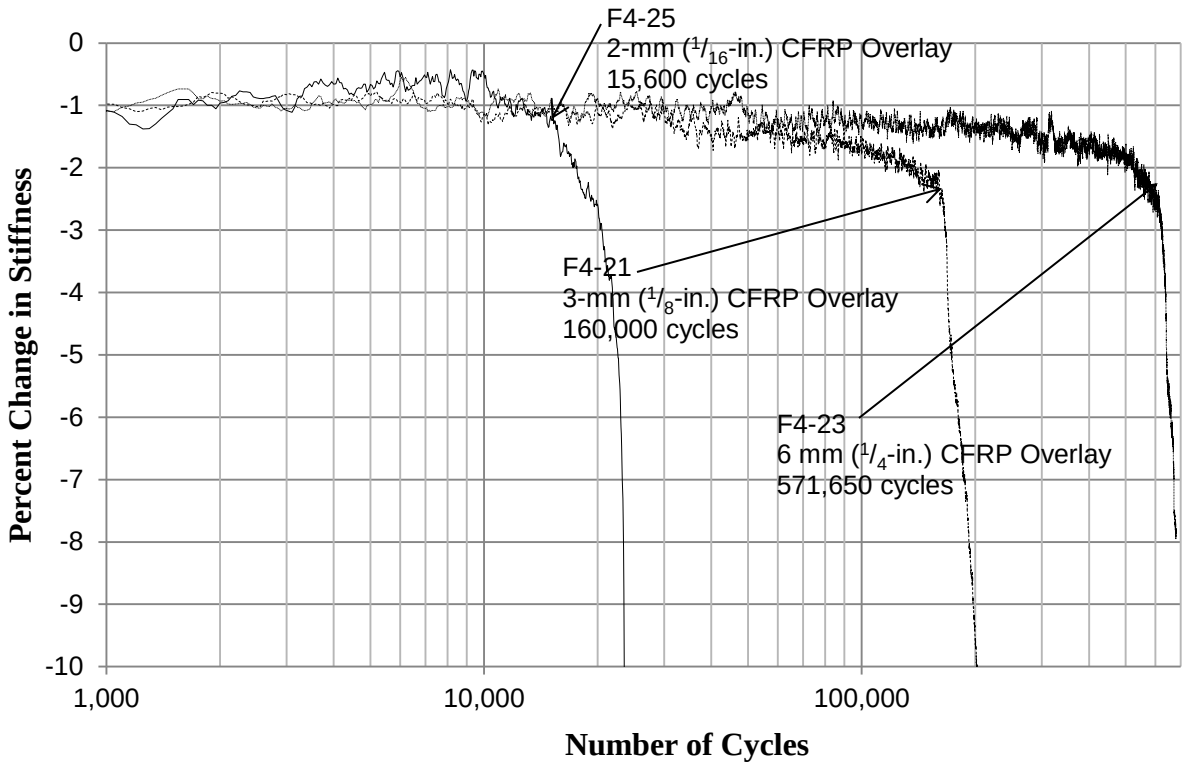

Figure 7: Percent change in stiffness of 6-mm ($^1/_4$-in.) thick specimens tested at 221 MPa (32 ksi).

EXPERIMENTAL RESULTS

The fatigue-crack propagation life of the steel substrate from an initial crack length of 7.6 mm (0.3 in.) to complete failure in the steel was determined based on the monitored change in stiffness calculated using Eq. 5. For all specimens a significant increase in compliance was observed at a given number of cycles during testing (Fig. 7). Because testing was performed under load control, any increase in compliance had to be caused by softening of the specimens, which is indicative of damage. An increase in compliance could be caused by loss of bond, damage in the composite overlays, or a reduction in the net cross sectional area of the steel specimen. Because the neither the composite overlays nor the interface layer showed signs of damage or distress, it was hypothesized that gradual increases in compliance were caused primarily by the reduction of the net cross sectional area of the steel specimen. Propagation of

the fatigue crack through the entire cross section of the specimen led to 100% of the load being transferred through the composite overlays. This new load path caused a rapid increase in the damage to the overlays in the vicinity of the fatigue crack and to local loss of bond, leading to a large increase in compliance. The number of cycles at which a sudden and significant change in compliance was observed was adopted as the fatigue propagation life for the specimen. Upon the conclusion of testing, the CFRP overlays were removed to inspect the steel specimen and confirm that the fatigue crack had in fact propagated through the entire net section of the steel. The number cycles to failure for each specimen determined in this manner are summarized in Table 2 and Figs. 8a and 8b.

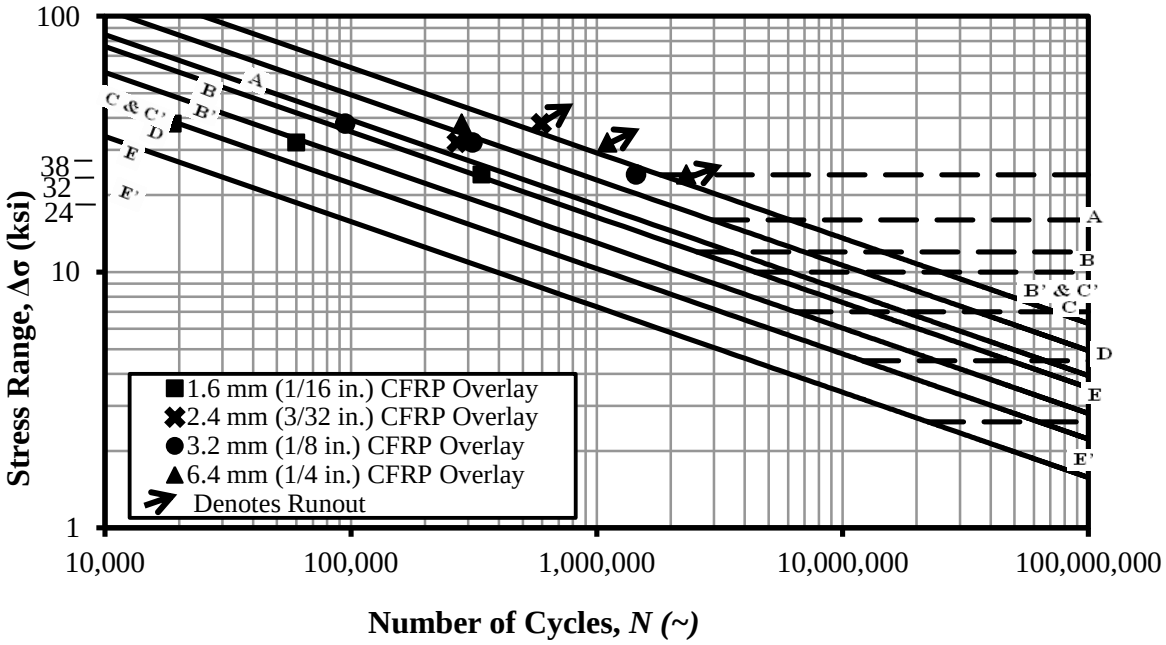

(a)

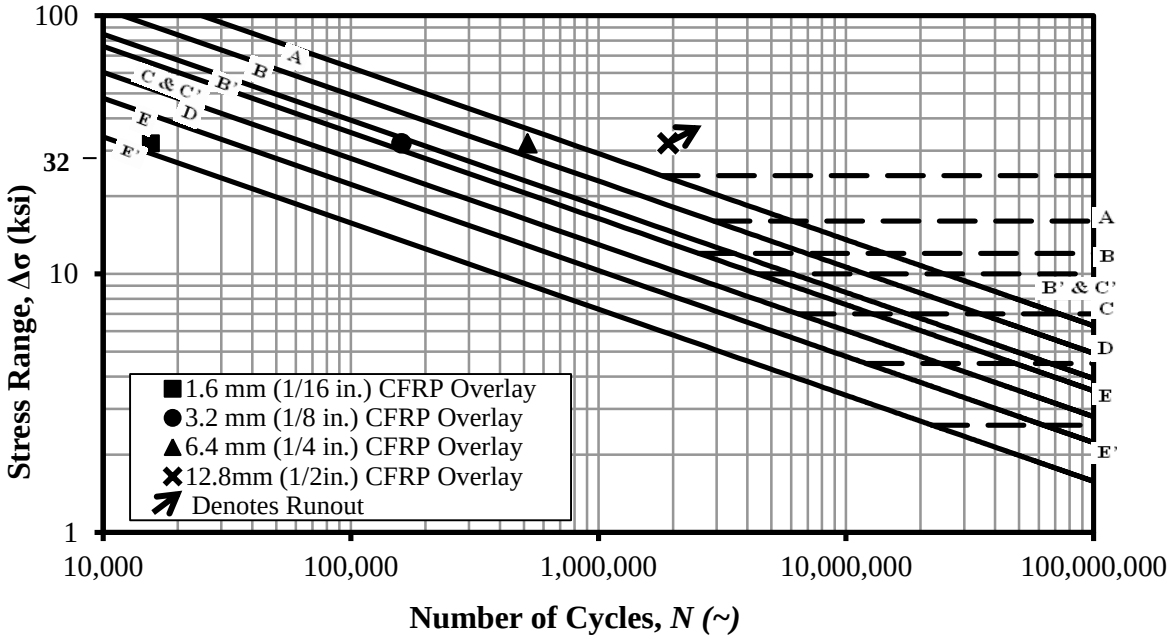

(b)

Figure 8: S-N diagram for propagation life for (a) 3-mm ($^1/_8$-in.) thick specimens and (b) 6-mm ($^1/_4$-in.) thick specimens

For Specimens Pick 13, Pick 7, F27, and F4-20, a significant change in compliance was never observed and these specimens were classified as run-out. The stress reduction in the steel due to the alternate load path provided by the CFRP overlay was sufficient to drive the demand below the fatigue crack propagation threshold (Barsom and Rolfe 1999). The composite overlays were removed for inspection after testing was complete, and it was confirmed that the fatigue cracks had not propagated fully through the steel cross-sections.

EFFECT OF STIFFNESS RATIO

The fatigue-crack propagation lives determined above were compared on the basis of the axial stiffness ratio. The value of *SR* was determined for each specimen based on E_{CFRP} = 83 GPa (12,000 ksi), the measured thickness of the steel, t_s, the CFRP overlay thickness used, t_{CFRP}, and

the modulus of elasticity of steel, E_s (200 GPa, 29,000 ksi). Figure9 shows the fatigue-crack propagation life of each specimen vs. the stiffness ratio, *SR*. For specimens that reached run-out (the last point of each curve, outside the range of the graph), the number of cycles to failure was extrapolated using accepted models of theoretical crack propagation presented by Barsom and Rolfe (1999). Extrapolated points (not shown) for the four curves were 22.9, 6.8, 3.9, and 3.2 million cycles, corresponding to *SR* values of 1.66, 1.66, 1.66, and 3.2, respectively.

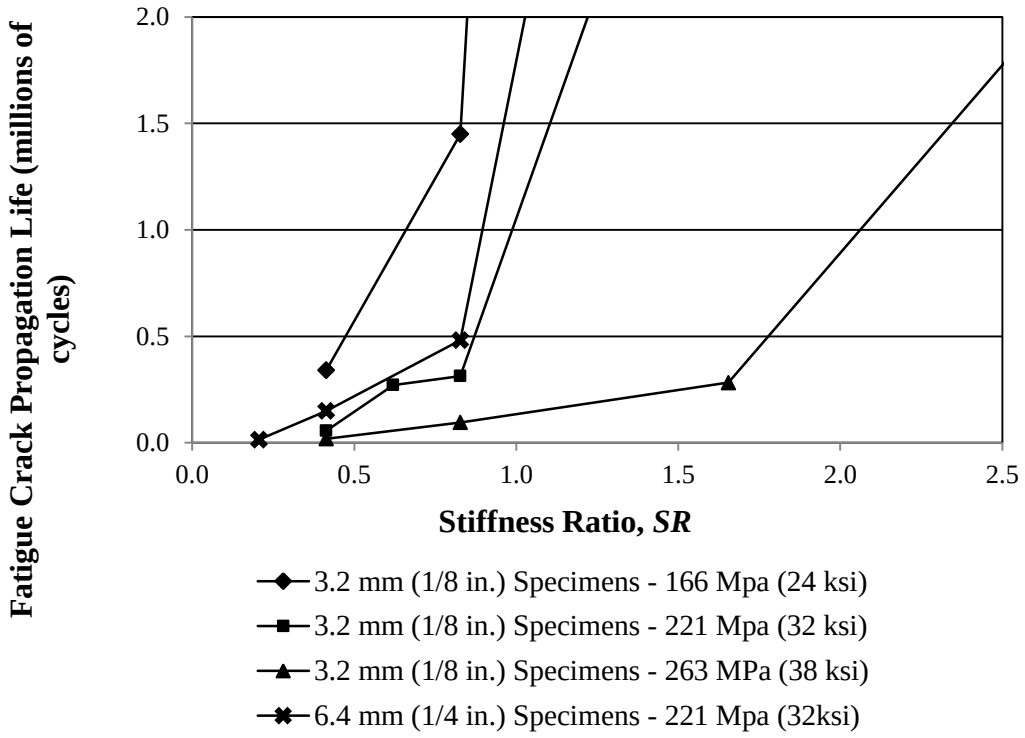

Figure 9: Fatigue-crack propagation life for all specimens treated with CFRP overlays and an initial crack length of 7 mm (0.3 in.)

Figure9 shows that the effect of the *SR* was dependent on the applied stress range. For a specific stiffness ratio, as the stress range increased the fatigue life decreased, as expected.

However, this trend was not proportional. Much greater improvement was observed when the stress range decreased from 221 MPa (32 ksi) to 166 MPa (24 ksi) than when the stress range decreased from 263 MPa (38 ksi) to 221 MPa (32 ksi).

Figure9 also shows a relationship between propagation life and *SR* that may be approximated as bilinear. For all specimens, the fatigue-crack propagation life increased as the stiffness ratio increased. For each stress range there was a stiffness ratio at which the slope of the curve had a sudden increase, trending towards infinity. Past this point, small increases in the stiffness ratio resulted in propagation lives that vastly exceeded run-out. It is clear from Fig. 9 that the critical *SR* at which each set of data trended towards infinity increased with stress range. The critical *SR* for specimens tested at stress ranges of 166 MPa (24 ksi), 221 MPa (32 ksi), and 263 MPa (38 ksi) were approximately 0.8, 1.0, and 1.6, respectively, regardless of specimen thickness. These results indicate that as stress range increases, the stiffness ratio must be increased to achieve infinite fatigue life.

Because the critical width of the 6-mm (¼-in.) thick specimens differed from that of the 3-mm ($^1/_8$-in.) thick specimens, failure of the former specimens was taken as the number of cycles at which the crack reached a length of 14 mm ($^9/_{16}$ in.). Therefore, the propagation life used in the comparisons corresponds to the same crack growth for all specimens, regardless of specimen thickness, allowing a direct comparison between the two. A direct comparison between the 3-mm ($^1/_8$-in.) thick and the 6-mm (¼-in.) thick specimens tested at 221 MPa (32 ksi) (Fig. 9) shows that for the same stiffness ratio the thicker specimen had the greater propagation life. However, both specimens had approximately the same critical stiffness ratio.

Given the relatively large initial crack size of 7.6 mm (0.3 in.) relative to the remaining steel net section, control specimens were not tested in this study as their fatigue lives would have

been quite low in the unreinforced condition. However, theoretical crack propagation lives for un-retrofitted specimens were determined using Eq. 3. With the calculation of ΔK from Eq. 4, the theoretical number of cycles to failure of an unretrofitted specimen can be found from Eq. 3 if the change in crack length (*da)* is set as the distance from an initial crack length of 7.6 mm (0.3 in.) to the edge of the specimen. The results of this theoretical fatigue crack propagation life for un-retrofitted specimens are shown in Table 5 designated as having a stiffness ratio of 0.

Table 5: Theoretical fatigue life of un-retrofitted specimen and comparative increase in fatigue life of CFRP repaired specimens

		3 mm ($^1/_8$ in.) steel specimens			6 mm ($^1/_4$ in.) steel specimens			
		Stress Range			Stress Range			
	Stiffness Ratio	166 MPa (24 ksi)	221 MPa (32 ksi)	263 MPa (38 ksi)	166 MPa (24 ksi)	221 MPa (32 ksi)	263 MPa (38 ksi)	Description
(a)	0	6,891	2,907	1,736	10,423	4,397	2,625	Theoretical fatigue crack propagation life (cycles) calculated using Equations 3 and 4
(b)	0.21	--	--	--	--	3	--	Increase in fatigue life from theoretical values to measured values (Table 4)
	0.41	49.4	19.2	10.9	--	34	--	
	0.62	--	93.3	--	--	--	--	
	0.83	210.4	107.7	54.8	--	109.5	--	
	1.66	run-out	run-out	162.8	--	run-out	--	
	3.31	--	--	run-out	--	--	--	

After the theoretical fatigue crack propagation life of unretrofitted specimens was calculated for an initial crack length of 7.6 mm (0.3 in.), it was compared with the fatigue crack propagation lives of CFRP repaired specimens, which are presented in Table 2. The ratio of observed fatigue crack propagation life of the various retrofitted specimens to calculated fatigue life of the unretrofitted specimen is presented in Table 5. Table 5 shows that the applied stress range played a crucial role in the level of fatigue life improvement that was achieved through use

of CFRP overlays. When the stress range decreased 16%, from 263 MPa (38 ksi) to 221 (32 ksi), the ratio of increase in fatigue crack propagation life was approximately doubled for stiffness ratios of 0.41 and 0.83. The same held true when the applied stress range was decreased form 221 MPa (32 ksi) to 166 MPa (24 ksi). Although this means that a CFRP overlay repair was more effective at a lower stress range, the improvements observed at very high stress ranges are still promising. For a specimen with a thickness of 6 mm ($^1/_4$ in.) tested at a stress range of 221 MPa (32 ksi), the smallest stiffness ratio tested (0.21) the fatigue propagation life increased by a factor of 3 when compared with the theoretical fatigue crack propagation life of an unretrofitted specimen. At 263 MPa (38 ksi) and a stiffness ratio of 0.41, the fatigue life of the specimen with the same thickness increased by a factor of 10.9. For specimens with a thickness of 3 mm ($^1/_8$ in.), increasing the stiffness ratio to 1.66 at 263 MPa (38 ksi) increased the fatigue life by a factor of 162, when compared with that of an unretrofitted specimen.

Drastic increases in fatigue crack propagation life can be attributed to the reduced applied stress imposed on the steel. The stress ranges corresponding to the fatigue crack propagation lives presented in Table 2 were determined using the relationships from Eq. 3 and 4. For example, specimen F15 was tested at a stress range of 263 MPa (38 ksi) based on the measured cross-section of the steel; however, the experimental fatigue crack propagation life presented in Table 2 corresponds to an effective applied stress range of approximately 118 MPa (17 ksi) based on the measured cross-section of the steel. Figure 10 presents the effective stress ranges for all steel tensile specimens based on their calculated stiffness ratio. The reductions in stress follow the same patterns determined during the FE analysis and shown in Fig. 3. Both Fig. 3 and Fig. 10show a relationship between stiffness ratio and stress reduction that is parabolic and inversely related in nature.

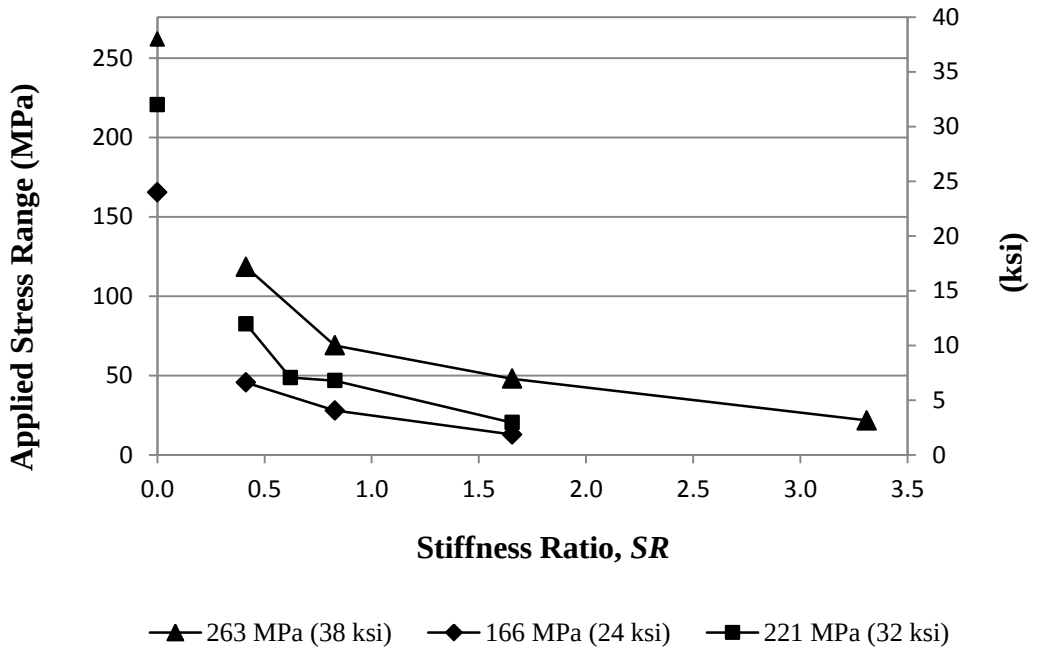

Figure 10: Equivalent applied stress of all specimens treated with CFRP overlays and an initial crack length of 7 mm (0.3 in.)

SPECIMEN DEBOND BEHAVIOR

Of the 15 specimens tested with initial crack lengths of 0.3 in., only one specimen, F4-20, experienced partial debonding between the steel and CFRP overlays. This specimen represented the thickest steel plate tested, combined with the thickest CFRP overlay tested. This suggests that the combination of very thick components led to independent behavior in terms of deformation, instead of system deformation. It is hypothesized that this behavior resulted in fatigue crack initiation in the resin layer at the bottom and top of the CFRP overlay, and subsequent crack propagation towards the center of the length of the overlay. The fatigue crack in the bond layer was noticed at a length of approximately 38 mm (1.5 in.). At this point, a steel collar consisting of two steel plates bolted around each end of the specimen was attached to prevent further debonding (Gangel, 2012). The debonding never approached the region of the

fatigue crack in the steel since it was arrested with the steel collar installation; therefore, the results from this specimen are presented as comparable to the others in the study.

CONCLUSIONS

Results of an experimental and analytical study examining the use of CFRP overlays to repair fatigue cracks in steel plates has resulted in the following conclusions:

- Experimental results showed that as stress range was increased, a greater stiffness ratio was required for the fatigue crack propagation life to tend towards infinity. At 166 MPa (24 ksi), 221 MPa (32 ksi), and 263 MPa (38 ksi) the number of cycles to failure tended towards infinity at stiffness ratios of 0.8, 1.0, and 1.6, respectively.
- Both FE analysis and experimental results showed a diminishing effect on stress demand as the stiffness ratio increased. Based on these results it is the opinion of the authors that the greatest benefit of using overlays to reduce the stress demand is achieved for stiffness ratios below unity.
- Experimental results showed that bonding of pre-fabricated multi-layered CFRP overlays increased the theoretical fatigue crack propagation life of unretrofitted steel specimens by at least three times and up to 162 times before experimental specimens reached run-out.
- The observed increase in fatigue-crack propagation life matched or was significantly higher than values ranging between 3 and 10 reported in previous studies on aluminum plates, steel plates, and steel beams. The main difference between the overlays used in this study and those used in other studies is that the stiffness ratio *SR* was significantly higher in this study than identified in previous literature.

Implications of the fundamental research described herein are significant. Research presented within this article has shown that use of CFRP overlays to repair cracks in steel members can be a highly effective means of reducing the stress demand and greatly prolonging the fatigue-crack propagation life of steel substrate. This work has provided a basis for proportioning CFRP overlays for effectiveness in halting/slowing fatigue crack propagation, based upon nominal stress range and the stiffness ratio between the overlay and the steel.

Future research is advised to better understand the demands upon and the behavior of CFRP overlays bonded to steel substrate. Topics that should be studied include testing thicker steel plates representative of bridge girder webs and investigating wide steel plates with a bonded overlay element of lesser width.

REFERENCES

AASHTO (2010). "AASHTO-LRFD Bridge Design Specifications: 5th." *American Association of State Highway and Transportation Officials (AASHTO)*, Washington D.C.

Alemdar, F. (2011). "Repair of bridge steel girders damaged by distortion-induced fatigue," thesis, presented to University of Kansas, at Lawrence, KS, in partial fulfillment of the requirments for the degree of Doctor of Philosophy in Civil Engineering.

ASTM D3039/D3039M-08, "Standard Test Method for Tensile Properties of Polymer Matrix Composite Materials," American Society for Testing and Materials, West Conshocken, PA, 2008.

Barsom, J.M., and Rolfe, S.T. (1999). "Fatigue and fracture behavior of welded components." Fracture and Fatigue Control in Structures, 3rd ed., (10), American Society for Testing and Materials, West Conshohocken, PA, 35-53.

Bocciarelli, M., Colombi, P., Fava, G., and Poggi, C. (2009)."Fatigue Performance of Tensile Steel Members Strengthened with CFRP Plates, *Composite Structures*, 87, pp. 334-343.

Crain, J. (2010). "Fatigue enhancement of undersized, drilled crack-stop holes," thesis, presented to University of Kansas, at Lawrence, KS, in partial fulfillment of the requirements for the degree of Master of Science in Civil Engineering.

Dexter, R.J. (2004). "Sign, Signal, and Light Support Structures and Manural for Repair of Fatigue Cracks." Third Annual Bridge Workshop: Fatigue and Fracture. March 5, 2004.

Gangel, R., (2012). "Use of CFRP Overlays to Repair Fatigue Damage in Steel Bridge Girders and Components," MS Thesis, Department of Civil, Architectural, and Environmental Engineering, University of Kansas, Lawrence, KS.

Hassel, H.L. (2011). "An analytical evaluation of distortion-indiced fatigue in steel bridges," thesis, presented to University of Kansas, at Lawrence, KS, in partial fulfilment of the requirements for the degree of Master of Science in Civil Engineering.

Hysol® 9412, Loctite 9412 Hysol Epoxy Adhesive, 2001, http://www.henkelna.com.

Kaan, B.N., Alemdar, F., Bennett, C.R., Matamoros, A., Barrett-Gonzalez, R., and Rolfe, S. (2012). "Fatigue enchancement of welded details in steel bridges using CFRP overlay elements." *Journal of Composites for Construction,* V. 16, N. 2, pp. 138-149.

Lee, W. Y., and Lee, J.J. (2004). "Successive 3D FE analysis technique for characterization of fatigue crack growth behavior in composite-repaired aluminum plate." *Composite Structures*, 66(1-4), 513-520.

Liu, H. B., Al-Mahaidi, R., and Zhao, X.L. (2009). "Experimental study of fatigue crack growth behaviour in adhesively reinforced steel structures." *Composite Structures,* 90(1), 12-20.

Liu, H. B., Xiao, Z. G., Zhao, X. L., and Al-Mahaidi, R. (2009). "Prediction of fatigue life for CFRP-strengthened steel plates." *Thin-Walled Structures,* 47(10), 1069-1077.

Mall, S., and Conley, D.S. (2009). "Modeling and validation of composite patch repair to cracked thick and thin metallic panels." *Composites Part A: Applied Science and Manufacturing,* 40(9), 1331-1339.

Marquis, G., and Kahonen, A. (1995). "Fatigue testing and analysis using the hot spot method." Technical Research Centre of Finland.

Naboulsi, S., and Mall, S. (1996). "Modeling of a cracked metallic structure with bonded composite patch using the three layer technique." *Composite Structures*, 35(3), 295-308.

Roddis, W. M., and Zhao, Y. (2001). "Out-of-Plane Fatigue Cracking in Welded Steel Bridges: why it happened and how it will be reapired." *Welding Inovation*, 27(2) , 2-7

Roy, M., Lang, C., & May, I. (2009). "Modelling composite repairs to cracked metal structures." *Proceedings of the Institution of Civil Engineers (ICE)-Structures and Building*s, 162(2), 107-113.

Sabelkin, V., Mall, S., and Avram J. B. (2006). "Fatigue crack growth analysis of stiffened cracked panel repaired with bonded composite patch." *Engineering Fracture Mechanics*, 73(11), 1553-1567.

Schubbe, J.J., and Mall, S. (1999). "Modeling of cracked thick metallic structure with bonded composite patch repair using three-layer technique." *Composite Structures*, 45(3), 185-193.

Simulia. (2009). ABAQUS FEA Version 6.10-2. Providence, RI. http://www.simulia.com.

Tavakkolizadeh, M., and Saadatmanesh, H. (2003). "Fatigue strength of steel girders strengthened with carbon fiber reinforced polymer patch." *Journal of Structural Engineering*, 129(2), 186-196.

Umamaheswar, T.V.R.S., and Singh, R. (1999). "Modelling of a patch repair to a thin cracked sheet." *Engineering Fracture Mechanics*, 62(2), 267-289.

Part 3

EFFECTIVENESS OF CRACK-ARREST HOLES UNDER DISTORTION-INDUCED FATIGUE LOADING

H. Liu[1], J. Zhou[2], S.H. Bun[3], G.G. Simmons[4], C.R. Bennett[5], A.B. Matamoros[6], J. Li[7]

ABSTRACT

Drilling crack-arrest holes to halt fatigue crack propagation is a simple technique that is commonly-used by bridge owners faced with controlling and/or repairing fatigue cracking in steel bridges. Well-established relationships exist for sizing the diameter of the crack-arrest holes for in-plane fatigue loading; however, the effectiveness of crack-arrest holes under out-of-plane (distortion-induced) fatigue is not well-understood and has received very little attention in the literature.

Distortion-induced fatigue cracking is much more common in steel bridge infrastructure than in-plane fatigue cracking, and bridge owners often utilize drilled crack-arrest holes in these cases as a "first response" against fatigue cracks discovered during inspections. The purpose of the crack-arrest hole is to smooth out the sharp crack tip, reducing the stress concentration and halting/delaying crack propagation. Common knowledge has been that large diameter crack-arrest holes are more effective at halting crack propagation under distortion-induced fatigue than

Department of Civil, Environmental, and Architectural Engineering
University of Kansas, 1530 W. 15th St, Lawrence, KS 66045
Tel. (785) 864-3235, Fax. (785) 864-5631

[1] Hao Liu, Graduate Research Assistant, University of Kansas, h781l127@ku.edu
[2] James Zhou, Graduate Research Assistant, University of Kansas, chenqiz@ku.edu
[3]Say H. Bun, Civil/Structural Engineer, Enercon Services, sayhakbun@gmail.com
[4]Gary G. Simmons, Graduate Research Assistant, University of Kansas, gsimmons@ku.edu
[5]Caroline R. Bennett, PhD, PE, Associate Professor, University of Kansas, crb@ku.edu
[6]Adolfo B. Matamoros, PhD, PE, Professor, University of Texas at San Antonio, adolfo.matamoros@utsa.edu
[7]Jian Li, PhD, PE, Assistant Professor, University of Kansas, jianli@ku.edu

small diameter crack-arrest holes. However, drilling large diameter crack-arrest holes can have strength implications for a structure, and may not be desirable. Additionally, there is little evidence in the literature that large diameter crack-arrest holes perform better than small diameter crack-arrest holes under distortion-induced fatigue.

A study examining the effectiveness of crack-arrest holes of varying diameters under distortion-induced fatigue loading was performed. The investigation was comprised of both experimental and analytical components. The experimental study was performed on segments of plate girder tested in the KU Structural Testing Laboratory, loaded under distortion-induced fatigue. Crack-arrest holes of various diameters were drilled at the tips of the cracks having different lengths, and their effectiveness was evaluated. A suite of three-dimensional, solid-element finite element analyses was also used to parametrically vary crack-arrest hole diameter, placement, and crack length to investigate the influence of those variables on stress demands in a girder web gap region subjected to distortion-induced fatigue.

The findings from the experimental and analytical components of this study were compared against common industry practices. The results showed that crack-arrest hole placement (inherently tied to cracking location and geometry), rather than hole diameter, had a much greater effect on the effectiveness of the crack-arrest hole in bridge girders susceptible to distortion-induced fatigue.

INTRODUCTION AND BACKGROUND

Fatigue cracking is a common problem afflicting thousands of steel bridges in the U.S. highway bridge inventory, and the scale of the problem is poised to increase over the next decade due to deferred maintenance and utilization of bridges well beyond their original design lives. As the

mean age of steel bridges increases, fatigue damage caused by cumulative vehicular loading cycles also increases.

Maintaining and repairing these bridges is an expensive and time-consuming endeavor, often requiring engineering of tailored retrofit solutions. However, a nearly universally-accepted first line of defense against fatigue crack propagation is the common practice of drilling a crack-arrest hole at the tip of a crack.

Crack-arrest holes are a time-honored, simple solution for stopping fatigue crack propagation. They stop fatigue crack propagation by blunting the crack tip and reducing the stress concentration at the crack tip. The radius of a crack tip is very small, approaching zero, and the curvature (*1/radius*) approaches infinity. Correspondingly, the stress concentration factor (Eqn. 1) at the crack tip approaches infinity. The crack-arrest hole changes the radius and curvature at the crack tip to that of the crack-arrest hole and reduces the stress concentration factor substantially. From Barsom and Rolfe (1997):

$$k_t = \frac{\sigma_{\max}}{\sigma_{nom}} \qquad \textbf{Equation 1}$$

Where k_t is the stress concentration factor, σ_{max} is the maximum at the edge of the crack, and σ_{nom} is the stress sufficiently far away from the crack that it is not influenced by the crack.

For example, the stress concentration factor at the edge of an ellipse is represented in Equation 2 (Barsom and Rolfe 1997):

$$k_t = \left(1 + 2\frac{a}{b}\right)$$ **Equation 2**

Where k_t is the stress concentration factor, *2a* is the length of the major axis of the ellipse and *2b* is the length of the minor axis of the ellipse.

For sharp cracks, *b* approaches 0and *a/b* becomes very large; thus k_t also becomes very large. By placing a crack-arrest hole of radius *r* at the tip of the crack, *r* replaces *b* and the stress concentration factor reduces from infinite to a relatively small finite number.

The formula for determining the diameter of the crack-arrest hole to stop fatigue crack propagation was first presented in Rolfe and Barsom (1977) and also appears in the latest edition of Barsom and Rolfe (1999). Fisher et al. (1980; 1990) used the same formula but developed a different constant, *C*, from different experimental testing. The formula (Eqn. 3) relates the required radius of the crack-arrest hole to the yield strength of the steel, the range of the stress intensity factor, and the half-length of the crack along with a constant from experimentation.

The formula was presented in the following form (Rolfe and Barsom 1977):

$$\frac{\Delta K}{\sqrt{\rho}} = C\sqrt{\sigma_{ys}}$$ **Equation 3**

where *C* is constant derived from experimental testing, ρ is required radius of the crack-arrest-hole, σ_{ys} is the yield strength of the steel and ΔK is the range of the stress intensity factor.

Equation 3 was based on a series of experiments performed by Barsom and Rolfe (1977) on various steel plates with edge notches; all the notches had the same length, *a*, and all had the same constant radius at the tip. Yield strengths of the steel plates varied between 248 MPa (36 ksi) to 758 MPa (110 ksi). The loading, which consisted of uniaxial, cyclical loads, was varied

to provide stress ratios ($R = s_{max}/s_{min}$) of –1.0 (full stress reversal), 0.1, and 0.5. This plate geometry combined with the uniaxial, tension-compression loading resulted in Mode I type fracture, where Mode I fracture is a tension-opening crack. For this edge notch configuration, the range of the stress intensity factor can be determined by:

$$\Delta K = \Delta\sigma\sqrt{\pi a} \qquad \textbf{Equation 4}$$

Where *ΔK is* range of the stress intensity factor, *Δσ* is cyclic stress range ($\sigma_{max} - \sigma_{min}$) for the fluctuating stresses, and *a* is the length of the edge crack ($^1/_2$ the length of the crack for an interior crack).

When Eqn. 4 is substituted into Eqn. 3, Eqn. 5 results:

$$\frac{\Delta\sigma\sqrt{\pi a}}{\sqrt{\rho}} = C\sqrt{\sigma_{ys}} \qquad \textbf{Equation 5}$$

This can be rearranged in terms of ρ and *a*, and becomes:

$$\rho = \left(\frac{\pi(\Delta\sigma)}{C^2\sigma_{ys}}\right)a \qquad \textbf{Equation 6}$$

The crack-arrest formula is also found in Fisher et al. (1980; 1990). Fisher et al. conducted a series of experiments on rolled, wide-flange shapes (Fisher et al. 1980) and welded-plate girders (Fisher et al. 1990) where the full-scale members were configured and loaded in such a manner that they were subjected to both in-plane bending stresses and out-of-plane distortion stresses. This combination resulted in distortion-induced fatigue cracking at locations where cross-bracing attached to the connection plates, which were in turn welded to the girder

webs. The steel used in the studies by Fisher (1980; 1990) was limited to Gr. A370 steel, which had a measured yield strength of 248 MPa (36 ksi).

The fatigue cracking was caused by a complex, triaxial stress field and resulted in a Mode III failure (shear in a plane perpendicular to direction of crack growth) or in a complex mode with both Mode III and bending stress components. When fatigue cracks developed in the members, holes were drilled at the ends of the crack tips; these holes typically had diameters of 19mm (¾ in), 25mm (1in), or 32mm (1¼ in). The test were restarted and continued until the cracks reinitiated or the test was stopped. For the tests performed on the rolled shapes, the control stress variable was the stress range in the normal flexural bending stresses as measured in the beam web at the bottom of the gusset at mid-span. The stress ranges were 41.4, 62.0, 82.7, or 103.4 MPa (6, 9, 12, or 15 ksi). For tests on the plate girders, testing was controlled by limiting the in-plane bending stress to either 41.4 or 82.7 MPa (6 or 12 ksi) and inducing out-of-plane distortion stress of either low, medium, or high values. The out-of-plane distortion stress was calculated from strains measured in the web gap with strain gages and then extrapolated back to the edge of the transverse stiffener.

Despite the differences in the testing methodology, Fisher et al. (1980) used Eqns. 3 & 4 for determining the required radius of the crack-arrest hole but developed a different constant, *C*. Using Eqns. 3 and 4 resulted in Eqn. 5 for both Rolfe and Barsom (1977) and Fisher et al. (1980, 1990). Since *C* was derived from different testing methodologies, the values for *C* depend on using consistent units. Table 1 provides the consistent units and the corresponding values for *C* from Rolfe and Barsom (1977) and from Fisher et al. (1980, 1990) in both SI and US Customary units.

Table 1: Values for *C* and Units for Crack -Arrest Hole Equations

Units	*C* – Rolfe and Barsom (1977)	*C* – Fisher et al. (1980)	$\Delta\sigma$	σ_{ys}	a	ρ
SI	26.3	10.5	MPa	MPa	mm	mm
US	10	4	ksi	ksi	in.	in.

Fisher et al. (1990) stated that, if the out-of-plane bending stress at the transverse stiffener is greater than 103 MPa (15 ksi) or if the in-plane bending stress in the web at the web to flange weld is greater than 41 MPa (6 ksi), the crack-arrest hole with a radius as calculated from the Eqn. 6 using the constant $C = 4$ will not prevent the crack from reinitiating on the other side of the hole. Rolfe and Barsom (1977) did not specify a restriction on in-plane load in their discussion of the formula.

In practice, crack-arrest holes have exhibited a wide range of performance. Typically, crack-arrest holes sized according to Eqn. 6 for in-plane fatigue have performed satisfactorily. However, crack-arrest holes have not exhibited the same propagation-halting performance under distortion-induced fatigue loading, and the reason for this is not entirely clear.

One reasonable hypothesis is that crack-arrest holes are not commonly drilled to the diameter required when using Eqn. 6 with C=4, as this often results in very large hole diameter requirements. Commonly-encountered crack lengths and grades of steel would often necessitate crack-arrest hole diameters greater than 4 in. when using that equation, which at best removes a significant amount of steel section, and more often than not is simply geometrically impossible. When faced with this situation, bridge engineers usually specify the largest crack-arrest hole that

they consider feasible and reasonable, which is often on the order of 1 in. diameter. Therefore, it is reasonable to consider whether the fact that such crack-arrest holes are "undersized" contributes to crack re-initiation.

Subscribing to this hypothesis, McGormley and Koob (2002) suggested the use of a large-hole retrofit to retrofit for distortion-induced fatigue. This procedure involves fabricating two large-diameter holes (3-4 in.) in the web gap region – one on both sides of the connection stiffener. No literature was found assessing the performance of this repair technique, but it has been implemented on numerous bridge structures across the U.S.

Another reasonable hypothesis as to why crack-arrest holes have not exhibited good crack-arresting capabilities under distortion-induced fatigue is that crack-arrest holes cannot be expected to perform similarly in distortion-induced fatigue as they do under in-plane fatigue. If this hypothesis is true, then the crack-arrest hole relationship introduced in Eqn. 3 may not be applicable for distortion-induced fatigue cracking.

Information is needed to determine the effects of crack-arrest hole diameter, placement, and crack type on propensity for crack re-initiation under distortion-induced fatigue loading for the purpose of providing guidance to bridge engineers making decisions when faced with active cracking in steel bridges. Decades of implementation with mixed results have shown that the level of information available to bridge engineers with respect to crack-arrest hole sizing for distortion-induced fatigue is inadequate.

OBJECTIVE AND SCOPE

The overall objective of this research was to examine the effectiveness of crack-arrest holes of varying diameters, placement, and crack length for steel bridge girders subjected to distortion-

induced fatigue. The scope of the study included both physical experimentation and finite element simulations.

RESEARCH APPROACH

The approach taken in this research utilized a suite of finite element models in which crack length, crack placement, and crack-arrest hole diameter were varied. In addition, a model of the hole retrofit described in McGormley and Koob (2002) was created and compared to the results from the broader suite of finite element (FE) models. A physical test was conducted on a girder segment loaded in distortion-induced fatigue to provide context to the finite element analyses.

MODELING METHODOLOGY

The effects of out-of-plane bending and cross-frame loading were studied through use of computational simulations performed using the commercially-available finite element software, Abaqus v.6.10. The baseline geometry for each model included a single 3.0 m [10 ft] long by 1.52 m [5.0 ft] deep simply-supported steel girder section, dimensioned in Figure 1 and Figure 2. In this simplified girder model, no bridge deck was included. The depth of this section was chosen to represent a reasonable girder depth for a multi-girder highway overpass. The length of the girder section was chosen to be twice the girder depth. The connection stiffener welded at mid-span was truncated 36 mm [1.4 in.] from the face of each adjacent flange. A 25 mm [1.0 in.] clip produced a web gap region of 35 mm [1.38 in.]. The end stiffeners were attached to both the top and bottom flange and welded to the entire depth of the web on sides. The flanges were connected to the web by welds on both the interior and fascia side along the width of the web.

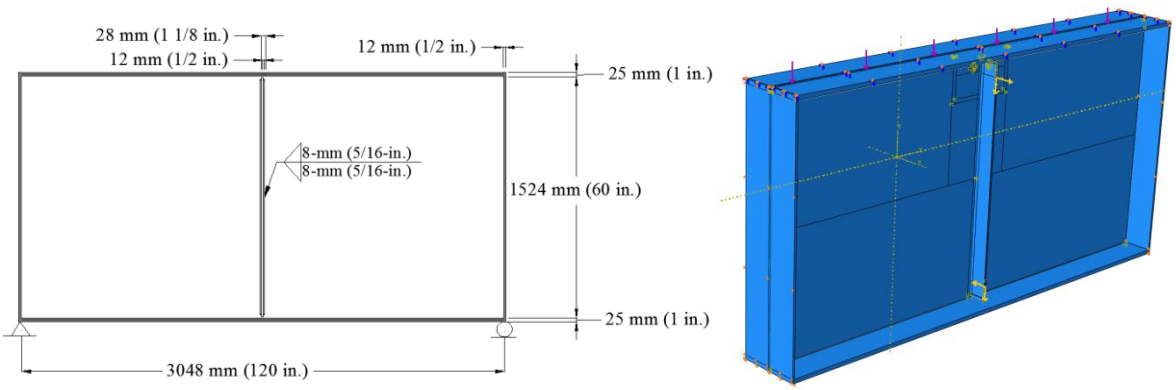

Figure 1: Elevation view of girder section and model geometry

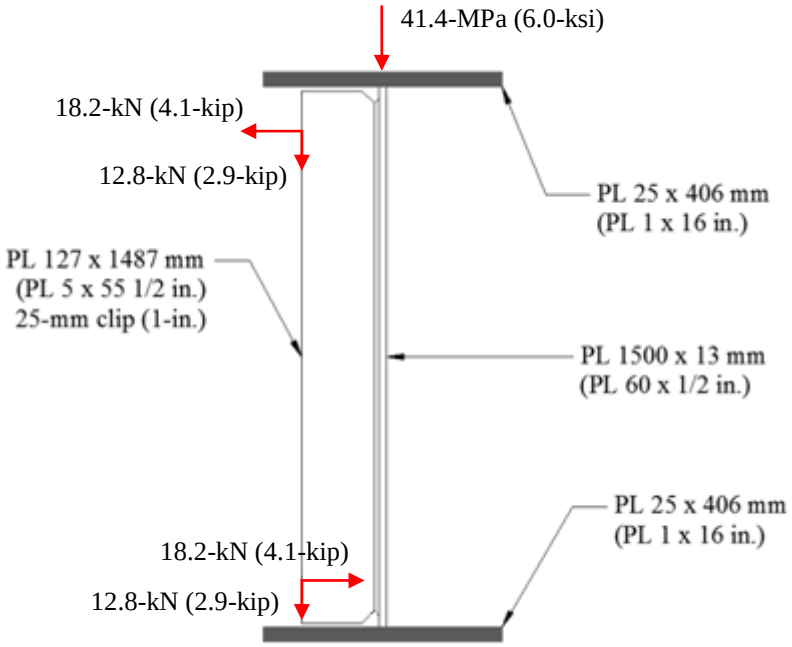

Figure 2: Girder cross-section

A 41.4 MPa [6.0 ksi] pressure load was placed over a 12 mm [1/2 in.] width at the center of the top flange, to simulate the maximum design truck load over this girder section. An 18.2 kN [4.1 kip] point load was placed 105 mm [4.1 in.] from the top of stiffener at the center of the exterior face of the stiffener, 127 mm [5.0 in.] from the interior surface of the web. The load was

directed perpendicular to the surface and pointed away from the girder. A 12.8 kN [2.87 kip] point load was placed at the same location as the 18.2 kN [4.1 kip] point load. This load was directed parallel to the surface and pointed toward the bottom flange. A corresponding 18.2 kN [4.1 kip] point load and a 12.8 kN [2.9 kip] point load was placed 105 mm [4.1 in.] from the bottom of stiffener at the center of the exterior face of the stiffener, 127 mm [5.0 in.] from the interior surface of the web. These force couples, shown in Figure 2, model the out-of-plane forces induced by cross-frame connections during bending deformation.

Eight-node, cubic elements with 24 degrees of freedom were used in the meshes for the flanges, web, and stiffeners. Four-node tetrahedral elements with 12 degrees of freedom each were utilized to conform to the special geometrical aspects of the weld. All the fillet welds were modeled as right triangle cross-sections. All steel sections and welds were modeled as isotropic, linear elastic materials with an elastic modulus of 200,000 MPa [29,000 ksi] and a Poisson's ratio of 0.3. Tie constraints were used to connect the fillet welds to the surfaces they bring together.

MODELING OF CRACKS, CRACK-ARREST HOLES, AND COMPUTING STRESSES

Cracks were modeled as a rectangular cut extruded through the thickness of the web and with a 0.25 mm [0.01 in.] width; length of the cracks was varied through the study. Crack-arrest holes were modeled as a circular cut extruded through the web thickness. Four different crack patterns were considered within the modeling effort, as diagrammed in Figure 4 and described here:

- Diagonal crack: a crack that occurs at the toe of the connection plate-to-web weld and extends diagonally into the web (Figure 4(a));

- Horseshoe-shaped crack: a crack that follows the toe of the connection plate-to-web weld (Figure 4(b));
- Horseshoe-shaped crack and web-to-flange crack: two cracks occurring simultaneously – a crack around the toe of the connection plate-to-web weld and a crack along the toe of the web-to-flange weld (Figure 4(c)); and
- Web-to-flange crack: a crack along the toe of the web-to-flange weld (Figure 4(d)).

As shown in Figure 3, for all models including diagonal cracks, total crack length was taken as the crack-arrest hole diameter combined with the undrilled crack length on one side of the stiffener. For web-to-flange cracks, (except for models including a 102 mm [4.0 in.] crack-arrest hole), total crack length was taken as the crack-arrest hole diameter combined with the undrilled crack length. For horseshoe-shaped cracks, (except for models including a 102 mm [4.0 in.] crack-arrest hole), total crack length was measured as the radius of the crack-arrest hole combined with existing crack length on one side of the stiffener. Hence, diagonal and horseshoe-shaped crack lengths refer to the length of one leg of the diagonal and horseshoe shapes, as dimensioned with the arrows in Figure 3. It should be noted that cracks are shown in Figure 3 as white lines. The total crack length was kept constant for all three crack types. For the 102 mm [4.0 in.] crack-arrest hole, hole placement was such that the hole was drilled 3 mm [1/8 in.] into both the flange weld and connection plate weld.

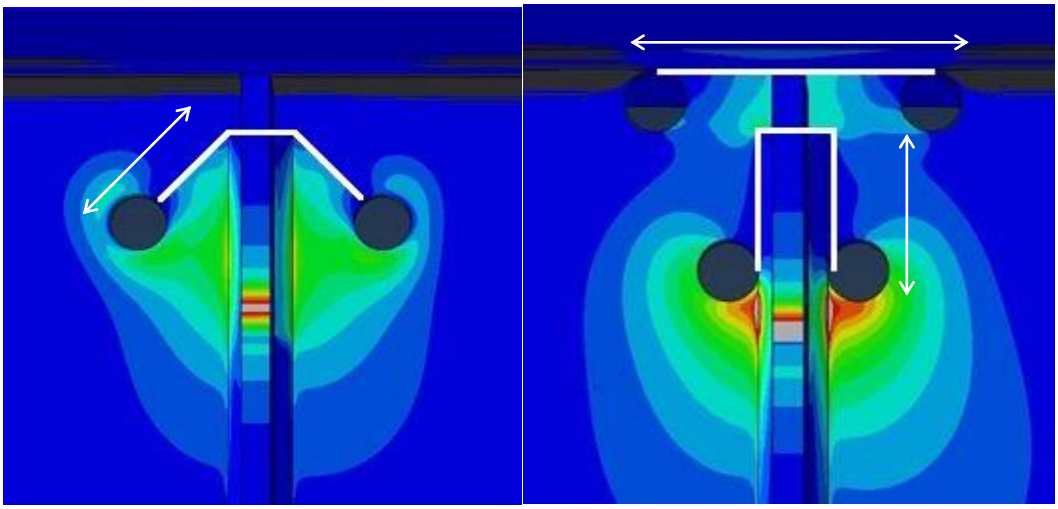

(a) **(b)**

Figure 3: (a) Dimension of the diagonal crack length; (b) dimension of the horseshoe-shaped and web-to-flange crack length

Comparisons in this research were performed on the basis of the Hot Spot Stress (HSS). In this paper, HSS was defined as the stress at a distance half the thickness of the web away from the edge of the web-to-flange weld, connection plate-to-web weld, and crack-arrest holes. To apply the HSS technique in the finite element models, peak stresses were extracted from paths in the models. The path that was used to determine the first peak stress followed the same horseshoe shape along the connection plate-to-web weld a distance of 229 mm [9.0 in.] down both sides of the stiffener, as shown the HSS-1 path in Figure 4. The path to determine the second peak stress followed the same horizontal path along the web-to-flange weld for a length of 406 mm [16.0 in.], as shown the HSS-2 path in Figure 4. A circular path around the crack-arrest hole was also examined to determine peak stress around the hole, as shown the CHSS-1 and CHSS-2 paths in Figure 4. It should be noted that cracks are shown in Figure 4 as yellow lines, and HSS paths are shown in red.

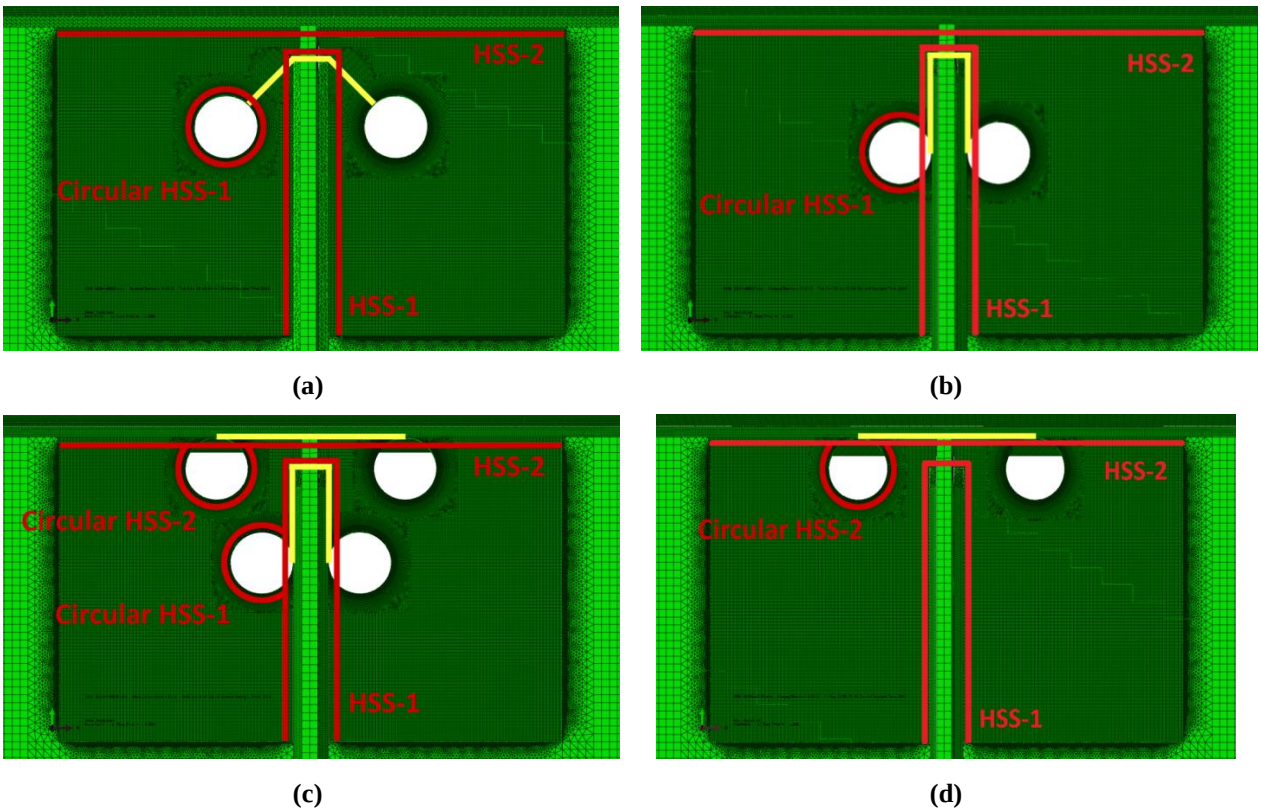

Figure 4: Crack placement and Hot Spot Stress paths for FE models: (a) Diagonal-type crack pattern; (b) Horseshoe-shaped crack; (c) Horseshoe-shaped crack and web-to-flange weld crack; (d) Web-to-flange weld crack

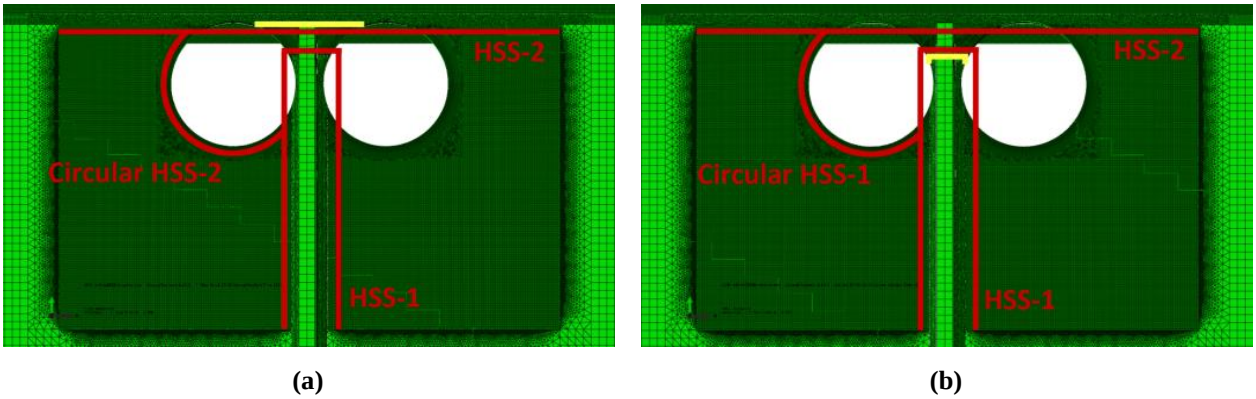

Figure 5: Crack placement and Hot Spot Stress paths for: (a) 101.6 mm [4.0 in] hole for the model including web-to-flange weld crack; (b) 101.6 mm [4.0 in] hole for the model including horseshoe-shaped crack

MESH CONVERGENCE STUDY

Stresses computed in the models near the locations of crack-arrest holes were found to be sensitive to mesh density, therefore, a mesh convergence study was performed. The mesh convergence study was conducted for a model that included a diagonal crack. A large enough area was partitioned such that all crack types with different lengths and varying hole diameters would fit within the partitioned region. The most coarse and most dense mesh configurations for the region near the crack-arrest hole in the girder web are shown in Figure 6(a) and (b), and consisted of three concentric circular regions around the holes which allowed gradually increasing element size away from the crack-arrest hole. Rectangular partitions were also created around the crack. The mesh was configured using several regions with increasing mesh density near the crack-arrest hole. The results for convergence study are illustrated in Figure 6(c). A minimum element size of 0.71 mm [0.028 in] at the path half the thickness of the web away from the edge of crack-arrest hole was selected in this study, which is the configuration shown in Figure 6(b).

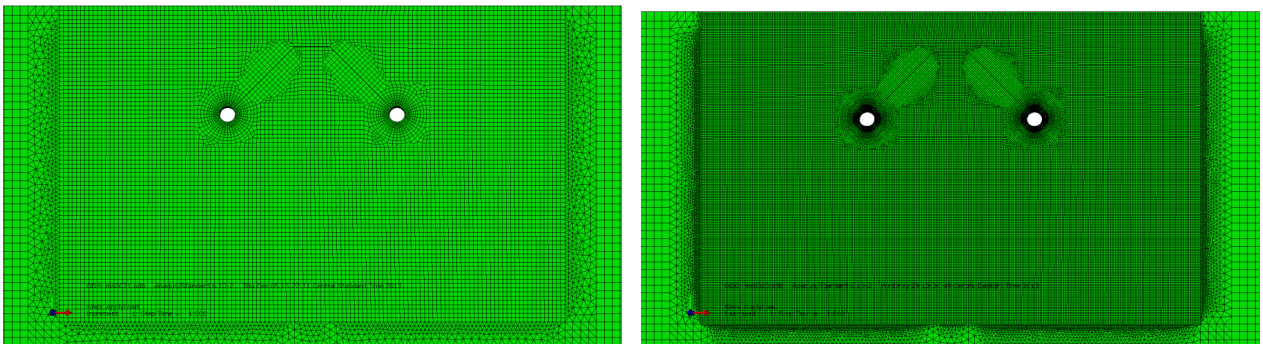

(a) (b)

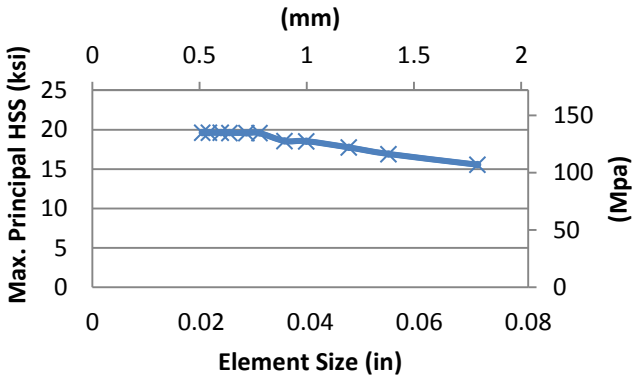

(c)

Figure 6: (a) Mesh in the vicinity of the crack-arrest holes for an element size of 1.80 mm [0.071 in]; (b) Mesh in the vicinity of the crack-arrest holes for an element size of 0.71 mm [0.028 in]; (c) Effect of element size around the crack-arrest hole path on maximum principal HSS.

MODEL VALIDATION

As described, the primary investigative technique used in this study was based upon a suite of refined, three-dimensional finite element simulations. To provide context to the simulations and to validate the finite element modeling approach, a physical test was performed on a built-up steel girder loaded in distortion-induced fatigue. A description of the physical test and findings pertinent to validating the FE simulations are presented in the following sections.

The physical test setup was comprised of a built-up welded steel girder that was connected to the concrete laboratory floor such that the girder was tested upside-down. The

bottom flange of the girder in the laboratory was restrained to the laboratory floor over its entire length. One end of a cross-frame was attached to a connection plate located at mid-length of the girder. The opposite end of the cross-frame was attached to an actuator, which pulled upwards on the cross-frame, simulating the effect of an adjacent bridge girder deflecting under load.

The web, bottom flange, and top flange of the test girder all had 345 MPa [50 ksi] yield strength. A connection plate 873 mm [34.4 in] tall and 127 mm [5.0 in.] wide was welded to the web at the middle of the girder. All stiffeners had a 32 mm [1 ¼ in.] cropped end and a thickness of 10 mm [3/8 in.]. A cross-frame was used to connect the connection plate and a WT; the WT section was used to connect the cross-frame to the actuator. The cross-frame was made up of three L76x76x10 mm [L3x3x3/8 in.] angles of which two were in a X-configuration, and one was as a horizontal member.

The girder subassembly was instrumented with three linear variable differential transformers (LVDTs) placed along the height of the girder, and nine bondable-type strain gages. Two strain gages were placed at the top and bottom web-gaps where the cracks were expected to initiate. The three LVDTs were used to capture the out-of-plane deflection at three locations through the girder depth.

The subassembly was tested under cyclic tensile load that ranged from 2.2 kN [0.5 kip] to 25.3 kN [5.7 kip] applied by an MTS actuator connected to a WT section that was connected to the cross-frame using load-control. The test progressed as described in the following, also illustrated in Figure 7. And the maximum principal stress screenshots corresponding to each step were shown in Figure 8:

Stage 1. Cyclic loading was applied to the girder, and a horseshoe-shaped crack initiated and propagated to 38 mm [1½ in.] long around the connection plate-to-web weld. The

girder was inspected often using UV light and dye penetrant to determine crack growth rate, and the data was collected continuously while being cycled.

Stage 2. Next, a pair of crack-arrest holes were drilled at the tips of the cracks, one on each side of the connection plate. The diameter of each of the holes was 51 mm [2 in.]. Since the cracking followed the connection plate weld, there was not enough room to drill the holes such that the tips of the cracks were located at the center of the holes; this is a common problem for cracking in this type of fatigue detail. Therefore, the holes were drilled approximately 3mm [$^1/_8$in.]into the weld instead of placing the holes' circumference right at the edge of the weld. Around the holes, strain gages were installed to capture the deformation.

Stage 3. The specimen was cycled at the same load range as in Stage 1 of the test. The inspection procedures were carried out the same ways as mentioned in Stage 1. The specimen was tested until new cracks appeared and propagated to 76mm [3in.] long. The two new cracks did not originate from the crack-arrest holes, but originated at the weld.

Stage 4. Another pair of 51 mm [2 in.] diameter holes was drilled at the tips of the cracks. The location of the hole placement and the testing procedures were carried in the same way as in Stage 2.

Stage 5. Small cracks were noted to appear at the toe of the web-to-flange weld.

Stage 6. Additional cracking occurred at the connection plate-to-web weld; this crack did not originate from the crack-arrest hole, but originated from the weld, a short distance from the crack-arrest hole.

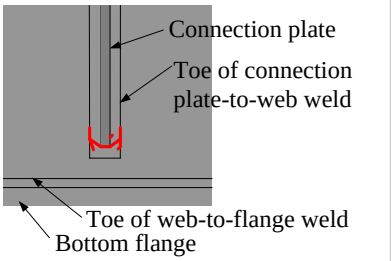

Stage 1- Initial crack formation

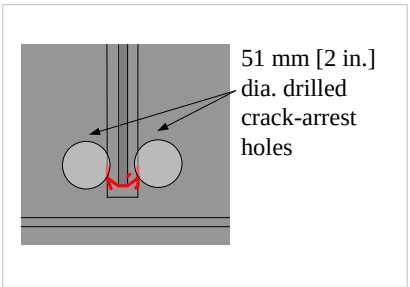

Stage 2 – Drilled crack-arrest holes at tips of cracks

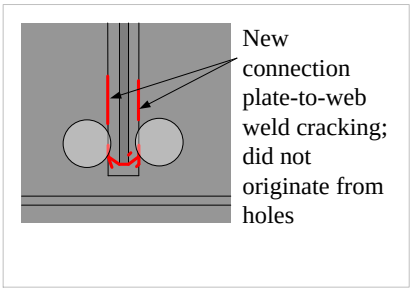

Stage 3 – New cracks initiate at the connection plate-to-web weld, above the drilled crack-arrest holes (but not out from the holes)

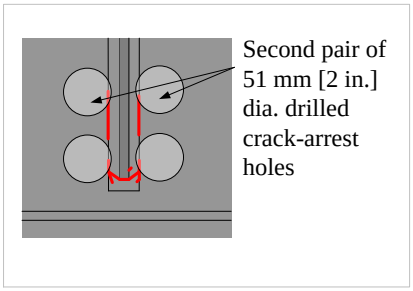

Stage 4 – New crack-arrest holes were drilled

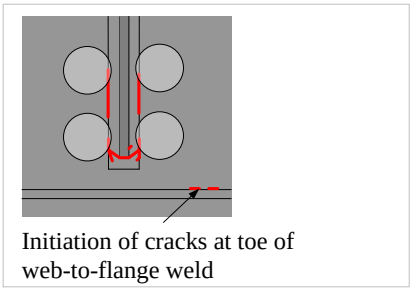

Stage 5 – Crack initiation was noted at web-to-flange weld

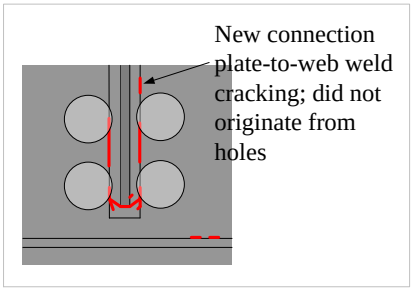

Stage 6 – New crack initiated at the connection plate-to-web weld, above the drilled crack-arrest hole (but not out from the hole)

Figure 7: Progression of cracking in physical test girder; red lines indicate crack locations

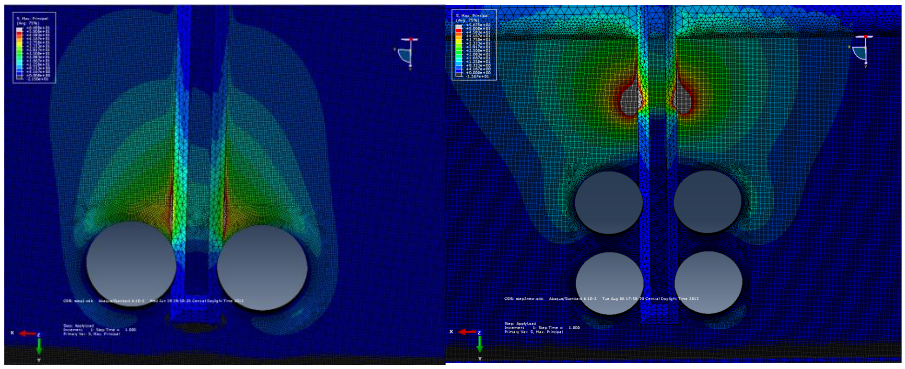

(a) **(b)**

Figure 8: (a) Maximum principal stress screenshot for Stage 2 and Stage 3; (b) Maximum principal stress screenshot for Stage 4, Stage 5 and Stage 6

The results from the FE model concluded that drilling a pair of 51 mm [2.0 in.]diameter crack-arrest holes at the tips of the horseshoe-shaped crack eliminated the high stress demand at the tips of the crack. However, the stress concentrated at new locations along the stiffener-to-web weld a small distance from the edge of the holes. The magnitude of stress was above the yield stress, resulting in cracking at those locations (Figure 9). These findings were in agreement with results from the experimental testing. In the physical testing, new cracks did not initiate until the cycle count reached approximately 420,000. The cracks were located along the stiffener-to-web weld at 13 mm [1/2 in.] away from the edge of the holes (Figure 10(c)),and there were no signs of cracks coming from the edge of the holes.

The deformation data collected from strain gages on the top of the holes, shown in Figure 11, indicated that magnitude of strain was close to the strain at yield. The strain on the left crack-arrest hole was higher than the strain value obtained on the right crack-arrest hole as well.

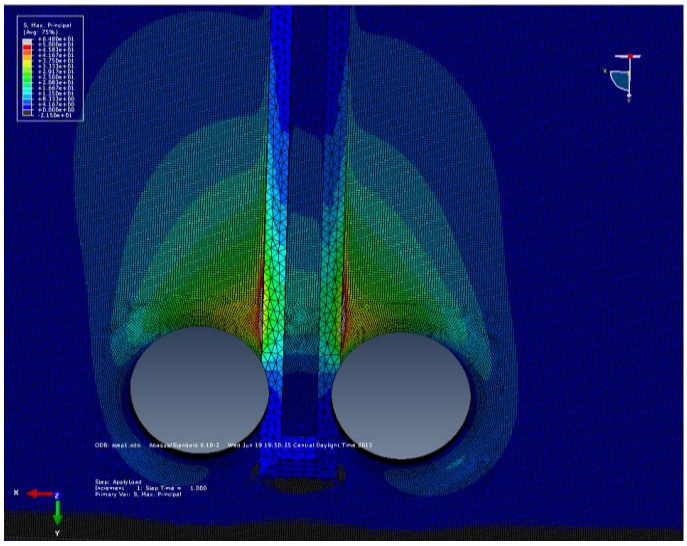

Figure 9: Finite element model for the girder including one pair crack-arrest holes

(a) **(b)** **(c)**

Figure 10: (a) Crack-arrest hole and strain gage (circled) on the left side of the connection plate; (b) Crack-arrest hole and strain gage (circled) on the right side of the connection plate; (c) Cracking forming after the first pair of crack-arrest holes had been drilled and tested on the left of connection plate

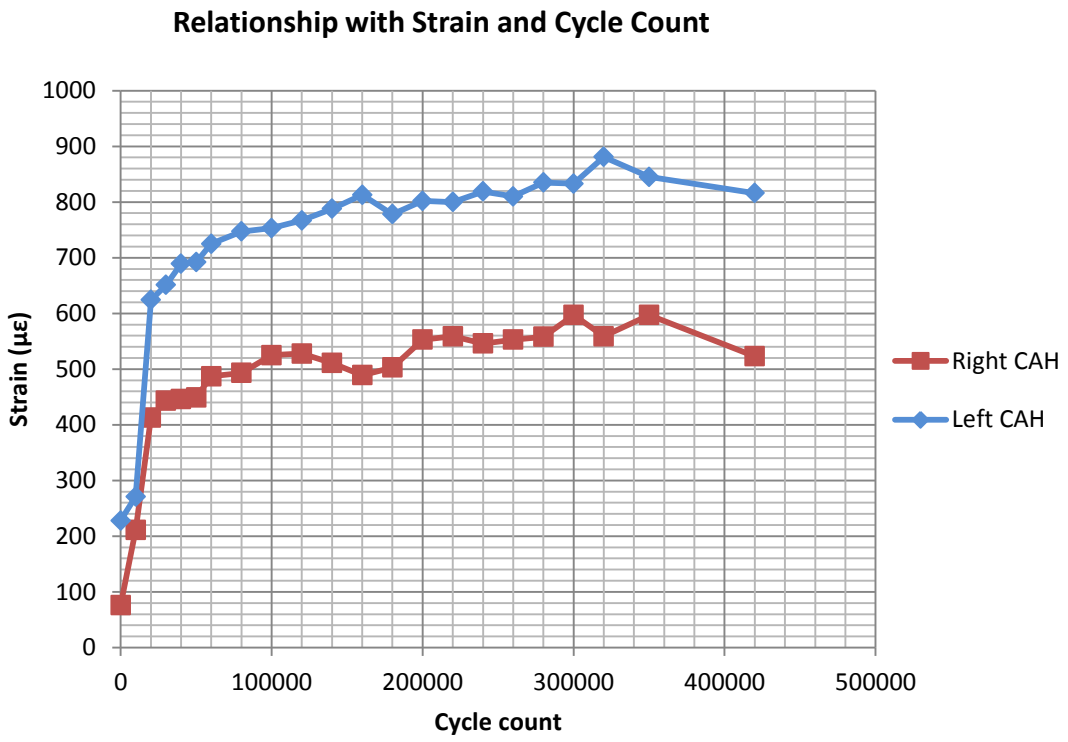

Figure 11: Strain data from left crack-arrest hole and right crack-arrest hole gages both measured at 10 mm (3/8 in) from the edge of the holefor one pair crack-arrest holes

As shown in Figure 12, the FE model results showed that adding the second pair of crack-arrest holes induced new locations of severe stress concentration along the stiffener-to-web weld at a distance approximately 38 mm [1 $^{1}/_{2}$ in.] from the edge of the new holes. This result was corroborated by the results from the physical testing. In the physical test, new cracks first initiated at a distance approximately 19 mm [3/4 in.] from the edge of the holes at approximately 980,000 cycles, and then propagated towards the edge of the holes. The deformation indicated that the highest strain was located on the right of the connection plate (Figure 13 and Figure 14).

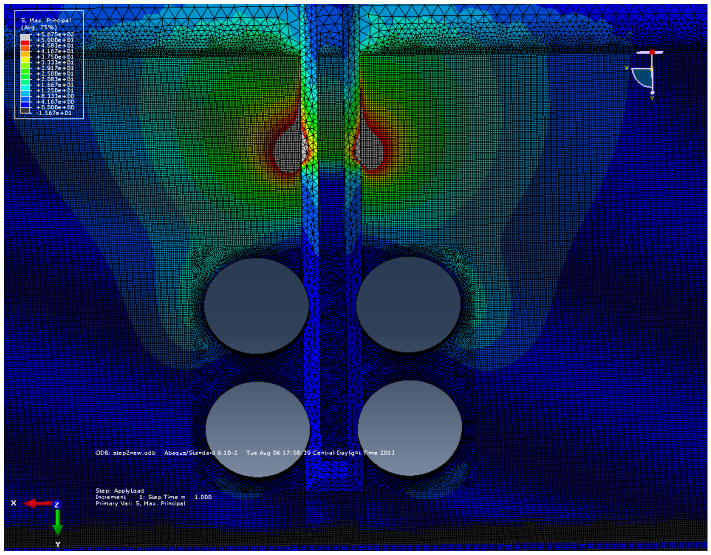

Figure 12: Finite element model results showing two pairs of crack-arrest holes (The stress contours are presented with limits from 0 to 345 MPa [50 ksi])

Figure 13: Strain gage placement around two pairs of crack-arrest holes in the physical testing: (a) Left side of the connection plate; (b) Right side of the connection plate

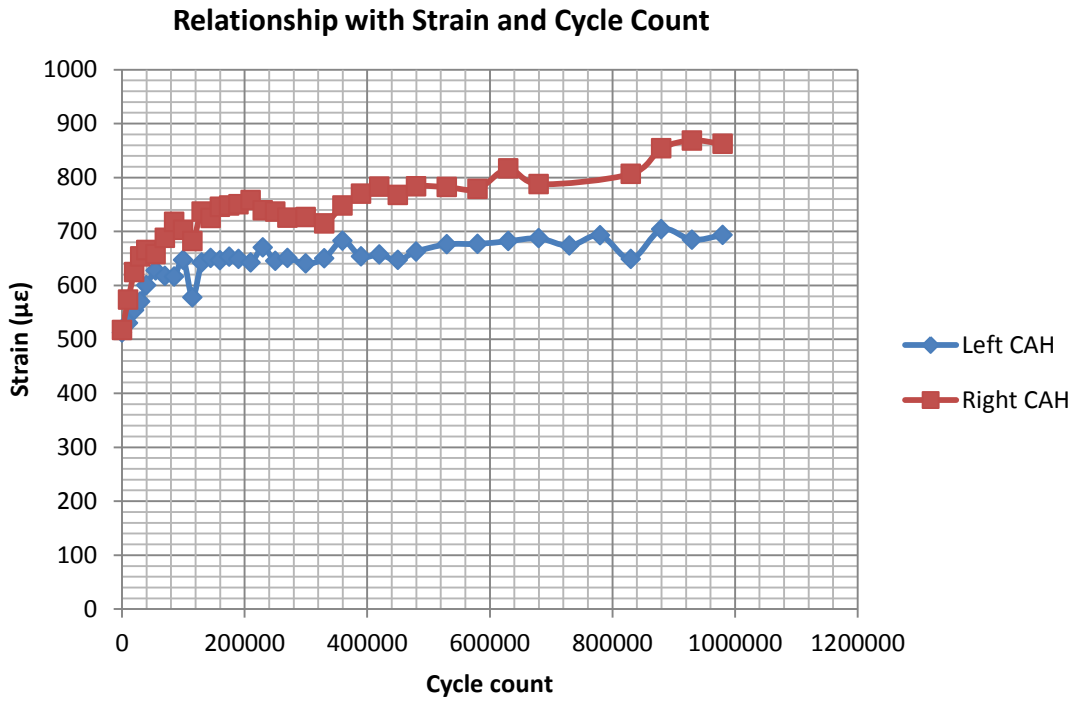

Figure 14: Strain data from left crack-arrest hole and right crack-arrest hole gages both measured at 10 mm (3/8 in) from the edge of the hole at the top of the second pair crack-arrest holes

MODEL INCLUDING PLATE WASHER & TENSIONED BOLT

This study also included an evaluation of the effect of a pretensioned bolt installed in a crack-arrest hole with a plate washer. The effects of this addition were studied in the FE model that included a diagonal crack with 152 mm [6 in.] crack length and a 25 mm [1.0 in.] crack-arrest hole diameter. A pretensioned bolt was modeled in each of the two crack-arrest holes in the model, along with a76 mm × 76 mm × 6 mm [3 in. × 3 in. × 1/4 in.] plate washerthat was modeled between the bolt and web, as shown in Figure 15. A 125 kN [28 kip] pretension force was applied to the bolt's shank. The material used for both the plate washer and bolt was steel (elastic modulus was 200,000 MPa [29,000 ksi] and Poisson's ratio was 0.3).

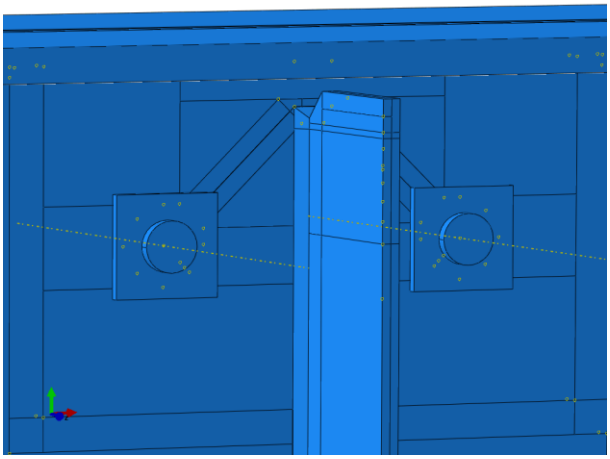

Figure 15: Diagonal crack model with plate washer & tensioned bolt

RESULTS AND DISCUSSION

For eachmodel including a diagonal crack, horseshoe-shaped crack, web-to-flange crack, and horseshoe-shaped&web-to-flange crack, the effect of crack-arrest hole diameter was evaluated by changing the diameter of the holes using values of 13 mm [1/2 in.], 25 mm [1.0 in.], 51 mm [2.0 in.], and 76 mm [3.0in.].To investigate the effect of crack length, the length of diagonal and horseshoe-shaped cracks were altered using values of 70 mm [2 $^{3}/_{4}$in.], 102 mm [4.0 in.], and 152 mm [6.0 in.]. The length of web-to-flange crack was varied between 140 mm [5 $^{1}/_{2}$in.], 203 mm [8.0 in.], and 305 mm [12.0 in.], as shown in Table 2. The results for varying stress paths are compiled in Table 3 through Table 7 for each crack type. Figure 17 though Figure 20 presents the results in terms of maximum principal stress as a function of hole diameter for each stress path. Representative plots for maximum principal stress for all crack placement types are shown in Figure 16. These stress contours are presented with limits from 0 to 345 MPa [50 ksi].

Table 2: Modeling test matrix: summary of hole diameters and crack lengths modeled for different crack patterns

Crack Patterns	Hole Diameter, mm [in.]				Crack Length, mm [in.]		
Diagonal	13 [0.5]	25 [1.0]	51 [2.0]	76 [3.0]	70 [2.75]	102 [4.0]	152 [6.0]
Horseshoe-shaped	13 [0.5]	25 [1.0]	51 [2.0]	76 [3.0]	70 [2.75]	102 [4.0]	152 [6.0]
Web-to-flange	13 [0.5]	25 [1.0]	51 [2.0]	76 [3.0]	140 [5.5]	203 [8.0]	3.5 [12.0]

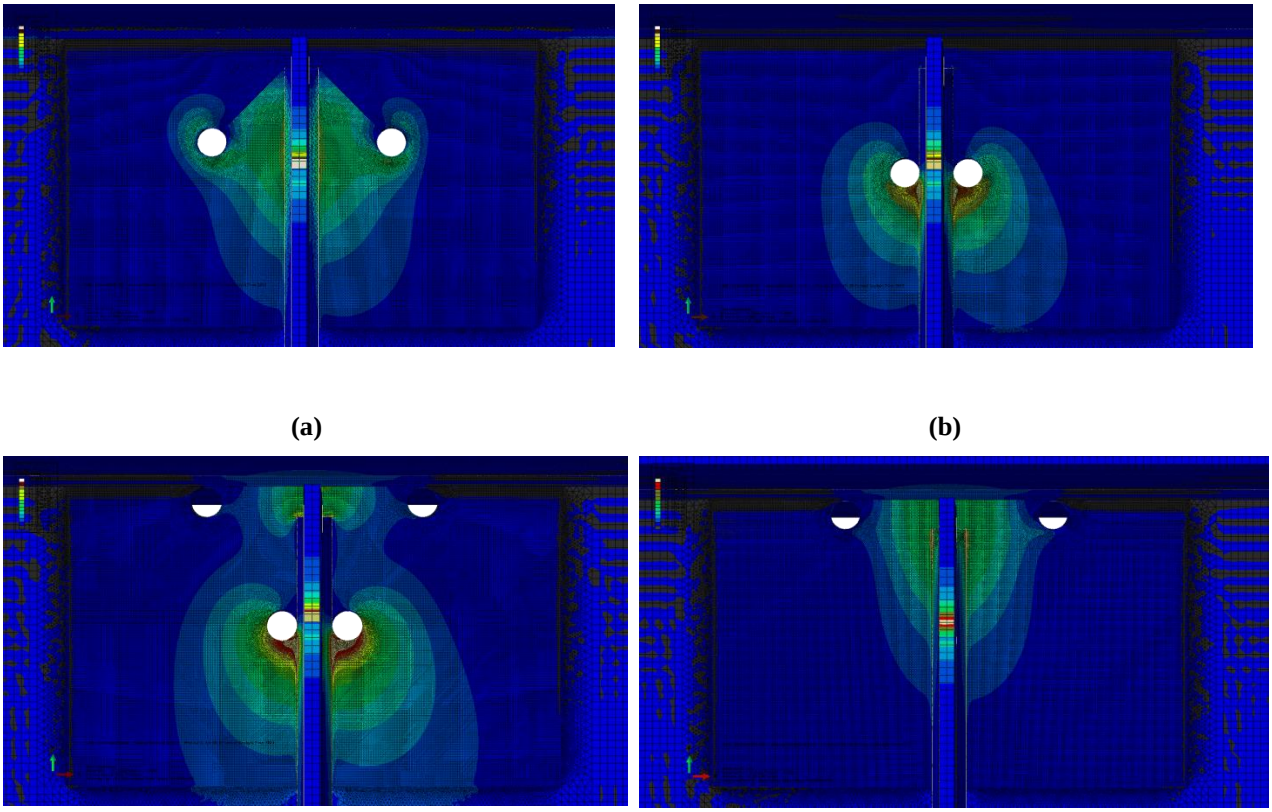

(a) **(b)**

(c) **(d)**

Figure 16: Maximum principal stresses for (a) diagonal crack pattern; (b) horseshoe-shaped crack pattern; (c) horseshoe-shaped crack and web-to-flange crack pattern; (d) web-to-flange crack pattern (The deflection scale was 1.0, and the stress contours are presented with limits from 0 to 345 MPa [50 ksi])

Table 3: Diagonal crack pattern stresses

Maximum Principal Stresses for 70 mm [2.75 in.] Crack

	Circular HSS-1	HSS-1	HSS-2
Diameter, mm [in.]	Peak Stress, MPa [ksi]	Peak Stress, MPa [ksi]	Peak Stress, MPa [ksi]
13 [0.5]	127 [18.4]	157 [22.7]	-0.41 [-0.06]
25 [1.0]	161 [23.4]	168 [24.3]	-0.22 [-0.03]
51 [2.0]	222 [32.2]	234 [33.9]	-0.25 [-0.04]

Maximum Principal Stresses for 102 mm [4.0 in.] Crack

	Circular HSS-1	HSS-1	HSS-2
Diameter, mm [in.]	Peak Stress, MPa [ksi]	Peak Stress, MPa [ksi]	Peak Stress, MPa [ksi]
13 [0.5]	150 [21.7]	170 [24.7]	-0.52 [-0.08]
25 [1.0]	150 [21.7]	172 [24.9]	-0.25 [-0.04]
51 [2.0]	197 [28.6]	196 [28.4]	-0.29 [-0.04]
76 [3.0]	237 [34.4]	247 [35.8]	8.19 [1.19]

Maximum Principal Stresses for 152 mm [6.0 in.] Crack

	Circular HSS-1	HSS-1	HSS-2
Diameter, mm [in..]	Peak Stress, MPa [ksi]	Peak Stress, MPa [ksi]	Peak Stress, MPa [ksi]
13 [0.5]	187 [27.1]	184 [26.7]	-0.42 [-0.06]
25 [1.0]	154 [22.3]	188 [27.2]	-0.22 [-0.03]
51 [2.0]	184 [26.7]	206 [29.9]	0.99 [0.14]

76 [3.0]	208 [30.2]	212 [30.8]	10.9 [1.58]

Table 4: Horseshoe-shaped crack pattern stresses

Maximum Principal Stresses for 70 mm [2.75 in.] Crack

	Circular HSS-1	HSS-1	HSS-2
Diameter, mm [in.]	Peak Stress, MPa [ksi]	Peak Stress, MPa [ksi]	Peak Stress, MPa [ksi]
13 [0.5]	252 [36.6]	364 [52.8]	-0.46 [-0.07]
25 [1.0]	263 [38.2]	286 [41.5]	-0.23 [-0.03]
51 [2.0]	250 [36.3]	263 [38.1]	-0.26 [-0.04]
76 [3.0]	241 [35.0]	252 [36.5]	16.7 [2.42]

Maximum Principal Stresses for 102 mm [4.0 in.] Crack

	Circular HSS-1	HSS-1	HSS-2
Diameter, mm [in.]	Peak Stress, MPa [ksi]	Peak Stress, MPa [ksi]	Peak Stress, MPa [ksi]
13 [0.5]	314 [45.6]	449 [65.1]	-0.48 [-0.07]
25 [1.0]	312 [45.2]	335 [48.6]	-0.21 [-0.03]
51 [2.0]	283 [41.0]	296 [42.9]	-0.21 [-0.03]
76 [3.0]	268 [38.8]	277 [40.2]	-0.27 [-0.04]

Maximum Principal Stresses for 152 mm [6.0 in.] Crack

	Circular HSS-1	HSS-1	HSS-2
Diameter, mm [in.]	Peak Stress, MPa [ksi]	Peak Stress, MPa [ksi]	Peak Stress, MPa [ksi]

13 [0.5]	408 [59.2]	583 [84.5]	-0.53 [-0.08]
25 [1.0]	389 [56.4]	414 [60.1]	-0.23 [-0.03]
51 [2.0]	338 [49.0]	350 [50.8]	-0.20 [-0.03]
76 [3.0]	312 [45.2]	320 [46.4]	-0.24 [-0.04]

Table 5: Horseshoe-shaped & web-to-flange crack pattern stresses

Maximum Principal Stresses for 70 mm [2.75 in.] Crack

	Circular HSS-1	Circular HSS-2	HSS-1	HSS-2
Diameter, mm [in.]	Peak Stress, MPa [ksi]	Peak Stress, MPa [ksi]	Peak Stress, MPa [ksi]	Peak Stress, MPa [ksi]
13 [0.5]	298 [43.2]	22.8 [3.3]	431 [62.5]	122 [17.7]
25 [1.0]	290 [42.1]	56.5 [8.2]	314 [45.6]	98.6 [14.3]

Maximum Principal Stresses for 102 mm [4.0 in.] Crack

	Circular HSS-1	Circular HSS-2	HSS-1	HSS-2
Diameter, mm [in.]	Peak Stress, MPa [ksi]	Peak Stress, MPa [ksi]	Peak Stress, MPa [ksi]	Peak Stress, MPa [ksi]
13 [0.5]	379 [54.9]	20.7 [3.0]	554 [80.4]	178 [25.8]
25 [1.0]	356 [51.7]	32.4 [4.7]	382 [55.4]	172 [25.0]
51 [2.0]	307 [44.5]	77.2 [11.2]	319 [46.2]	100 [14.5]

Maximum Principal Stresses for 152 mm [6.0 in.] Crack

	Circular HSS-1	Circular HSS-2	HSS-1	HSS-2
Diameter, mm [in.]	Peak Stress, MPa [ksi]	Peak Stress, MPa [ksi]	Peak Stress, MPa [ksi]	Peak Stress, MPa [ksi]

13 [0.5]	501 [72.6]	29.6 [4.3]	748 [109]	259 [37.5]
25 [1.0]	461 [66.8]	22.1 [3.2]	488 [70.8]	267 [38.7]
51 [2.0]	385 [55.9]	52.4 [7.6]	394 [57.1]	244 [35.4]
76 [3.0]	346 [50.2]	100 [14.5]	349 [50.6]	161 [23.3]

Table 6: Web-to-flange crack pattern stresses

Maximum Principal Stresses for 140 mm [5.5 in.] Crack

	Circular HSS-2	HSS-1	HSS-2
Diameter, mm [in.]	Peak Stress, MPa[ksi]	Peak Stress, MPa[ksi]	Peak Stress, MPa[ksi]
13 [0.5]	16.2 [2.4]	141 [20.4]	154 [22.3]
25 [1.0]	88.1 [12.8]	147 [21.3]	129 [18.7]
51 [2.0]	192 [27.9]	203 [29.5]	7.6 [1.1]

Maximum Principal Stresses for 203 mm [8.0 in.] Crack

	Circular HSS-2	HSS-1	HSS-2
Diameter, mm[in.]	Peak Stress, MPa[ksi]	Peak Stress, MPa[ksi]	Peak Stress, MPa[ksi]
13 [0.5]	1.72 [0.3]	179 [26.0]	179 [25.9]
25 [1.0]	41.4 [6.0]	180 [26.1]	168 [24.4]
51 [2.0]	141 [20.5]	169 [24.5]	93.1 [13.5]
76 [3.0]	205 [29.7]	212 [30.8]	4.5 [0.65]

Maximum Principal Stresses for 305 mm [12 in.] Crack

	Circular HSS-2	HSS-1	HSS-2
Diameter,	Peak Stress,	Peak Stress,	Peak Stress,

mm [in.]	MPa[ksi]	MPa[ksi]	MPa[ksi]
13 [0.5]	2.2 [0.3]	219 [31.8]	201 [29.1]
25 [1.0]	4.3 [0.6]	220 [31.9]	199 [28.8]
51 [2.0]	88.0 [12.8]	205 [29.7]	167 [24.2]
76 [3.0]	151 [21.9]	188 [27.3]	102 [14.8]

Table 7: 102 mm [4.0 in.] diameter hole stresses

Maximum Principal Stresses for 102 mm [4.0 in.] Diameter Hole

	Circular HSS	HSS-1	HSS-2
	Peak Stress, MPa [ksi]	Peak Stress, MPa [ksi]	Peak Stress, MPa [ksi]
Horizontal 102 mm [4.0 in.]	245 [35.6]	256 [37.1]	0.7 [0.1]
Horseshoe 102 mm [4.0 in.]	245 [35.6]	255 [37.0]	50.7 [7.4]

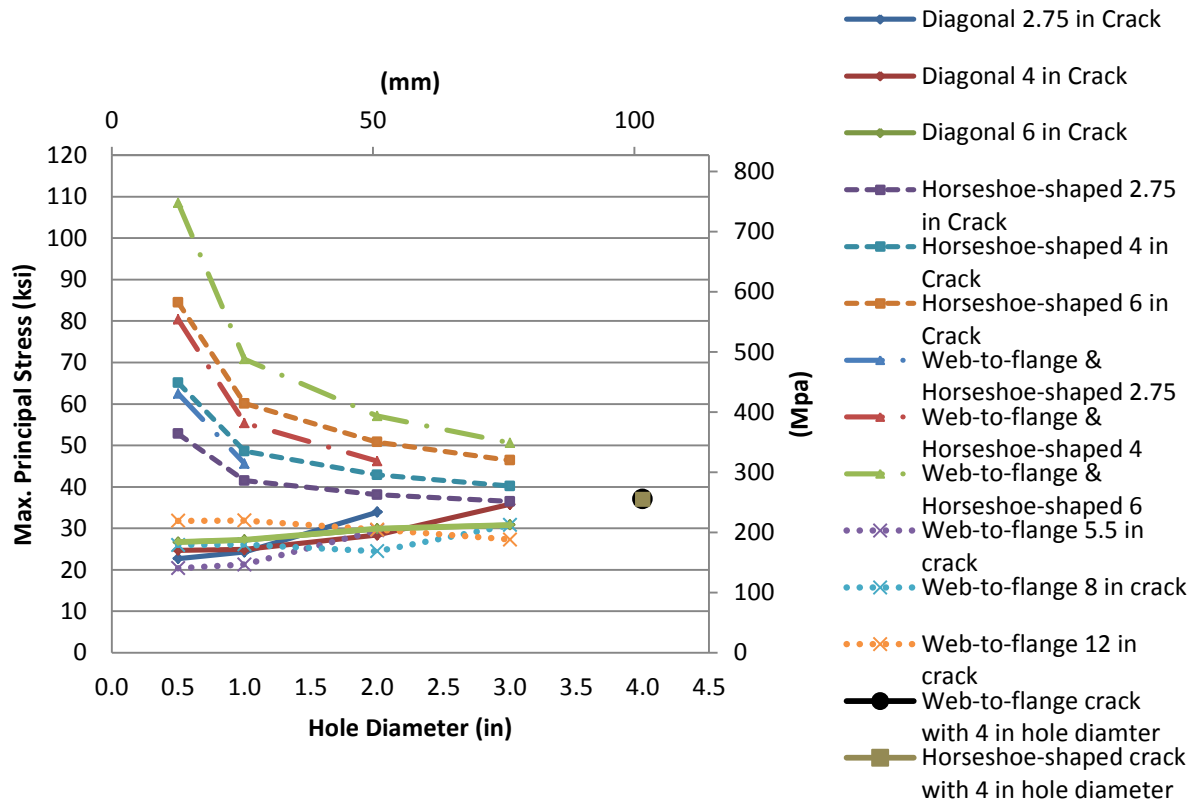

Figure 17: HSS-1 for various crack placements, lengths, and hole diameters

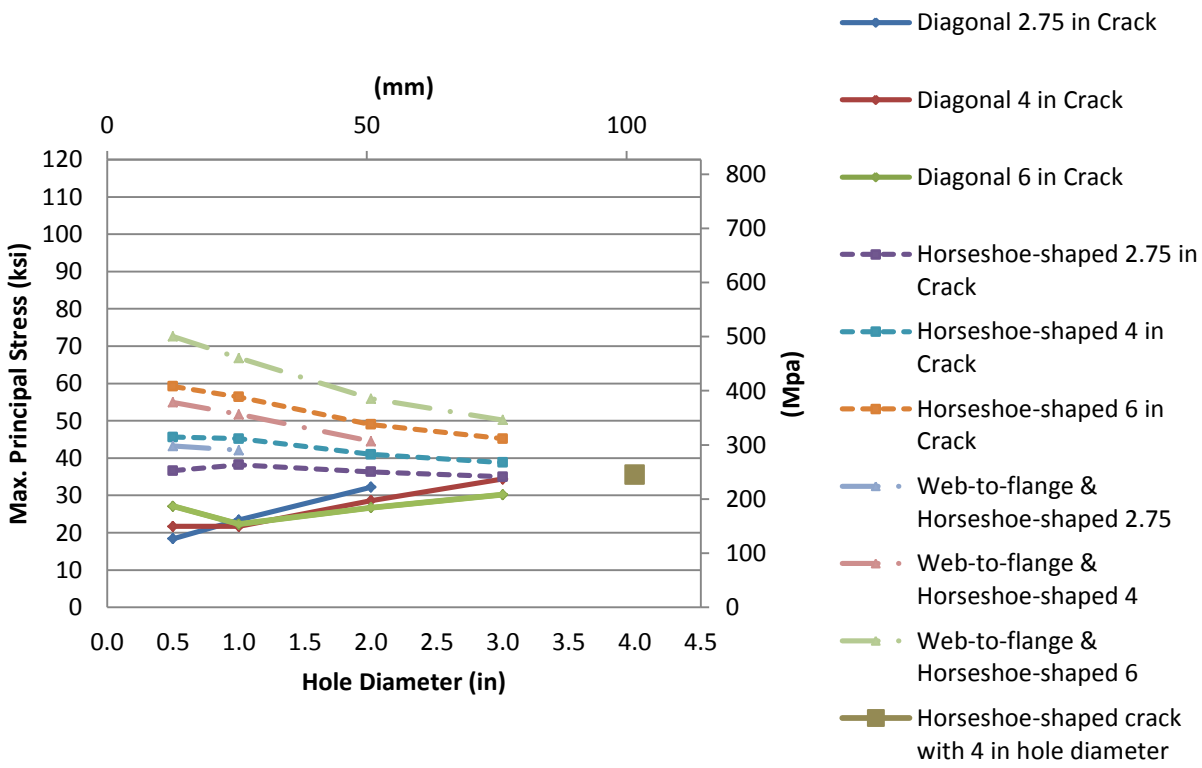

Figure 18: CHSS-1 for various crack placements, lengths, and hole diameters

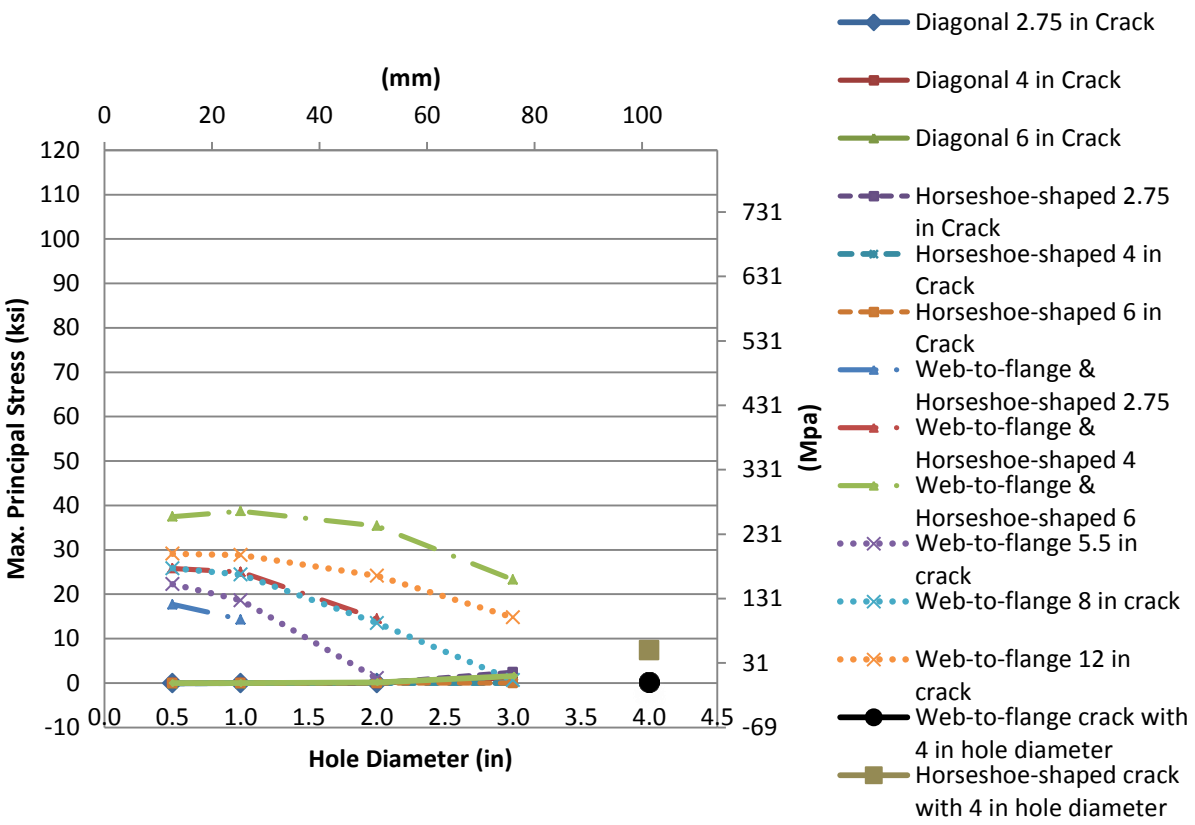

Figure 19: HSS-2 for various crack placements, lengths, and hole diameters

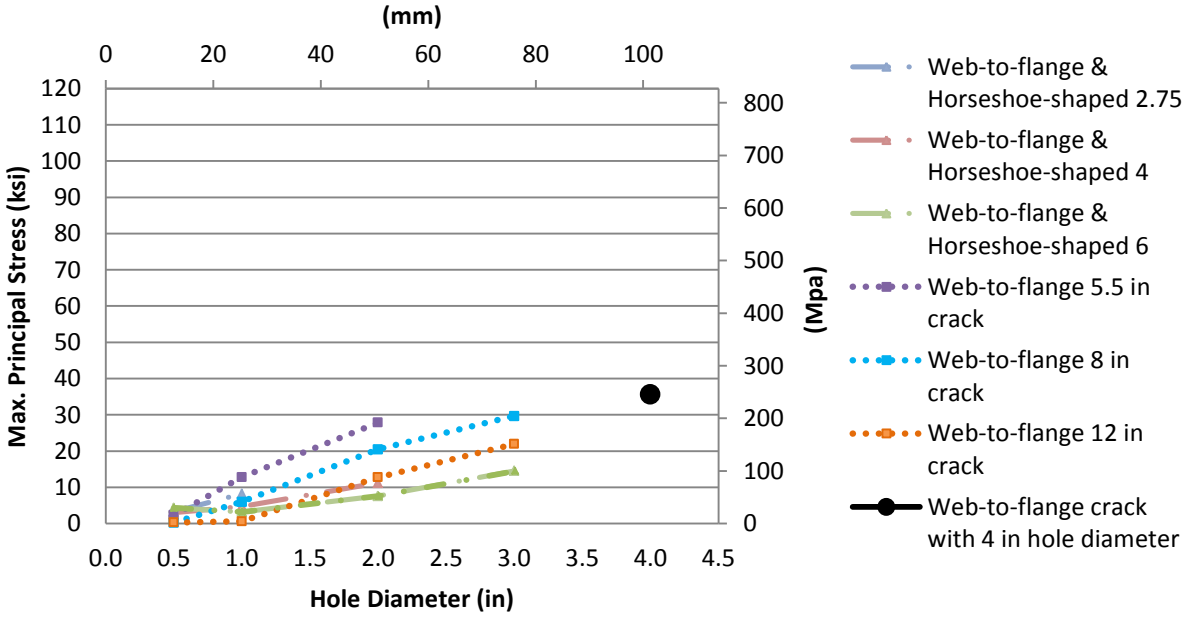

Figure 20: CHSS-2 for various crack placements, lengths, and hole diameters

Table 8: Optimal diameter of crack-arrest hole for each crack type with different crack length

Crack Type	Crack Length, mm [in.]		
	70 [2 3/4]	**102 [4.0]**	**152 [6.0]**
Diagonal	13 [1/2]	13 [1/2]	25 [1.0]
Horseshoe-shaped	76 [3.0]	76 [3.0]	76 [3.0]
Horseshoe-shaped & Web-to-flange	25 [1.0]	51 [2.0]	76 [3.0]
Web-to-flange	25 [1.0]	51 [2.0]	51 [2.0]

EFFECT OF CRACK-ARREST HOLES FOR DIAGONAL CRACK

As shown in Figure 4(a), the crack was modeled to occur as a diagonal crack and the paths from which stresses were measured are referred to as HSS-1, HSS-2 and circular HSS-1 (CHSS-1) respectively. The effect of crack-arrest holes on HSS in the steel girder section is shown in Table 3, as well as in Figure17, Figure 18, and Figure 19. As can be seen in Figure 15, it was found that HSS-1 increased with increasing hole diameter for 70 mm [2 3/4 in.], 102 mm [4.0 in.], and 152 mm [6.0 in.] crack lengths. By increasing the hole diameter, the edge of the hole translated closer to the connection plate and adjacent flange, causing a stress concentration to form at the welds. Under distortion-induced fatigue, large diameter crack-arrest holes do not perform better than small diameter crack-arrest holes. The data showed that for diagonal crack occurring on the steel girder section, drilling smaller crack-arrest holes for shorter crack lengths was most effective. The rate of stress change decreased with increasing crack length. The rate of stress change varied the most for the shortest crack length, which was 70 mm [2 3/4 in.]. The magnitude of HSS-2 remained very small for all crack lengths and hole diameters studied, as shown in Figure 19. In Figure 18, CHSS-1 has the same trend with HSS-1. As shown in Table 8, the optimal crack-arrest hole diameter for 70 mm [2 3/4 in.] long diagonal crack was recommended as 13 mm [1/2

in.], the optimal crack-arrest hole diameter for 102 mm [4.0 in.] long crack was recommended as 13 mm [1/2 in.], and the optimal crack-arrest hole diameter for 152 mm [6.0 in.] long crack was recommended as 25 mm [1.0 in.].

EFFECT OF CRACK-ARREST HOLES FOR HORSESHOE-SHAPED CRACK

Figure 4(b) shows the crack modeled as a horseshoe-shaped crack. The paths will be referred to as HSS-1, HSS-2 and CHSS-1 respectively. The results for these variations are compiled in Table 4 and presented graphically in Figure17, Figure 18, and Figure 19. In general, increasing the diameter of holes resulted in a reduction of HSS-1 and CHSS-1. When hole diameter was held constant, increasing crack length correlated with increased magnitudes of HSS-1 and CHSS-1, as expected. Small diameter holes with short length cracks were associated with lower HSS magnitudes than large diameter holes with longer length cracks.Similar to the relationship for diagonal models, the magnitude of HSS-2 remained very small for all crack lengths and hole diameters studied. As shown in Table 8, the optimal crack-arrest hole diameter for 70 mm [2 $^{3}/_{4}$ in.] long horseshoe-shaped crack was recommended as 76 mm [3.0 in.], the optimal crack-arrest hole diameter for 102 mm [4.0 in.] long crack was recommended as 76 mm [3.0 in.], and the optimal crack-arrest hole diameter for 152 mm [6.0 in.] long crack was recommended as 76 mm [3.0 in.].

EFFECT OF CRACK-ARREST HOLES FOR A SIMULTANEOUSLY-OCCURING HORSESHOE-SHAPED&WEB-TO-FLANGE CRACK

Another crack pattern is a horseshoe-shaped and web-to-flange crack occurring simultaneously. Shown in Figure 4(c), these paths will be referred to as HSS-1, HSS-2, CHSS-1 and CHSS-2

respectively. The results are shown in Table 5, as well as in Figure 17 through Figure 20. Similar to the resultsobserved for models with horseshoe-shaped crack, increasing the diameter of crack-arrest holes resulted in a reduction of HSS-1, HSS-2 and CHSS-1 for each length combination of cracks. However, the CHSS-2 increased when the crack-arrest holes diameter increased for different crack lengths. Due to the crack edge translating closer to the flange, the stress concentrated near the web-to-flange weld.As shown in Table 8, the optimal crack-arrest hole diameter for 70 mm [2 $^{3}/_{4}$ in.] horseshoe-shaped & web-to-flange crack was recommended as 25 mm [1.0 in.], the optimal crack-arrest hole diameter for 102 mm [4.0 in.] long crack was recommended as 51 mm [2.0 in.], and the optimal crack-arrest hole diameter for 152 mm [6.0 in.] long crack was recommended as 76 mm [3.0 in.].

EFFECT OF CRACK-ARREST HOLES FOR WEB-TO-FLANGE CRACK

For the web-to-flange crack shown in Figure 4(d), the paths will be referred to as HSS-1, HSS-2 and CHSS-2 respectively. The results presented in Table 6, Figure17, Figure 19, and Figure 20 show that the HSS-1 for a 140 mm [$5^{1}/_{2}$in.] crack increased with an increase in hole diameter. However, the HSS-1 for the 203 mm [8.0 in.] crack decreased then increased for increasing hole diameters. The HSS-1 for a 305 mm [12.0 in.] crack always decreased with increasing holes diameters. The HSS-1 magnitudes showed slightly different trends, depending on crack length. In general, HSS-1 magnitudes were not extremely sensitive to either the length of the web-to-flange crack, or the diameter of the crack-arrest holes. HSS-2 stress magnitudes clearly decreased with increasing hole diameter, while the CHSS-2 stresses around the crack-arrest hole showed a clear trend of increasing with increasing hole size.As shown in Table 8, the optimal crack-arrest hole diameter for 140 mm [5 $^{1}/_{2}$ in.] web-to-flange crack was recommended as 25

mm [1.0 in.], the optimal crack-arrest hole diameter for 203 mm [8.0 in.] long crack was recommended as 51 mm [2.0 in.], and the optimal crack-arrest hole diameter for 305 mm [12.0 in.] long crack was recommended as 51 mm [2.0 in.].

LARGE-HOLE RETROFIT

To examine the performance of the McGormley and Koob (2002) large-diameter hole retrofit against the suite of models examined in this study, a horseshoe-shaped crack model and a web-to-flange crack model with 102 mm [4.0 in.] diameter holes were developed, as shown in Figure 5. The results are presented in Table 7, as well as in Figure 17 through Figure 20. For the model having a web-to-flange crack, the HSS-2 magnitudes for the 102 mm [4.0 in.] diameter hole model was less than the stress magnitudes found in the smaller diameter hole models. However, the HSS-1 and circular HSS magnitudes for the 102 mm [4.0 in.] diameter hole model were larger than the stress magnitudesresulting in smaller diameter hole models. From the model including a horseshoe-shaped crack, the HSS-1 and circular HSS magnitudes for a 102 mm [4.0 in.] diameter hole were nearly the same as the stresses found in the 70 mm [$2^{3}/_{4}$in.] crack model having a 76 mm [3.0 in.] diameter hole. The HSS-2 magnitude for the model with a horseshoe-shaped crack and a 102 mm [4.0 in.] diameter hole was greater than the stresses measured in the smaller diameter hole models. This showed that large diameter crack-arrest holes did not perform better than small diameter crack-arrest holes for certain crack configurations.

EFFECT OF INCLUDING PRETENSIONED BOLT WITH PLATE WASHER

The effect of a pretensioned bolt used in combination with a plate washer was also evaluated for the diagonal crack model with 152 mm [6.0 in.] crack length and 25 mm [1.0 in.] hole diameter.

The maximum principal stresses around the crack for the model with the plate washer and pretensioned bolt, and for the diagonal crack-arrest hole model that did not includethe plate washer & pretensioned bolt are shown in Figure 21. The results compared with the diagonal crack-arrest hole model that did not include the plate washer& pretensioned bolt are presented in Figure 22. The peak circular HSS for the model that included a plate washer and a pretensioned bolt was found to be slightly higher than found from the crack-arrest hole model that did not include the pretensioned bolt and plate washer. The peak HSS-1 magnitude obtained from the model with an empty crack-arrest holewas slightly higher than the HSS-1 stress from the model that includeda plate washer& pretensioned bolt. The HSS-2 values fromthe model that includeda plate washer & pretensioned bolt and the model with empty crack-arrest holes weresimilar in magnitude. Given these mixed findings,the effect of adding a plate washer & pretensioned bolt did not appear to satisfactorily mitigate distortion induced fatigue concerns around the crack arrest holes, or around the connection plate weld.

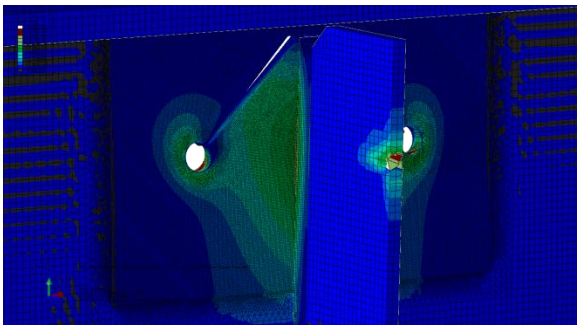

(a)

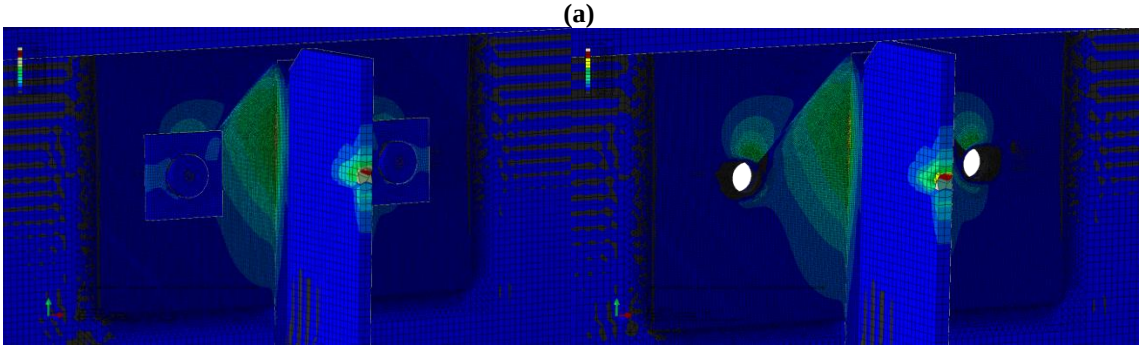

(b) **(c)**

Figure 21: (a) Maximum principal stress for diagonal crack-arrest hole model without plate washer& pretensioned bolt; (b) Maximum principal stress for diagonal crack model with plate washer& pretensioned bolt; (c) Maximum principal stress for diagonal crack model with plate washer& pretensioned bolt (plate washer & pretensioned bolt are not shown)

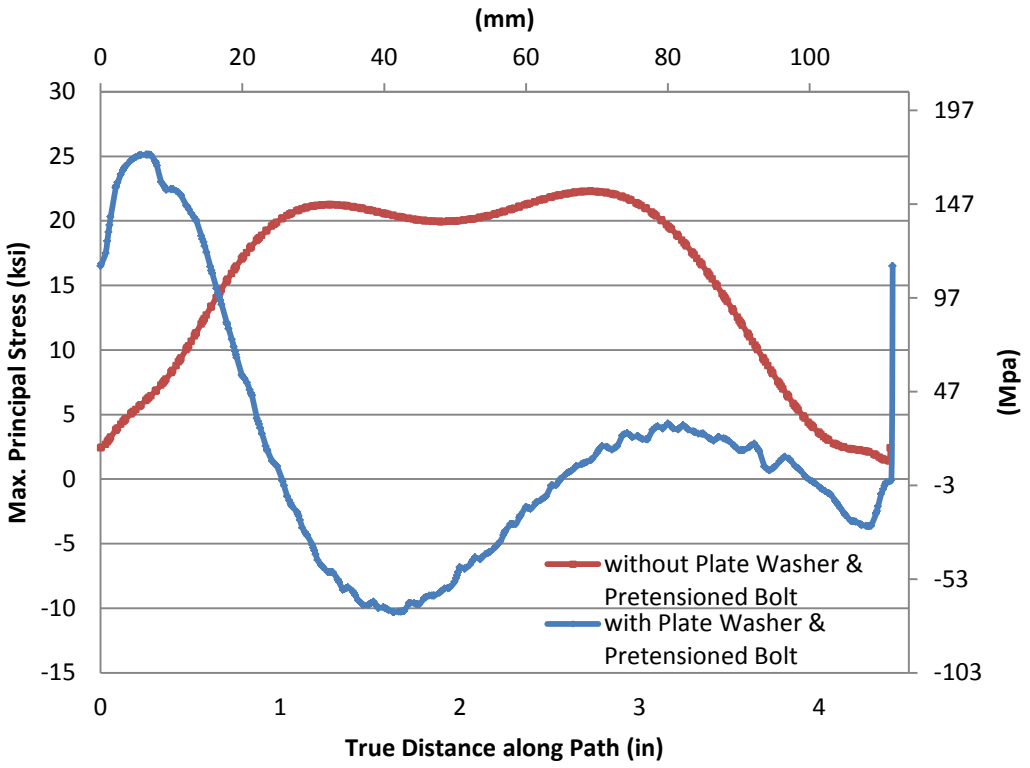
(mm)
0
20
40
60
80
100
30
25
20
15
10
5
0
-5
-10
-15
197
147
97
47
-3
-53
-103
Max. Principal Stress (ksi)
(Mpa)
without Plate Washer & Pretensioned Bolt
with Plate Washer & Pretensioned Bolt
0
1
2
3
4
True Distance along Path (in)

(a)

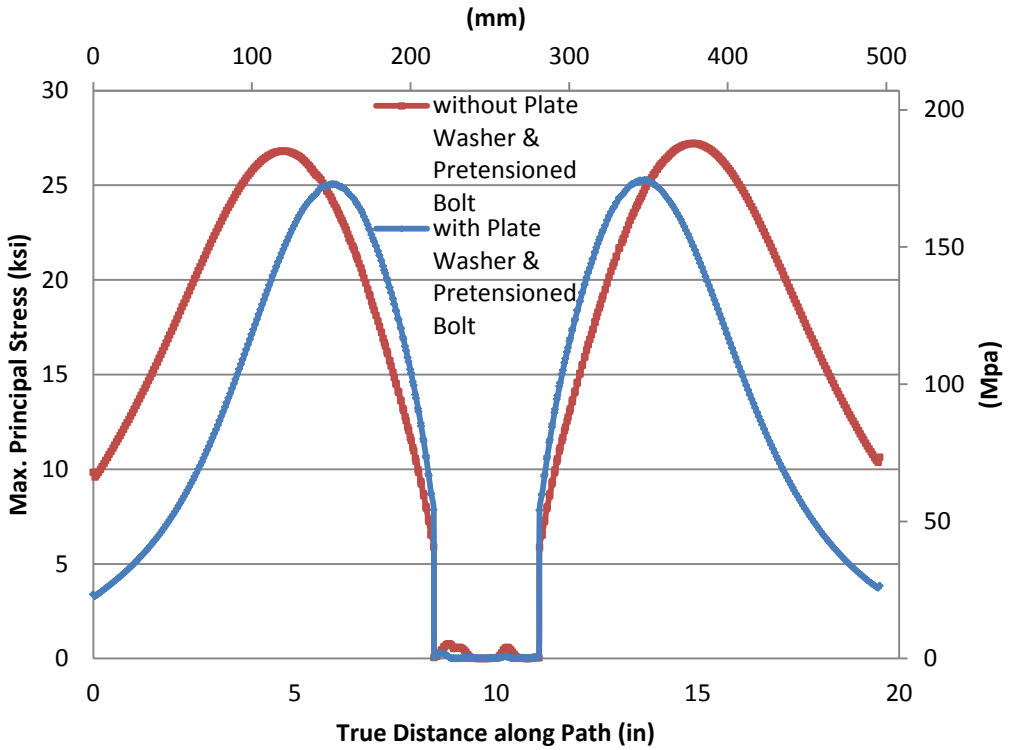
(mm)
0
100
200
300
400
500
30
25
20
15
10
5
0
200
150
100
50
0
Max. Principal Stress (ksi)
(Mpa)
without Plate Washer & Pretensioned Bolt
with Plate Washer & Pretensioned Bolt
0
5
10
15
20
True Distance along Path (in)

(b)

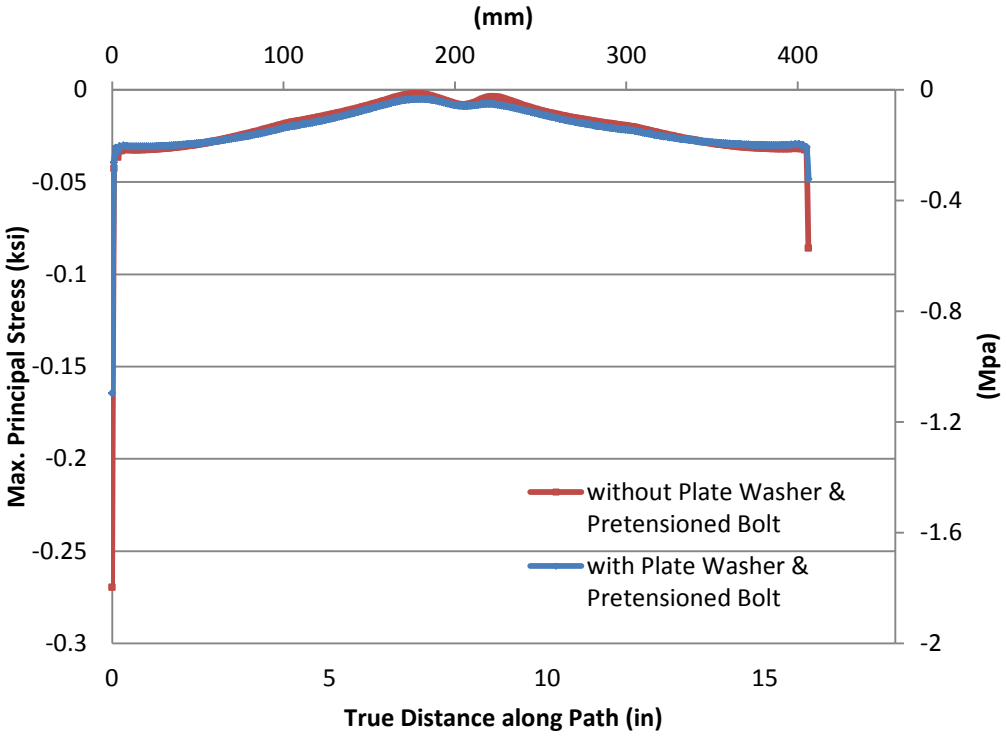

(c)

Figure 22: (a) Circular HSS comparison between diagonal crack-arrest hole model and the model with plate washer& pretensioned bolt; (b) HSS-1 comparison between diagonal crack-arrest hole model and the model with plate washer& pretensioned bolt; (c) HSS-2 comparison between diagonal crack-arrest hole model and the model with plate washer & pretensioned bolt along the path

CONCLUSIONS

Common knowledge has been that large diameter crack-arrest holes are more effective at halting crack propagation under distortion-induced fatigue than small diameter crack-arrest holes. However, because the cracks often occur in the girder webs at connection plate-to-web or flange-to-web welds, drilling large diameter crack-arrest holes can produce stress concentrations near welds in the vicinity. This study, which was focused on evaluating the effectiveness of crack-arrest holes for various crack placements, crack lengths, and crack-arrest hole diameters has led to the following conclusions:

- The models showed that stress magnitudes were less for shorter crack lengths than for longer crack lengths having the same size crack-arrest hole at the crack tip. This result is in-line with engineering expectations and common knowledge. The reader is reminded that the crack lengths reported in this paper include the either the hole diameter or hole radius, depending on the hole placement (Figure 4).
- In general, the weld around the connection plate was the most sensitive location when a crack existed around the connection plate. In fact, the presence of a horseshoe-shaped crack was consistently correlated with greater stress demands than other crack patterns. When a horseshoe-shaped crack was combined with a crack at the web-to-flange weld, the stress demands increased further. It was found that stresses at the connection plate weld were reduced significantly (Figure 17) when a crack-arrest hole having a diameter at least 25 mm (1 in.) was implemented. Diminishing returns were observed for crack-arrest holes having diameters greater than 38 mm (1.5 in.). Therefore, while the trend was to see decreasing stresses with increasing hole diameter for this crack placement,

very large-diameter crack arrest holes may not be necessary, especially for shorter crack lengths.

- When the crack placement studied was diagonal (the crack extended out into the web base material), larger crack-arrest hole diameters tended to correspond to increased stress demands, especially stresses around the hole circumference. Therefore, for this crack type, use of small diameter crack arrest holes appears to be more advisable than large diameter holes.
- When a crack along the web-to-flange weld was included in the model (with crack-arrest holes at the crack tips), stress demands around that crack arrest hole tended to increase nearly linearly with increasing hole diameter. Therefore, if a particular case of cracking due to distortion-induced fatigue tends to be represented by significant cracking around the web-to-flange weld, use of a small-diameter crack arrest hole may be better than use of a larger hole.
- Installing a pretensioned boltwith a plate washer did not result in performance that was significantly better than simply drilling crack-arrest holes on reducing the hot spot stress caused by the distortion-induced fatigue.

The findings of this study showed that crack-arrest hole placement (a function of crack geometry), rather than crack-arrest hole diameter, has a much greater effect on the effectiveness of the crack-arrest hole in mitigating distortion-induced fatigue. The results of this study are expected to help guide engineers faced with repairing and retrofitting aging steel bridge infrastructure susceptible to distortion-induced fatigue.

The experimental findings corroborated the analytical results. From the results of inspection, cracks never reinitiated from the crack-arrest holes. However, new cracks tended to form along the stiffener-to-web weld a short distance from the holes. The holes provided a wider area in the web for stresses to be distributed away from the stiffener. The experimental investigation showed that a 51 mm [2.0 in.]diameter crack-arrest hole was effective in stopping a horseshoe-shaped crack from propagating. However, since the stress demand at the connection plate-to-web weld wasvery large, new cracks initiated along the stiffener-to-web weld at a small distance away from the drilled holes.

REFERENCES

Alemdar, F. (2011) “Repair of bridge steel girders damage by distortion-induced fatigue”.

Castiglioni, C., et. al. (1988). “Evaluation of fatigue cracking at cross diaphragms of a multigirder steel bridge”. Journal of Constructional Steel Research, vol. 9, no. 2, pp. 95-110.

Jajich, D., and Schultz, A. E. (2003). “Measurement and Analysis of Distortion-Induced Fatigue in Mutligirder Steel Bridges”. Journal of Bridge Engineering, vol. 8, no. 2, pp. 84-91.

Keating, P. B. (1994). “Focusing on fatigue”. Civil Engineering—ASCE, vol. 64, no. 11, pp. 54-57.

Marquis, G., and Kahonen, A. (1995). "Fatigue testing and analysis using the hot spot method". Technical Research Centre of Finland.

McGormley, J. C., and Koob, M. J. (2002). “Large Hole Retrofits to Address Distortion-Induced Cracking”.

Roddis, W. M. Kim, and Zhao, Yuan (2001). “Out-of-Plane Fatigue Cracking in Welded Steel Bridges: Why It Happened and How It Can Be Repaired”. Welding Innovation, vol. 27, no. 2, pp. 2-7.

Tedesco, J. W., et. al. (1995). “Finite Element Method Analysis of Bridge Girder-Diaphragm Interaction”. Computers and Structures, vol. 56, no. 2-3, pp. 461-473.

Part 4

EVALUATION OF THREE COMPUTATIONAL TECHNIQUES FOR QUANTIFYING DISTORTION-INDUCED FATIGUE CRACK PROPENSITY USING FINITE ELEMENT ANALYSIS

H. Liu[1], J.C. Przywara[2], T.I. Overman[3], C.R. Bennett*[4], A.B. Matamoros[5], S. T. Rolfe[6]

ABSTRACT

In many bridges built prior to 1985, distortion-induced fatigue near transverse connection plate web-gaps is a serious problem. Retrofits aimed at mitigating the effects of distortion-induced fatigue and stopping fatigue crack growth are constantly being analyzed both experimentally and computationally. Traditional finite element analysis techniques often explicitly model web-gap cracks and employ stress-based analysis techniques such as the Hot Spot Stress method in order to evaluate retrofit performance. The recent implementation of the Extended Finite Element Method (XFEM) in the finite element analysis software program Abaqus v.6.10 has enabled more accurate crack modeling to be conducted as well as fracture mechanics-based analyses such as the computation of J-Integrals and Stress Intensity Factors to be utilized. Using several crack states modeled by the XFEM, the computation of Hot Spot Stress, J-Integrals, and Stress Intensity Factors was used in simulations to analyze the performance of an angles-with-plate retrofit with varying angle and back plate thickness. All three analysis techniques were able to

Department of Civil, Environmental, and Architectural Engineering
University of Kansas, 1530 W. 15th St, Lawrence, KS 66045
Tel. (785) 864-3235, Fax. (785) 864-5631

[1]Hao Liu, Graduate Research Assistant, University of Kansas, h781l127@ku.edu
[2] John C. Przywara, EIT, Structural Engineer, The SK&A Group, jackp@skaengineers.com
[3] Temple I. Overman, EIT, Junior Bridge Engineer, HNTB Corporation, toverman@hntb.com
[4] Caroline R. Bennett, PhD, PE, Corresponding Author, Associate Professor, University of Kansas, crb@ku.edu
[5] Adolfo B. Matamoros, PhD, PE, Professor, University of Texas at San Antonio, adolfo.matamoros@utsa.edu
[6] Stanley T. Rolfe, PhD, PE, Professor, University of Kansas, srolfe@ku.edu

determine that the addition of any angles-with-plate retrofit had the greatest positive effect at the largest crack state modeled and the stiffest angles-with-plate retrofits were able to improve performance the best. The findings from the experimental testing have been compared against the results from the analytical components of this study.

INTRODUCTION

One of the major threats to the longevity of highway bridges is distortion-induced fatigue cracking in the transverse connection plate web-gap regions of bridge girders. In many bridges, a commonly-used detail to laterally transfer traffic loads and prevent lateral-torsional buckling during construction involves attaching lateral bracing to transverse connection plates [1]. In bridges built prior to 1985, these transverse connection plates were typically cut short of the tension flange due to historic concerns of producing susceptibility to brittle fracture [2]. These concerns arose from failures of European bridges early in the last century [3]. However, this particular cross-bracing detail has accounted for the largest amount of fatigue-cracking in surveys in 1994 [4] and 2003 [5]. The reason for this is that, when a particular girder experiences greater bending deformation than an adjacent girder connected by this cross-bracing detail, significant out-of-plane stress concentrations occur in the web-gap between the transverse connection plate and either flange during each loading cycle. Thus, after numerous cycles, fatigue cracks initiate and begin to propagate in these web-gap regions, ultimately decreasing the fatigue life of the bridge.

There are a number of solutions currently utilized to mitigate the effects of distortion-induced fatigue in bridge girders. Most of these solutions attempt to reduce the stress demand in the web-gap region by either making the connection plate-to-web connection more flexible or by creating an alternate load path from the connection plate to the flange. One of the most common

ways to provide an alternate load path around the web-gap is to weld or bolt angles between the transverse connection plate and the adjacent girder flange. Previous studies [6,7] have experimentally investigated this detail, and a common conclusion was that performing this type of repair on a top web-gap can require removal of portions of the concrete bridge deck. For this reason, it is necessary to explore the effectiveness of other possible solutions.

One recently proposed solution is called the angles-with-plate retrofit technique. This solution avoids the problems of having to remove a portion of the concrete bridge deck by providing connectivity between the transverse connection plate and the girder web. A two-part study [8, 9] investigated this retrofit technique applied to 2.7-m (9-ft) girder specimens through computer simulations and experimental verification. Computer simulations showed that the angles-with-plate retrofit was able to prevent distortion of the web-gap region and was able to significantly reduce stresses in the web-gap region. The experimental portion of the study observed that fatigue cracks propagated along the transverse connection plate-to-web welds and the flange-to-web welds in the test girders and that the angles-with-plate retrofit was effective at limiting fatigue crack growth in both crack locations.

OBJECTIVE AND SCOPE

The objective of this study was to evaluate three analysis techniques for determining the effectiveness of the angles-with-plate distortion-induced fatigue retrofit: Hot Spot Stress analysis, J-integrals, and Stress Intensity Factors. Previous computational studies aimed at investigating the performance of the angles-with-plate distortion induced fatigue retrofit only utilized the analysis technique of Hot Spot Stresses to quantitatively evaluate the effectiveness of the angles-with-plate retrofit. Detailed finite element models of 2.7-m (9-ft) girder specimens with the angles-with-plate retrofit were created using the commercially-available finite element

modeling software Abaqus v.6.10 [10]. These models were simulated with cracks along both the connection plate-to-web welds and the flange-to-web welds at varying lengths. The three analysis techniques were employed, compared against results from physical testing, and their results are discussed in this paper.

FINITE ELEMENT MODELS

All finite element models discussed in this paper were based off of 2.7-m (9-ft) long experimental girder-cross frame assemblies used in studies conducted at KU. These subassemblies were designed to exist as a segment of an external girder in a composite bridge. In an actual bridge, the top flange of the girder would be restrained against lateral motion by the bridge deck. This boundary condition was simulated in the subassembly by inverting the girder and bolting the top flange (now on the bottom) to a series of channels connected to the laboratory strong floor. When the top flange is referred to in this paper, it is the bottom flange on the subassembly since the girder in the subassembly is inverted. One of the effects of supporting the girder in this manner is that longitudinal bending of the girder was not allowed, leaving only out-of-plane loads applied via the cross frame element. This type of stress field is assumed to be representative of the behavior near inflection points in bridges or points where the bending stresses due to live loads are very small compared to the stresses induced by out-of-plane forces.

MODELING METHODOLOGY

Detailed three-dimensional finite element models were created using the commercially-available finite element modeling software Abaqus v.6.10 to simulate the behavior of the experimental test girders. The girder specimens modeled in this study were 2.7-m (9-ft) long built-up I-sections, with a 876-mm x 10-mm (34 ½-in. x 3/8-in.) web, a 279-mm x 16-mm (11-in. x 5/8-in.) top

flange, and a 279-mm x 25-mm (11-in. x 1-in.) bottom flange. 5-mm (3/16-in.) fillet welds were used to attach the flanges to the web. In the experimental set-up, the girders were inverted and connected to the laboratory floor through a series of eight post-tensioned C310x45-mm (C12x30-in.) channels and ten post-tensioned C130x13-mm (C5x9-in.) channels, which served to simulate the presence of an axially stiff concrete deck. Three L76x76x10-mm (L3x3x3/8-in.) angles constituting the cross frame were attached to two 305-mm x 191-mm x 10-mm (12-in. x 7 ½-in. x 3/8-in.) gusset plates by 5-mm (3/16-in.) fillet welds, which were, in turn, bolted to a 876-mm x 127-mm x 10-mm (34 ½-in. x 5-in. x 3/8-in.) connection plate. This connection plate was welded all-around to the web with a 5-mm (3/16-in.) fillet weld but was not welded to either flange. The opposite end of the three angles constituting the cross bracing were bolted to a WT267x700-mm (WT10.5x27.5-in.) section. This was attached to an actuator connected to a loading frame that could apply a vertical load to the cross frame. Two L76x76x10-mm (L3x3x3/8-in.) angles were used to apply restraint to the girder ends in order to capture the effects of girder continuity in a bridge. The opposite ends of these angles were bolted to a 3500-mm (138-in.) long MC310x74-mm (MC12x50-in.) section which was attached to the loading frame. The experimental girder subassembly and the finite element model of the subassembly are shown in Figure 1.

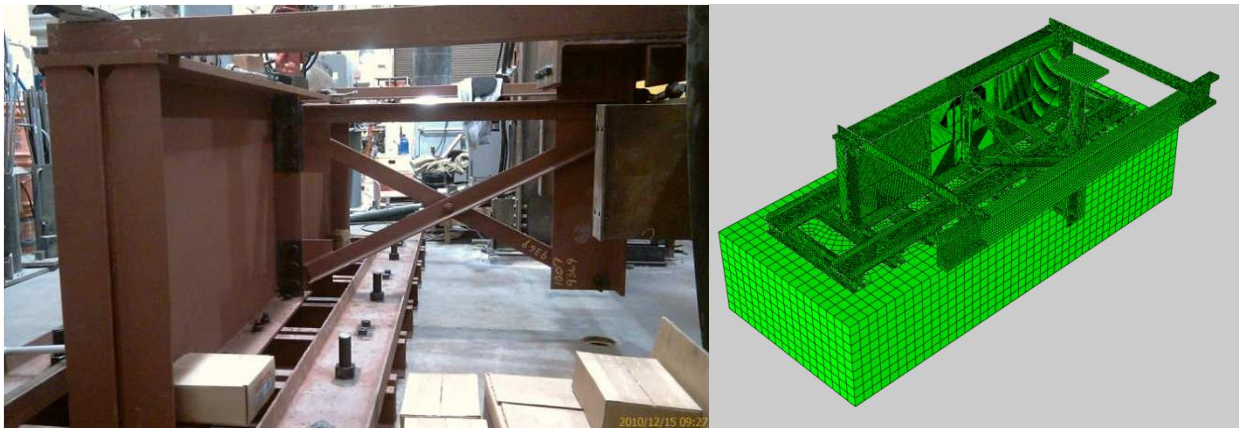

(a) **(b)**

Figure 1: (a) Experimental girder subassembly and (b) the finite element model of the subassembly

Eight-node, cubic elements with 24 degrees of freedom each were used wherever possible to model the physical geometry. In some instances, four-node, tetrahedral elements having 12 degrees of freedom were utilized to conform to special geometric aspects of the set-up. All fillet welds were modeled as right triangle cross-sections and tie constraints were used to connect the fillet welds to the surfaces that they were bringing together. Additionally, surfaces in the model expected to make contact with one another were assigned interaction properties with a coefficient of friction of 0.35 to simulate hard contact. Finally, the actuator was modeled with steel properties and an 86x86-mm (3.4x3.4-in) square cross-section with a length of 584 mm (23 in.). It was capable of moving in the vertical plane and a 22.2-kN (5-kip) linearly progressing upward load was applied to it to simulate half of one cycle of the actual loading.

Each part in the finite element model was assigned material properties. All steel sections and welds were modeled as isotropic, linear-elastic materials with an elastic modulus of 200,000-MPa (29,000-ksi) and a Poisson's ratio of 0.3. The laboratory floor was the only component of the finite element models modeled as concrete, and it was simulated to be an isotropic, linear-elastic material with an elastic modulus of 27,780 MPa (4,030 ksi) and a Poisson's ratio of 0.2.

EXTENDED FINITE ELEMENT METHOD (XFEM)

Two different methods can be used to simulate web-gap cracks in the computational models created in the finite element modeling software Abaqus v.6.10. The first method involves explicitly modeling the discontinuity created by the cracks by removing thin sections of elements in the web at the crack locations. The second method utilizes components of the Extended Finite Element Method (XFEM) theory embedded in Abaqus v.6.10, which can be used to model crack discontinuities independent of the model mesh. In this study, cracks were simulated using XFEM.

The XFEM concept was first published in 1999 [11] and was first implemented in version 6.9 of Abaqus. Modeling cracks using XFEM can simulate a crack discontinuity independent of the finite element mesh geometry. In other words, cracks can be modeled as occurring *through* individual elements as opposed to having to occur at element boundaries. XFEM accomplishes this by enhancing the finite element approximation by adding discontinuous functions to the solution at nodes in elements cut by a crack or a crack tip. Thus, three distinct sets of nodes are used to approximate behavior in a cracked model [12]. These node sets are as follows:

(1) All nodes in the model domain;

(2) Nodes whose shape function support is intersected by a crack; and

(3) Nodes whose shape function support contains the crack front.

Subsequently, there are three different approximations for the displacement, *U*, for the three sets of nodes in the model. The first of these approximations is applicable to all nodes in the model and is represented by Equation 1:

$$U = U_I = \sum_{i \epsilon I} u_i N_i \quad (1)$$

where:

I = set of all nodes in the domain

u_i = classical degrees of freedom for node i

N_i = shape function for node i

When there is an existing crack in a region of a model where crack initiation and propagation is allowed, other approximations are utilized in addition to U_I to obtain a refined solution. One of these approximations represents a solution refinement to calculate the effect of the discontinuity across a fully-developed crack. Equation 2 represents this refinement:

$$U = U_I + U_J = U_I + \sum_{j \epsilon J} b_j N_j H(x) \quad (2)$$

where:

J = set of nodes whose shape function support is cut by a crack

b_j = jump in displacement field across the crack at node j

N_j = shape function for node j

$H(x)$ = Heaviside jump function (+1 on one side of crack, -1 on other side)

The final approximation characterizes a solution refinement for the calculation of nodal displacements around both crack tips. This is represented by the expression in Equation 3:

$$U = U_I + U_{K1} + U_{K2} = U_I + \sum_{k \epsilon K1} N_k \left(\sum_{l=1}^{4} c_k^{l1} F_l^1(x) \right) + \sum_{k \epsilon K2} N_k \left(\sum_{l=1}^{4} c_k^{l2} F_l^2(x) \right) \quad (3)$$

where:

$K1$ = set of nodes whose shape function support contains one crack front

$K2$ = set of nodes whose shape function support contains the other crack front

N_k = shape function for node k

c_k^l = additional degrees of freedom associated with crack-tip enrichment functions

F_l = crack tip enrichment functions

Any number of crack tip enrichment functions may be used to refine the approximation at the crack tip. However, Abaqus v.6.10 only uses four enrichment functions, and these functions are given in polar coordinates as presented in Equation 4:

$$F_l(r,\theta) = \left\{\sqrt{r}cos\left(\frac{\theta}{2}\right), \sqrt{r}sin\left(\frac{\theta}{2}\right), \sqrt{r}sin\left(\frac{\theta}{2}\right)sin\theta, \sqrt{r}cos\left(\frac{\theta}{2}\right)sin\theta\right\} \quad (4)$$

Crack lengths and locations were chosen based on observed cracks in the experimental specimen. As shown in Figure 2, cracks were observed to occur in two locations: around the connection plate-to-web weld and along the flange-to-web weld. These will be referred to as Type 1 crack and Type 2 crack respectively. In Abaqus v.6.10, the cracks were modeled using XFEM as through-thickness cracks.

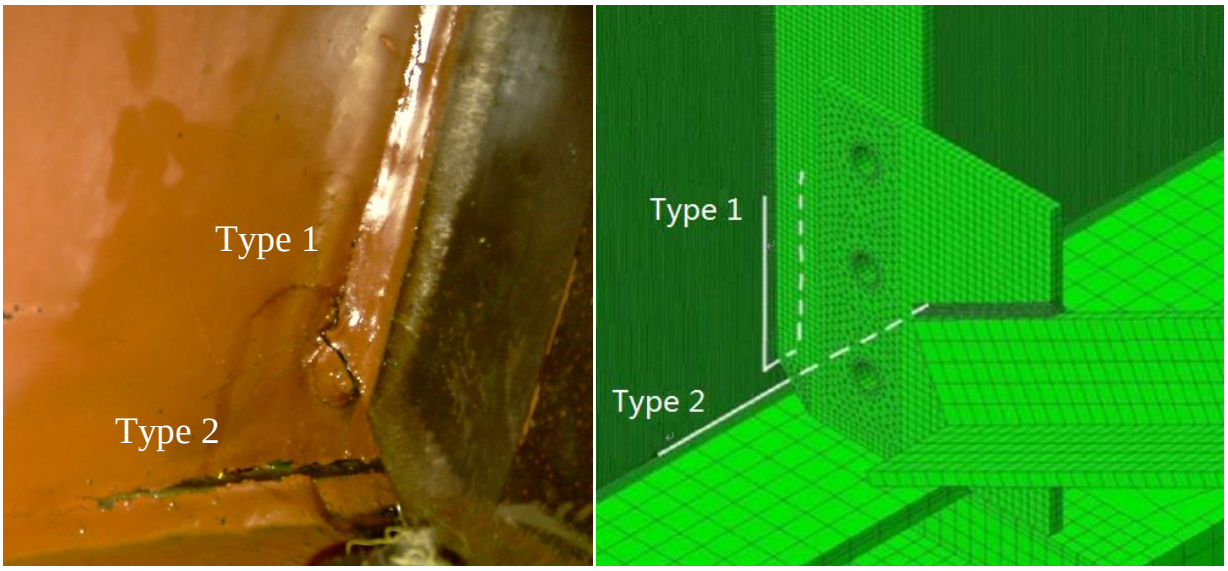

(a) **(b)**

Figure 2: (a) Cracks on the experimental girder subassembly and (b) cracks modeled in the finite element model of the subassembly

FINITE ELEMENT ANALYSIS TECHNIQUES

Three analysis techniques were employed in this study to quantify results of the completed finite element analyses and to evaluate the web-gap regions for fatigue damage potential. The first technique, called the Hot Spot Stress (HSS) technique, involved the extrapolation of stresses to approximate the complex stress state along weld toes in the web-gap region. The second technique, the determination of J-Integrals, involved the interpolation of stress field information from elastic regions to the plastic zones around crack tips to quantify the likelihood of crack growth. The third technique, the determination of Modes I, II, and III Stress Intensity Factors (SIFs), involved the application of an interaction integral to provide more descriptive information about the likelihood of crack growth.

HOT SPOT STRESSES

The first analysis technique utilized was the Hot Spot Stress technique. A hot spot refers to a point, such as would occur at a weld toe, where fatigue cracking is most likely to initiate, and the Hot Spot Stress refers to the combined multi-directional stress at that point [13]. Since direct stress computations are mesh-sensitive, and often the desired stresses occur within regions of very significant stress gradients, Hot Spot Stresses are determined by extrapolating stresses at adjacent elements sufficiently removed from the discontinuity, to reduce mesh sensitivity error. A variety of methods exist to evaluate Hot Spot Stresses in finite element analyses [14], and these methods have all proven to be somewhat sensitive to mesh geometry [15]. In this study, the technique used was based on a one-point analysis procedure that extracts stress values at a distance equal to half the web thickness away from the weld toe [16].

As mentioned previously, observation of the experimental test girders showed that distortion-induced fatigue resulted in two primary cracking patterns along welds in the bottom web gap of the specimens. The first main crack formed a U-shape around the connection plate-to-web weld (Type 1), while the second main crack ran horizontally along the flange-to-web weld (Type 2). These cracks are shown in Figure 2. To apply the HSS technique along these cracks in finite element models, peak stresses were extracted from paths offset 5-mm (0.2-in.) from the weld toes. The path that was used to determine the first peak stress, at the Type 1 crack, followed the same U-shaped path around the connection plate-to-web weld a distance of 102-mm (4-in.) down both sides of the connection plate. The path to determine the second peak stress, at the Type 2 crack, followed the same horizontal path along the flange-to-web weld for a length of 203-mm (8-in.). Since the maximum principal stress distribution was found to have the best correlation with the cracks observed from the experimental test girders (Figure 3), peak maximum principal stress was taken along each of these paths to determine the two Hot Spot Stresses.

It is important to note that the HSS technique described can be applied to cracks modeled explicitly and to cracks modeled using XFEM, which is an advantage of this technique. When the HSS data from the simulations was analyzed, as shown in Figure 4 (results for the 51-mm (2-in.) horseshoe-shaped crack and 51-mm (2-in.) web-to-flange crack unretrofitted model), it was found that the HSS "spiked" around the area of the crack tips, which has the potential to affect the precision of the data comparison between each retrofit combination model. Therefore, peak values were extracted a distance 3.8-mm (0.15-in.) away from the tips of crack to avoid extreme stress gradient in those regions, as shown by the black boundary lines included in Figure 4.

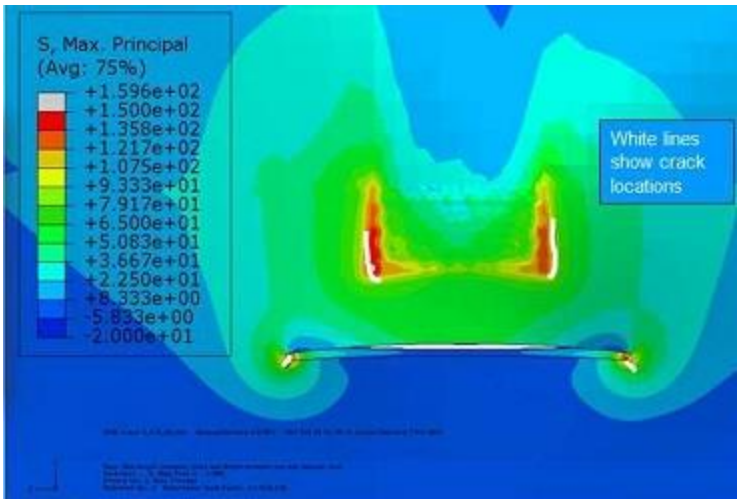

Figure 3: Agreement between observed experimental crack locations and peak maximum principal stress

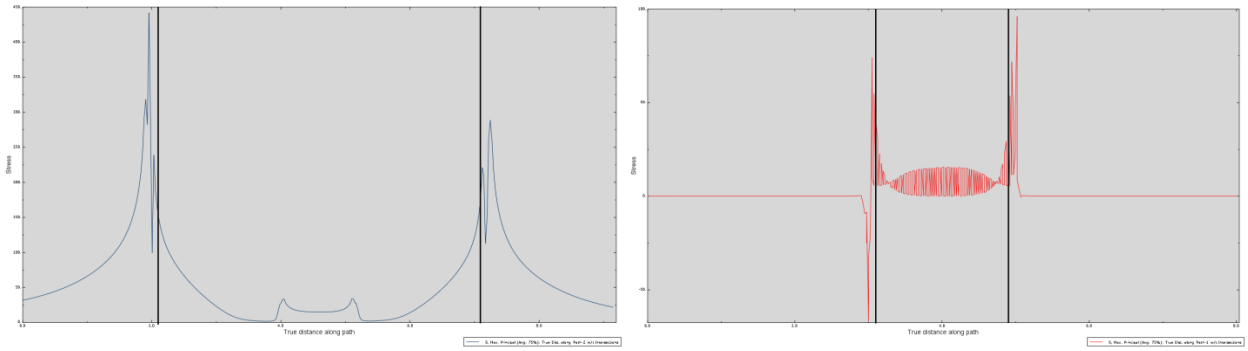

(a) **(b)**

Figure 4: (a) Hot spot stresses for Type 1 crack along the path for 51-mm (2-in.) horseshoe crack and 51-mm (2-in.) horizontal crack unretrofitted model with black boundary lines; (b) Hot spot stresses for Type 2 crack along the path for 51-mm (2-in.) horseshoe crack and 51-mm (2-in.) horizontal crack unretrofitted model with black boundary lines

J-INTEGRALS

The second analysis technique utilized was the computation of J-Integrals. Since significant yielding may occur directly surrounding a crack tip, also known as a plastic zone, it is difficult to quantify the fracture characteristics of the crack directly. A linear-elastic model does a poor job of computing the actual stress-strain behavior at the crack tip because of this plastic zone. A J-Integral is intended as a method to infer the stress-strain behavior at the crack tip by finding the

stress-strain behavior in an elastic region sufficiently removed from the plastic zone around the crack tip [17]. An advantage of this technique is that the computations are performed automatically by Abaqus v.6.10 when XFEM is utilized. Abaqus v.6.10 performs this calculation by taking a surface integral that encloses the crack front from one crack surface to the other and is represented by the following mathematical expression:

$$J(s) = \lim_{\Gamma \to 0} c_l(s) \int_{\Gamma(s)} \left(W \delta_{lj} - \sigma_{ij} u_{i,l} \right) n_j d\Gamma \tag{5}$$

Wheres is some point along the crack front, Γ is any contour surrounding the crack, W is the loading work per unit volume, and σ_{ij} is the stress field [18]. The loading work per unit volume, W, is represented by the following expression:

$$W = \int_0^{\varepsilon} \sigma d\varepsilon \tag{6}$$

Since linear-elastic behavior was assumed for steel in this study, the J-Integral computed is the same as the strain energy release rate per unit crack extension, G. Therefore, a J-Integral parameter, J_I, can be defined as the energy required togrow a crack and can be related to the Mode I stress intensity factor, ΔK_I, by the following expression:

$$J_I = G_I = \frac{(1-\nu^2)\Delta K_I^2}{E} \tag{7}$$

Where$E$ and ν are the elastic modulus and Poisson's ratio, respectively, and were taken as 200,000 MPa (29,000 ksi) and 0.3. Rearranging Equation 7 enables the computed J-Integrals to be converted into Mode I stress intensity factors, which can subsequently be compared with the threshold stress intensity factor ΔK_{TH} and the critical stress intensity factorΔK_{IC}.

STRESS INTENSITY FACTORS

The final analysis technique used in this study was the evaluation of Mode I, II, and III stress intensity factors: ΔK_I, ΔK_{II}, and ΔK_{III}. Specifically, a stress intensity factor is the susceptibility of a material to failure ahead of a sharp crack, with a higher stress intensity factor indicating that material failure ahead of the crack tip is more likely. Modes I, II, and III indicate the local deformation behavior ahead of the crack tip. Mode I indicates tensile opening of the crack surfaces, Mode II indicates in-plane shear or sliding of the crack surfaces, and Mode III indicates out-of-plane shear or tearing of the crack surfaces. These modes of fatigue loading are illustrated in Figure 5.

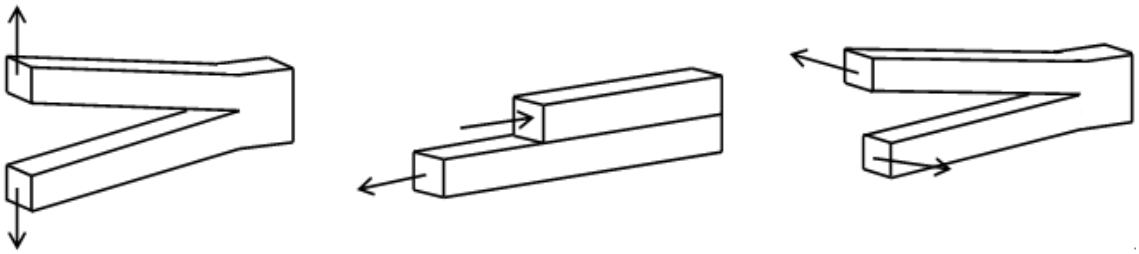

(a) **(b)** **(c)**

Figure 5: Crack opening (a) Mode I, (b) Mode II, and (c) Mode III

The computations of the stress intensity factors can also be performed automatically in Abaqus v.6.10. Abaqus uses an interaction integral method to extract the Mode I, II, and III stress intensity factors by relating the real and auxiliary stress fields [19]. The interaction integral is given by the following expression:

$$I(s) = \lim_{\Gamma \to 0} c_l(s) \int_{\Gamma(s)} \left(\sigma_{ik} \varepsilon_{ik}^{aux} \delta_{lj} - \sigma_{ij} u_{i,l}^{aux} - u_{i,l} \sigma_{ij}^{aux} \right) n_j d\Gamma \qquad (8)$$

Where σ_{ij}^{aux} is the auxiliary stress field, ε_{ij}^{aux} is the auxiliary strain field, and u_i^{aux} is the auxiliary displacement field. Abaqus computes the interaction integral and then substitutes the definitions of the actual and auxiliary fields into Equation 9 to yield an expression for the interaction integral in terms of the actual and auxiliary Mode I, II, and III stress intensity factors:

$$I(s) = \frac{2(1-\nu^2)}{E}(\Delta K_I \Delta K_I^{aux} + \Delta K_{II} \Delta K_{II}^{aux}) + \frac{1}{G}\Delta K_{III} \Delta K_{III}^{aux} \quad (9)$$

To determine ΔK_I, ΔK_I^{aux} was set to 1 while ΔK_{II}^{aux} and ΔK_{III}^{aux} were set to 0 [20]. ΔK_{II} and ΔK_{III} were determined in the same manner.

Computing the Mode I, II, and III stress intensity factors for the material around a crack can provide descriptive information about the contribution of different modes of loading. However, when stress intensity factors are recorded to describe the properties of a material, they are usually provided for ΔK_I, assuming that loading is only contributed by Mode I. Therefore, certain relationships must be applied to quantify the additional contribution of ΔK_{II} and ΔK_{III}. Since the steel in this study was assumed to be a homogeneous isotropic material, the expression shown in Equation 10 [21, 22] can be used to compute the J-Integral in terms of ΔK_I, ΔK_{II}, and ΔK_{III}:

$$J = \frac{(1-\nu^2)}{E}(\Delta K_I^2 + \Delta K_{II}^2) + \frac{1}{2G}\Delta K_{III}^2 \quad (10)$$

Where E is the elastic modulus, ν is Poisson's ratio, and G is the shear modulus [20, 21]. The shear modulus was taken equal to 79,300 MPa (11,200 ksi) for this study. Applying Equation 7, the J-Integral computed with Equation 10 can be converted into a Mode I stress intensity factor, ΔK_I, which subsequently can be compared against ΔK_{TH} and ΔK_{IC}. Thus, this

allows the Mode I, II, and III stress intensity factors at a crack to be analyzed as single stress intensity factor.

It is important to ensure that the contour integral taken for the determination of the J-Integral and K factors does not include the plastic zone around the crack tip. Integrals were automatically computed as output parameters by Abaqus v.6.10 for the contours surrounding each crack tip in the model. The first contour taken was the shortest path around the crack tip to conform to the mesh and each subsequent contour was the next shortest path around the crack tip that conformed to the mesh. Figure 6 shows an example of contours around a crack tip in two-dimensions. A convergence study for J-Integral and K factors for the unretrofitted models with 102-mm (4-in.) Type 1 and 203-mm (8-in.) Type 2 cracks was performed in the elastic zone. Figure 7 shows an example of the results for the convergence study which is the J-Integral value for 203-mm (8-in.) long crack. The mesh size around the crack tip was 0.64-mm (0.03-in). The data started to converge from contour 5. At the fifth contour, sixteen J-Integral values and K factors were produced since the modeled webs were fifteen elements (sixteen nodes) thick. Data for the first, second, fifteenth and sixteenth contour were not considered because those data were impacted by the contact constraint between the web and the angles & back plate. Finally, these twelve through-thickness values at the fifth contour were averaged for the final result.

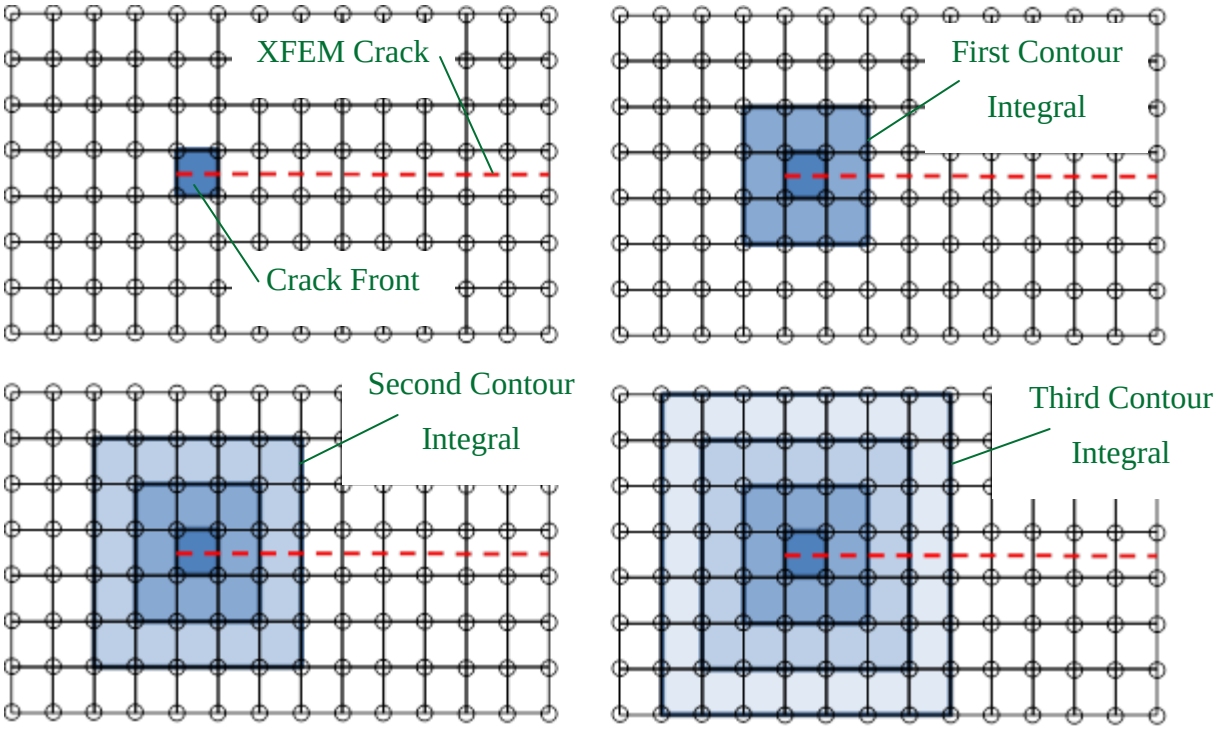

Figure 6: Example of how contour integrals are taken in a finite element mesh

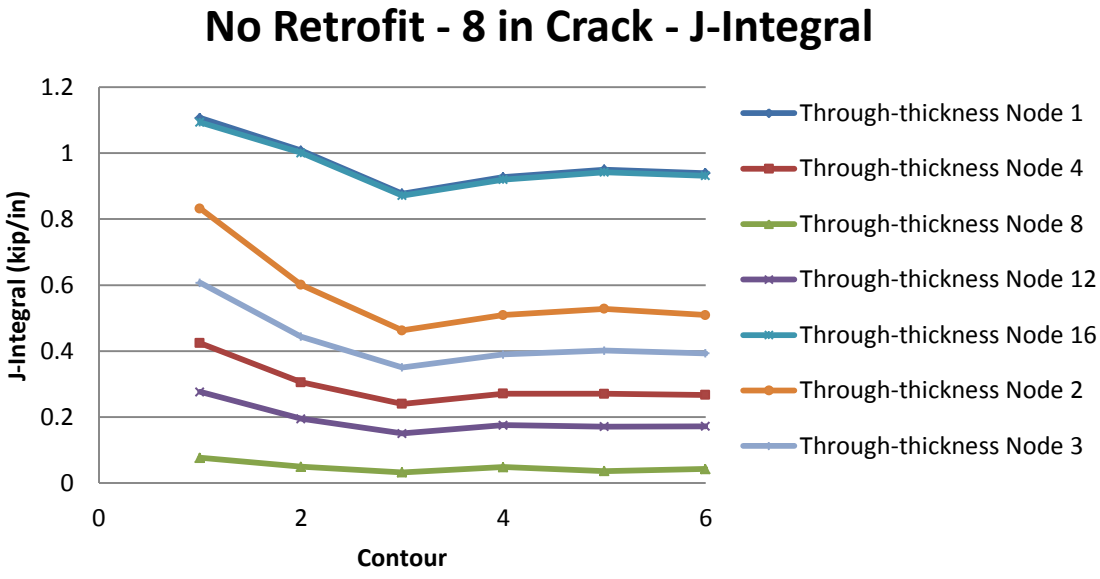

Figure 7: Example of Convergence study for J-Integral and K factors for the unretrofitted models with 102-mm (4-in.)Type 1 and 203-mm (8-in.) Type 2 cracks

FATIGUE CRACK PROPAGATION THEORY

Understanding the theory of fatigue crack propagation is important when conducting a finite element analysis to determine fatigue susceptibility. Fatigue crack propagation occurs in three stages, generalized in Figure 8.

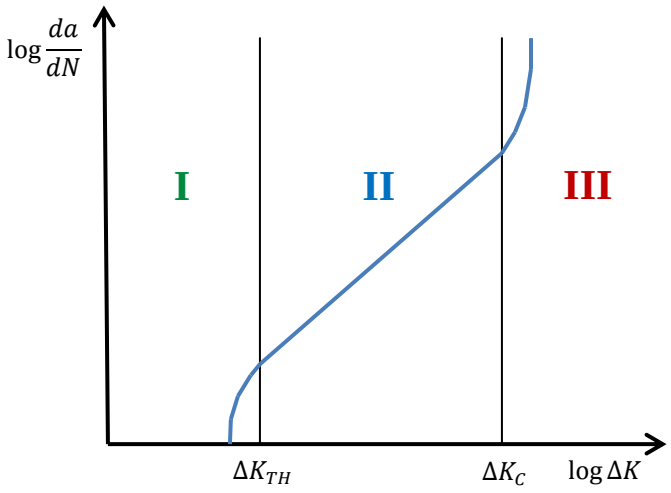

Figure 8: Logarithmic plot of typical fatigue crack growth rate vs. stress intensity factor range

Figure 8 is a logarithmic plot of the crack growth rate, *da*/*dN*, versus stress intensity factor range, *ΔK*. In Stage I, cracks propagate on the microscopic level. Crack growth in this stage is difficult to predict since it is driven by shear and interacts with the microstructure of the material. In fact, it is possible that cracks do not grow at all in fatigue during this stage [17]. Stage II crack growth is marked by a change to macroscopic, tension-driven crack growth, which is insensitive to microstructure effects. This stage of fatigue crack growth is very well known and is commonly modeled by Paris' law [23]. This law relates crack growth rate with the stress intensity factor range and is given by the following expression:

$$da/dN = A(\Delta K)^m \tag{11}$$

Where A and m are material's constants. When plotted logarithmically as in Figure 8, this appears linearly. In the final stage of crack growth, Stage III, crack growth rates accelerate and eventually lead to unstable fracture. Behavior of cracks characterized by this stage of growth is difficult to predict, since crack growth rates are accelerating exponentially.

The important material parameters in regards to fatigue crack growth are the threshold stress intensity factor, ΔK_{TH}, and the critical stress intensity factor, ΔK_{IC}. The threshold stress intensity factor, ΔK_{TH}, represents the boundary between Stage I and Stage II crack growth. Below ΔK_{TH}, macroscopic fatigue crack growth will not occur. This value is dependent on the load ratio, R, where the relationship between ΔK_{TH} and R is given by Barsom and Rolfe [16]. In this study, the specimen is loaded from 0 to 22.2-kN (5-kip), therefore the load ratio is 0 and, subsequently, the threshold stress intensity factor for this study is 6.0 MPa-m$^{1/2}$ (5.5 ksi-in$^{1/2}$). The critical stress intensity factor represents the boundary between Stage II and Stage III crack growth and is the maximum value for which Paris' law for crack growth is applicable. As a material parameter, the critical stress intensity factor is also known as the fracture toughness [17]. For steel, the fracture toughness can vary even between steels of the same grade. AASHTO requires a minimum ΔK_{IC} for fracture critical members of 82 MPa-m$^{1/2}$(75 ksi-in$^{1/2}$) [24]. Stress intensity factors above this value indicate unstable crack growth and the potential for fracture.

RESULTS AND DISCUSSION

Finite element analyses performed using Abaqus v.6.10 of 2.7-m girder (9-ft) subassemblies utilized several different types of crack combinations to evaluate the performance of the angles-with-plate retrofit previously evaluated through experimental study. As discussed, these cracks were simulated using XFEM capabilities embedded within Abaqus and were modeled as

through-thickness. As shown in Figure 2, U-shaped cracks were modeled along the connection plate-to-web weld and are referred to as Type 1 cracks, while horizontal cracks were modeled along the flange-to-web weld and are referred to as Type 2 cracks. Four different combinations of Type 1 and Type 2 cracks were employed in this study: 13-mm (1/2-in.) Type 1 and 13-mm (1/2-in.) Type 2 cracks, 25-mm (1.0-in.) Type 1 and 25-mm (1.0-in.) Type 2 cracks, 51-mm (2.0-in.) Type 1 and 51-mm (2.0-in.) Type 2 cracks, and 102-mm (4.0-in.) Type 1 and 203-mm (8.0-in.) Type 2 cracks. It should be noted that the length of the horseshoe-shaped, Type 1 crack refers to the length of one leg of the "U" shape.

Table 1: Naming convention for retrofit combinations used in this study

		Angle Thickness			
	Dimension	0	6-mm (1/4-in)	13-mm (1/2-in)	25-mm (1.0-in)
Back Plate Thickness	0	NR	---	---	---
	6-mm (1/4-in)	---	F-F	M-F	S-F
	13-mm (1/2-in)	---	F-M	M-M	S-M
	25-mm (1.0-in)	---	F-S	M-S	S-S

Table 2: Summary of crack combinations and retrofits applied

	Combination #1	**Combination #2**	**Combination #3**	**Combination #4**
Type 1 Crack	13-mm (1/2-in.)	25-mm (1-in.)	51-mm (2-in.)	102-mm (4-in.)
Type 2 Crack	13-mm (1/2-in.)	25-mm (1-in.)	51-mm (2-in.)	203-mm (8-in.)
Retrofits	All	All	All	All

For each of these crack combinations, nine variations of the angles-with-plate retrofit were investigated, and one additional simulation was examined with no retrofit to serve as a baseline against which the level of improvement provided by the retrofits could be evaluated. These simulations were compared with the experimental results of angles-with-plate retrofits. Thickness of the angles and backing plate were varied such that the nine variations studied used all combinations of 178-mm (7-in.) long L152x127x6-mm (L6x5x1/4-in.), L152x127x13-mm (L6x5x1/2-in.), and L152x127x25-mm (L6x5x1-in.) angles connecting the web to each side of the connection plate, and 457x203x6-mm (18x8x1/4-in.), 457x203x13-mm (18x8x1/2-in.), and 457x203x25-mm (18x8x1-in.) plate on the other side of the web from the angles. Table 1 summarizes the naming convention used for the retrofit combinations and Table 2 summarizes the crack combinations investigated. The retrofit naming convention can be interpreted as follows: the first letter F, M or S represents the thickness of angels as either6-mm (1/4-in.), 13-mm (1/2-in.)or 25-mm (1.0-in.), respectively. The second letter in the name(F, M or S) represents the thickness of back plate as either6-mm (1/4-in.), 13-mm (1/2-in.)or 25-mm (1.0-in.), respectively. Figure 9 shows the angles & back plate as applied to a test girder as well as a sketch of the retrofits. The findings from these simulations are discussed in the following sections.

(a) **(b)** **(c)**

Figure 9: (a) Angles-with-plate retrofit applied to a test girder (stiffener side), (b) Angles-with-plate retrofit applied to a test girder (fascia side) and (c) Sketch of the angles-with-plate retrofit

EXPERIMENTAL RESULTS

In a previous study, an angles-with-plate retrofit consisting of a 178-mm (7-in.) long L152x127x19-mm (L6x5x3/4-in.) angle and a 457x203x19-mm (18x8x3/4-in.) backing plate was applied to a 2.7-m (9-ft) subassembly with cracks along the stiffener-to-web weld (Type 1 crack) and flange-to-web weld (Type 2 crack) in the bottom web-gap [8]. This retrofit was used for four different trials of 1.2 million fatigue cycles, each of which had different Type 1 and Type 2 crack lengths. The Type 1 crack, however, was much more complex than a simple "U" shape. It did progress along both sides of the stiffener-to-web weld, albeit at different rates, and it also branched horizontally into the web on both sides of the stiffener. The vertical crack branches along the weld will be referred to as "Vertical" and the horizontal branches into the web will be referred to as "Spider." Table 3 shows a summary of the cracks during each trial. As shown in the table, there was no observed crack propagation in the bottom web-gap during each 1.2 million cycle trial with the angles-with-plate retrofit applied. In the trials with no retrofit applied, there was clearly observed crack propagation in a significantly less number of cycles.

Table 3: Bottom web-gap crack growth for angles-with-plate retrofit applied to 2.7-m (9-ft) subassembly

Retrofit Applied	Number of Cycles	Type 1 Crack, mm (in.)				Type 2 Crack, mm (in.)
		Vertical-R	Spider-R	Vertical-L	Spider-L	
No	349,000	51 (2)	13 (0.5)	44 (1.75)	13 (0.5)	51 (2)
Yes	1,549,000	51 (2)	13 (0.5)	44 (1.75)	13 (0.5)	51 (2)
No	1,620,700	51 (2)	19 (0.75)	51 (2)	19 (0.75)	102 (4)
Yes	2,820,700	51 (2)	19 (0.75)	51 (2)	19 (0.75)	102 (4)
No	3,142,700	70 (2.75)	30 (1.19)	52 (2.06)	22 (0.88)	152 (6)
Yes	4,342,700	70 (2.75)	30 (1.19)	52 (2.06)	22 (0.88)	152 (6)
No	4,617,700	83 (3.25)	37 (1.44)	64 (2.5)	22 (0.88)	206 (8.1)
Yes	5,817,700	83 (3.25)	37 (1.44)	64 (2.5)	22 (0.88)	206 (8.1)

HOT SPOT STRESSES

The first analysis technique utilized in each of the simulations was the Hot Spot Stress technique. Figure 10 shows the computed Hot Spot Stresses as compared to the Type 1 crack lengths and the Type 2 crack lengths respectively (it is important to remember that Type 1 and Type 2 cracks were modeled as occurring together, as described previously). The hot spot stresses taken at the most flexible retrofit, the F-F retrofit (6-mm (1/4-in.) thick angle, 6-mm(1/4-in.) thick back plate), and at the stiffest retrofit, the S-S retrofit (25-mm (1-in.), 25-mm (1-in.)), are shown on these plots compared against the hot spot stresses extracted from the model with no retrofit. For the scenario in which there was no retrofit, Figure 10 shows that the hot spot stresses increased significantly for longer crack combinations.

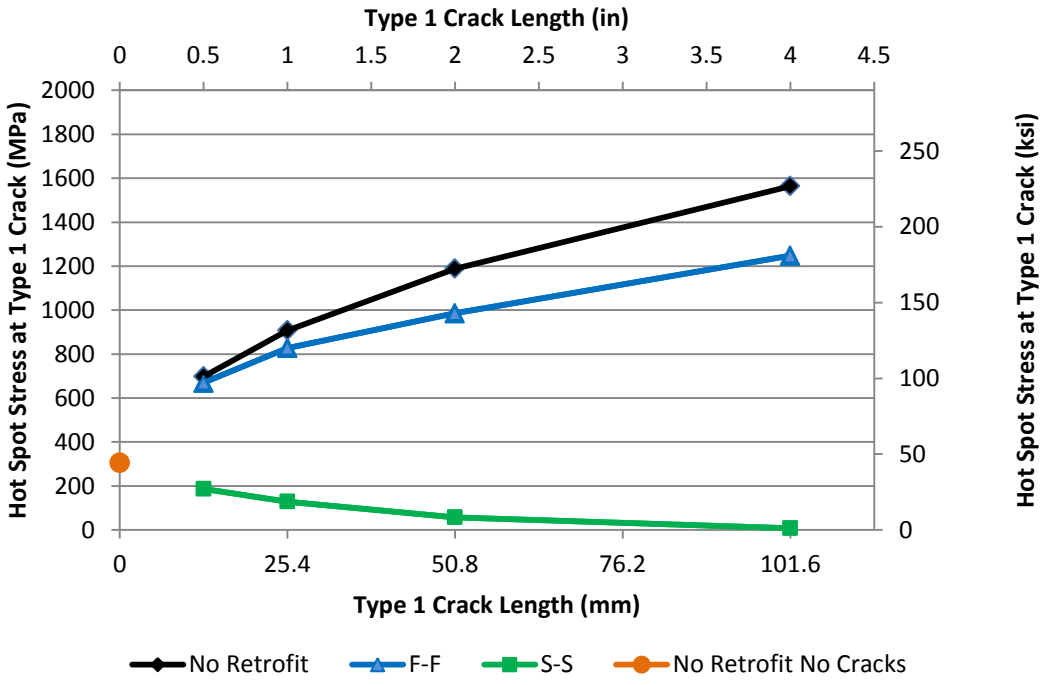

(a)

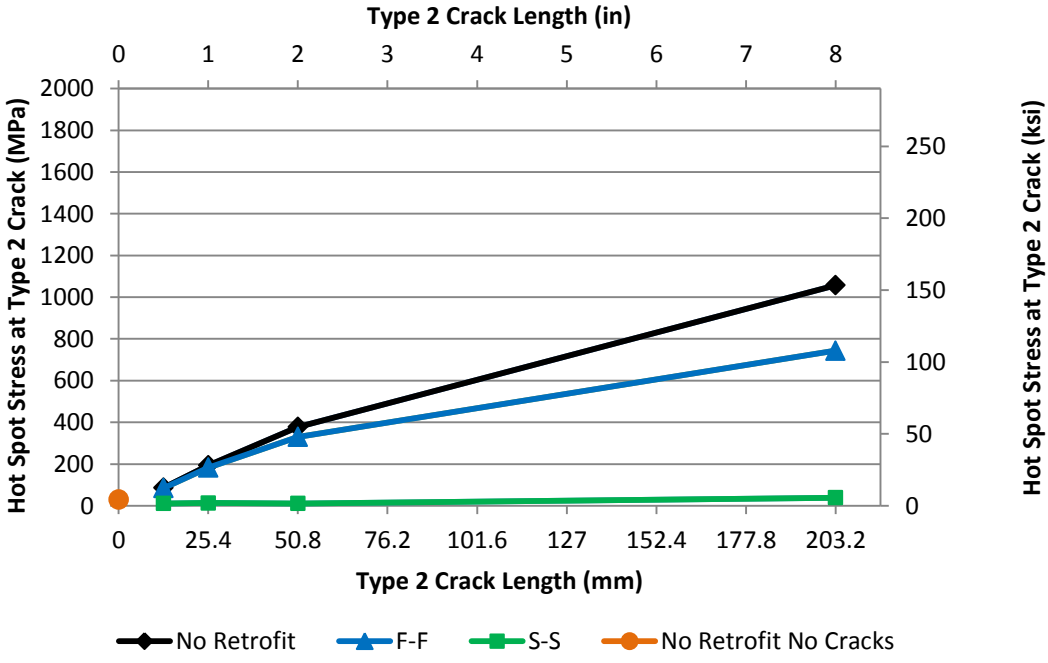

(b)

Figure 10: (a) Hot Spot Stress at Type 1 crack with no retrofit, F-F retrofit, and S-S retrofit; (b) Hot Spot Stress at Type 2 crack with no retrofit, F-F retrofit, and S-S retrofit

The hot spot stresses computed in simulations that were representative of girders retrofitted with the angles-with-plate technique (including the entire range of retrofit stiffness studied) indicated an improvement over those simulations of a girder with no retrofit. For the stiffest retrofit, the computed hot spot stresses at each crack were approximately constant regardless of the crack combination. The difference between the hot spot stresses for the most flexible retrofit and the hot spot stresses for the models with no retrofit increased with increasing crack length. Thus, the level of improvement imparted by the retrofit tended to increase with increasing crack length. The stiffest retrofit (stiff angles used in combination with a stiff back plate) was significantly more effective in reducing hot spot stresses than the most flexible retrofit. Comparing the hot spot stresses for the simulations of a girder without cracks and without retrofits with the hot spot stresses for each retrofit variation and each crack combination, the hot spot stresses for the stiffest retrofit were even smaller than the hot spot stress for the models with no cracks and with no retrofit. This finding indicated that the stiffest retrofit was significantly effective.

Some of the retrofits were more effective in reducing hot spot stresses than others. Figure 11 shows the improvement in hot spot stresses in all retrofit simulations at the Type 1 and Type 2 cracks, respectively. As noted previously, the level of improvement was more significant for larger crack combinations. Additionally, it can be observed that the stiffer retrofits had the tendency to provide a much greater reduction in hot spot stresses than the more flexible ones. The best performing retrofit at each crack was the S-S retrofit (25-mm (1-in.) angles, 25-mm (1-in.) plate), while the worst performing retrofit was the F-F retrofit (6-mm (1/4-in.), 6-mm (1/4-in.)). It can also be seen that the hot spot stresses at the web-to-flange weld (hot spot stresses for Type 2 crack) exhibited greater sensitivity to the level of retrofit stiffness than the Type 1 crack.

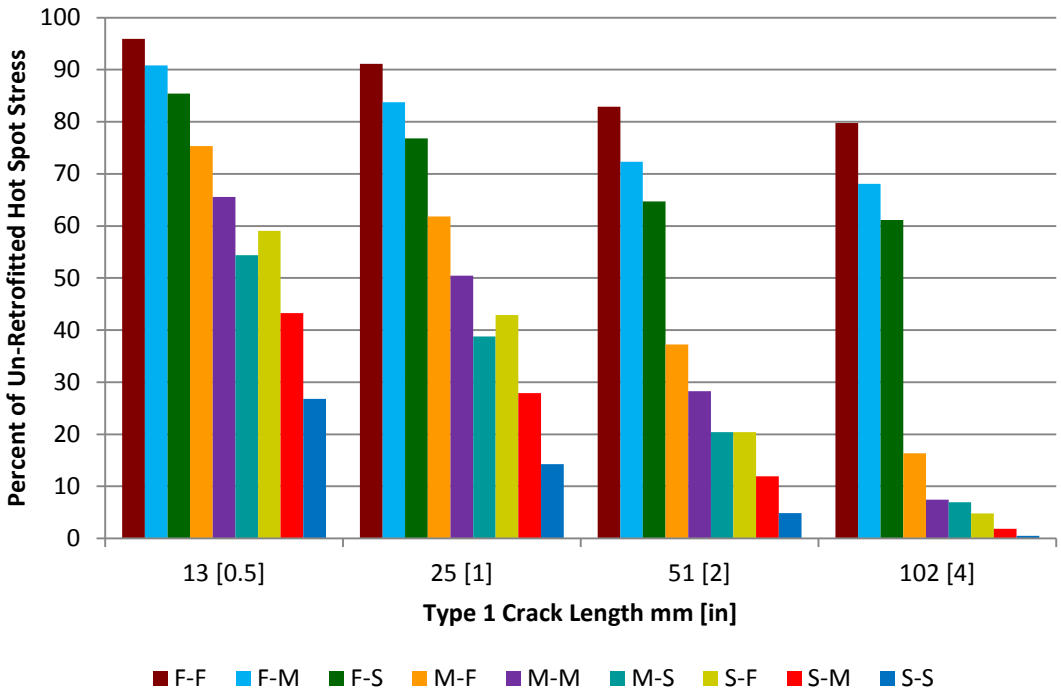

(a)

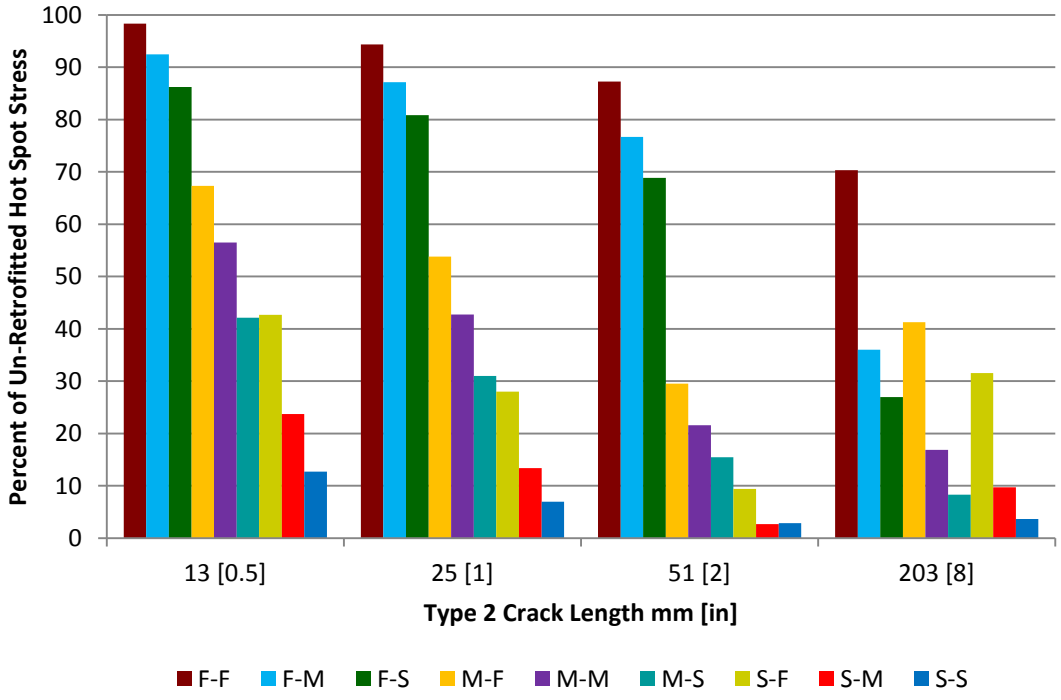

(b)

Figure 11: (a) Hot Spot Stress performance of each retrofit combination at Type 1 crack; (b) Hot Spot Stress performance of each retrofit combination at Type 2 crack

J-INTEGRALS

While higher values for maximum principal stress usually indicate a higher propensity for crack growth, higher values for J-Integrals do so by definition. Thus, the second analysis technique used in each of the simulations was the computation of J-Integrals. As mentioned previously, this was accomplished by the automatic calculation of contour integrals around each crack-tip in a particular simulation. Figure 12 shows the computed J-Integrals compared against Type 1 and Type 2 cracks, respectively. The J-Integrals taken at the most flexible retrofit and at the stiffest retrofit are shown on these plots compared against the J-Integrals taken with no retrofit. The difference of J-Integrals for the unretrofitted models and retrofitted models decreased as crack lengths decreased. This finding indicated that the level of improvement experienced due to the retrofits decreased as crack lengths decreased.It also can be seen that the J-Integral magnitudes increased when the crack lengths increased. With no retrofit, the largest crack combination clearly produced the greatest J-Integrals. The J-Integrals computed for both the stiffest and most flexible retrofits indicated an improvement for the largest crack combination, thus predicting that little or no crack propagation would occur. This confirmed the experimental results from [8] at the largest crack combination.

However, at the other three crack combinations, the improvements in the J-Integrals were significantly less, and in some cases minimal, with the addition of the retrofits. In fact, the J-Integrals computed at 13-mm (1/2-in.), 25-mm (1-in.),and 51-mm (2-in.) Type 1 cracks indicated a greater propensity for cracking after the application of the F-F retrofit (6-mm (1/4-in.), 6-mm (1/4-in.)). This was not supported by the experimental results in [8], where no crack propagation occurred with the addition of the retrofit under any crack combination. However, a possible explanation for this discrepancy is that the 13-mm (1/2-in.) Type 1 and 13-mm (1/2-in.) Type 2

crack combination as well as the 25-mm (1-in.) Type 1 and 25-mm (1-in.) Type 2 crack combination were significantly smaller than the cracks in any of the experimental trials. In fact, even the 51-mm (2-in.) Type 1 and 51-mm (2-in.) Type 2 crack combination was smaller than any of the experimental trials when the spider cracks as part of the Type 1 crack were factored in.

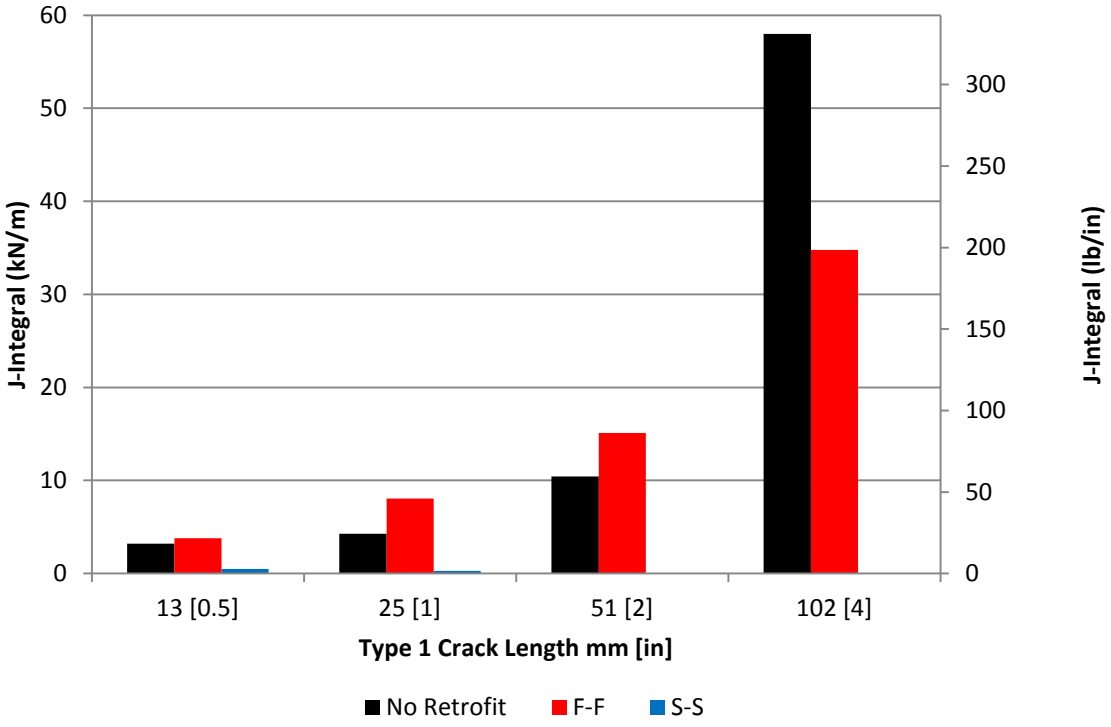

(a)

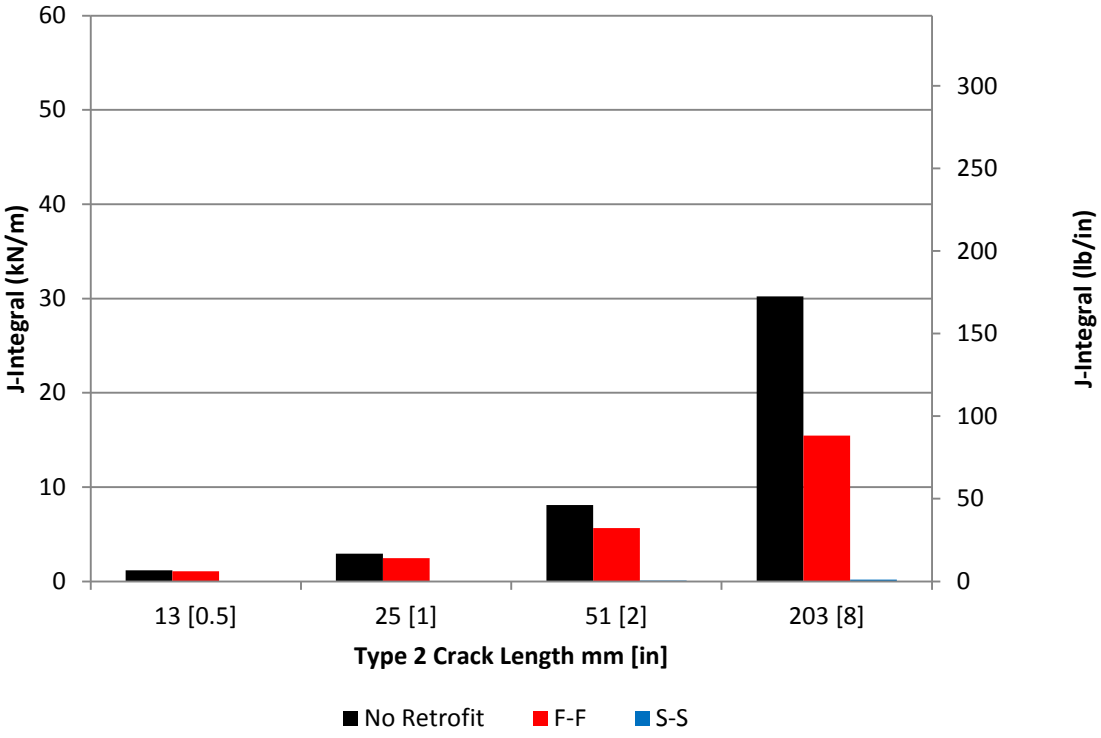

(b)

Figure 12: (a) J-Integrals at Type1 crack with no retrofit, F-F retrofit, and S-S retrofit; (b) J-Integrals at Type 2 crack with no retrofit, F-Fretrofit, and S-S retrofit

As discussed previously, fatigue and fracture concepts and laws can be applied to the computed J-Integral values. Thus, instead of just tracking the improvement in J-Integral values with the addition of various retrofits, more qualitative information can be obtained. Figure 13 shows the computed J-Integral values at the Type 1 and Type 2 cracks, respectively, converted into equivalent Mode I stress intensity factors. In both of these plots, the equivalent Mode I stress intensity factors, $\Delta K_{I,eq}$, can be compared with the threshold stress intensity factor, 6.0 MPa-m$^{1/2}$ (5.5 ksi-in$^{1/2}$), and the critical stress intensity factor, at least 82 MPa-m$^{1/2}$ (75 ksi-in$^{1/2}$) [17].

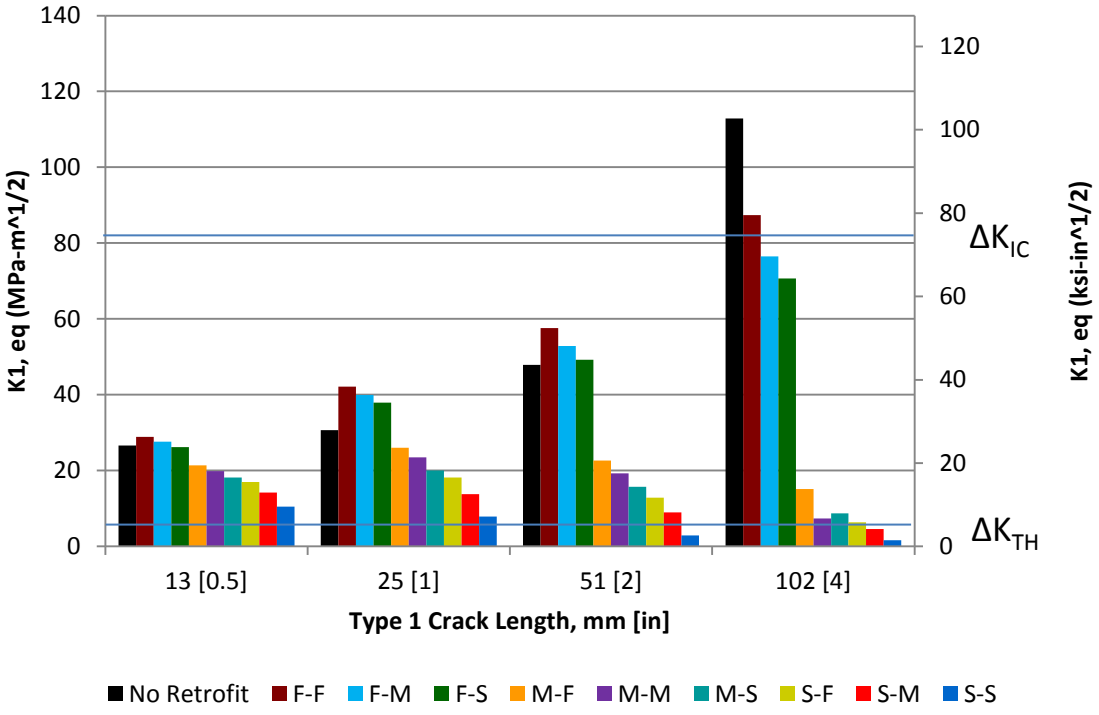

(a)

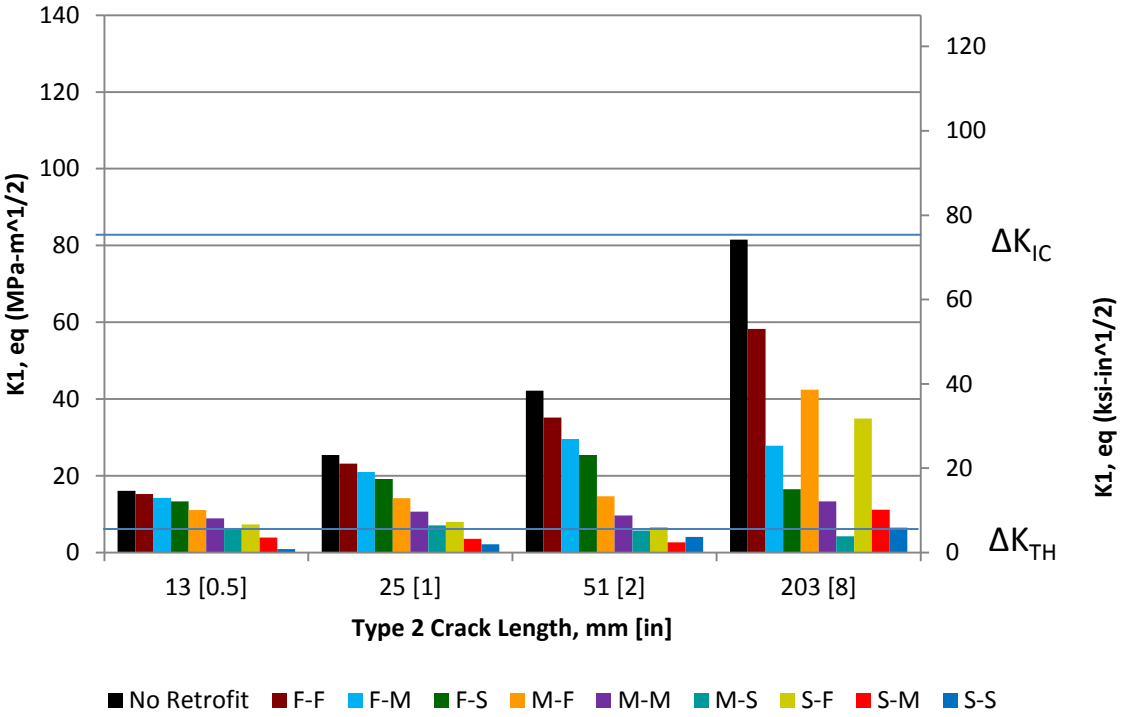

(b)

Figure 13: (a) Equivalent Mode I Stress Intensity Factors at Type 1 crack based on J-Integral computation; (b) Equivalent Mode I Stress Intensity Factors at Type 2 crack based on J-Integral computation

From Figure 13, the level of improvement experienced due to the retrofits increased as crack lengths increased and the stiffer retrofits had the tendency to provide a greater reduction in Mode I stress intensity factors $\Delta K_{I,eq}$than the more flexible ones.Except for the of S-S retrofit (25-mm (1-in.), 25-mm (1-in.)), S-M retrofit (25-mm (1-in.), 12-mm (0.5-in.)) and M-S retrofit (12-mm (0.5-in.), 25-mm (1-in.)), the values for $\Delta K_{I,eq}$were all significantly larger than ΔK_{TH}, which would indicate that crack growth should continue even with the angles-with-plate retrofits applied. Once again, these results were not supported by the experimental results from [8]. For the S-S retrofit (25-mm (1-in.), 25-mm (1-in.)), S-M retrofit (25-mm (1-in.), 12-mm (0.5-in.)) and M-S retrofit (12-mm (0.5-in.), 25-mm (1-in.)), the values for $\Delta K_{I,eq}$weresmaller than ΔK_{TH}, which would indicate that little or no crack propagation would occur. This confirmed the experimental results from [8] with the angles-with-plate retrofits applied.

STRESS INTENSITY FACTORS

The automatic calculation of contour integrals around XFEM crack-tips in Abaqus allowed for the computation of J-Integrals as discussed in the previous section. This capability also allowed for the computation of Mode I, Mode II, and Mode III stress intensity factors via the computation of an interaction integral. It is important to point out that this is a different computation than the one performed for J-Integrals, and that the Mode I stress intensity factor determined through this method is not the same as the equivalent Mode I stress intensity factor determined using the J-Integrals (also, the equivalent Mode I stress intensity factor based on all three modes is not the same either). The computation of Mode I, Mode II, and Mode III stress intensity factors showed how much of an effect the out-of-plane deformation had on fatigue crack propagation for unretrofitted models as well as how much the retrofits were able to mitigate the three deformation modes. Figure 14 shows the Mode I, Mode II, and Mode III stress intensity factors

compared against the Type 1 and Type 2 cracks, respectively, for the unretrofitted models as well as the most flexible (F-F retrofit) and the stiffest (S-S retrofit) angles-with-plate retrofits.

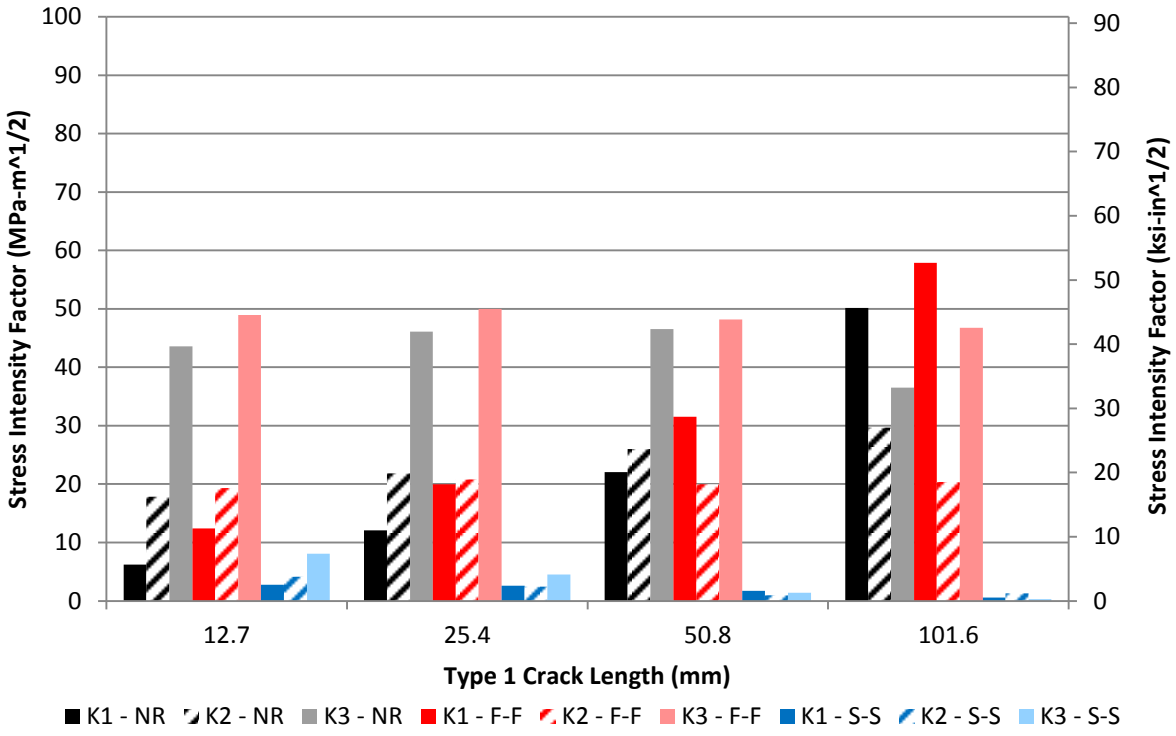

(a)

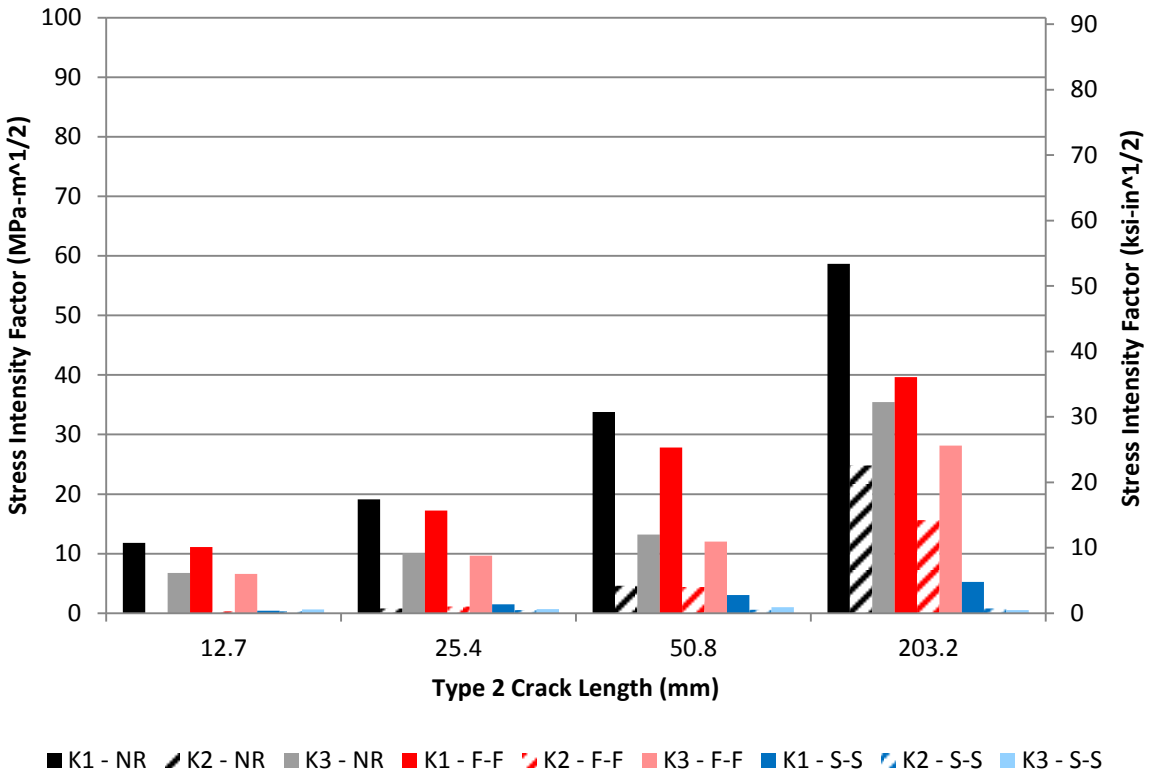

(b)

Figure 14: (a) K1, K2, andK3 at Type 1 crack for no retrofit, F-F retrofit, and S-S retrofit; (b)K1, K2, and K3 at Type 2 crack for no retrofit, F-F retrofit, and S-S retrofit

When analyzing the results for the unretrofitted simulations, it was apparent that Mode I (opening) for the simulations at the Type 2 crack and Mode III (out-of-plane shear) for the simulations at the Type 1crack were dominant modes. Mode II (in-plane shear) appeared to have a more significant impact in the simulations at the Type 1 crack and the Type 2 crack for all crack combinations with increasing the crack lengths. This would make sense based on observed deformation in unretrofitted web-gaps. When analyzing results for the most flexible and stiff retrofits, the retrofits once again seemed to have the largest positive effect for the largest crack combination. These results matched the general trends seen in the J-Integral analysis.

Since the retrofits had the greatest positive impact for the largest crack combination, it is important to note the effect that the retrofits had on each stress intensity factor mode at the largest crack combination. The addition of the most flexible retrofit enabled a reduction in the Mode II stress intensity factors at the Type 1 crack, while having worse impact on the Mode I and Mode III stress intensity factors, which was not supported by the experimental results. The stiffest retrofit reduced each stress intensity factor mode significantly, decreasing it to close to zero. Both the flexible and stiff retrofits had a remarkably positive effect on the Mode I, Mode II and Mode III stress intensity factors at the Type 2 crack.

For all simulations, the computation of the Mode I, Mode II, and Mode III stress intensity factors enabled fatigue and fracture principles to be applied in order to gain more quantitative information about fatigue crack growth under distortion-induced fatigue. Figure 15 shows the computed Mode I, Mode II, and Mode III stress intensity factors at the Type 1 and Type 2 cracks, respectively, converted into equivalent Mode I stress intensity factors, $\Delta K_{I,eq}$.

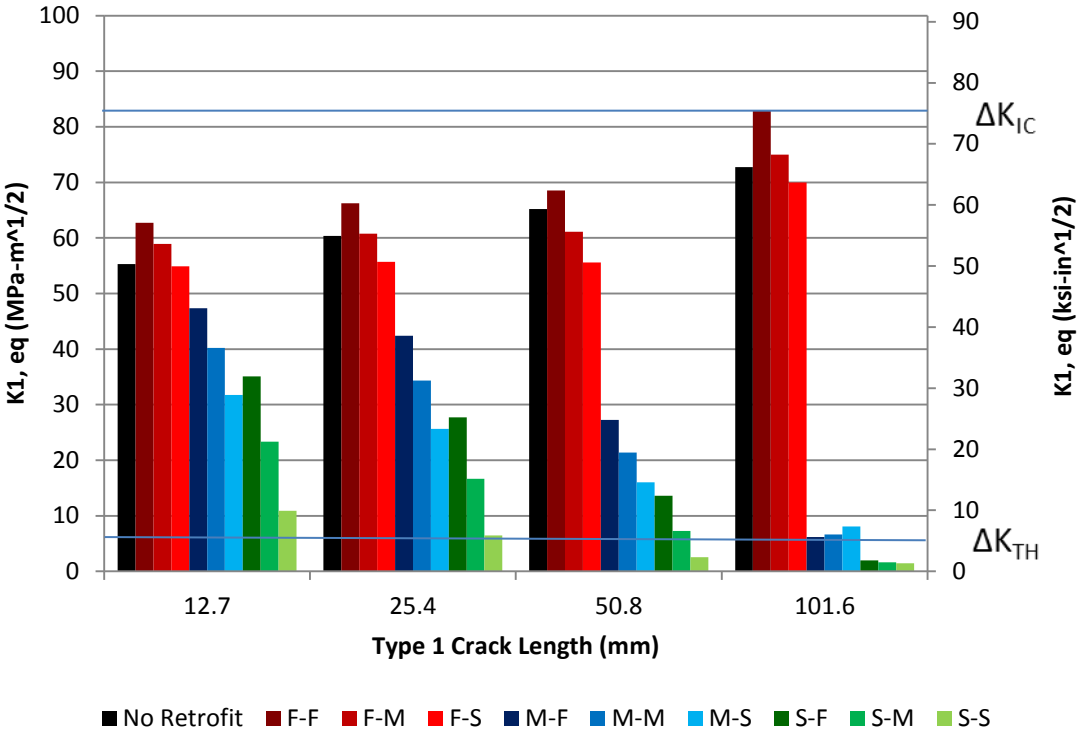

(a)

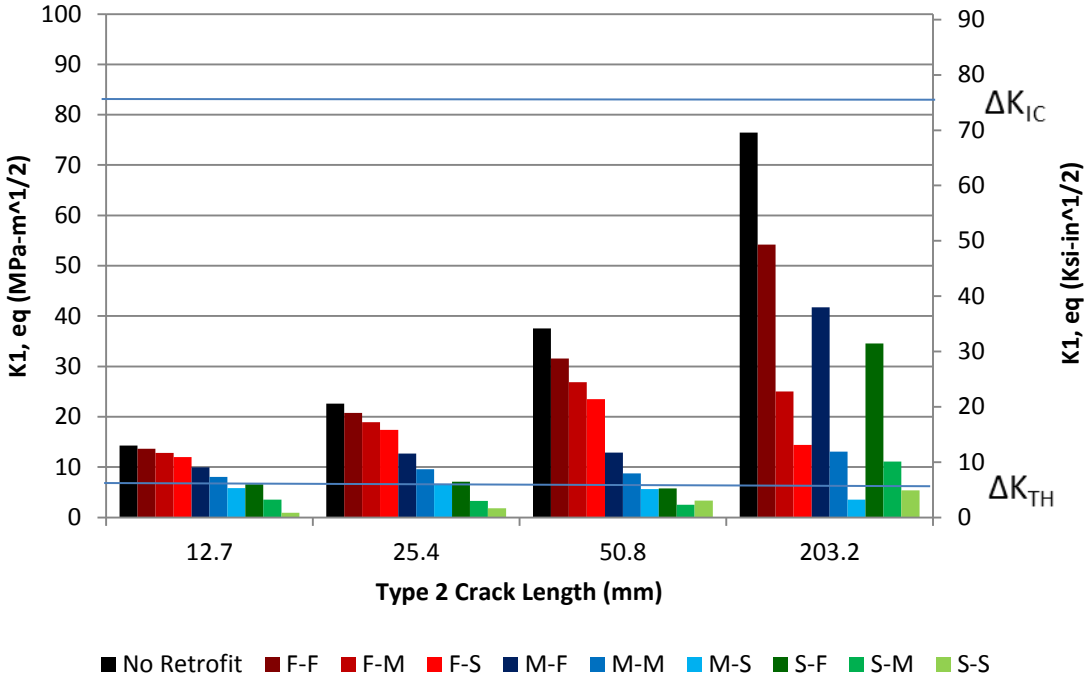

(b)

Figure 15: (a) Equivalent Mode I Stress Intensity Factors at Type 1 crack based on K1, K2, K3 computation; (b) Equivalent Mode I Stress Intensity Factors at Type 2 crack based on K1, K2, K3 computation

For the Type 1 crack, the simulations indicated that the addition of the three retrofits with stiff angles (S-S, S-M, and S-F) for the longest crack combination and the S-S retrofit for the 51-mm (2.0-in) Type 1 crack and 51-mm (2.0-in) Type 2 crack combination produced values for $\Delta K_{I,eq}$ that were less than ΔK_{TH}, indicating retrofit effectiveness. For the Type 2 crack, the addition of the S-S and M-S retrofits for the longest crack combination and the S-S and S-M retrofits for the two smallest crack combinations and the S-S, S-M, S-F, and M-S retrofits for the51-mm (2.0-in) Type 1 crack and 51-mm (2.0-in) Type 2 crack model produced $\Delta K_{I,eq}$ values that were less than ΔK_{TH}. These findings indicate that little or no fatigue crack growth would occur for these combinations, resulting in a favorable comparison with the experimental results. However, other retrofits combinations did not appear to have a positive effect, specifically, the results for some F-F and F-M retrofits cases, predicted that crack propagation would likely occur at a high rate even under the applied retrofits.

As also indicated by the J-Integral analysis, the computation of Mode I, Mode II, and Mode III stress intensity factors indicated that the addition of the angles-with-plate retrofits had the greatest impact for the largest crack combination (102-mm (4.0-in) Type 1 crack, 203-mm (8.0-in) Type 2 crack). The addition of the retrofits with flexible angles (F-F, F-M, and F-S) at the Type 1 crack and the retrofits with flexible back plates (F-F, M-F, and S-F) at the Type 2 crack did not have a significant impact compared with the other retrofits. As also shown through the Hot Spot Stress analysis and the J-Integral analysis, the stiffer retrofits had the tendency to provide a greater reduction in Mode I stress intensity factors $\Delta K_{I,eq}$ than the more flexible ones.

CONCLUSIONS

The implementation of the Extended Finite Element Method (XFEM) for modeling cracks in Abaqus has enabled more detailed analyses to be performed in investigating distortion-induced

fatigue and retrofits aimed at mitigating distortion-induced fatigue. This has made it possible to implement analysis techniques such as the computation of J-Integrals and the computation of Mode I, Mode II, and Mode III stress intensity factors to evaluate performance. Along with the Hot Spot Stress analysis, these techniques were used to computationally analyze a 2.7-m (9-ft) girder subassembly experiencing fatigue cracking due to distortion-induced fatigue. Angles-with-plate retrofits with varying angle thickness and varying back plate thickness were implemented in the finite element models of this subassembly, and their performance was evaluated at several different crack states. The results of these simulations were compared with observations from a previous experimental study. Based on the results of this parametric study, several conclusions have been reached:

- Each of the three analysis techniques showed that the addition of the angles-with-plate retrofits had the greatest positive effect for the largest crack combination analyzed.
- Each of the three analysis techniques showed that increasing retrofit stiffness corresponded with greater effectiveness at reducing hot spot stresses for both Type 1 and Type 2 cracks.
- The Hot Spot Stress analysis found better improvement with the addition of retrofits at the smaller crack combinations than other analysis techniques. Thus, the results from the Hot Spot Stress analysis were most similar to the experimental observations.
- Both the J-Integral analysis and Stress Intensity Factor analysis predicted considerable crack propensity, and in some cases even unstable crack growth, at smaller crack combinations even with the addition of retrofits. These results were significantly different from experimental observations.

- The Stress Intensity Factor analysis was effective at determining the contribution of each of Mode I, II, and III crack growth modes to overall crack growth. Mode I and Mode III both contributed significantly, while Mode II only contributed minutely.

A key advantage of the Hot Spot Stress analysis technique was that the results were very similar to the experimental observations, and the stresses were more independent from the mesh than the J-Integral analysis and Stress Intensity Factor analysis techniques. A disadvantage of the HSS analysis technique was that maximum principal stresses tended to show extremely severe stress gradients around the crack tips which affected the accuracy of the data comparison between different retrofit combinations. To solve this problem, peak maximum principal stresses were extracted a distance 3.8-mm (0.15-in.) away from the tips of the cracks to avoid the data spikes. This method improved the accuracy of data comparison between each retrofit combination model.

The advantage of the J-Integral and Stress Intensity Factor analysis techniques is that the J-Integral values and the Stress Intensity factors can be automatically computed as output parameters by Abaqus v.6.10 for the contours surrounding each crack tip in the model. However, consequent to this, a contour convergence study was necessitated in the elastic zone around the crack tips since the results can be expected to be affected by mesh size.

Based upon the finding of this study, the Hot Spot Stress analysis technique is recommended for the problem of distortion induced fatigue over the other two techniques studied.

REFERENCES

[1] Tedesco, J. W., Stallings, J. M., Tow, D. R. (1995). "Finite Element Method Analysis of Bridge Girder-Diaphragm Interaction."*Computers and Structures*, vol. 56, no. 2-3, pp.

461-473.

[2] Castiglioni, C., Fisher, J. W., Yen, B. T. (1988). “Evaluation of fatigue cracking at cross diaphragms of a multigirder steel bridge.” *Journal of Constructional Steel Research*, vol. 9, no. 2, pp. 95-110.

[3] Roddis, W. M. K., and Zhao, Y. (2001). “Out-of-Plane Fatigue Cracking in Welded Steel Bridges: Why It Happened and How It Can Be Repaired.” *Welding Innovation*, vol. 27, no. 2, pp. 2-7.

[4] Keating, P. B. (1994). “Focusing on fatigue.”*Civil Engineering—ASCE*, vol. 64, no. 11, pp. 54-57.

[5] Jajich, D., and Schultz, A. E. (2003). “Measurement and Analysis of Distortion-Induced Fatigue in MultigirderSteel Bridges.”*Journal of Bridge Engineering*, vol. 8, no. 2, pp. 84-91.

[6] Keating, P. B. and Fisher, J. W. (1987). “Fatigue behavior of variable loaded bridge details near the fatigue limit.” *Transportation Research Record*, no. 1118, pp. 56-64.

[7] Fisher, J. W. (1990). “Distortion-induced fatigue cracking in steel bridges.” *National Cooperative Highway Research Program Report*, no. 336.

[8] Alemdar, F., Nagati, D., Matamoros, A., Bennett, C., and Rolfe, S. (2013). "Repairing Distortion-Induced Fatigue Cracks in Steel Bridge Girders using Angles-with-Plate Retrofit Technique, Part I: Physical Simulations."*Journal of Structural Engineering*, ASCE, 140(5).

[9] Alemdar, F., Overman, T., Matamoros, A., Bennett, C., and Rolfe, S. (2013). "Repairing Distortion-Induced Fatigue Cracks in Steel Bridge Girders using Angles-with-Plate Retrofit Technique, Part II: Computer Simulations."*Journal of Structural Engineering*, ASCE, 140(5).

[10] Simulia (2011). Abaqus, Version 6.10. http://www.simulia.com

[11] Moes, N., Dolbow, J., Belytschko, T. (1999). “A finite element method for crack growth without remeshing.” *International Journal for Numerical Methods in Engineering*, vol. 46, pp. 131-150.

[12] Yazid, A., Abdelkader, N., Abdelmadjid, H. (2009). “A state-of-the-art review of the X-FEM for computational fracture mechanics.” *Applied Mathematical Modeling*, vol. 33, pp. 4269-4282.

[13] Marquis, G., and Kahonen, A. (1996). "Fatigue testing and analysis using the hot spot method." *VTT Publications*, no. 239, pp. 3-35.

[14] Adams, C. A. (2010). "Finite Element Study on Bridge Details Susceptible to Distortion-Induced Fatigue," thesis, submitted to the University of Kansas in partial fulfillment of requirements for the degree of Master of Science in Civil Engineering.

[15] Bhargava, A. (2010). "Fatigue Analysis of Steel Bridge Details: Hot Spot Stress Approach," dissertation, submitted to The George Washington University in partial satisfaction of the requirements for the degree of Doctor of Philosophy in Civil Engineering.

[16] Maddox, S. J. (2002). "Hot-Spot Stress Design Curves for Fatigue Assessment of Welded Structures." *International Journal of Offshore and Polar Engineering*, vol. 12, no. 2, pp. 134-141.

[17] Barsom, J. M., and Rolfe, S. T. (1999). *Fracture and Fatigue Control in Structures: Application of Fracture Mechanics*, 3rd Edition. American Society for Testing and Materials, West Conshohocken, PA.

[18] Rice, J. R. (1968). "A Path Independent Integral and the Approximate Analysis of Strain Concentration by Notches and Cracks."*Journal of Applied Mechanics*, vol. 35, pp. 379-386.

[19] Shih, C. F., and Asaro, R. J. (1988). "Elastic-Plastic Analysis of Cracks on BimaterialInteraces: Part I—Small Scale Yielding." *Journal of Applied Mechanics*, vol. 55, no. 2, pp. 299-316.

[20] Gosz, M. (2005). "An Interaction Integral Method for Computation of T-Stress along the Fronts of General Non-Planar Cracks in Three-Dimensions." *11th International Conference on Fracture Proceedings*, Turin, Italy.

[21] Sih, G. C., and Macdonald, B. (1974). "Fracture mechanics applied to engineering problems - strain energy density fracture criterion." *Engineering Fracture Mechanics*, vol. 6, no. 2, pp. 361-386.

[22] Sih, G. C., and Cha, B. C. K. (1974). "A fracture criterion for three-dimensional crack problems."*Engineering Fracture Mechanics*, vol. 6, no. 4, pp. 699-723.

[23] Paris, P., and Erdogan, F. (1963). "A critical analysis of crack propagation laws."*Journal of Basic Engineering*, vol. 85, no. 4, pp. 528-533.

[24] FHWA (2012). *Steel Bridge Design Handbook: Bridge Steels and Their Mechanical*

Properties. Federal Highway Administration, Washington, DC.

Part 5

CONCLUSION

This dissertation has presented three separate investigations aimed at evaluating fatigue retrofit effectiveness. The three retrofit techniques studied were a CFRP overlay for tensile (in-plane) fatigue, crack-arrest holes under distortion-induced fatigue, and an angles-with-plate retrofit under distortion-induced fatigue used as a means to assess various analysis techniques (hot spot stress, J-integral, and stress intensity factors).

Given that the three techniques studied tend to occupy different "niches" in terms of fatigue repair applicability, the suite of investigations presented in this volume will be useful in a broad range of applications, and thus represent a significant contribution to the various literature on repairing fatigue damage in steel bridges. In addition to providing specific recommendations to engineers and researchers for applying effective retrofits, one of the three studies provided guidance on the selection of techniques for best analyzing the problem of distortion-induced fatigue in the context of finite element modeling.

To provide greater context to the results reported in Parts 2 - 4, a short comparative exercise was performed to examine the relative performance of crack-arrest holes with pretensioned bolts against the angle-with-plate repair when both were loaded under distortion-induced fatigue. The effects of this addition were studied in the FE model described in Part 3 of this dissertation that included a horseshoe-shaped and web-to-flange crack with 102 mm [4 in.] horseshoe-shaped crack length and 203 mm [8 in.] web-to-flange crack length. As shown in Figure 1, the girder was a single 3.0 m [10 ft] long by 1.52 m [5.0 ft] deep simply-supported steel girder section. The angles were L152x127x13-mm [L6x5x1/2-in.] connecting the web to each side of the connection plate, and the backing plate was a 457x203x13-mm [18x8x1/2-in.] plate on the other side of the web from the angles (M-M retrofit). The material used for the angles,

backing plate and bolts was steel (elastic modulus was 200,000 MPa [29,000 ksi] and Poisson's ratio was 0.3).

A 41.4 MPa [6.0 ksi] pressure load was placed over a 12 mm [1/2 in.] width at the center of the top flange, to simulate the maximum design truck load over this girder section. An 18.2 kN [4.1 kip] point load was placed 105 mm [4.1 in.] from the top of stiffener at the center of the exterior face of the stiffener, 127 mm [5.0 in.] from the interior surface of the web. The load was directed perpendicular to the surface and pointed away from the girder. A 12.8 kN [2.87 kip] point load was placed at the same location as the 18.2 kN [4.1 kip] point load. This load was directed parallel to the surface and pointed toward the bottom flange. A corresponding 18.2 kN [4.1 kip] point load and a 12.8 kN [2.9 kip] point load was placed 105 mm [4.1 in.] from the bottom of stiffener at the center of the exterior face of the stiffener, 127 mm [5.0 in.] from the interior surface of the web. These force couples, shown in Figure 2, model the out-of-plane forces induced by cross-frame connections during bending deformation.

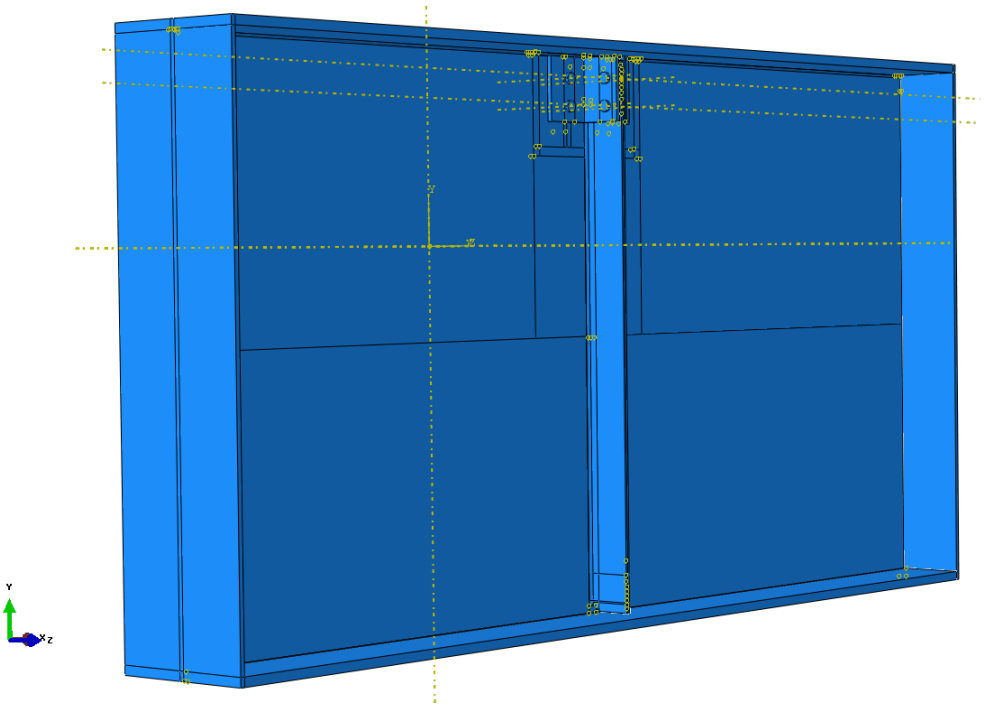

(a)

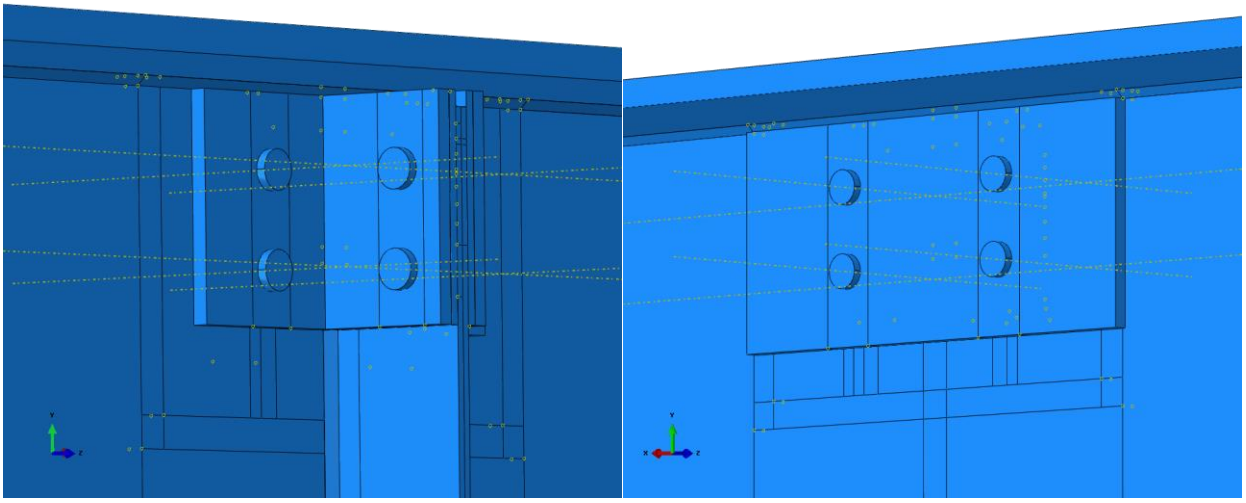

(b) **(c)**

Figure 1: (a) Girder section finite element model geometry; (b) Angles on the front side of the girder; (c) Backing plate on the fascia side of the girder

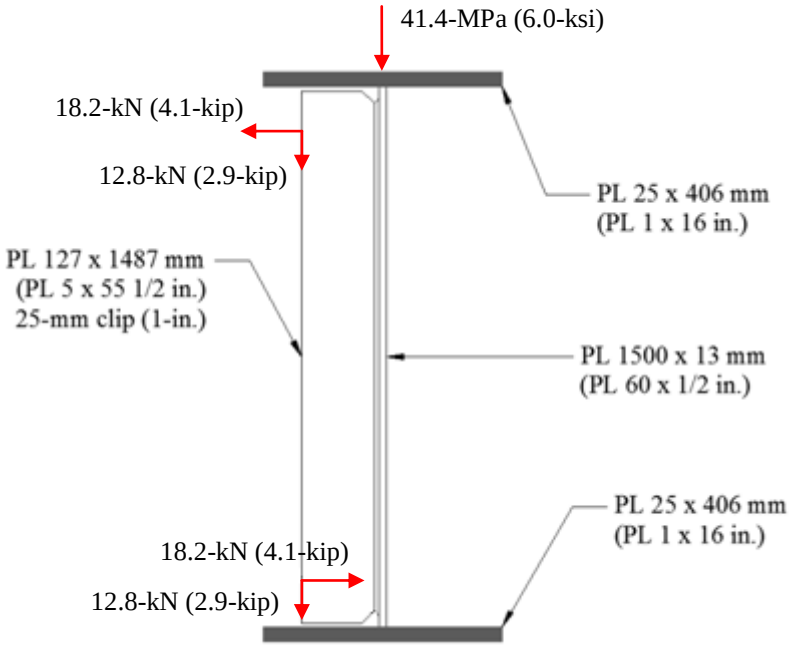

Figure 2: Girder cross-section

The comparison of the maximum principal stresses between the model with the angles-with-plate retrofit and the model with the crack-arrest holes with the same horseshoe-shaped and web-to-flange crack length was evaluated, as shown in Table 1. The path that was used to determine the first peak stress (HSS-1) followed the same horseshoe shape along the connection plate-to-web weld a distance of 229 mm [9.0 in.] down both sides of the stiffener. The path to determine the second peak stress (HSS-2) followed the same horizontal path along the web-to-flange weld for a length of 406 mm [16.0 in.].The maximum principal stresses in the web gap region for the model with the angles-with-plate retrofit, and for the model with the crack-arrest holes retrofit are shown in Figure 3.

Table 1: Horseshoe-shaped & web-to-flange crack pattern stresses

Maximum Principal Stresses for 102 mm [4.0 in.] Crack

Retrofit Method		**HSS-1**	**HSS-2**
	Diameter, mm [in.]	Peak Stress, MPa [ksi]	Peak Stress, MPa [ksi]
Crack-arrest hole Retrofit	13 [0.5]	554 [80.4]	178 [25.8]
	25 [1.0]	382 [55.4]	172 [25.0]
	51 [2.0]	319 [46.2]	100 [14.5]
Angles-with-plate Retrofit		128 [18.5]	114 [16.5]

From the results, the HSS-1 values for the model with the M-M angles-with-plate retrofit was much smaller than the stress values for the crack-arrest hole model with 13 mm [0.5 in.], 25 mm [1.0 in.] or 51 mm [2.0 in.] hole diameter. The HSS-2 values for the model with the M-M angles-with-plate retrofit was smaller than the stress values for the crack-arrest hole model with 13 mm [0.5 in.] or 25 mm [1.0 in.] hole diameter, and almost the same with stress for the crack-arrest hole model with 51 mm [2.0 in.] hole diameter. Given these findings, the angles-with-plate retrofit generally performed significantly better than the crack-arrest holes retrofit at mitigating distortion induced fatigue. A visual comparison of the results is shown in Figure 3.

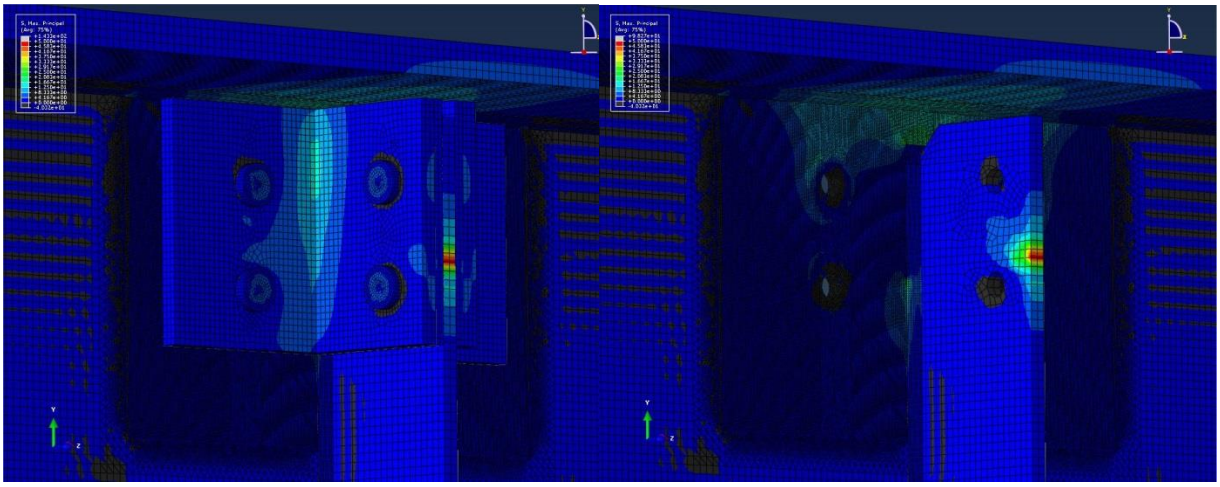

(a) **(b)**

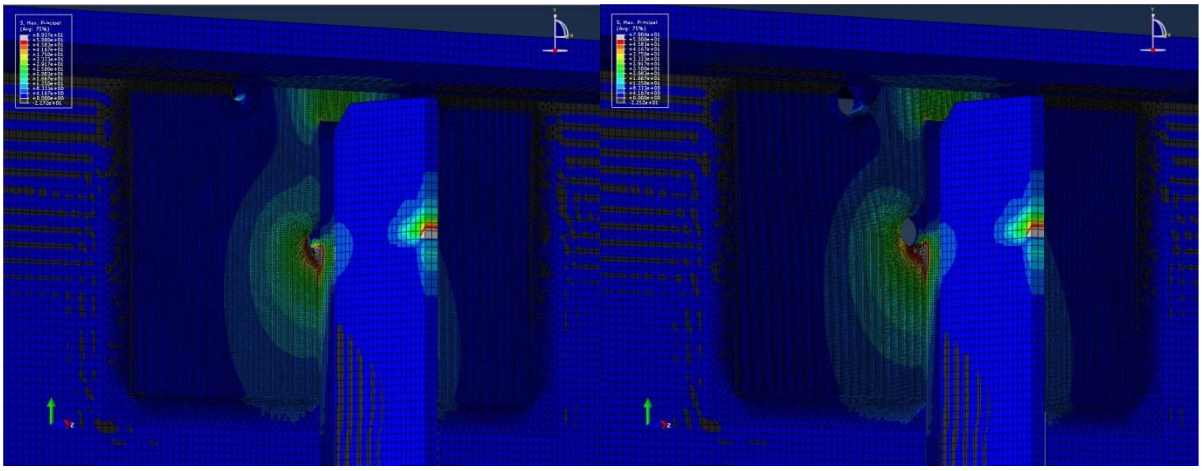

(c) **(d)**

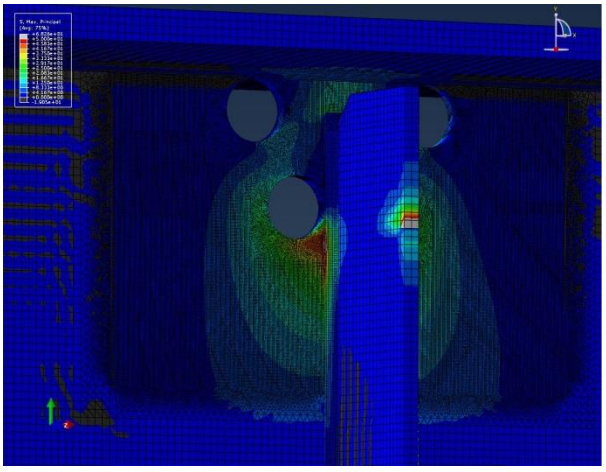

(e)

Figure 3: (a) Maximum principal stress for angles-with-plate retrofit model; (b) Maximum principal stress for angles-with-plate retrofit model (angles and plate were not shown); (c) Maximum principal stress for crack-arrest hole model with 13 mm [0.5 in.] hole diameter; (d) Maximum principal stress for crack-arrest hole model with 25 mm [1.0 in.] hole diameter; (e) Maximum principal stress for crack-arrest hole model with 51 mm [2.0 in.] hole diameter

While the results presented in this dissertation have been presented primarily in three discrete parts, there has been a consistent theme: repairing fatigue damage in steel bridges. Each of the three papers has presented an investigation aimed at improving engineers' and researchers' capabilities to design effective fatigue retrofits and to assess fatigue susceptibility. It is envisioned that work presented in this thesis will be of use to both practicing structural engineers and researchers as they work to responsibly extend the lives of aging steel bridge infrastructure.

Appendices

APPENDIX A: MAXIMUM PRINCIPAL STRESS AROUND CRACK-ARREST HOLES FOR DIAGONAL CRACK TYPE

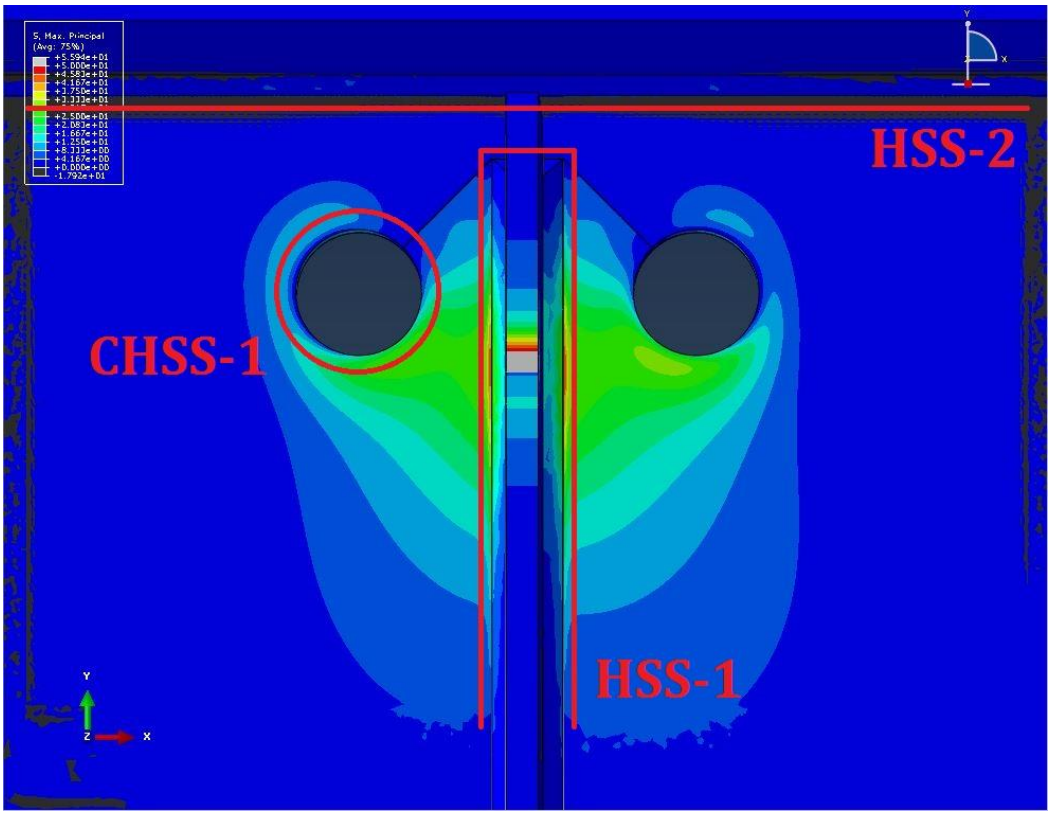

Figure A. 1: Hot Spot Stress Paths for Diagonal Crack Type

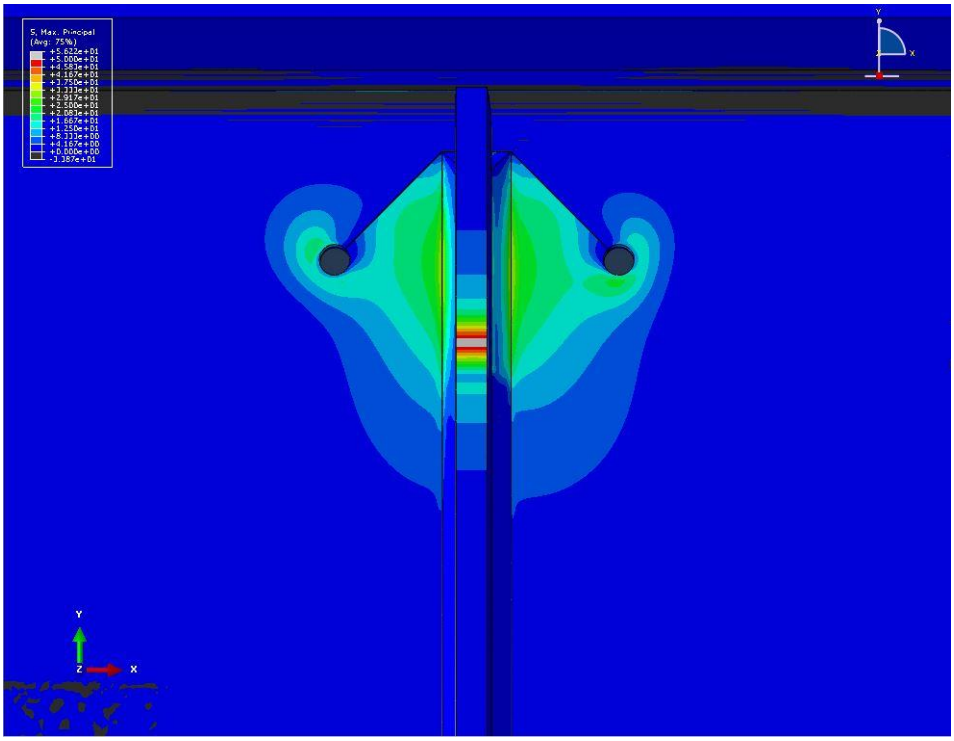

CHSS-1 = 127 Mpa [18.4 ksi]
HSS-1 = 157 Mpa [22.7 ksi]
HSS-2 = -0.41 Mpa [-0.059 ksi]

Figure A.2: 70 mm [2.75 in.] Crack Length & 13 mm [0.5 in.] Hole Diameter

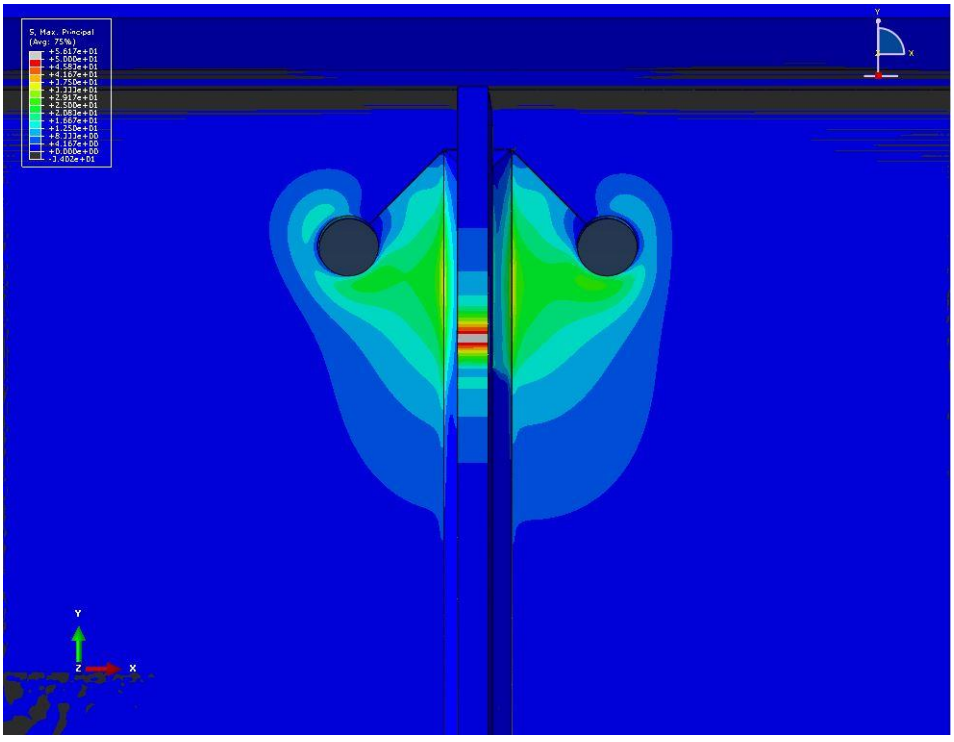

CHSS-1 = 161 Mpa [23.4 ksi]
HSS-1 = 168 Mpa [24.3 ksi]
HSS-2 = -0.22 Mpa [-0.032 ksi]

Figure A.3: 70 mm [2.75 in.] Crack Length & 25 mm [1.0 in.] Hole Diameter

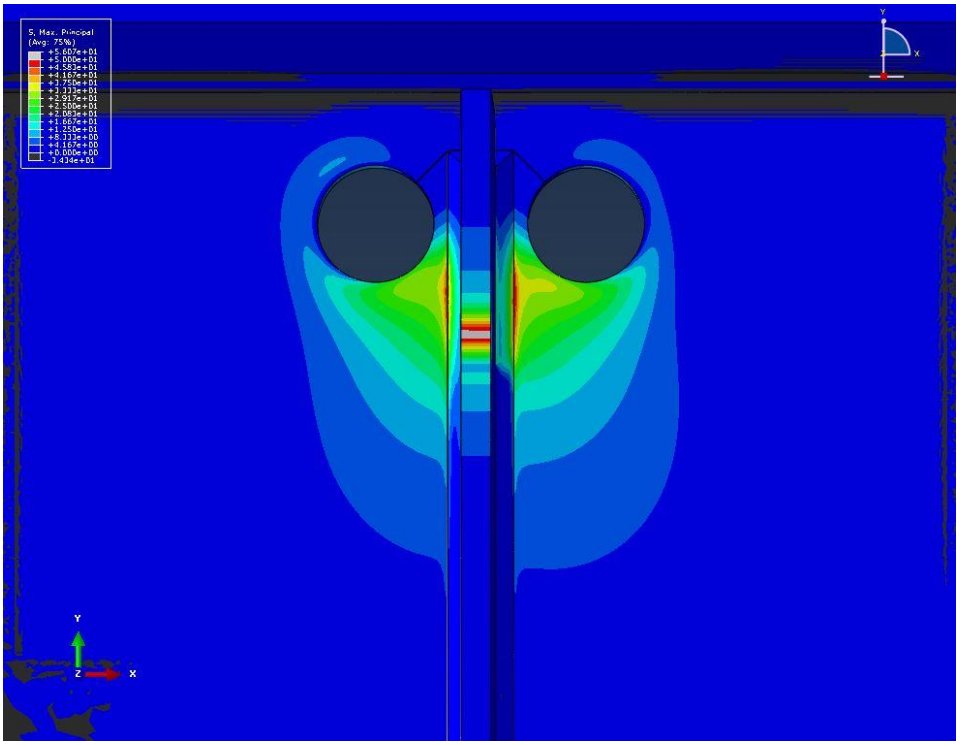

CHSS-1 = 222 Mpa [32.2 ksi]

HSS-1 = 234 Mpa [33.9 ksi]

HSS-2 = -0.25 Mpa [-0.036 ksi]

Figure A. 4: 70 mm [2.75 in.] Crack Length & 51 mm [2.0 in.] Hole Diameter

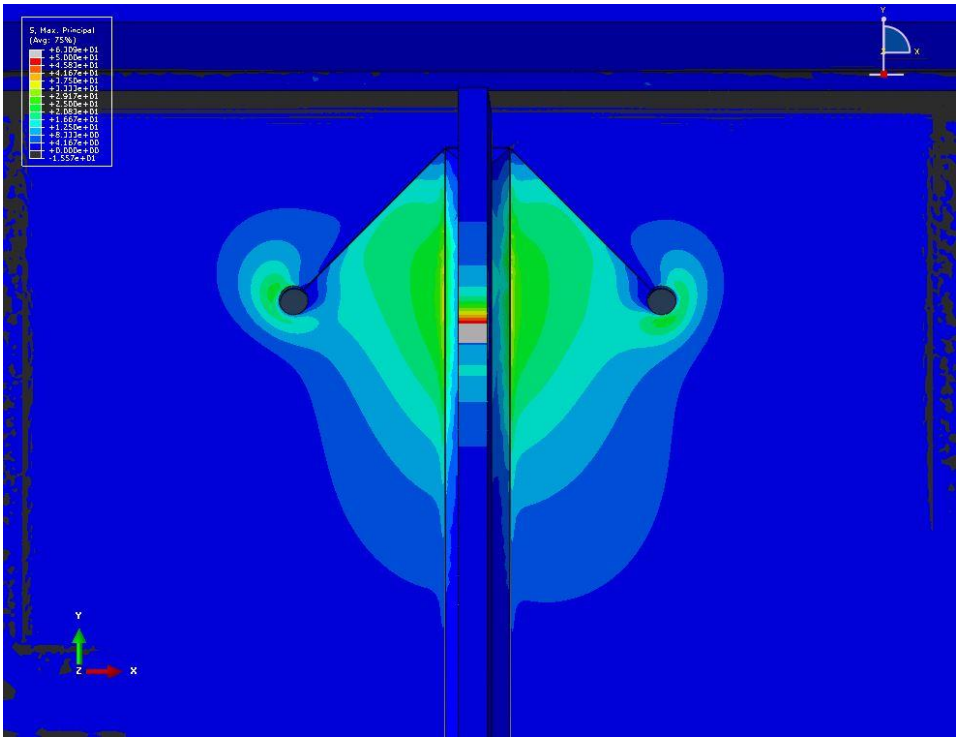

CHSS-1 = 150 Mpa [21.7 ksi]

HSS-1 = 170 Mpa [24.7 ksi]

HSS-2 = -0.52 Mpa [-0.076 ksi]

Figure A. 5: 102mm [4.0 in.] Crack Length & 13 mm [0.5 in.] Hole Diameter

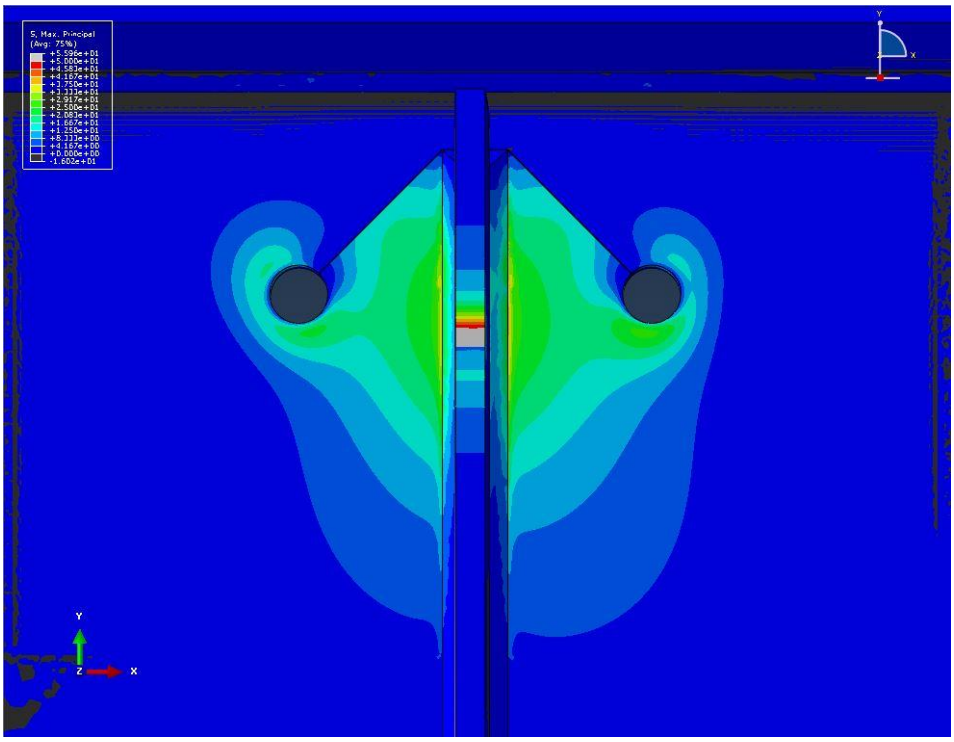

CHSS-1 = 150 Mpa [21.7 ksi]
HSS-1 = 172 Mpa [24.9 ksi]
HSS-2 = -0.25 Mpa [-0.036 ksi]

Figure A. 6: 102mm [4.0 in.] Crack Length & 25 mm [1.0 in.] Hole Diameter

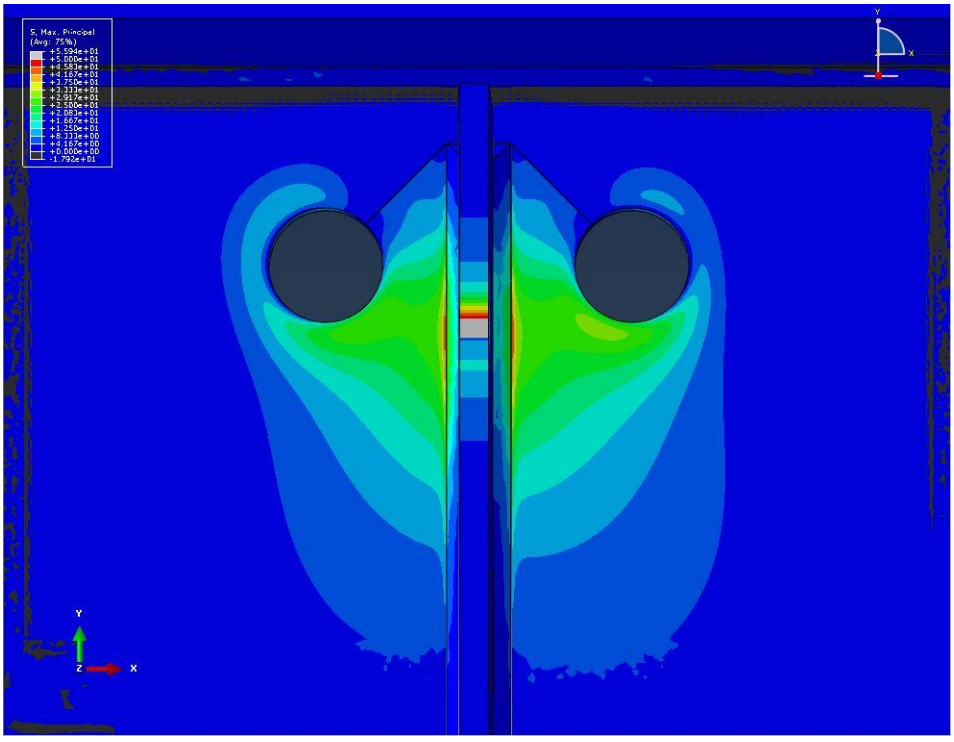

CHSS-1 = 197 Mpa [28.6 ksi]
HSS-1 = 196 Mpa [28.4 ksi]
HSS-2 = -0.29 Mpa [-0.042 ksi]

Figure A. 7: 102mm [4.0 in.] Crack Length & 51 mm [2.0 in.] Hole Diameter

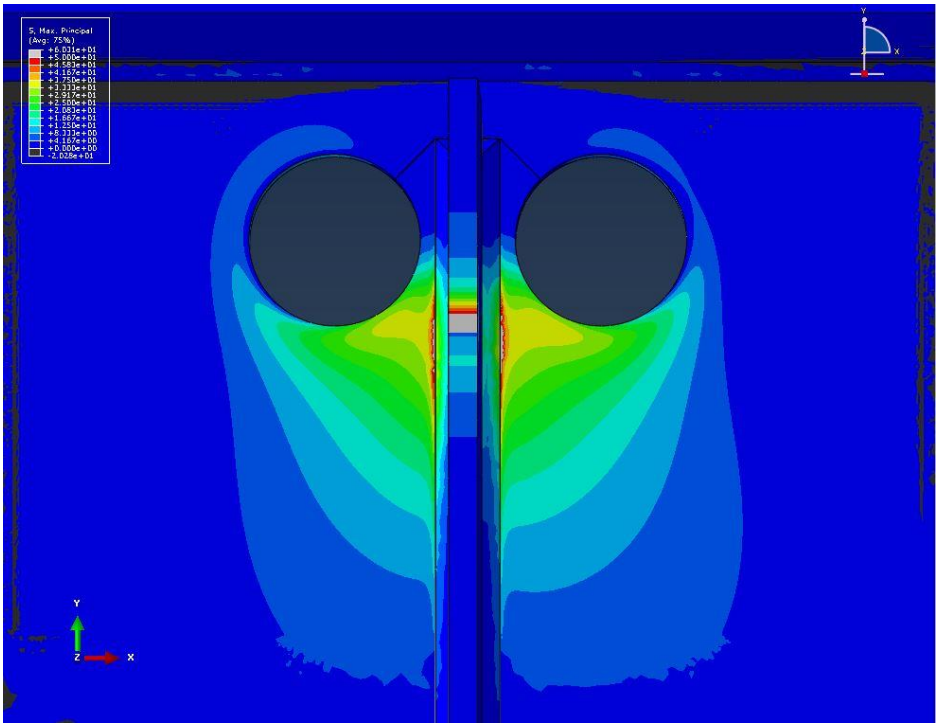

CHSS-1 = 237 Mpa [34.4 ksi]

HSS-1 = 247 Mpa [35.8 ksi]

HSS-2 = 8.19 Mpa [1.19 ksi]

Figure A. 8: 102mm [4.0 in.] Crack Length & 76 mm [3.0 in.] Hole Diameter

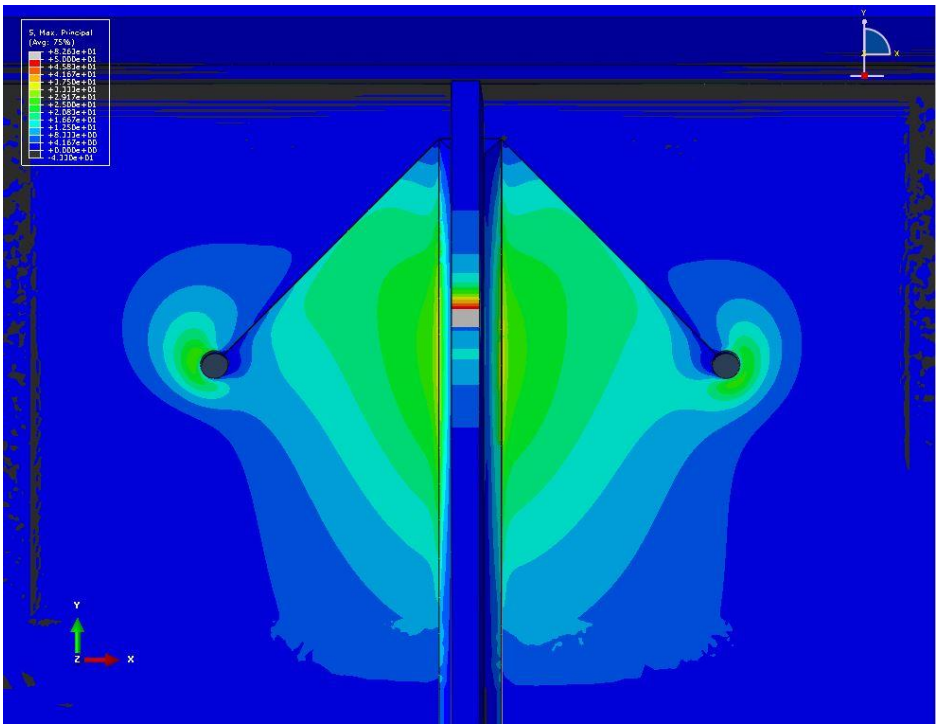

CHSS-1 = 187 Mpa [27.1 ksi]

HSS-1 = 184 Mpa [26.7 ksi]

HSS-2 = -0.42 Mpa [-0.061 ksi]

Figure A. 9: 152 mm [6 in.] Crack Length & 13 mm [0.5 in.] Hole Diameter

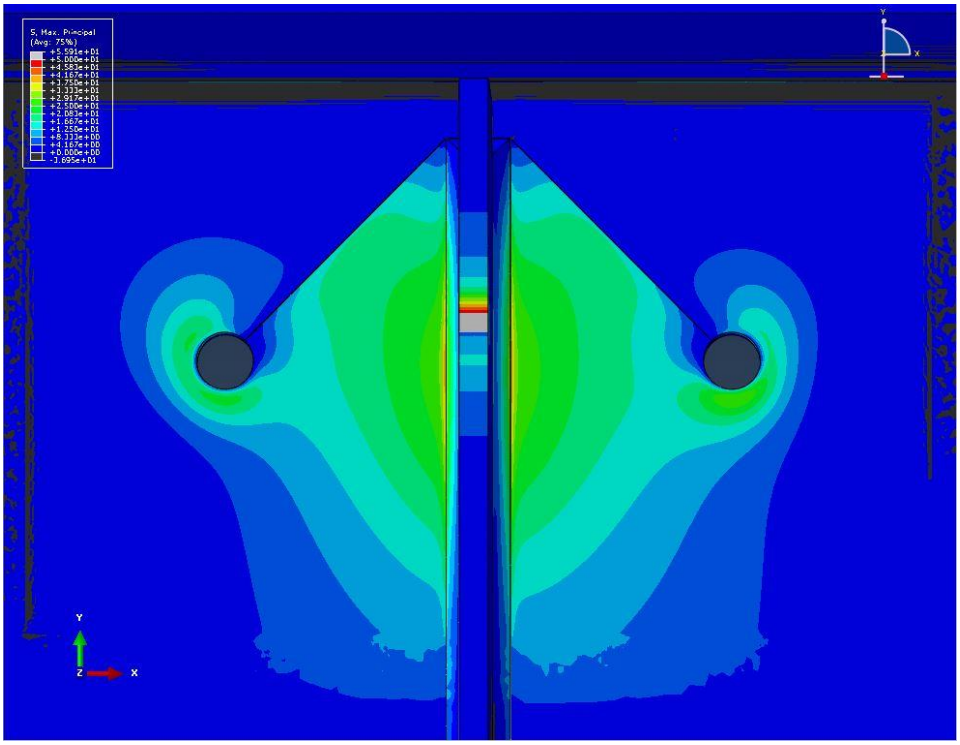

CHSS-1 = 154 Mpa [22.3 ksi]

HSS-1 = 188 Mpa [27.2 ksi]

HSS-2 = -0.22 Mpa [-0.032 ksi]

Figure A. 10: 152 mm [6 in.] Crack Length & 25 mm [1.0 in.] Hole Diameter

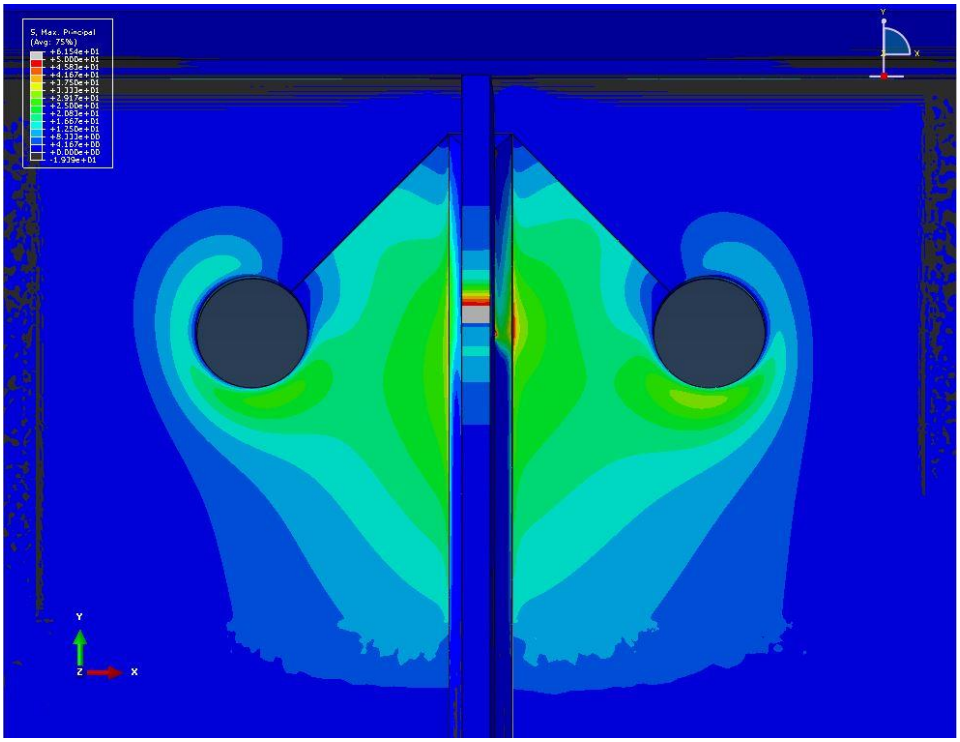

CHSS-1 = 184 Mpa [26.7 ksi]

HSS-1 = 206 Mpa [29.9 ksi]

HSS-2 = 0.99 Mpa [0.143 ksi]

Figure A. 11: 152 mm [6 in.] Crack Length & 51 mm [2.0 in.] Hole Diameter

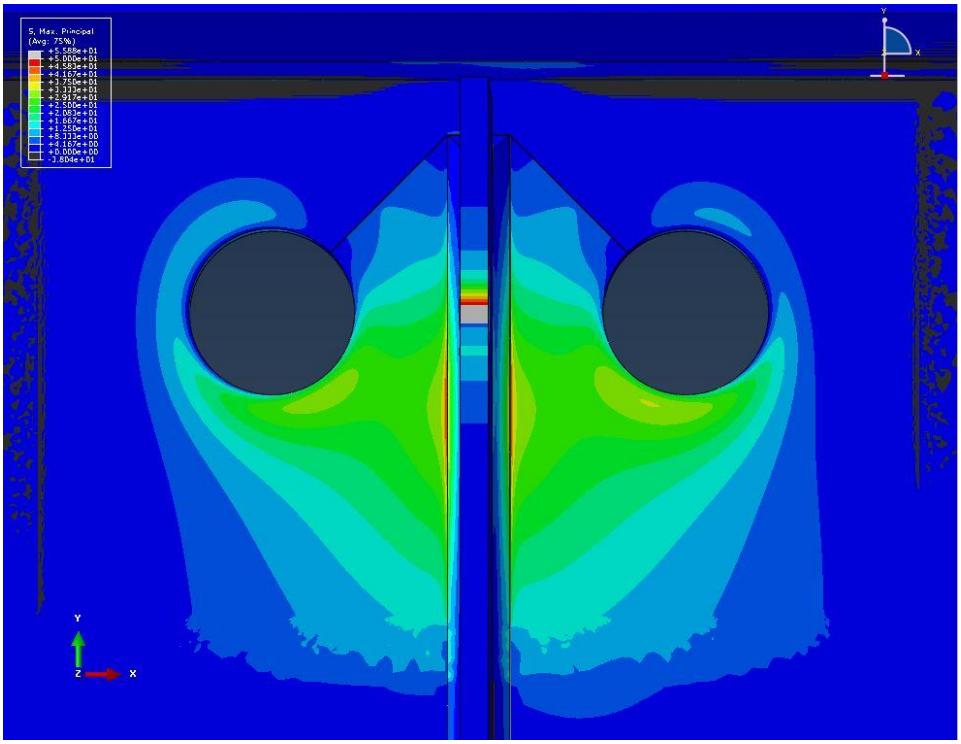

CHSS-1 = 208 Mpa [30.2 ksi]

HSS-1 = 212 Mpa [30.8 ksi]

HSS-2 = 10.9 Mpa [1.579 ksi]

Figure A. 12: 152 mm [6 in.] Crack Length & 76 mm [3.0 in.] Hole Diameter

APPENDIX B: MAXIMUM PRINCIPAL STRESS AROUND CRACK-ARREST HOLES FOR HORSESHOE-SHAPED CRACK TYPE

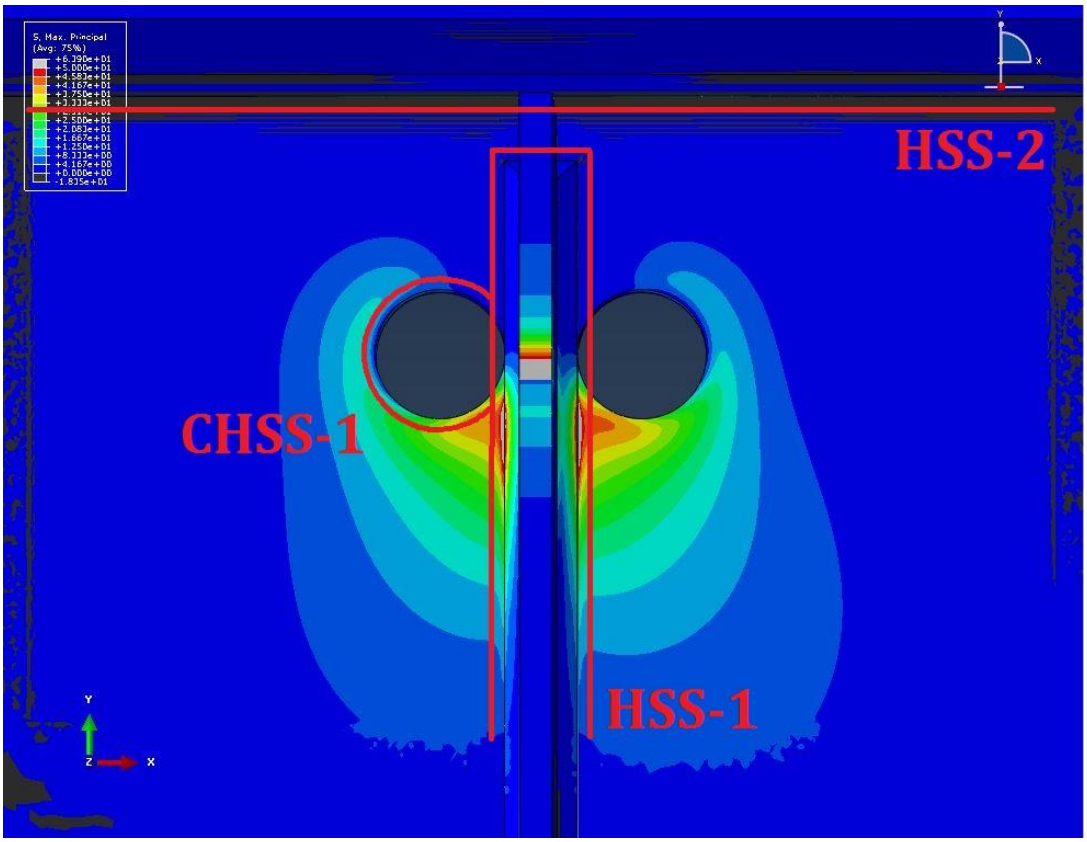

Figure B. 1: Hot Spot Stress Paths for Horseshoe-Shaped Crack Type

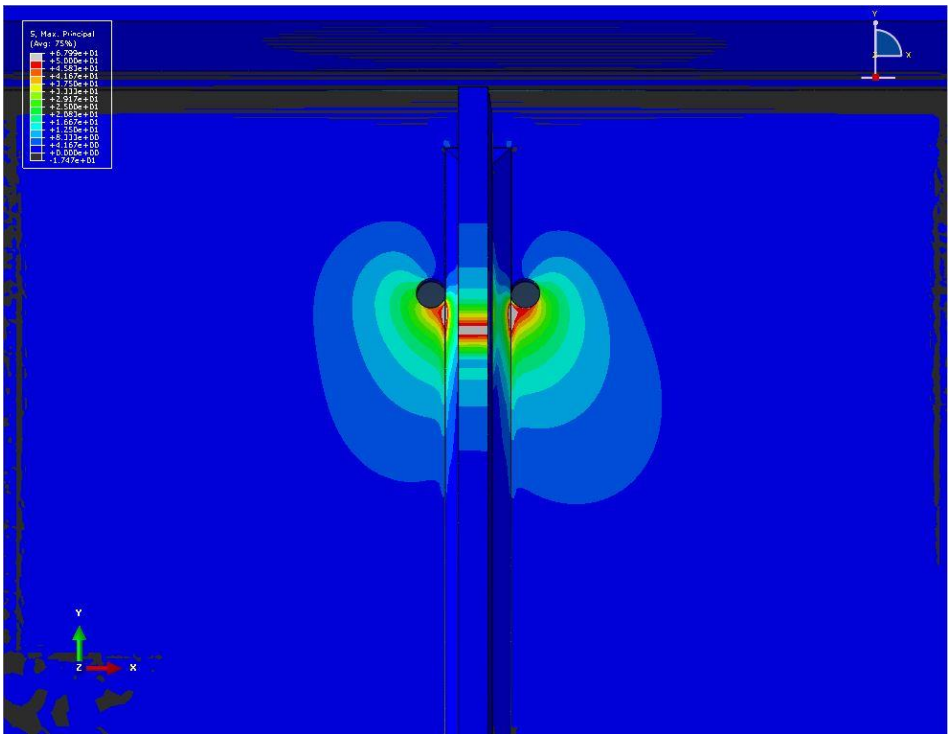

CHSS-1 = 252 Mpa [36.6 ksi]

HSS-1 = 364 Mpa [52.8 ksi]

HSS-2 = -0.46 Mpa [-0.067 ksi]

Figure B. 2: 70 mm [2.75 in.] Crack Length & 13 mm [0.5 in.] Hole Diameter

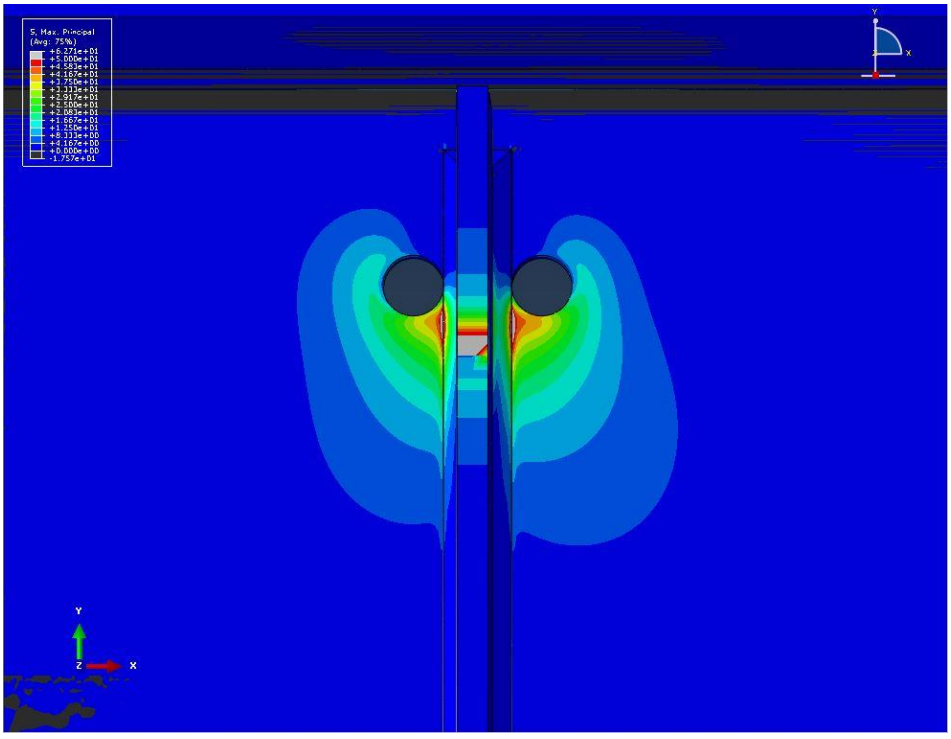

CHSS-1 = 263 Mpa [38.2 ksi]

HSS-1 = 286 Mpa [41.5 ksi]

HSS-2 = -0.23 Mpa [-0.034 ksi]

Figure B. 3: 70 mm [2.75 in.] Crack Length & 25 mm [1.0 in.] Hole Diameter

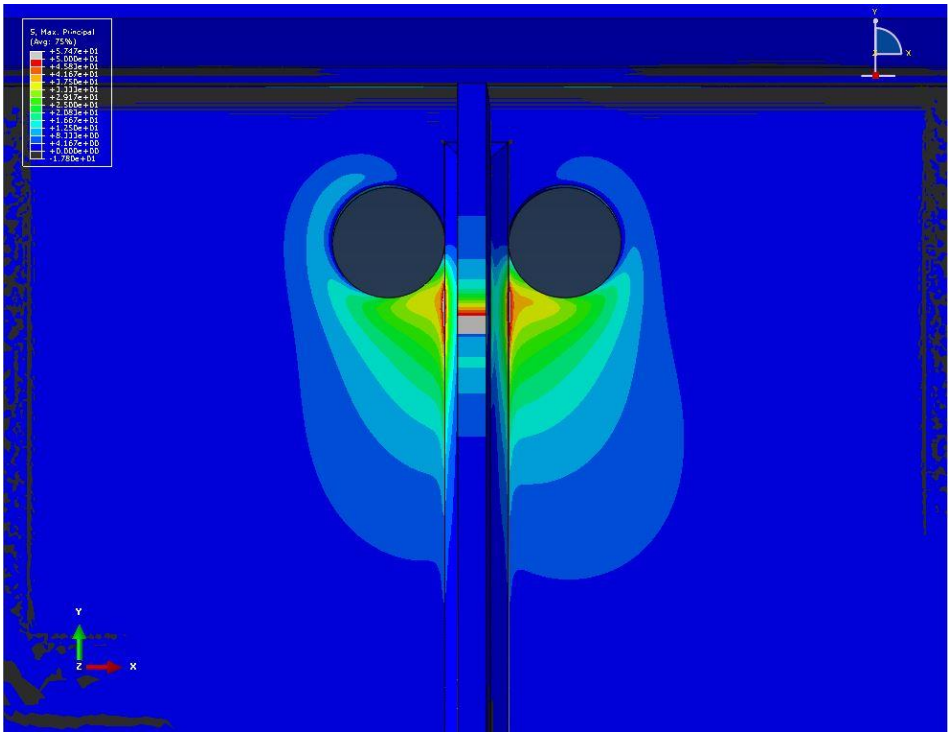

CHSS-1 = 250 Mpa [36.3 ksi]

HSS-1 = 263 Mpa [38.1 ksi]

HSS-2 = -0.26 Mpa [-0.037 ksi]

Figure B. 4: 70 mm [2.75 in.] Crack Length & 51 mm [2.0 in.] Hole Diameter

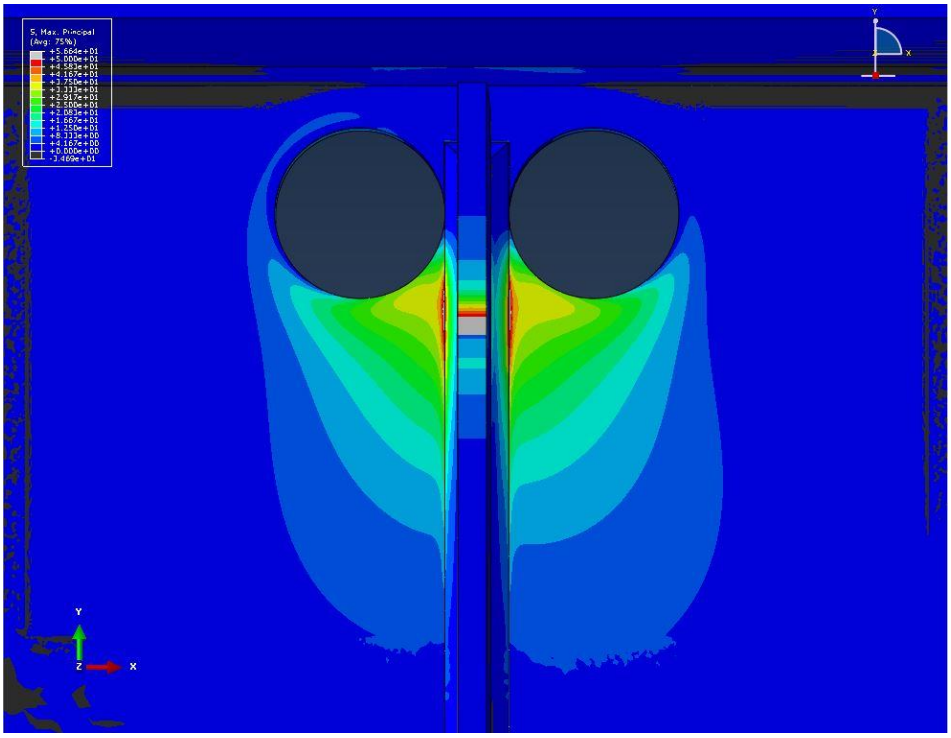

CHSS-1 = 241 Mpa [35.0 ksi]

HSS-1 = 252 Mpa [36.5 ksi]

HSS-2 = 16.7 Mpa [2.42 ksi]

Figure B. 5: 70 mm [2.75 in.] Crack Length & 76 mm [3.0 in.] Hole Diameter

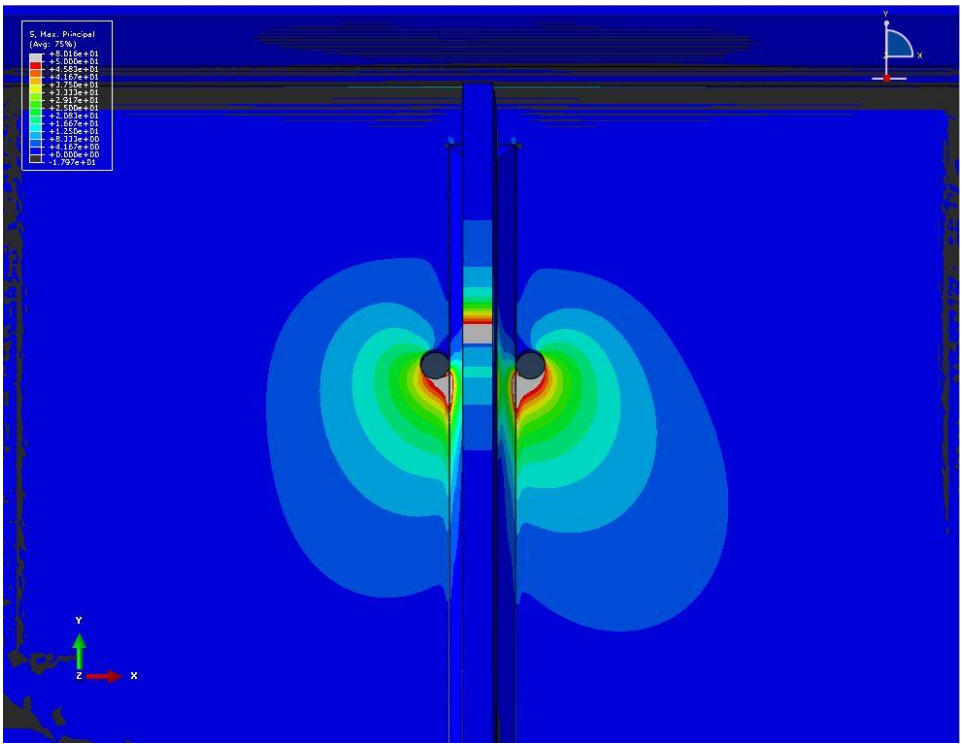

CHSS-1 = 314 Mpa [45.6 ksi]
HSS-1 = 449 Mpa [65.1 ksi]
HSS-2 = -0.48 Mpa [-0.070 ksi]

Figure B. 6: 102mm [4.0 in.] Crack Length & 13 mm [0.5 in.] Hole Diameter

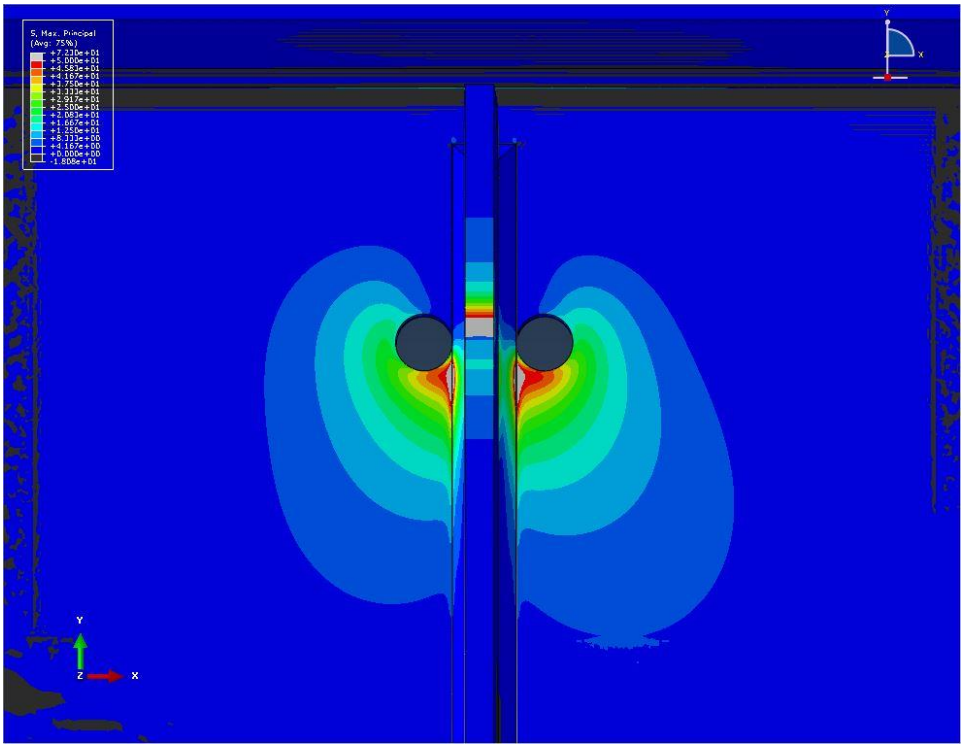

CHSS-1 = 312 Mpa [45.2 ksi]
HSS-1 = 335 Mpa [48.6 ksi]
HSS-2 = -0.21 Mpa [-0.030 ksi]

Figure B. 7: 102mm [4.0 in.] Crack Length & 25 mm [1.0 in.] Hole Diameter

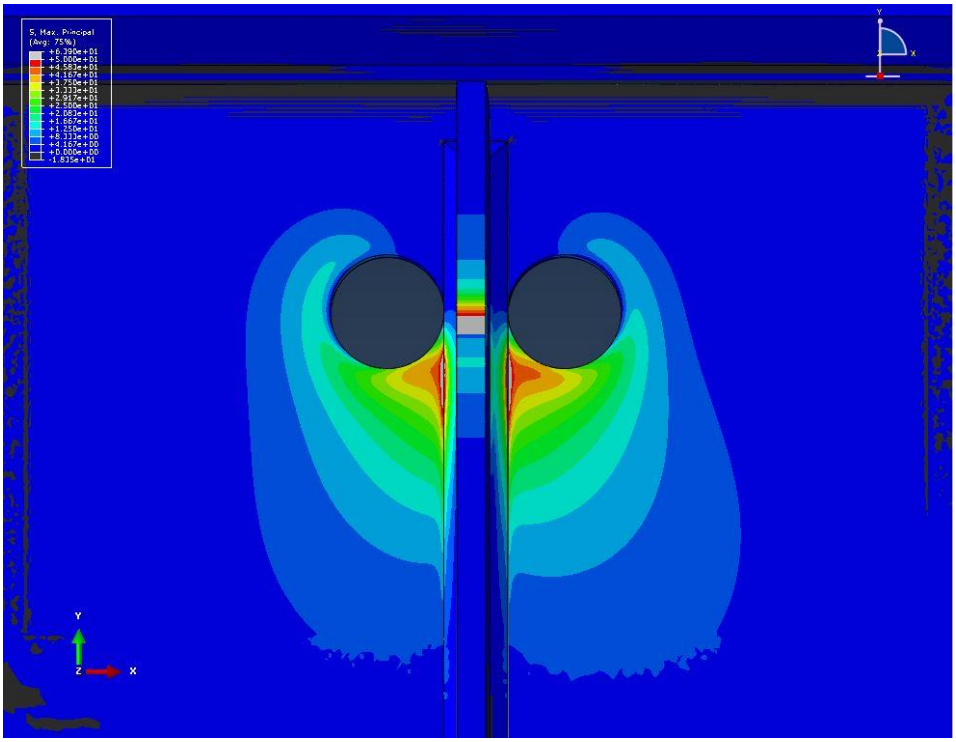

CHSS-1 = 283 Mpa [41.0 ksi]
HSS-1 = 296 Mpa [42.9 ksi]
HSS-2 = -0.21 Mpa [-0.030 ksi]

Figure B. 8: 102mm [4.0 in.] Crack Length & 51 mm [2.0 in.] Hole Diameter

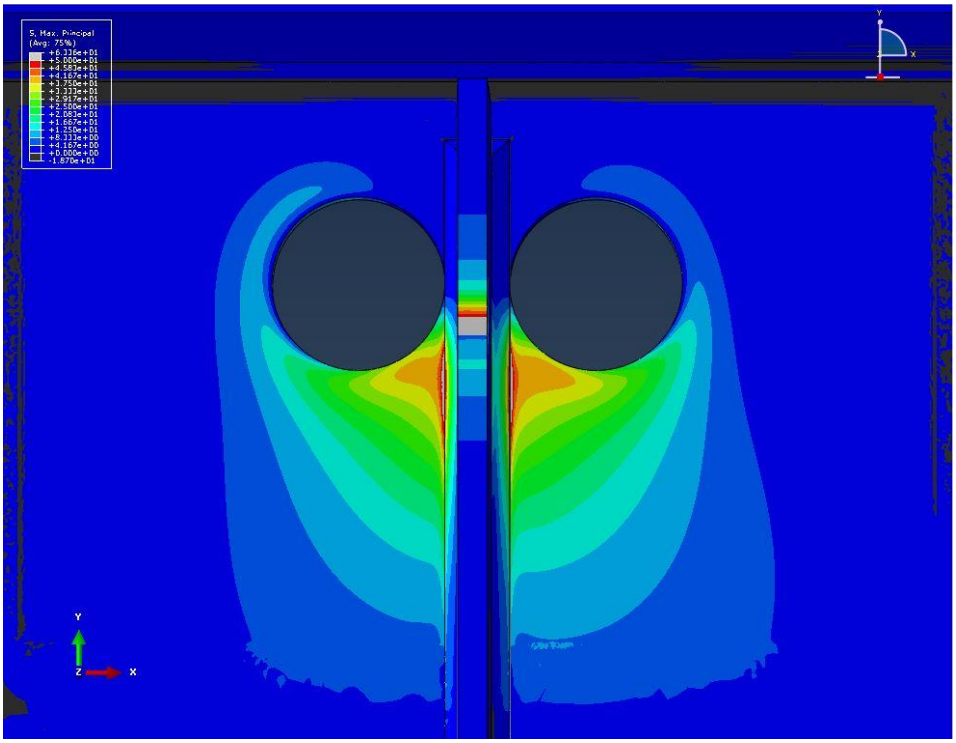

CHSS-1 = 268 Mpa [38.8 ksi]
HSS-1 = 277 Mpa [40.2 ksi]
HSS-2 = -0.27 Mpa [-0.039 ksi]

Figure B. 9: 102mm [4.0 in.] Crack Length & 76 mm [3.0 in.] Hole Diameter

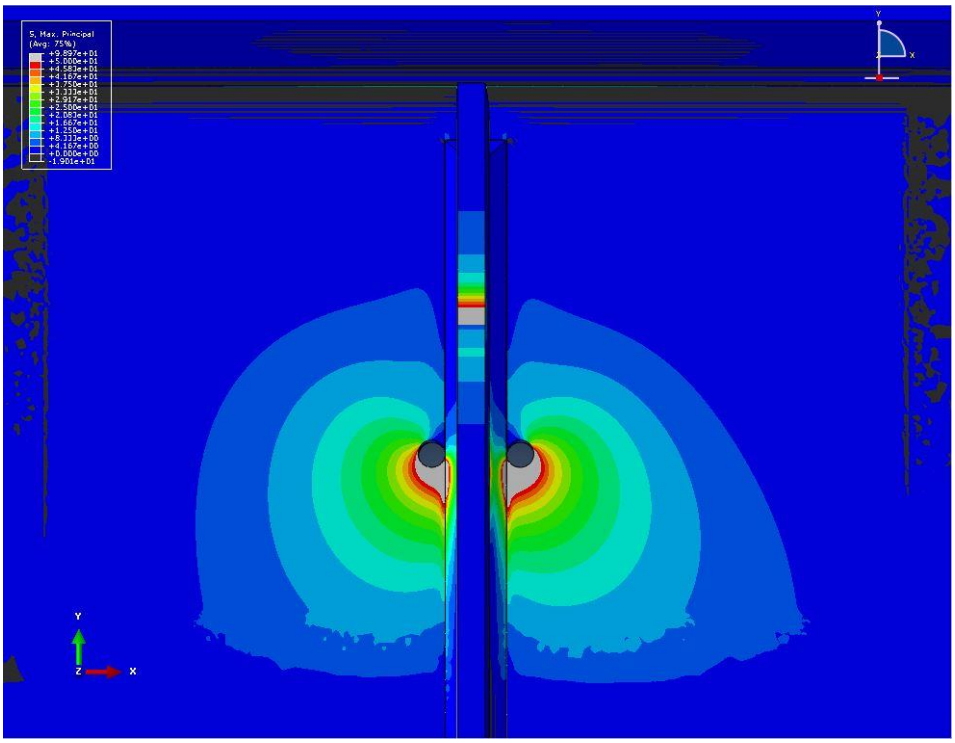

CHSS-1 = 408 Mpa [59.2 ksi]
HSS-1 = 583 Mpa [84.5 ksi]
HSS-2 = -0.53 Mpa [-0.077 ksi]

Figure B. 10: 152 mm [6 in.] Crack Length & 13 mm [0.5 in.] Hole Diameter

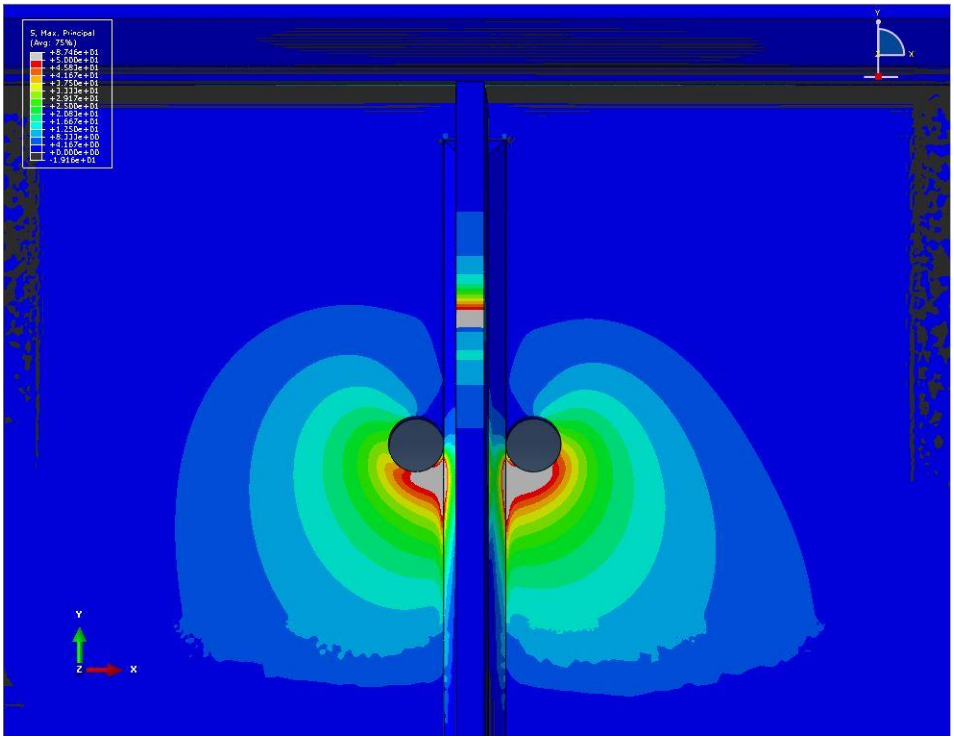

CHSS-1 = 389 Mpa [56.4 ksi]
HSS-1 = 414 Mpa [60.1 ksi]
HSS-2 = -0.23 Mpa [-0.033 ksi]

Figure B. 11: 152 mm [6 in.] Crack Length & 25 mm [1.0 in.] Hole Diameter

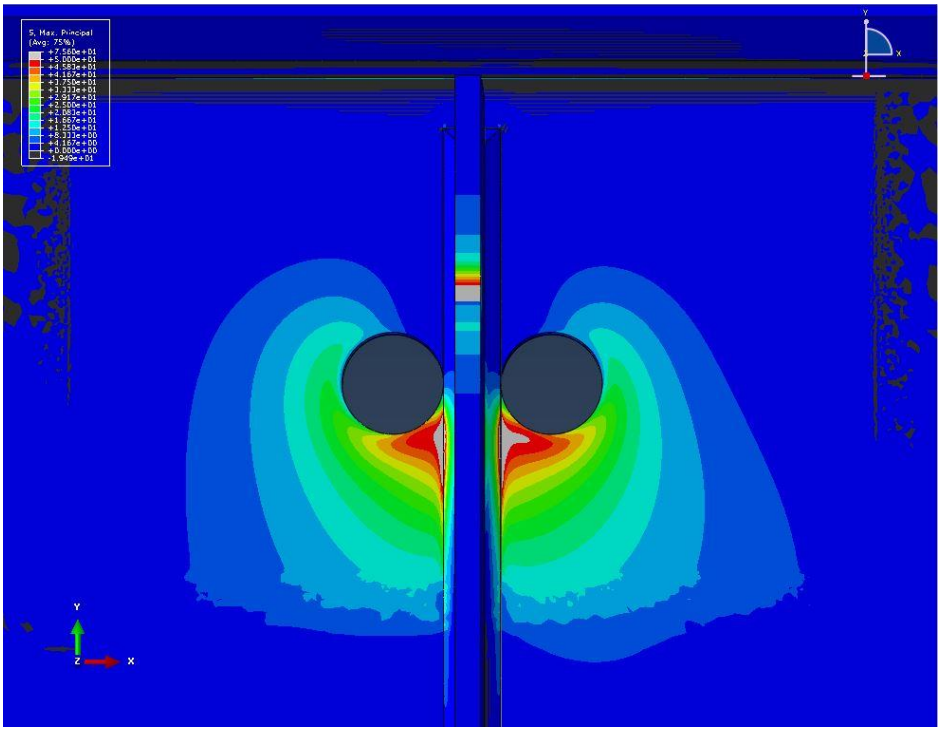

CHSS-1 = 338 Mpa [49.0 ksi]

HSS-1 = 350 Mpa [50.8 ksi]

HSS-2 = -0.20 Mpa [-0.029 ksi]

Figure B. 12: 152 mm [6 in.] Crack Length & 51 mm [2.0 in.] Hole Diameter

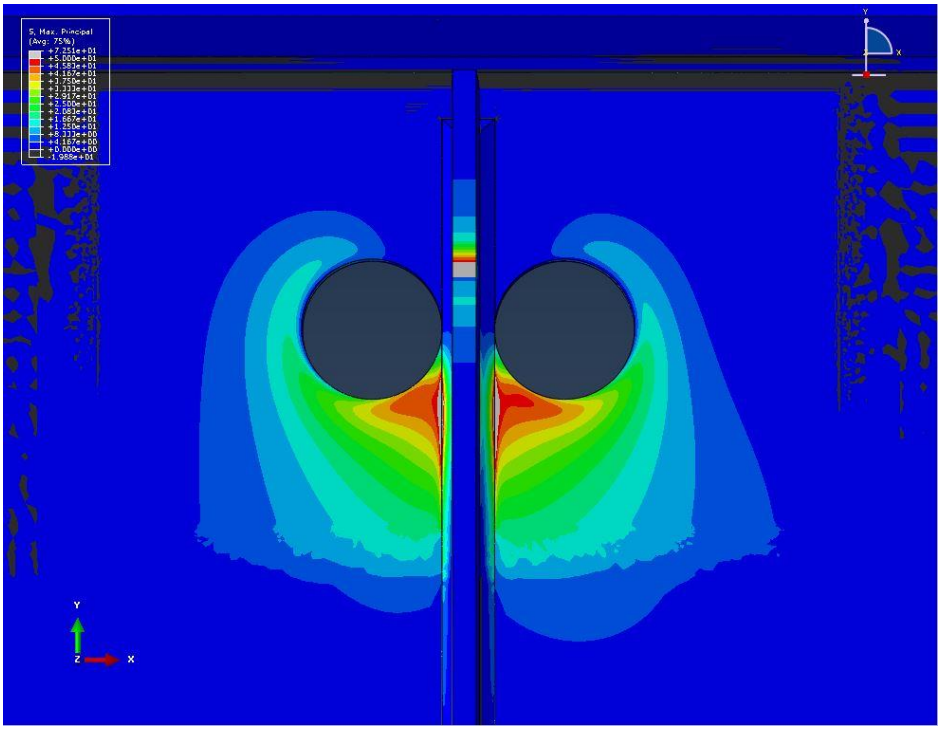

CHSS-1 = 312 Mpa [45.2 ksi]

HSS-1 = 320 Mpa [46.4 ksi]

HSS-2 = -0.24 Mpa [-0.035 ksi]

Figure B. 13: 152 mm [6 in.] Crack Length & 76 mm [3.0 in.] Hole Diameter

APPENDIX C: MAXIMUM PRINCIPAL STRESS AROUND CRACK-ARREST HOLES FOR HORSESHOE-SHAPED&WEB-TO-FLANGE CRACK TYPE

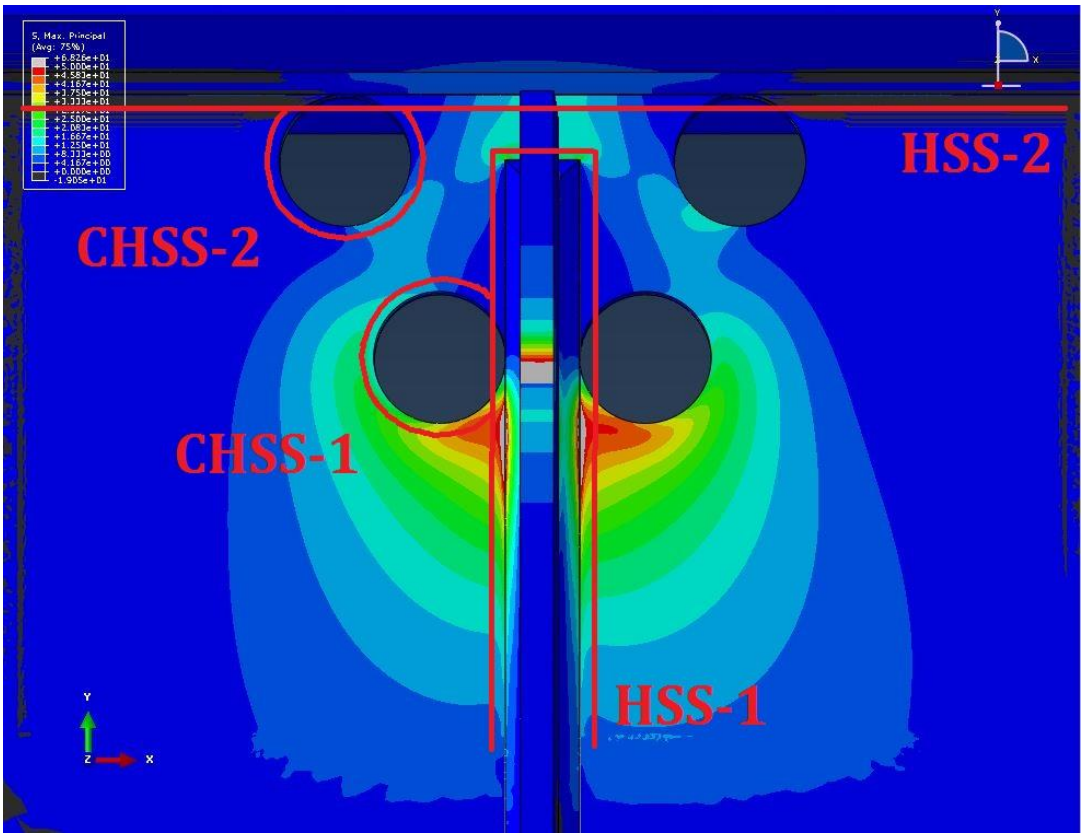

Figure C. 1: Hot Spot Stress Paths for Horseshoe-Shaped&Web-To-Flange Crack Type

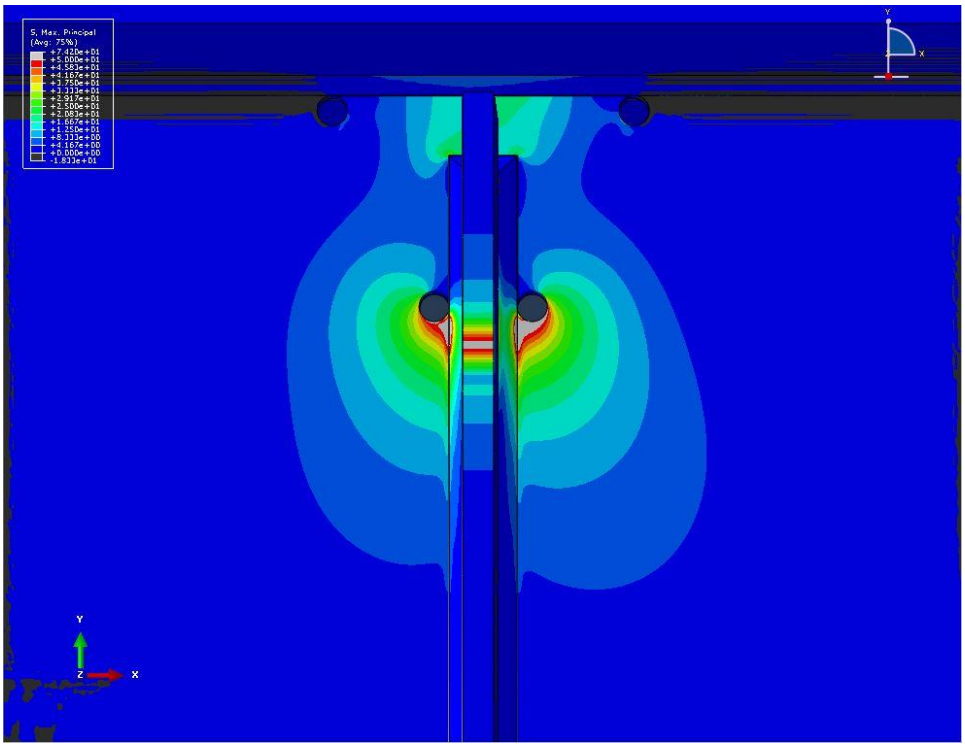

CHSS-1 = 298 Mpa [43.2 ksi]
CHSS-2 = 22.8 Mpa [3.30 ksi]
HSS-1 = 431 Mpa [62.5 ksi]
HSS-2 = 122 Mpa [17.7 ksi]

Figure C. 2: 70 mm [2.75 in.] Crack Length & 13 mm [0.5 in.] Hole Diameter

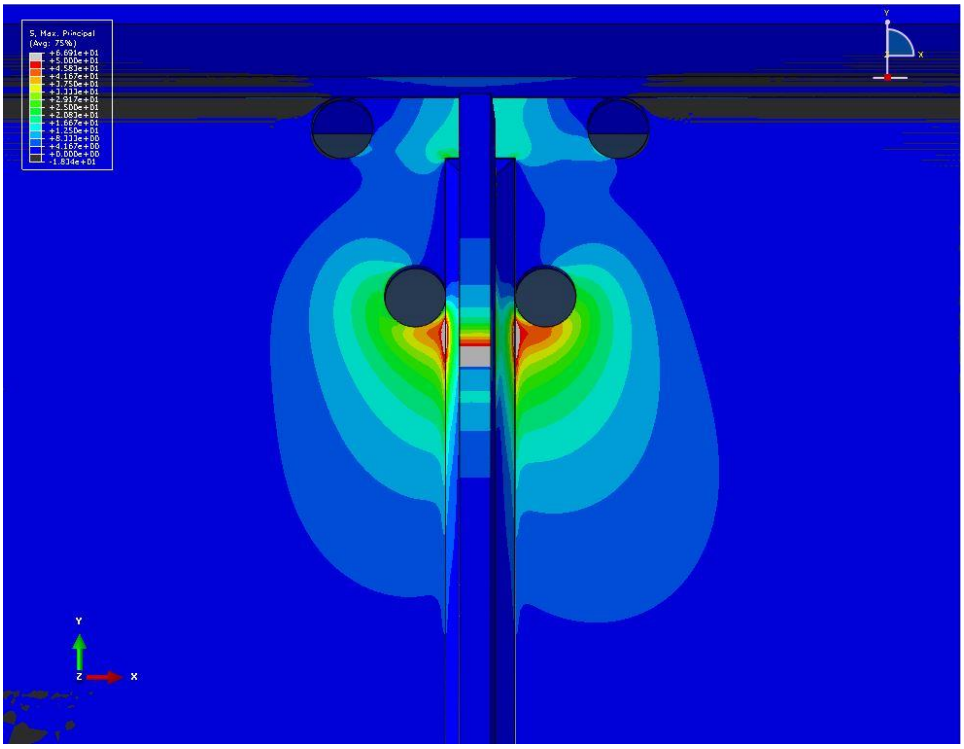

CHSS-1 = 290 Mpa [42.1 ksi]
CHSS-2 = 56.5 Mpa [8.20 ksi]
HSS-1 = 314 Mpa [45.6 ksi]
HSS-2 = 98.6 Mpa [14.3 ksi]

Figure C. 3: 70 mm [2.75 in.] Crack Length & 25 mm [1.0 in.] Hole Diameter

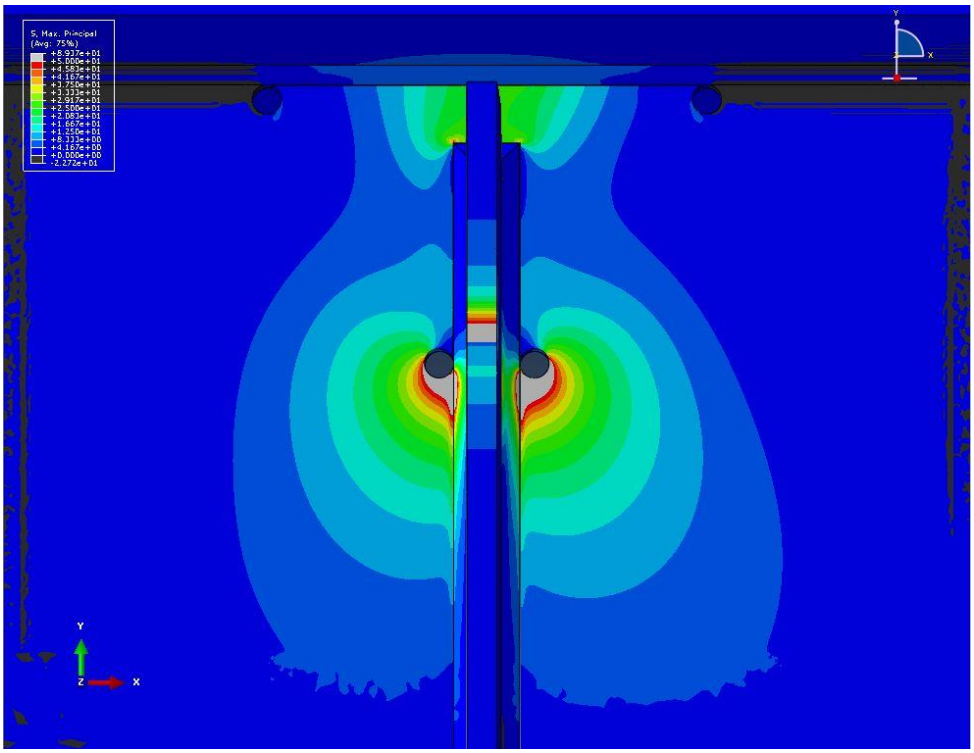

CHSS-1 = 379 Mpa [54.9 ksi]
CHSS-2 = 20.7 Mpa [3.0 ksi]
HSS-1 = 554 Mpa [80.4 ksi]
HSS-2 = 178 Mpa [25.8 ksi]

Figure C. 4: 102mm [4.0 in.] Crack Length & 13 mm [0.5 in.] Hole Diameter

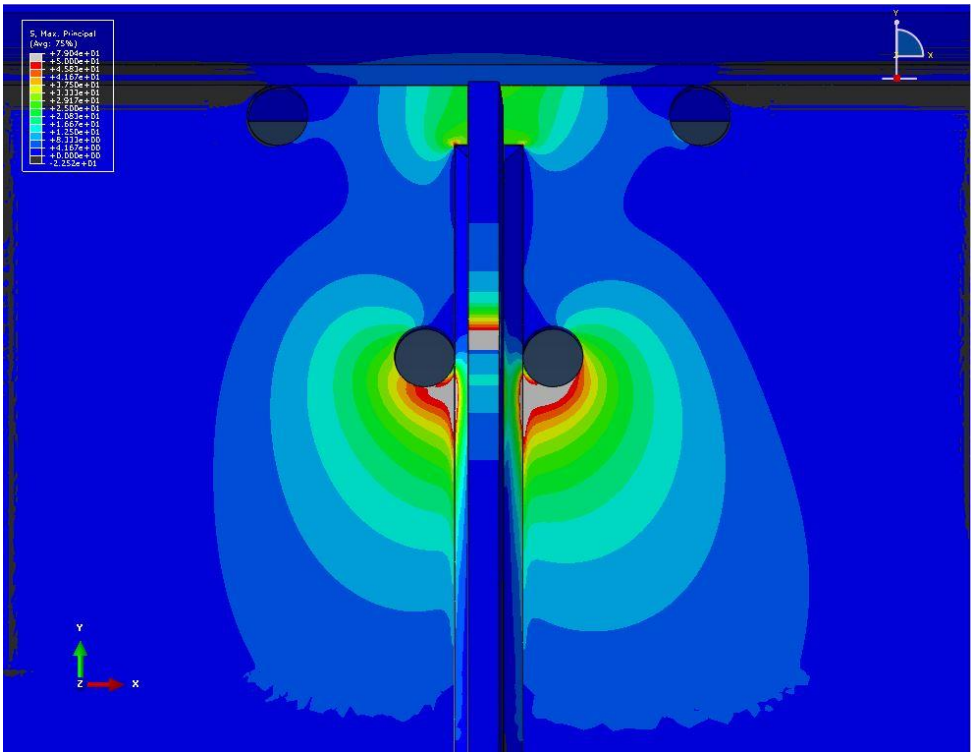

CHSS-1 = 356 Mpa [51.7 ksi]
CHSS-2 = 32.4 Mpa [4.7 ksi]
HSS-1 = 382 Mpa [55.4 ksi]
HSS-2 = 172 Mpa [25.0 ksi]

Figure C. 5: 102 mm [4.0 in.] Crack Length &25 mm [1.0 in.] Hole Diameter

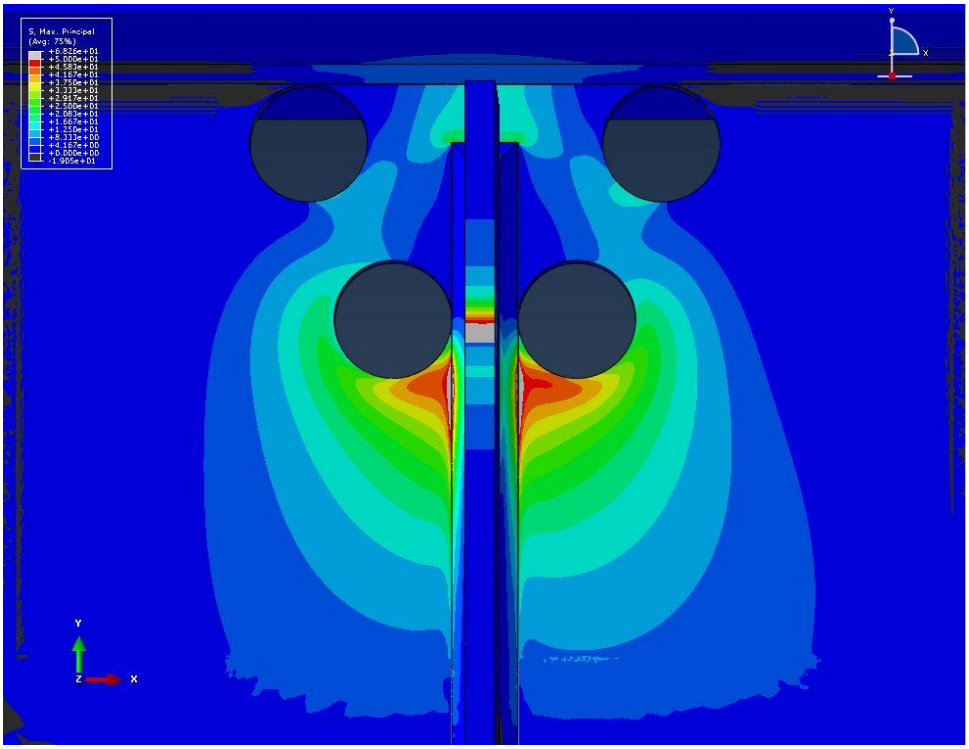

CHSS-1 = 307 Mpa [44.5 ksi]

CHSS-2 = 77.2 Mpa [11.2 ksi]

HSS-1 = 319 Mpa [46.2 ksi]

HSS-2 = 100 Mpa [14.5 ksi]

Figure C. 6: 102mm [4.0 in.] Crack Length & 51 mm [2.0 in.] Hole Diameter

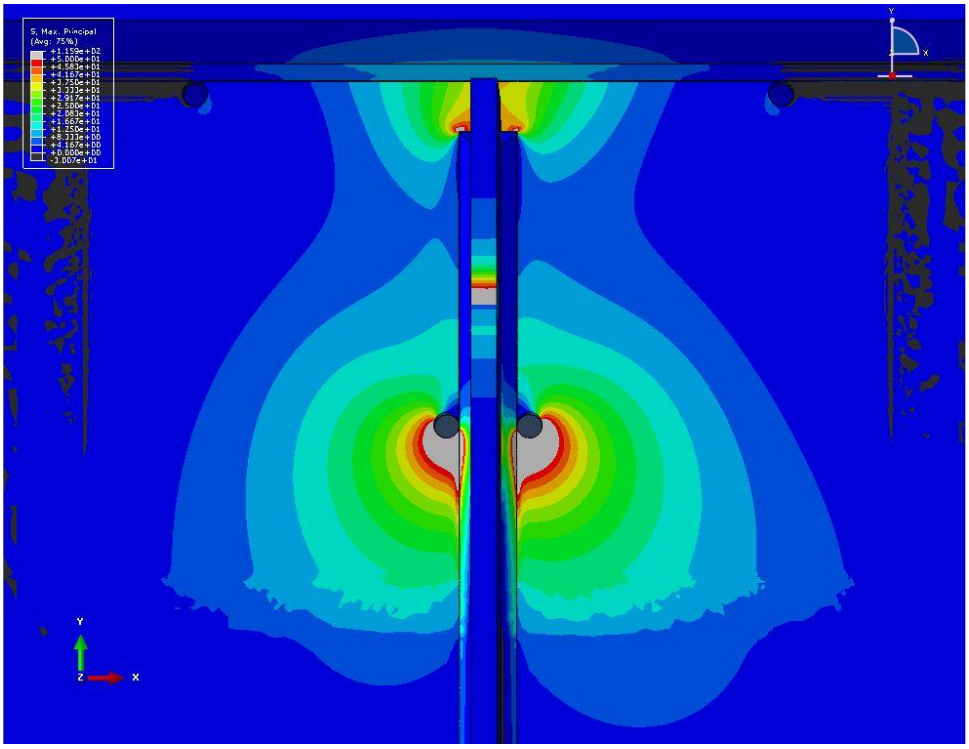

CHSS-1 = 501 Mpa [72.6 ksi]

CHSS-2 = 29.6 Mpa [4.3 ksi]

HSS-1 = 748 Mpa [109 ksi]

HSS-2 = 259 Mpa [37.5 ksi]

Figure C. 7: 152 mm [6 in.] Crack Length & 13 mm [0.5 in.] Hole Diameter

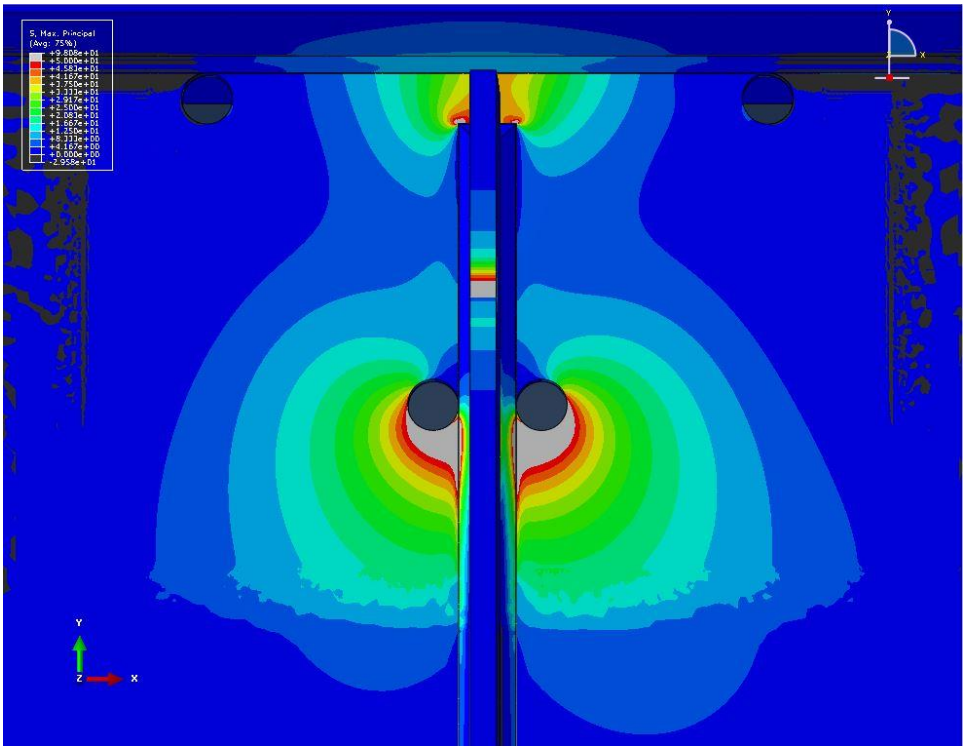

CHSS-1 = 461 Mpa [66.8 ksi]
CHSS-2 = 22.1 Mpa [3.2 ksi]
HSS-1 = 488 Mpa [70.8 ksi]
HSS-2 = 267 Mpa [38.7 ksi]

Figure C. 8: 152 mm [6 in.] Crack Length & 25 mm [1.0 in.] Hole Diameter

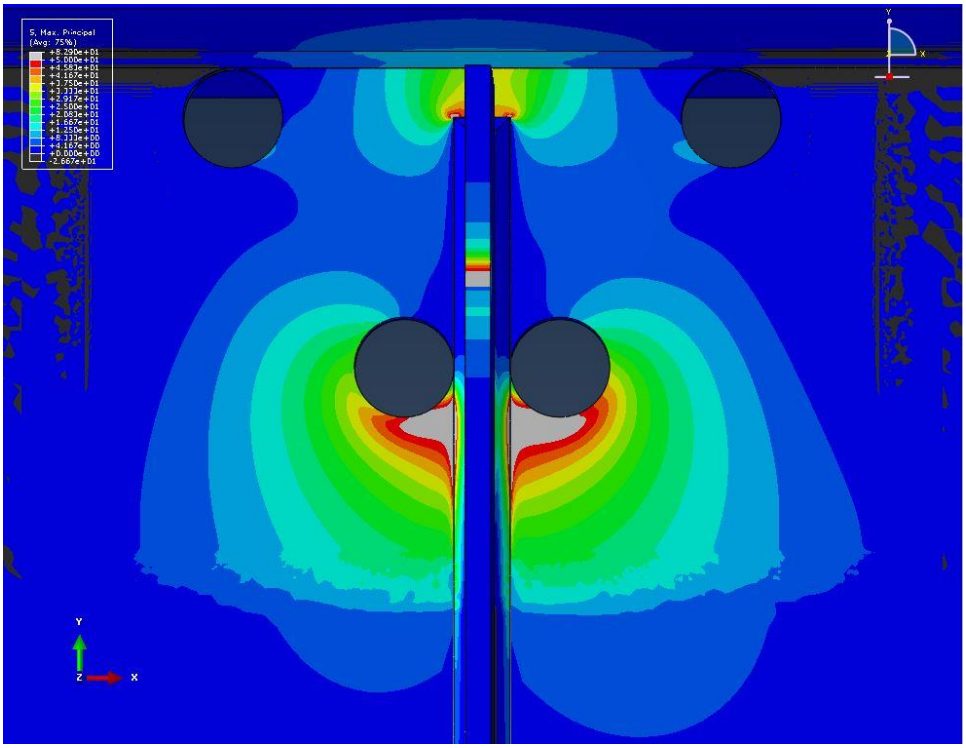

CHSS-1 = 385 Mpa [55.9 ksi]
CHSS-2 = 52.4 Mpa [7.6 ksi]
HSS-1 = 394 Mpa [57.1 ksi]
HSS-2 = 244 Mpa [35.4 ksi]

Figure C. 9: 152 mm [6 in.] Crack Length & 51 mm [2.0 in.] Hole Diameter

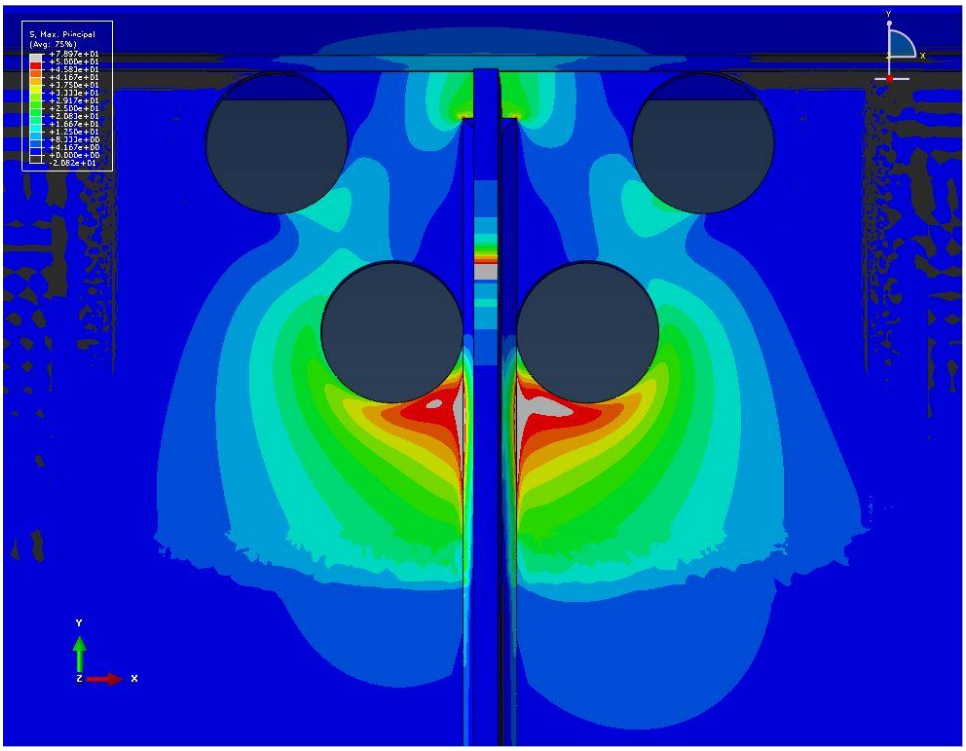

CHSS-1 = 346 Mpa [50.2 ksi]

CHSS-2 = 100 Mpa [14.5 ksi]

HSS-1 = 349 Mpa [50.6 ksi]

HSS-2 = 161 Mpa [23.3 ksi]

Figure C. 10: 152 mm [6 in.] Crack Length & 76 mm [3.0 in.] Hole Diameter

APPENDIX D: MAXIMUM PRINCIPAL STRESS AROUND CRACK-ARREST HOLES FOR WEB-TO-FLANGE CRACK TYPE

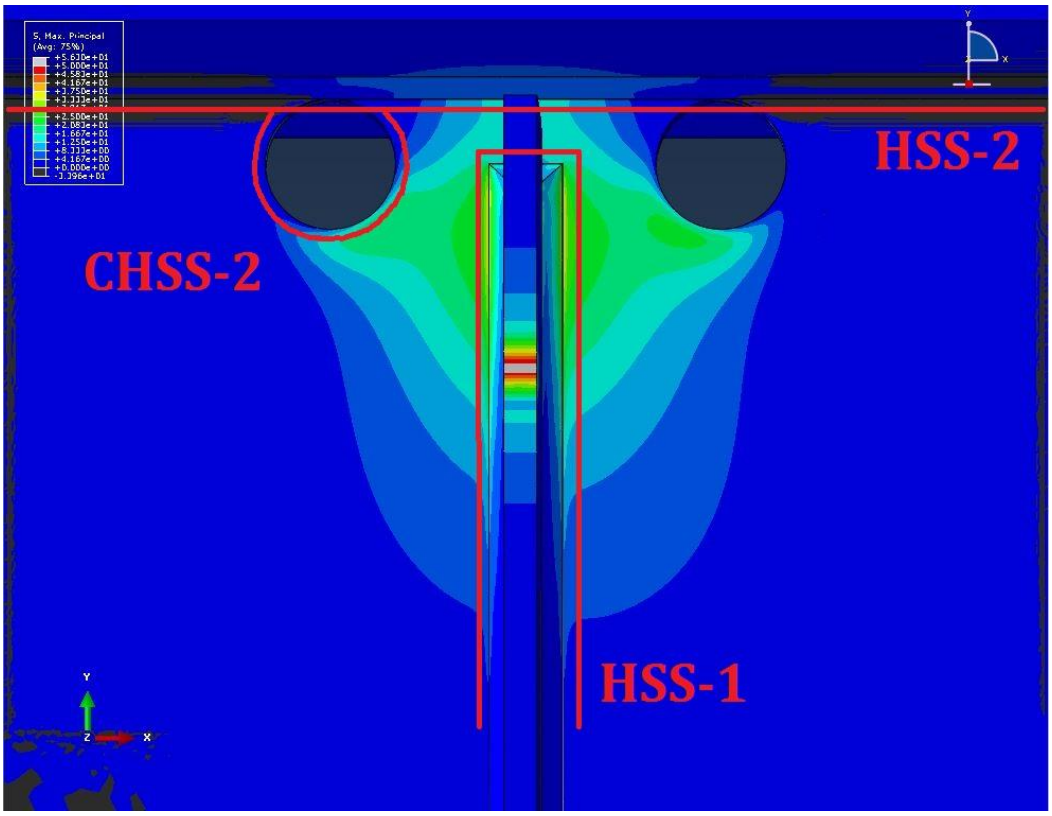

Figure D. 1: Hot Spot Stress Paths for Web-To-Flange Crack Type

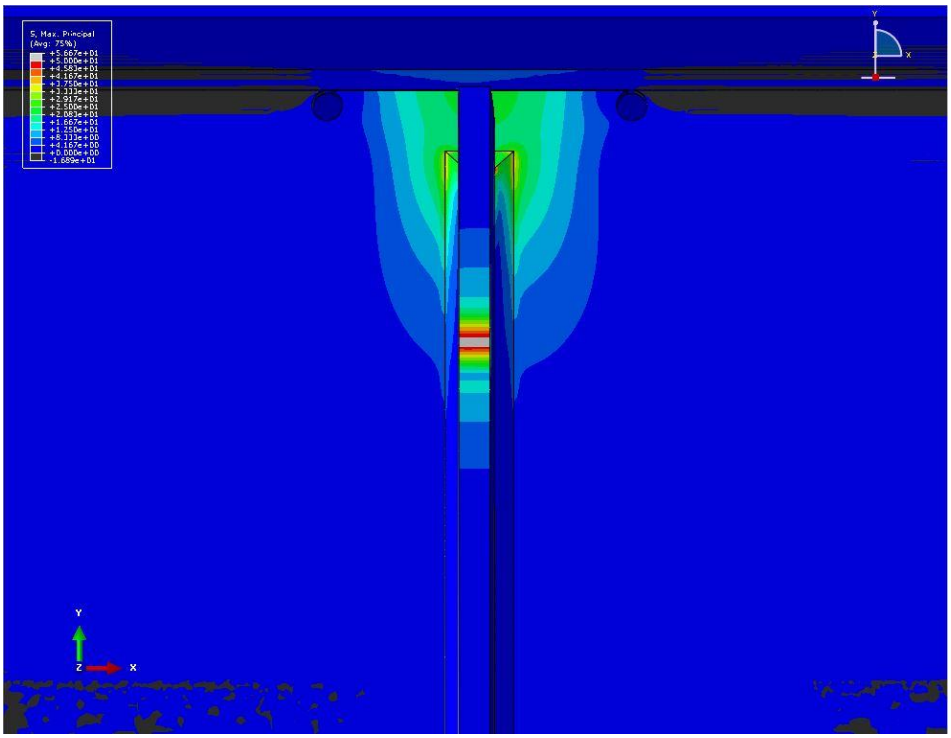

CHSS-2 = 16.2 Mpa [2.35 ksi]

HSS-1 = 141 Mpa [20.4 ksi]

HSS-2 = 154 Mpa [22.3 ksi]

Figure D. 2: 140mm [5.5 in.] Crack Length & 13 mm [0.5 in.] Hole Diameter

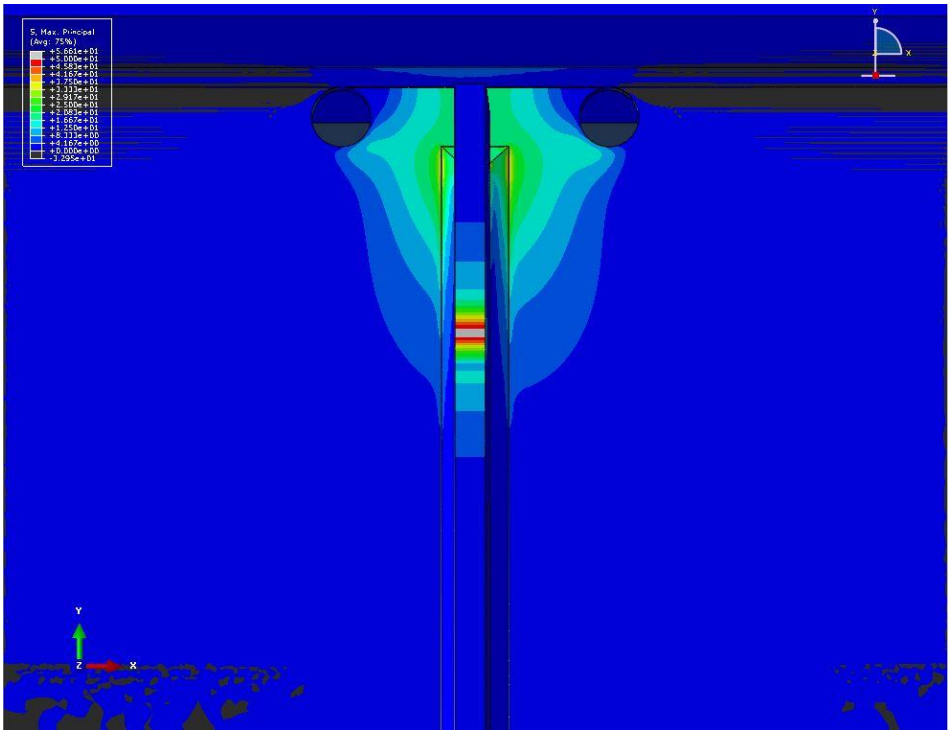

CHSS-2 = 88.1 Mpa [12.78 ksi]

HSS-1 = 147 Mpa [21.3 ksi]

HSS-2 = 129 Mpa [18.7 ksi]

Figure D. 3: 140mm [5.5 in.] Crack Length & 25 mm [1.0 in.] Hole Diameter

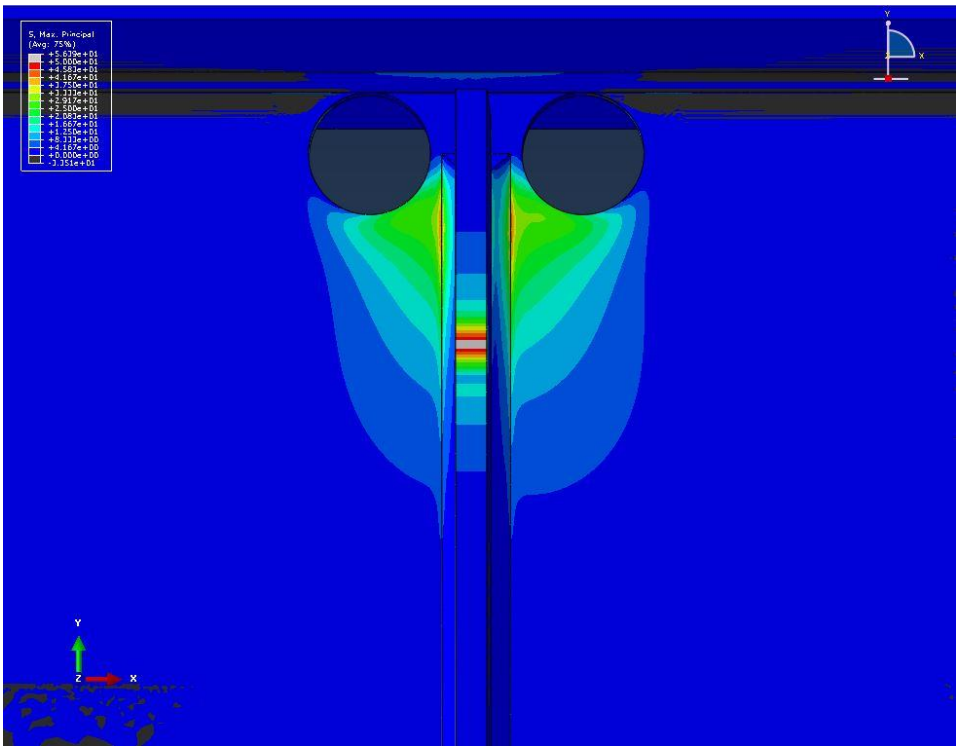

CHSS-2 = 192 Mpa [27.86 ksi]

HSS-1 = 203 Mpa [29.5 ksi]

HSS-2 = 7.58 Mpa [1.10 ksi]

Figure D. 4: 140 mm [5.5 in.] Crack Length & 51 mm [2.0 in.] Hole Diameter

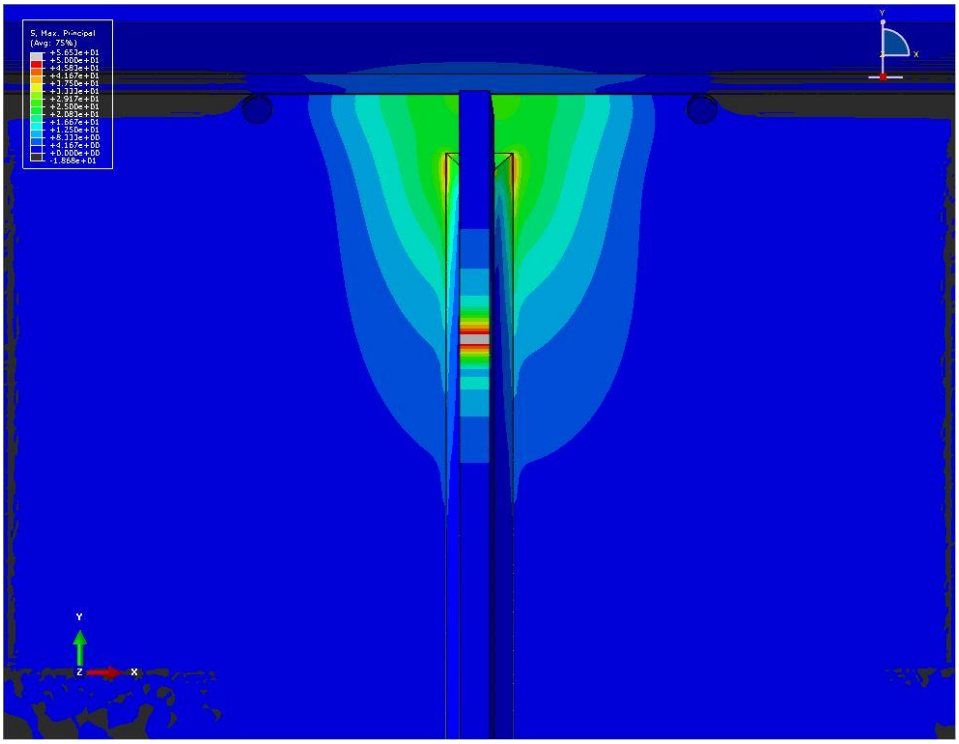

CHSS-2 = 1.72 Mpa [0.25 ksi]

HSS-1 = 179 Mpa [26.0 ksi]

HSS-2 = 179 Mpa [25.9 ksi]

Figure D. 5: 203 mm [8 in.] Crack Length & 13 mm [0.5 in.] Hole Diameter

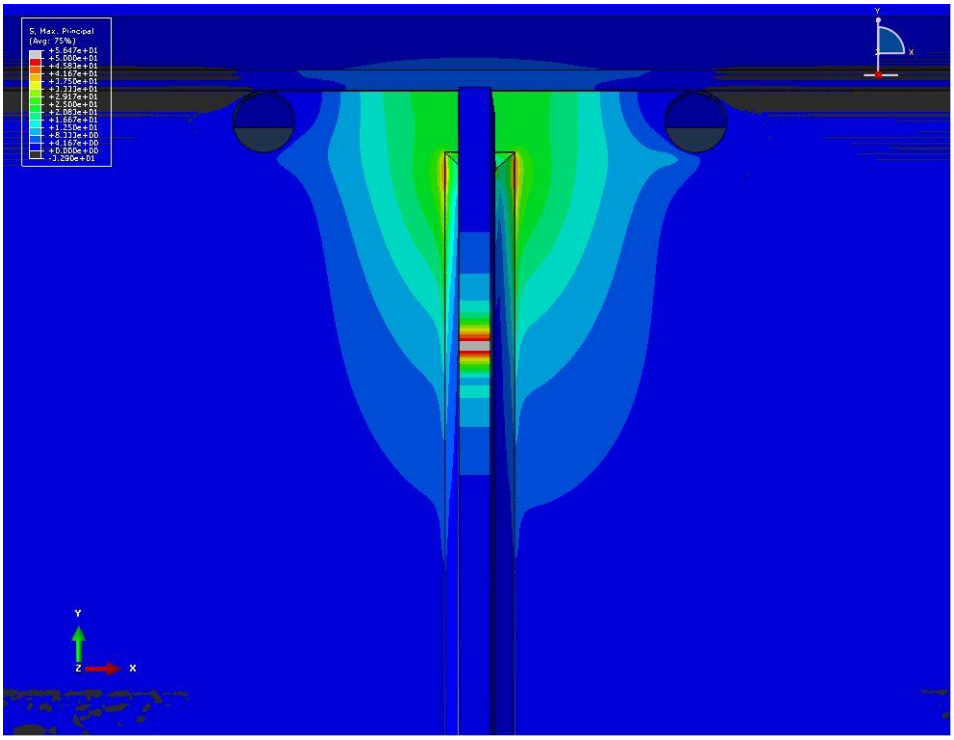

CHSS-2 = 41.4 Mpa [6.0 ksi]

HSS-1 = 180 Mpa [26.1 ksi]

HSS-2 = 168 Mpa [24.4 ksi]

Figure D. 6: 203 mm [8 in.] Crack Length & 25 mm [1.0 in.] Hole Diameter

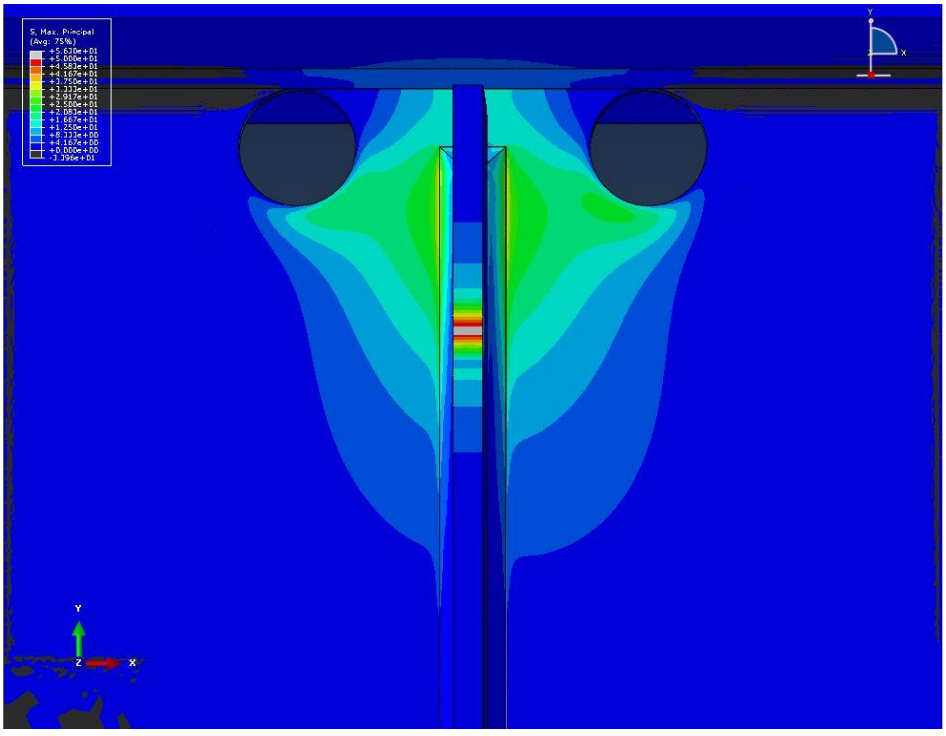

CHSS-2 = 141 Mpa [20.48 ksi]

HSS-1 = 169 Mpa [24.5 ksi]

HSS-2 = 93.1 Mpa [13.5 ksi]

Figure D. 7: 203 mm [8 in.] Crack Length & 51 mm [2.0 in.] Hole Diameter

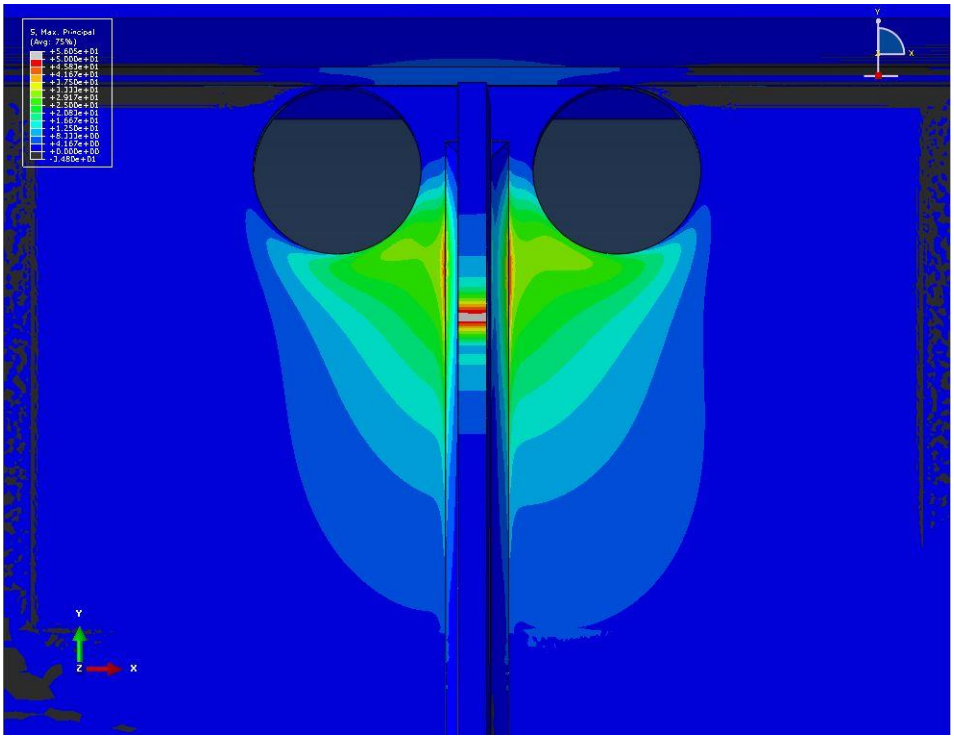

CHSS-2 = 205 Mpa [29.67 ksi]

HSS-1 = 212 Mpa [30.8 ksi]

HSS-2 = 4.48 Mpa [0.65 ksi]

Figure D. 8: 203 mm [8 in.] Crack Length & 76 mm [3.0 in.] Hole Diameter

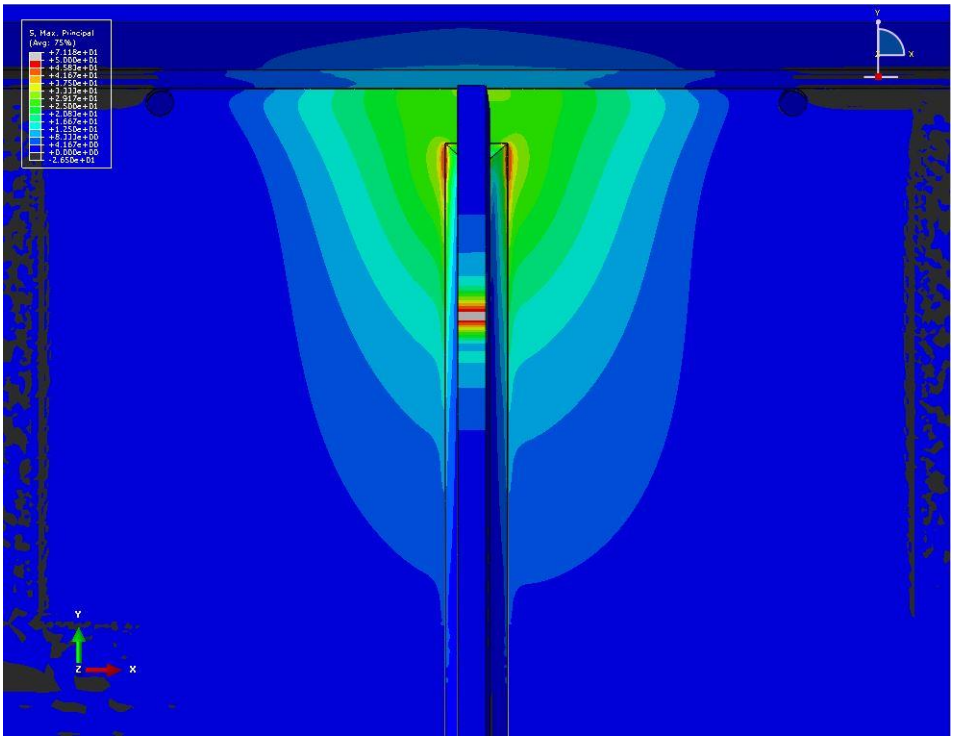

CHSS-2 = 2.21 Mpa [0.32 ksi]

HSS-1 = 219 Mpa [31.8 ksi]

HSS-2 = 201 Mpa [29.13 ksi]

Figure D. 9: 305 mm [12 in.] Crack Length & 13 mm [0.5 in.] Hole Diameter

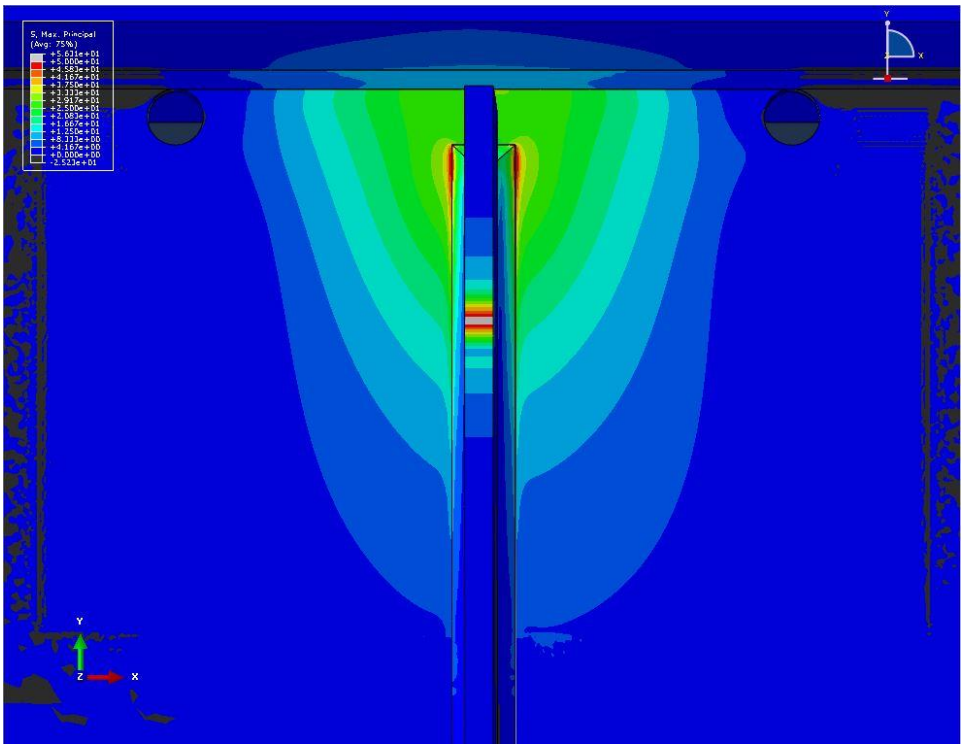

CHSS-2 = 4.34 Mpa [0.63 ksi]

HSS-1 = 220 Mpa [31.9 ksi]

HSS-2 = 199 Mpa [28.83 ksi]

Figure D. 10: 305 mm [12 in.] Crack Length & 25 mm [1.0 in.] Hole Diameter

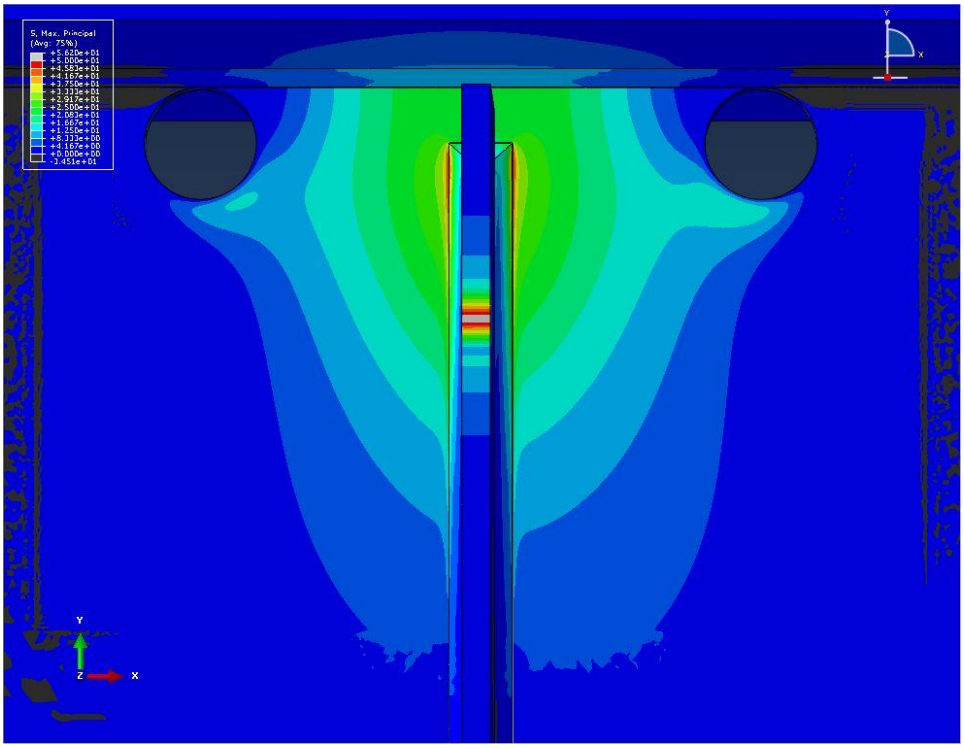

CHSS-2 = 88 Mpa [12.76 ksi]

HSS-1 = 205 Mpa [29.7 ksi]

HSS-2 = 167 Mpa [24.16 ksi]

Figure D. 11: 305 mm [12 in.] Crack Length & 51 mm [2.0 in.] Hole Diameter

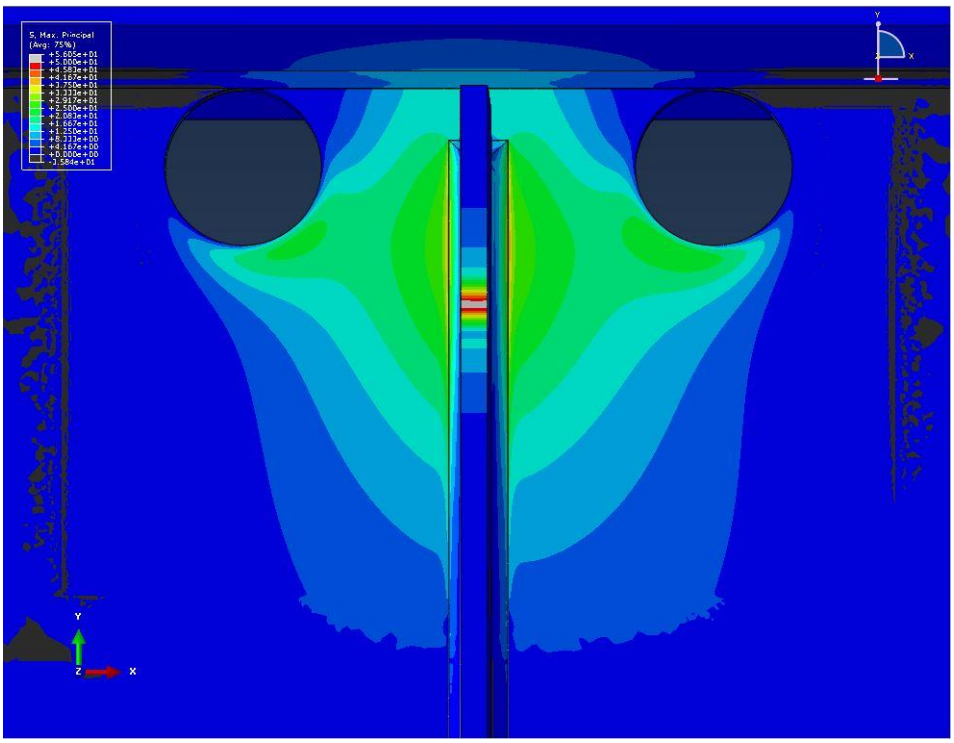

CHSS-2 = 151 Mpa [21.91 ksi]

HSS-1 = 188 Mpa [27.3 ksi]

HSS-2 = 102 Mpa [14.79 ksi]

Figure D. 12: 305 mm [12 in.] Crack Length & 76 mm [3.0 in.] Hole Diameter

APPENDIX E: MAXIMUM PRINCIPAL STRESS AROUND CRACK-ARREST HOLES FOR LARGE-HOLE RETROFIT

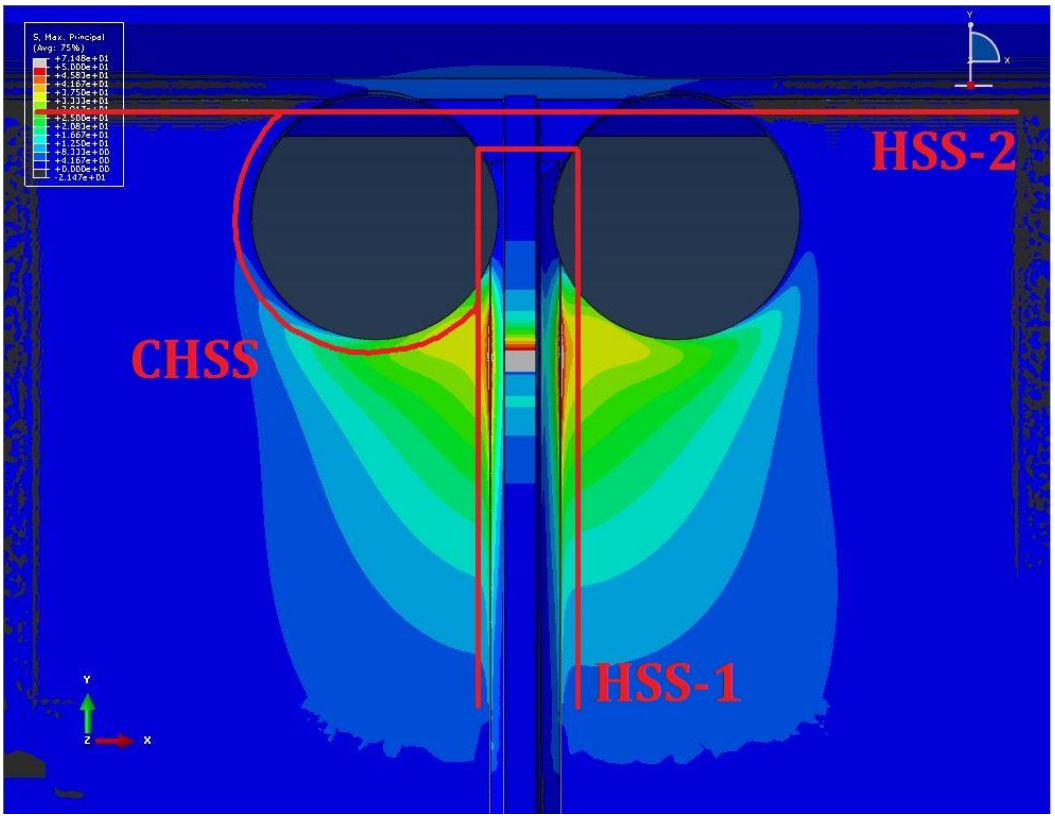

Figure E. 1: Hot Spot Stress Paths for Large-hole Retrofit Model

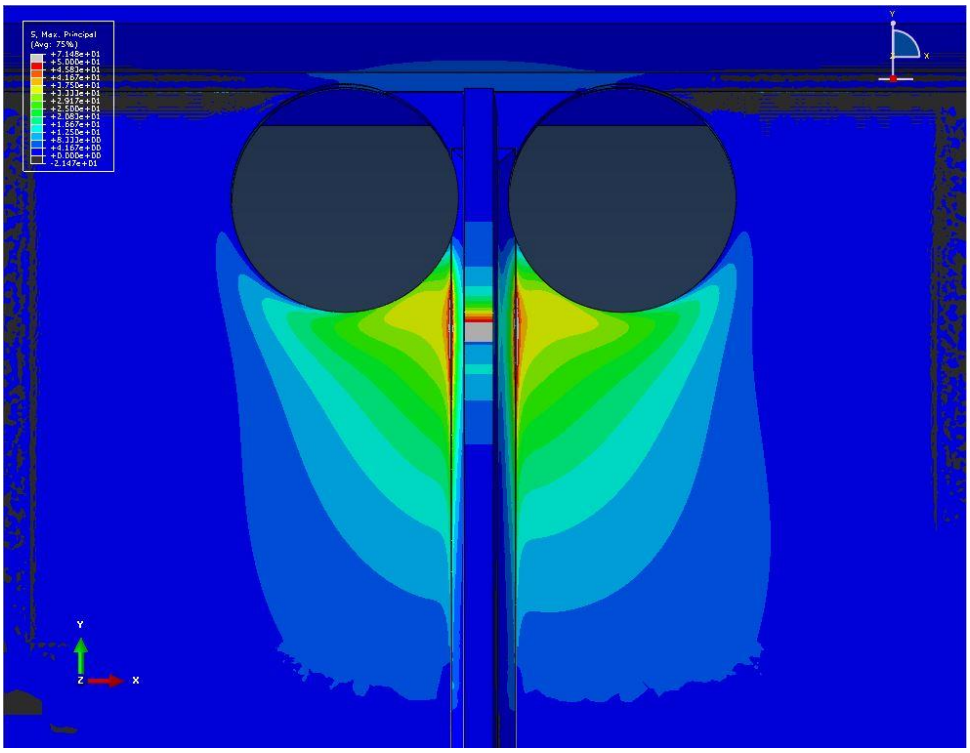

CHSS = 245 Mpa [35.6 ksi]
HSS-1 = 256 Mpa [37.1 ksi]
HSS-2 = 0.717 Mpa [0.10 ksi]

Figure E. 2: Web-To-Flange Crack with 102 mm [4.0 in.] Hole Diameter

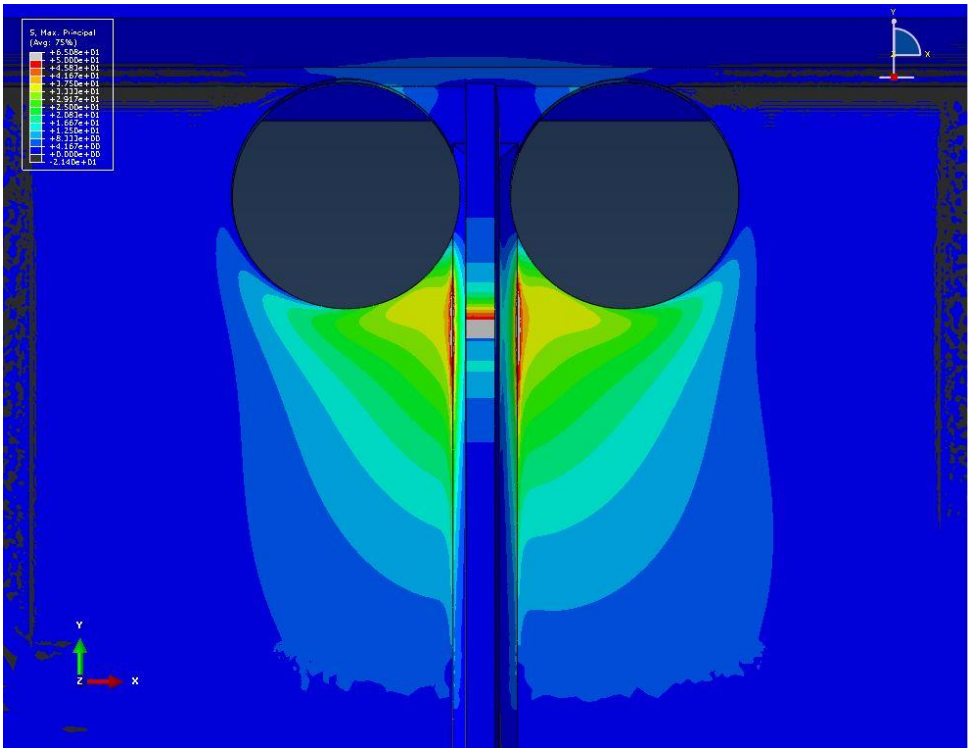

CHSS = 245 Mpa [35.6 ksi]
HSS-1 = 255 Mpa [37.0 ksi]
HSS-2 = 50.7 Mpa [7.35 ksi]

Figure E. 3:Horseshoe-Shaped Crack with 102 mm [4.0 in.] Hole Diameter

APPENDIX F: LAB NOTES RECORDED DURING TESTING CRACK-ARREST HOLES

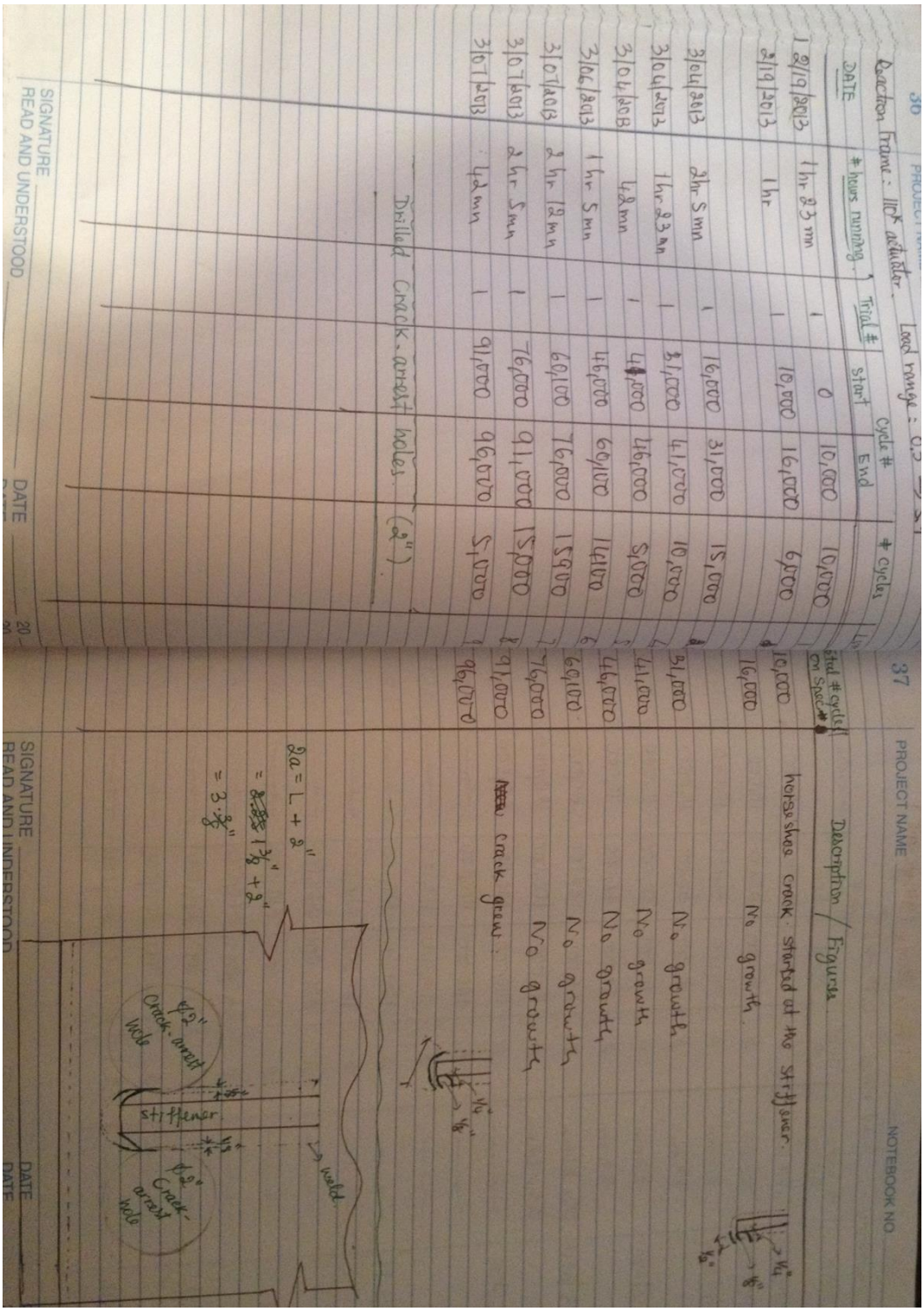

38 PROJECT NAME Hot

Continued. Load range : 0.7K -> 5.3K

DATE	# hours testing	Trial #	Cycle# Start	Cycle# End	# cycles	total cycles on spec.
1 4/05/2013	83mn	8	97,467	107,467	10,000	107,467
4/05/2013	83mn	2	10,000	20,000	10,000	117,467
4/11/2013	83mn	2	20,000	30,000	10,000	127,467
	83mn	2	30,000	40,000	10,000	137,467
4/12/2013	83mn	2	40,000	50,000	10,000	147,467
	83mn	2	50,000	60,000	10,000	157,467
4/15/2013	2hr 46mn	2	60,000	80,000	20,000	177,467
	8hr 46mn	2	80,000	100,000	20,000	197,467
4/16/2013	—	2	100,000	120,000	20,000	217,467
	—	2	120,000	140,000	—	237,467
	—	2	140,000	160,000	—	257,467
4/17/2013	—	2	160,000	180,000	—	277,467
	—	2	180,000	200,000	—	297,467
	—	2	200,000	220,000	—	317,467
4/18/2013	—	2	220,000	240,000	—	337,467
	—	2	240,000	260,000	—	357,467
4/19/2013	—	2	260,000	280,000	—	377,467
	—	2	280,000	300,000	—	397,467
4/23/2013	—	2	300,000	320,000	—	417,467

SIGNATURE _____ DATE _____ 20

39 PROJECT NAME _____ NOTEBOOK NO _____

Description / Figures

No growth.

SIGNATURE _____ DATE _____
READ AND UNDERSTOOD _____ DATE _____

42 PROJECT NAME Pool Fluid Study (Sft. Spec #5) NOTEBOOK NO.

Continued....

DATE	# hrs Testing	Trial #	Cycles Start	Cycles End	# cycles	Total cycles on spec
5/01/2013	2hr 46mn	2	515,000	535,000	20,000	28
	2hr 46mn	2	535,000	555,000	20,000	29
5/02/2013	2hr 46mn	2	555,000	575,000	20,000	30
5/02/2013	2hr 46mn	2	575,000	595,000	20,000	31
5/03/2013	2hr 46mn	2	595,000	615,000	20,000	32
5/06/2013	2hr 46mn	2	615,000	635,000	20,000	33
5/06/2013	4h 10mn	2	635,000	665,000	30,000	34
5/07/2013	2hr 46mn	2	665,000	685,000	20,000	35
	〃	2	685,000	705,000	〃	36
5/08/2013	〃	2	705,000	725,000	〃	37
	〃	2	725,000	745,000	〃	38

SIGNATURE DATE 20

DATE 20

43 PROJECT NAME NOTEBOOK NO.

Total cycles on spec

Descriptions / Figures

No growth

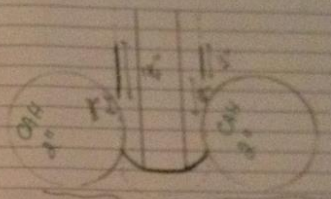

the crack on the right of stiffener grew to 9/16"

The left crack grew to 1 5/8", the right crack grew to 5/8" downwards

The left crack grew to 1 5/8"

The left is 1 3/4" with which is 1/8" from CSH

The right is 3/4" which is 7/8" above CSH

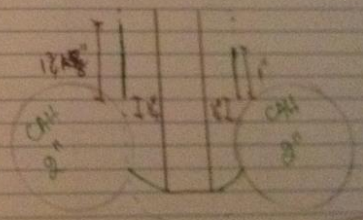

No additional growth

grew! see figure on next

SIGNATURE DATE 20

READ AND UNDERSTOOD DATE 20

48

PROJECT NAME Pool Fund Study (gft-spec #5) NOTEBOOK NO.

Date	Trial #	cycle start	cycle End	# cycles	Lion file
6/16/2013	3	190,000	210,000	20,000	(15)
6/17/2013	3	210,000	230,000	〃	
6/18/2013	3	230,000	250,000	〃	
6/19/2013	3	250,000	270,000	〃	
6/20/2013	3	270,000	300,000	30,000	
6/21/2013	3	300,000	330,000	30,000	
6/21/2013	3	330,000	360,000	30,000	
6/24/2013	3	360,000	390,000	30,000	
6/26/2013	3	390,000	420,000	〃	

SIGNATURE DATE 20

49

total cycles on spec

Description / Figures

No growth.

Cracks on the fascia side

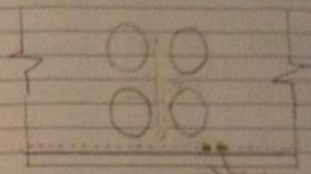

Two horizontal cracks along the weld (Flange-to-web weld) on the right side of fascia side web. The length of the cracks were 1/16"

No growth.

1/16" horizontal crack on left on fascia side about 1/2" from CSH

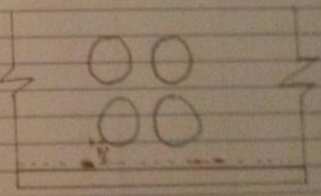

No growth

Two horizontal cracks on stiffener side 0.45" and @ 1/16" long with 0.125 apart.

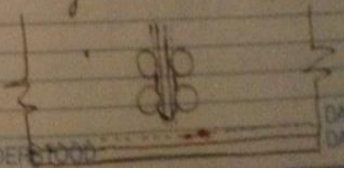

SIGNATURE DATE 20
READ AND UNDER DATE 20

APPENDIX G: CONVERGENCE STUDY FOR J-INTEGRAL, J-INTEGRAL FORM KS, AND K FACTORS FOR THE UNRETROFITTED MODELS WITH 102-MM (4-IN.) TYPE 1 AND 203-MM (8-IN.) TYPE 2CRACKS

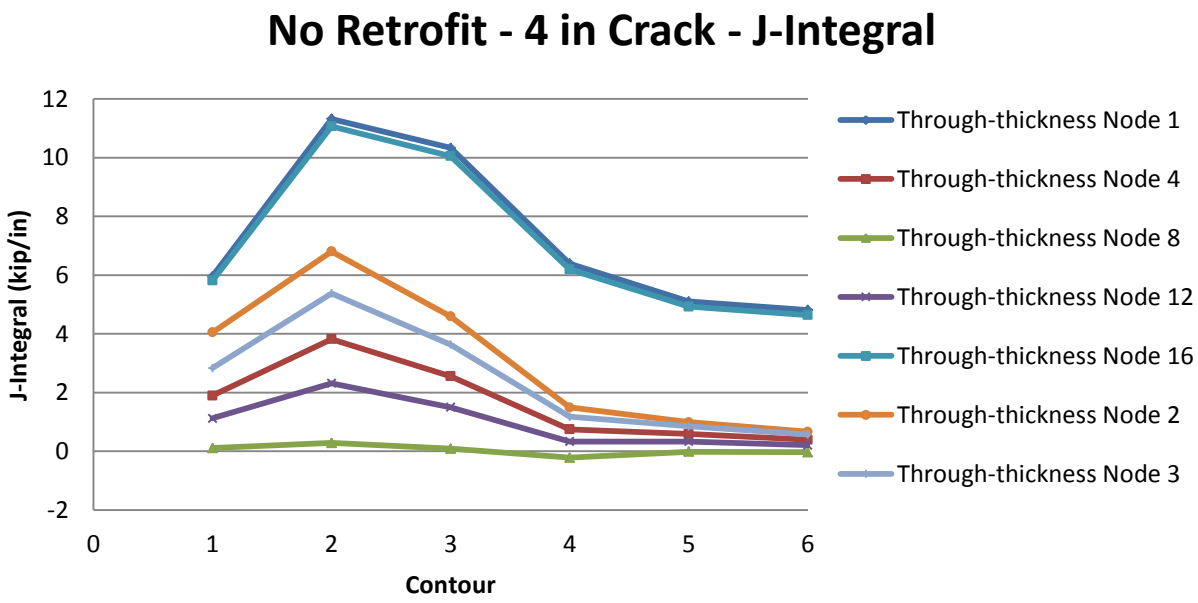

Figure G. 1: Convergence study of J-Integral for 102-mm (4-in.) Type 1 crack

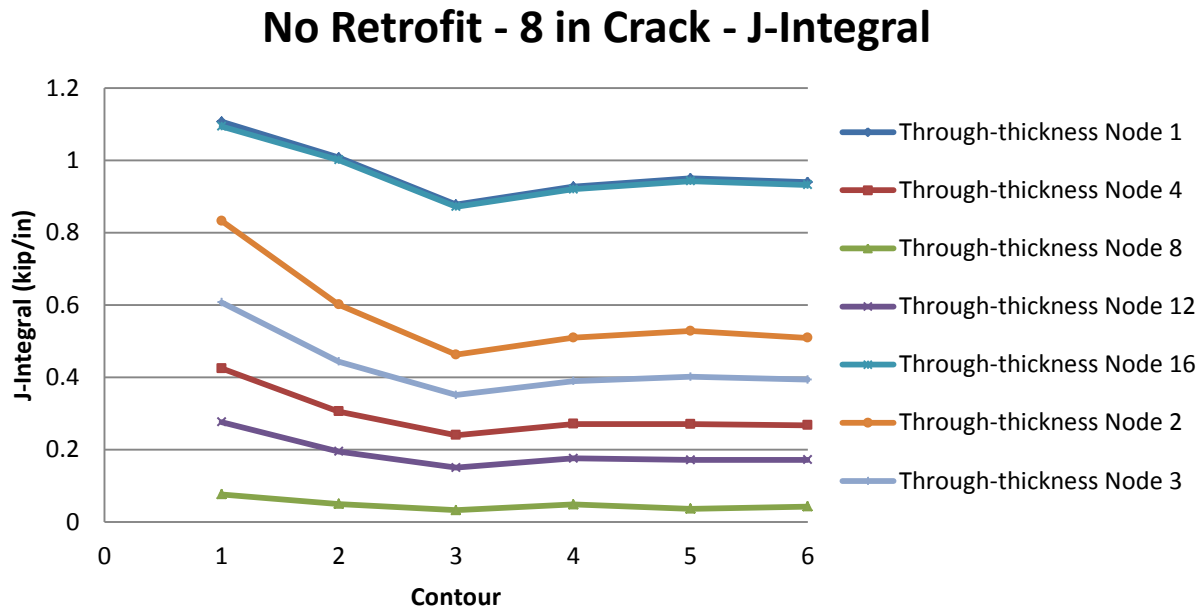

Figure G. 2: Convergence study of J-Integral for 203-mm (8-in.) Type 2 crack

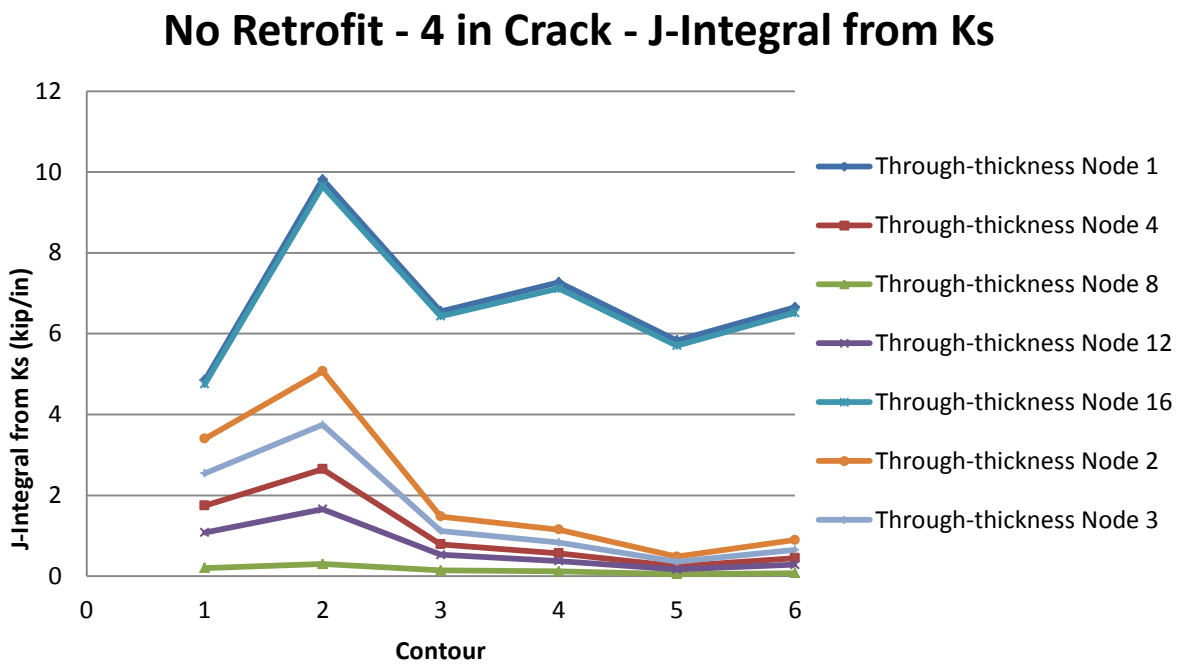

Figure G. 3: Convergence study of J-Integral from Ks for 102-mm (4-in.) Type 1 crack

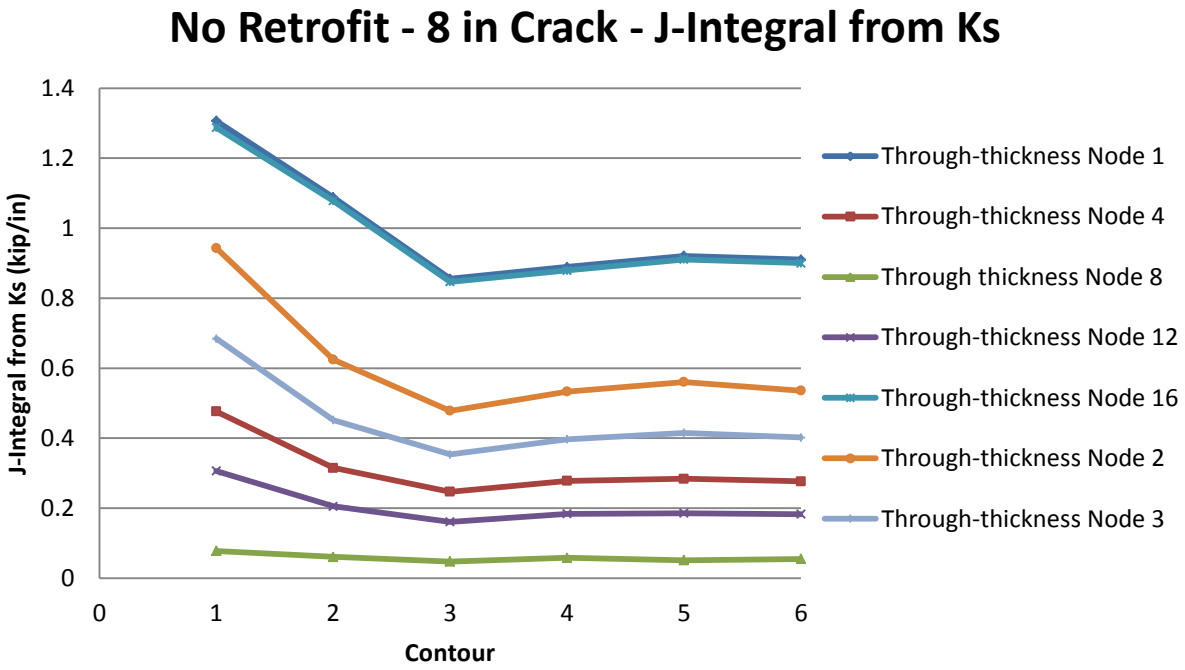

Figure G. 4: Convergence study of J-Integral from Ks for 203-mm (8-in.) Type 2 crack

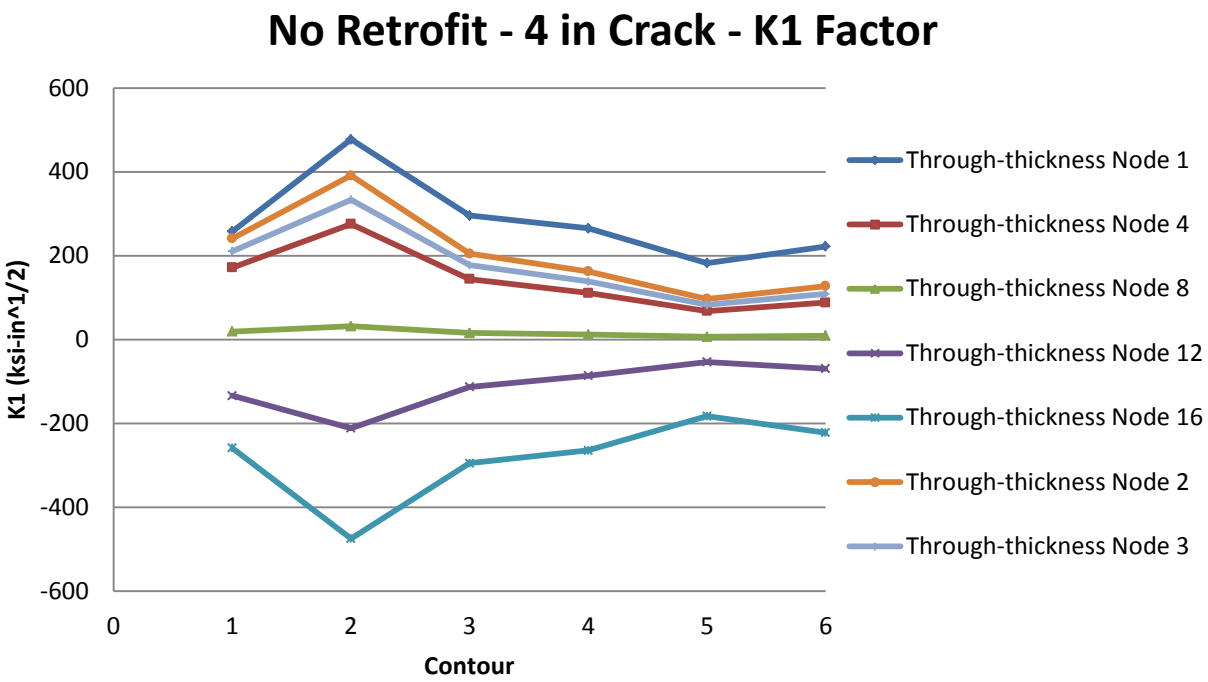

Figure G. 5: Convergence study of K1 factor for 102-mm (4-in.) Type 1 crack

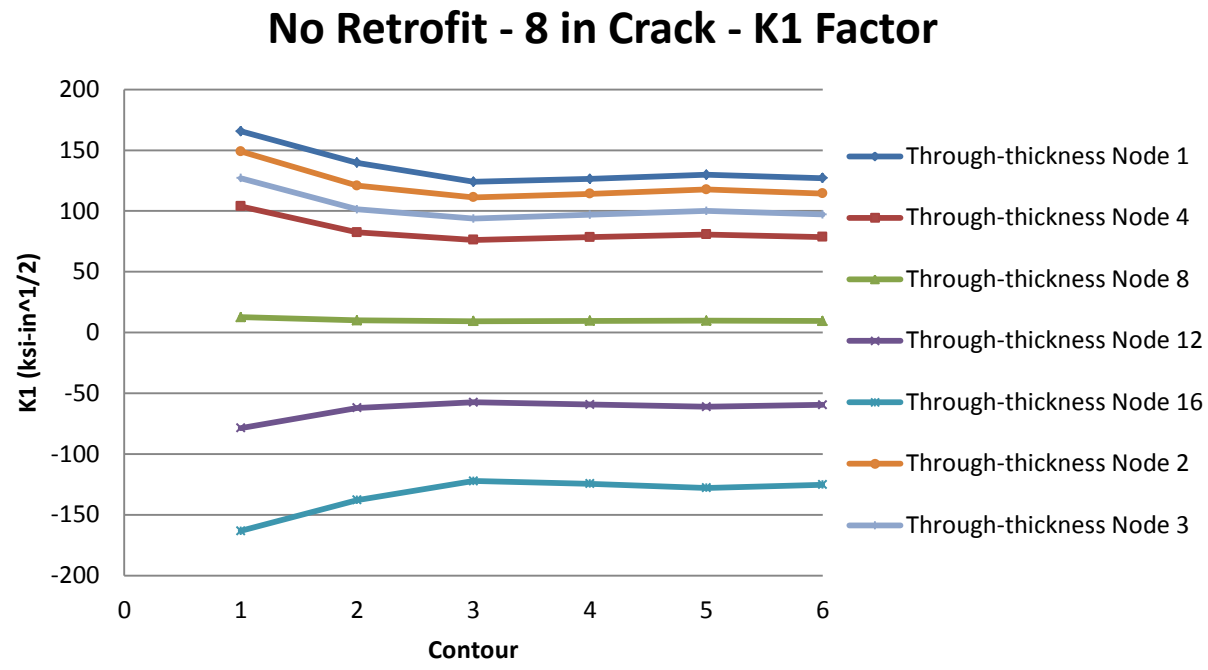

Figure G. 6: Convergence study of K1 factor for 203-mm (8-in.) Type 2 crack

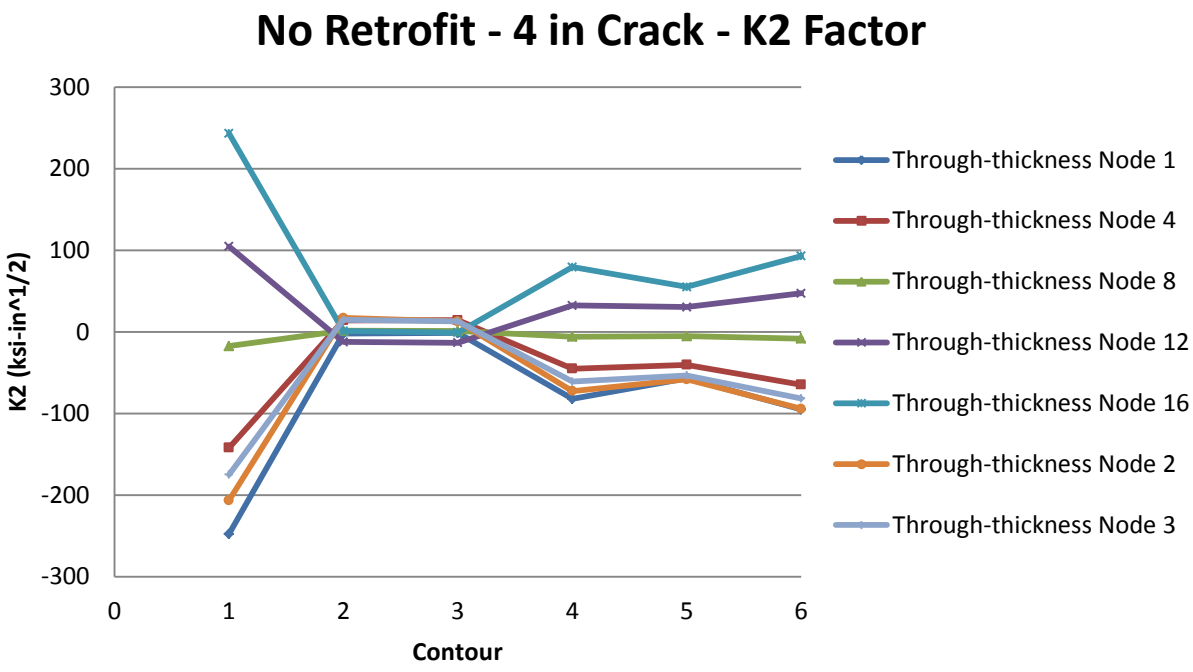

Figure G. 7: Convergence study of K2 factor for 102-mm (4-in.) Type 1 crack

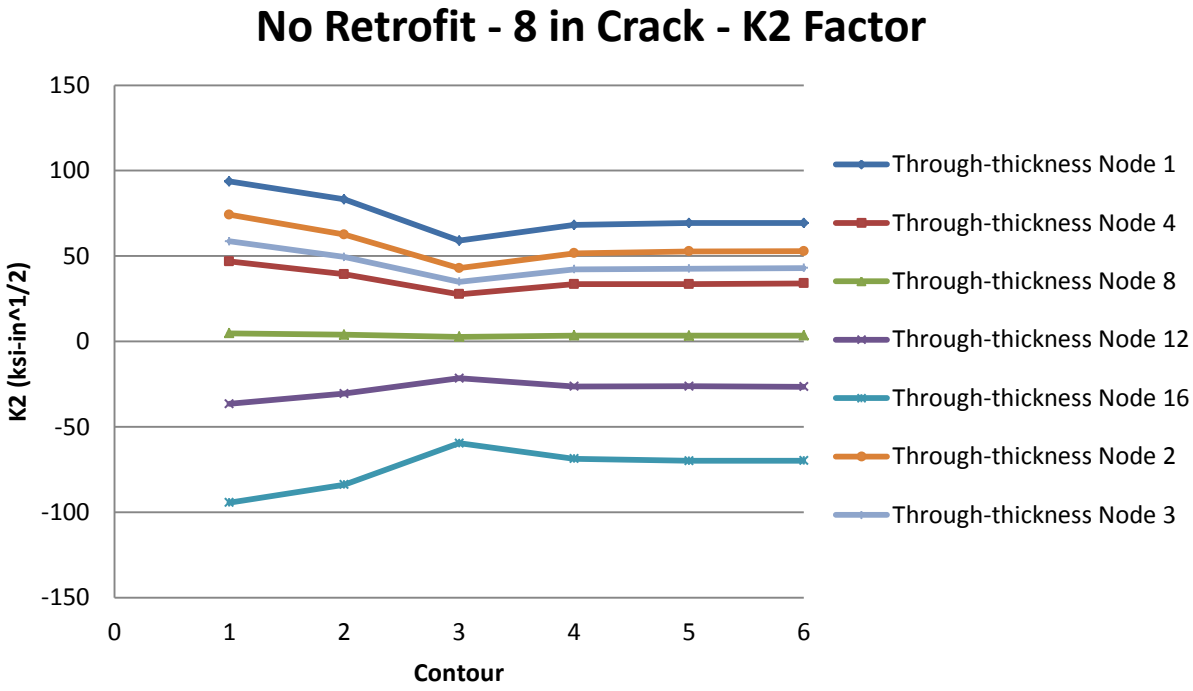

Figure G. 8: Convergence study of K2 factor for 203-mm (8-in.) Type 2 crack

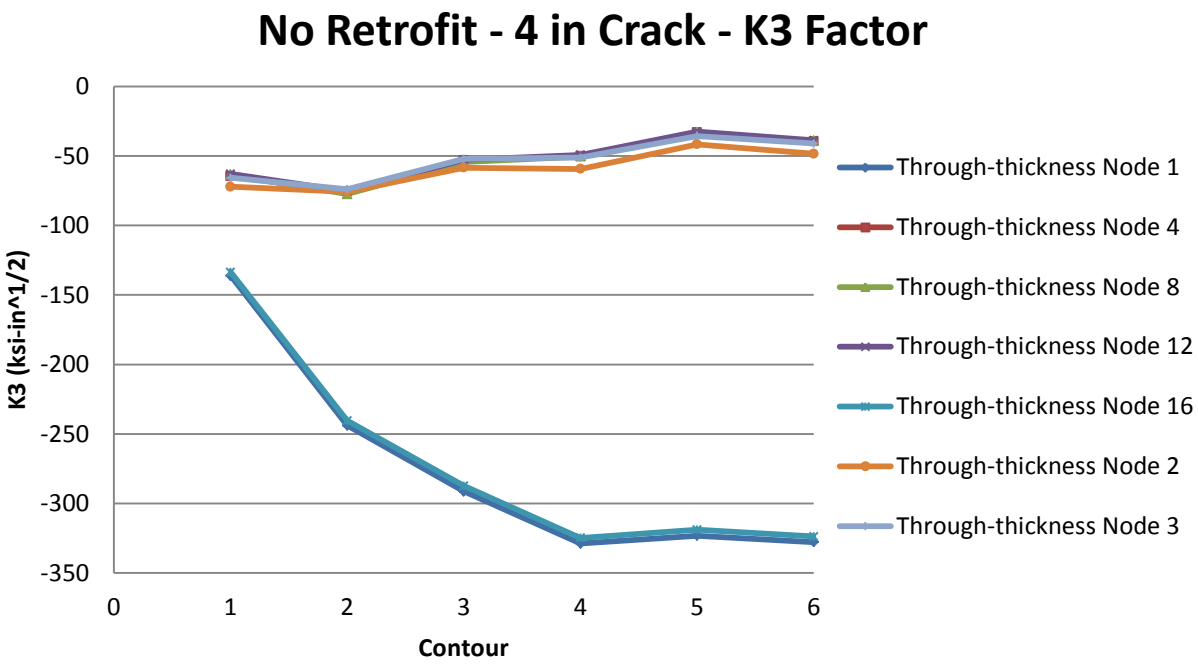

Figure G. 9: Convergence study of K3 factor for 102-mm (4-in.) Type 1 crack

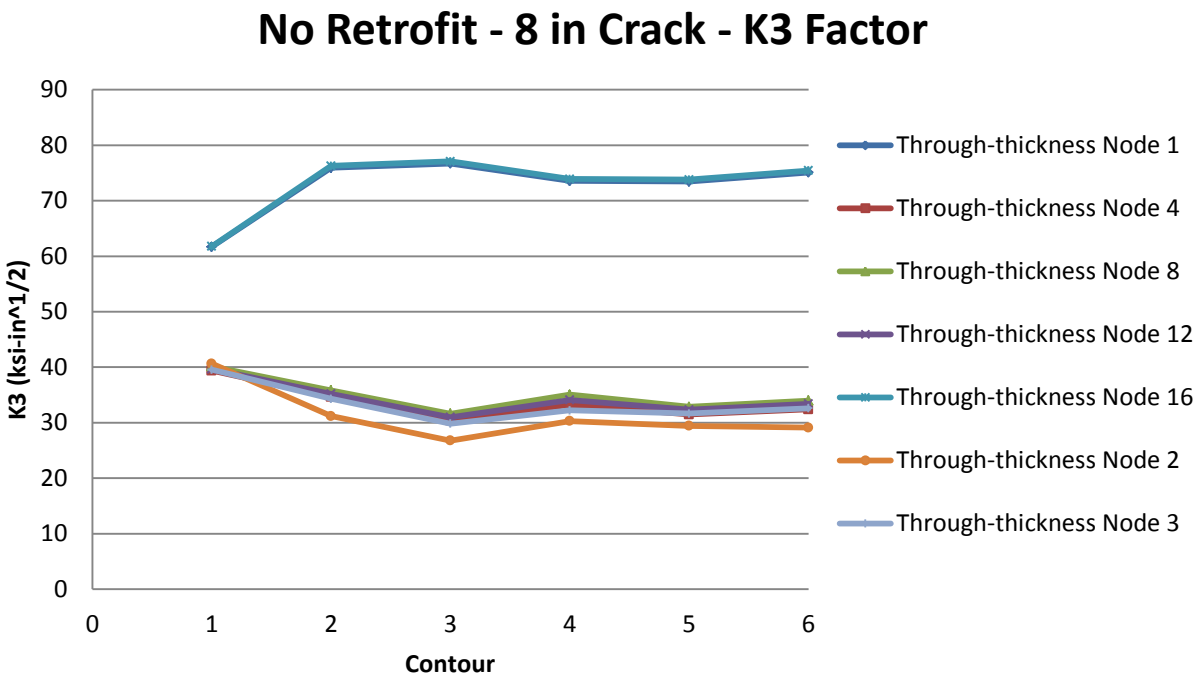

Figure G. 10: Convergence study of K3 factor for 203-mm (8-in.) Type 2 crack

APPENDIX H: MAXIMUM PRINCIPAL STRESS IN THE WEB GAP REGION FOR THE ANGLES-WITH-PLATE RETROFIT MODELS

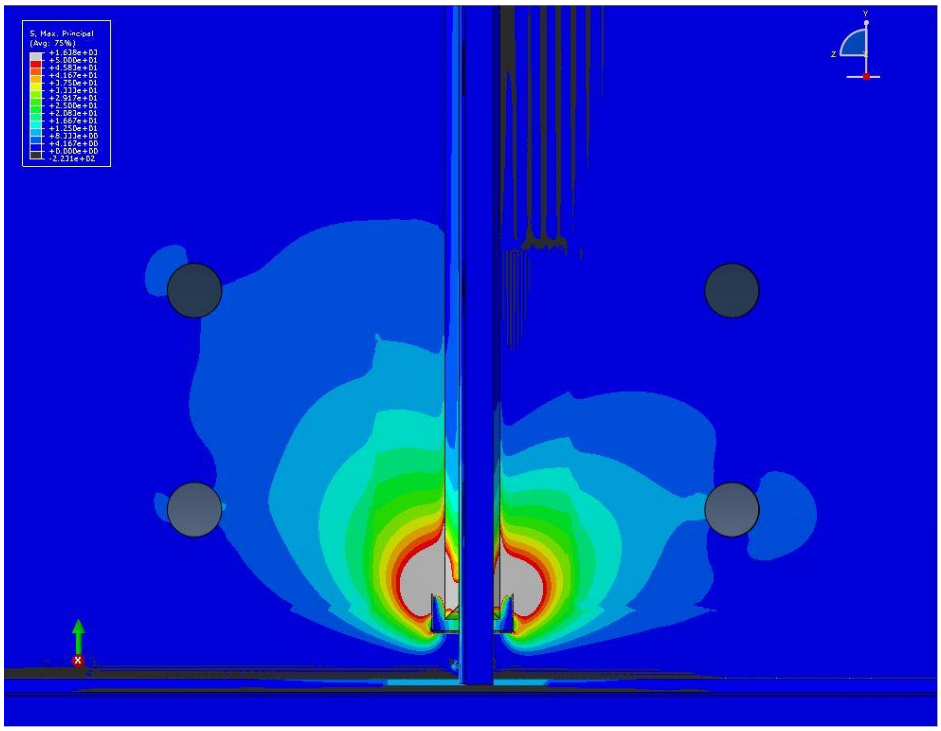

Figure H. 1: 13 mm [1/2 in.] Type 1 Crack &13 mm [1/2 in.] Type 2 Crack with No Retrofit

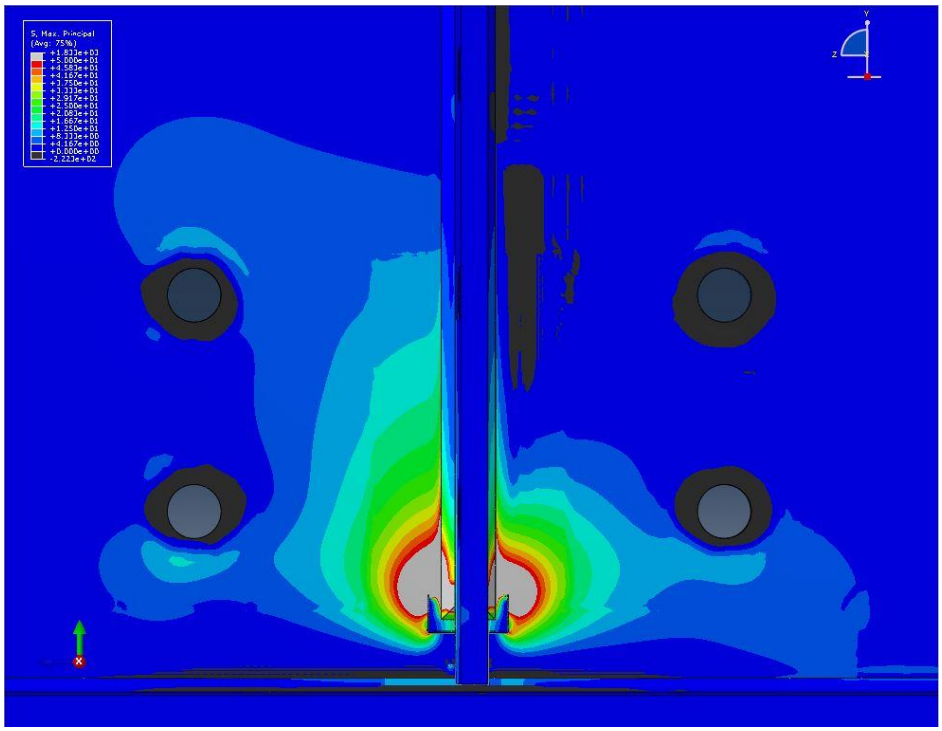

Figure H. 2: 13 mm [1/2 in.] Type 1 Crack & 13 mm [1/2 in.] Type 2 Crack with F-F Retrofit

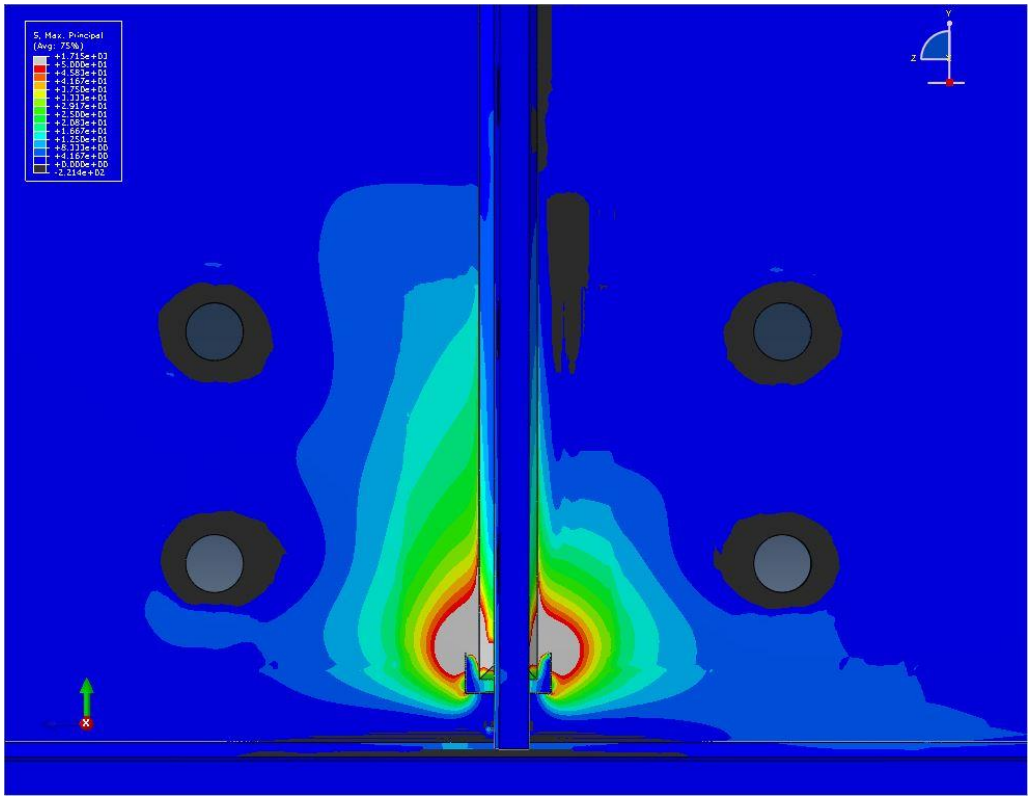

Figure H. 3: 13 mm [1/2 in.] Type 1 Crack & 13 mm [1/2 in.] Type 2 Crack with F-M Retrofit

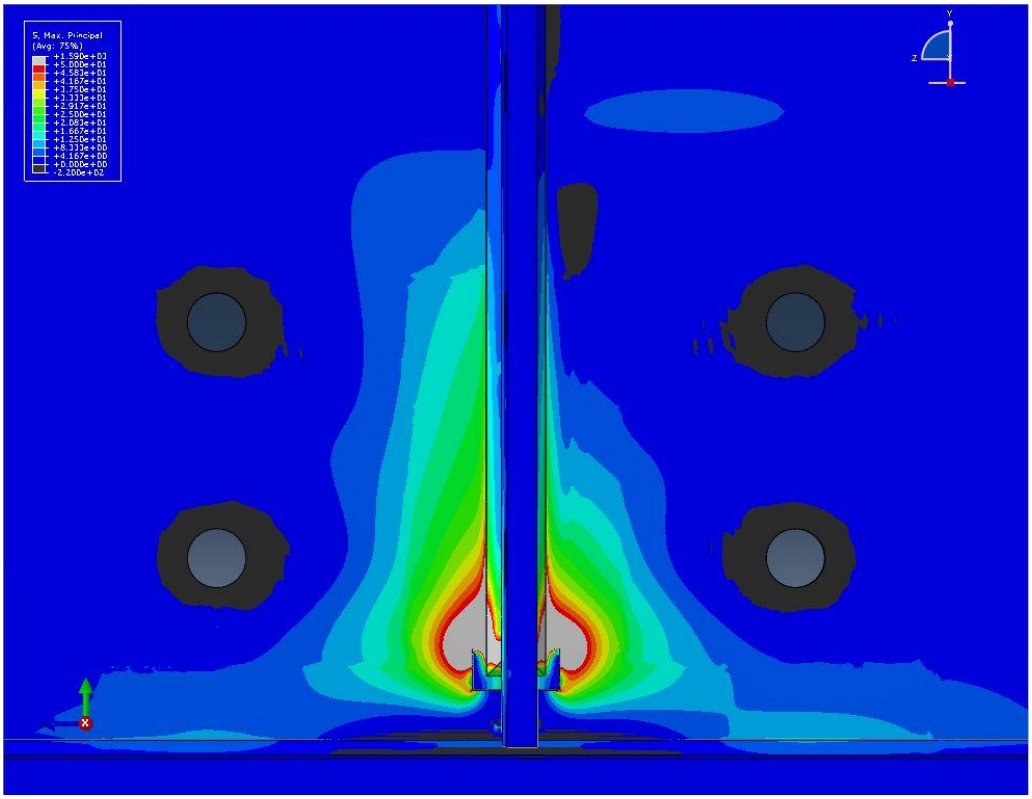

Figure H. 4: 13 mm [1/2 in.] Type 1 Crack & 13 mm [1/2 in.] Type 2 Crack with F-S Retrofit

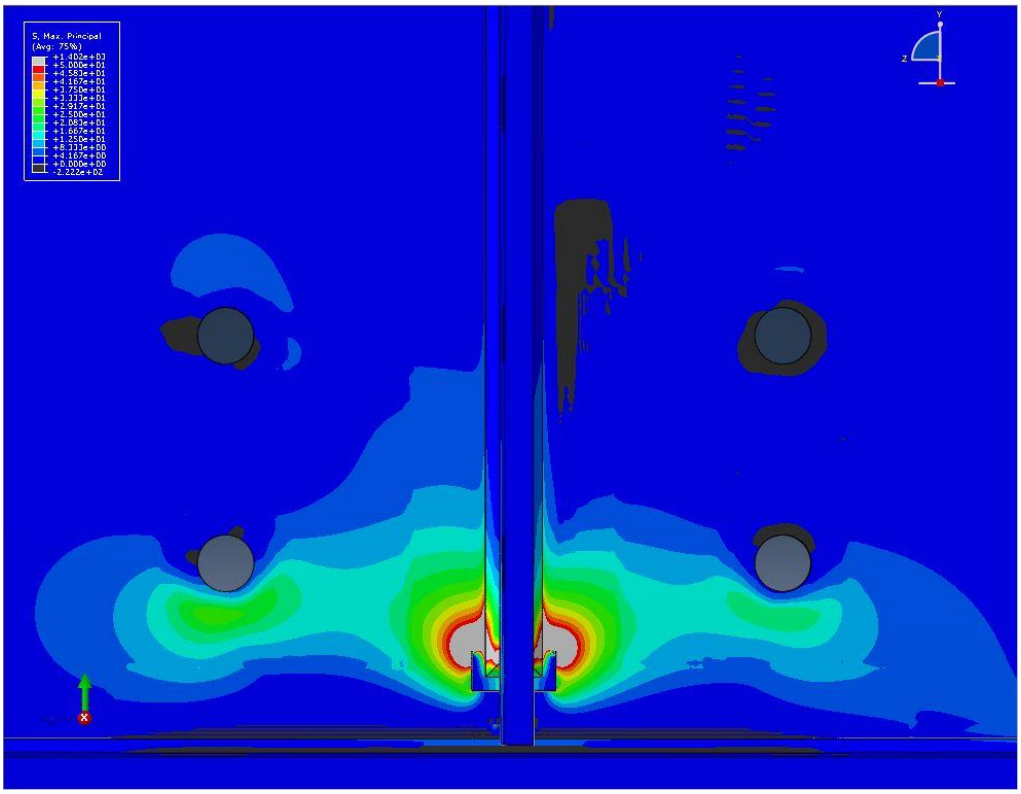

Figure H. 5: 13 mm [1/2 in.] Type 1 Crack & 13 mm [1/2 in.] Type 2 Crack with M-F Retrofit

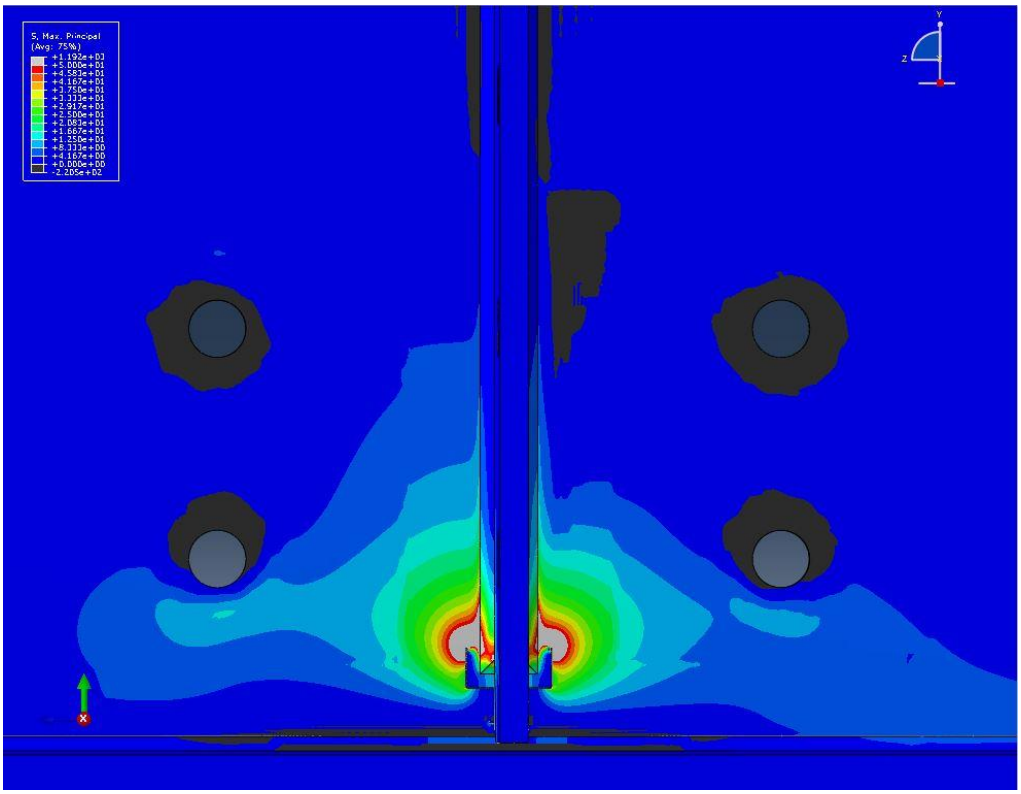

Figure H. 6: 13 mm [1/2 in.] Type 1 Crack & 13 mm [1/2 in.] Type 2 Crack with M-M Retrofit

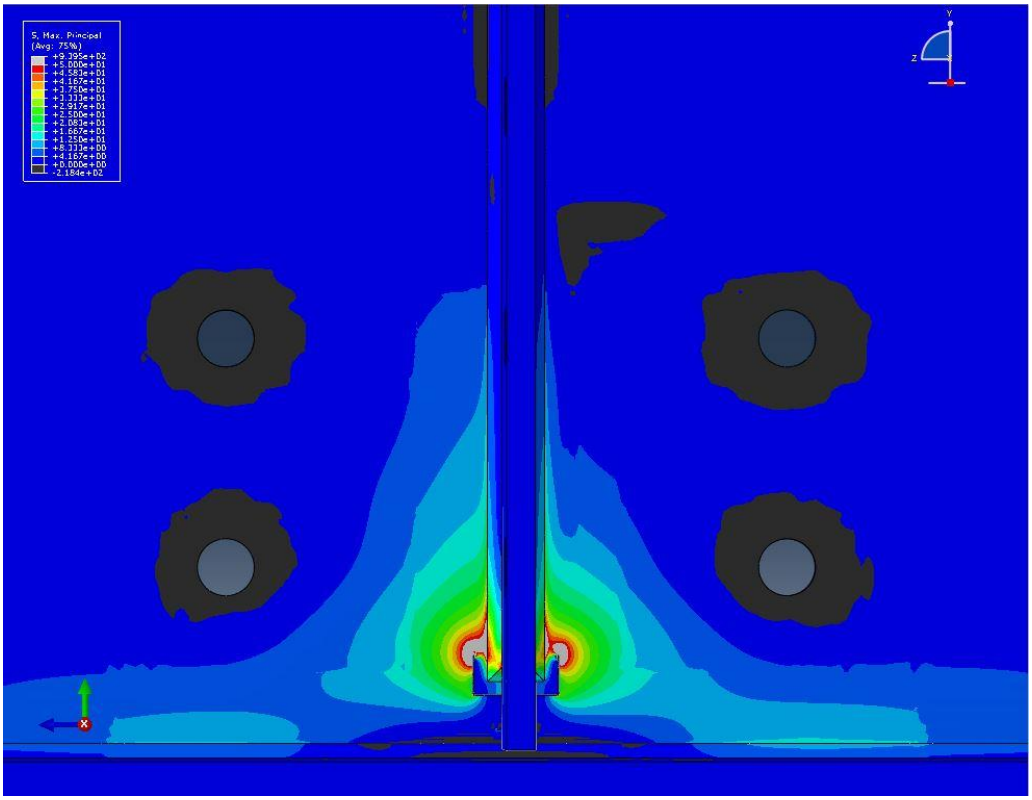

Figure H. 7: 13 mm [1/2 in.] Type 1 Crack & 13 mm [1/2 in.] Type 2 Crack with M-S Retrofit

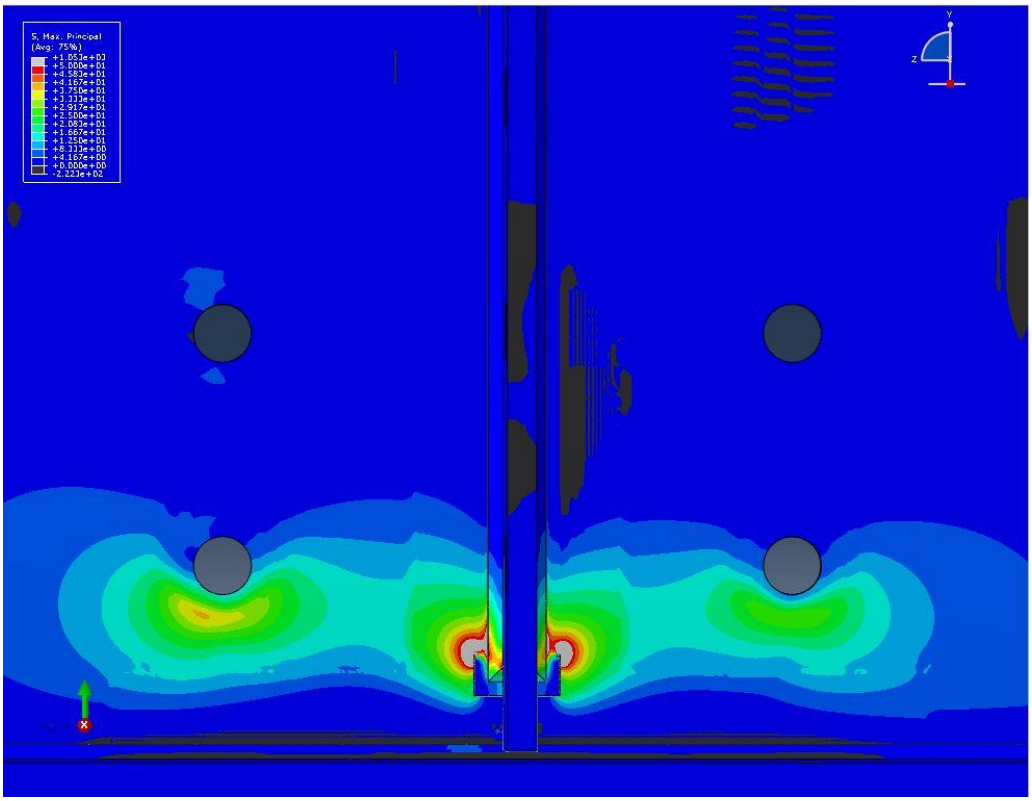

Figure H. 8: 13 mm [1/2 in.] Type 1 Crack & 13 mm [1/2 in.] Type 2 Crack with S-F Retrofit

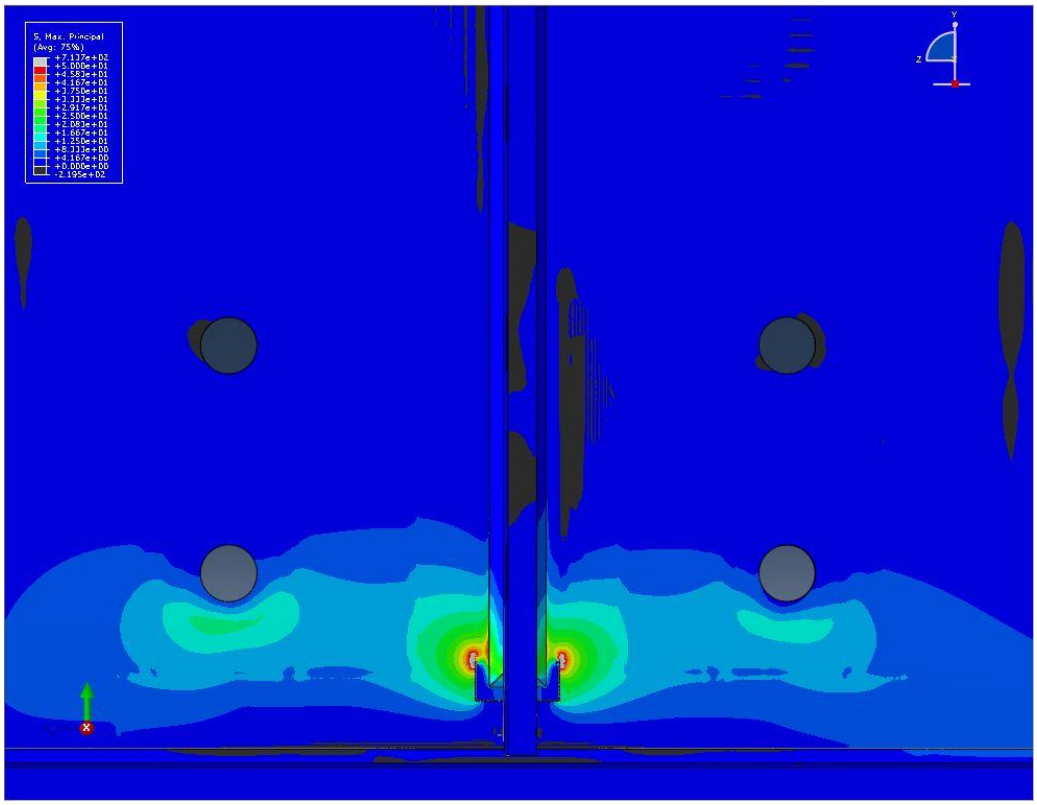

Figure H. 9: 13 mm [1/2 in.] Type 1 Crack & 13 mm [1/2 in.] Type 2 Crack with S-M Retrofit

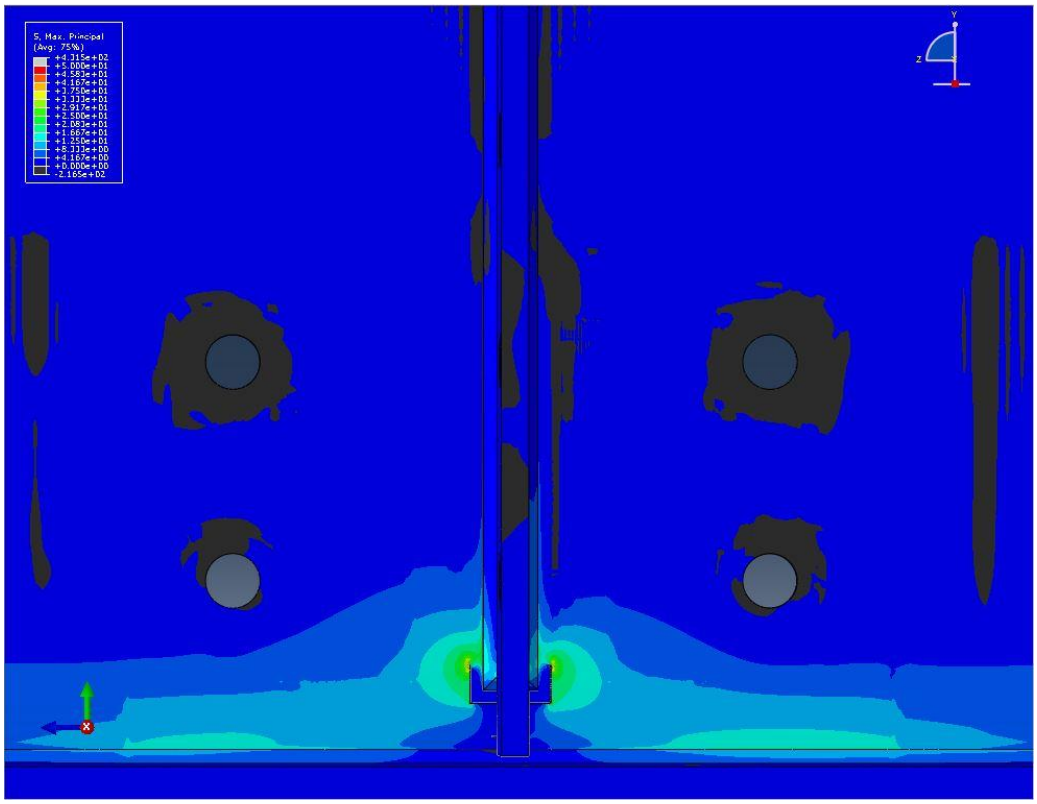

Figure H. 10: 13 mm [1/2 in.] Type 1 Crack & 13 mm [1/2 in.] Type 2 Crack with S-S Retrofit

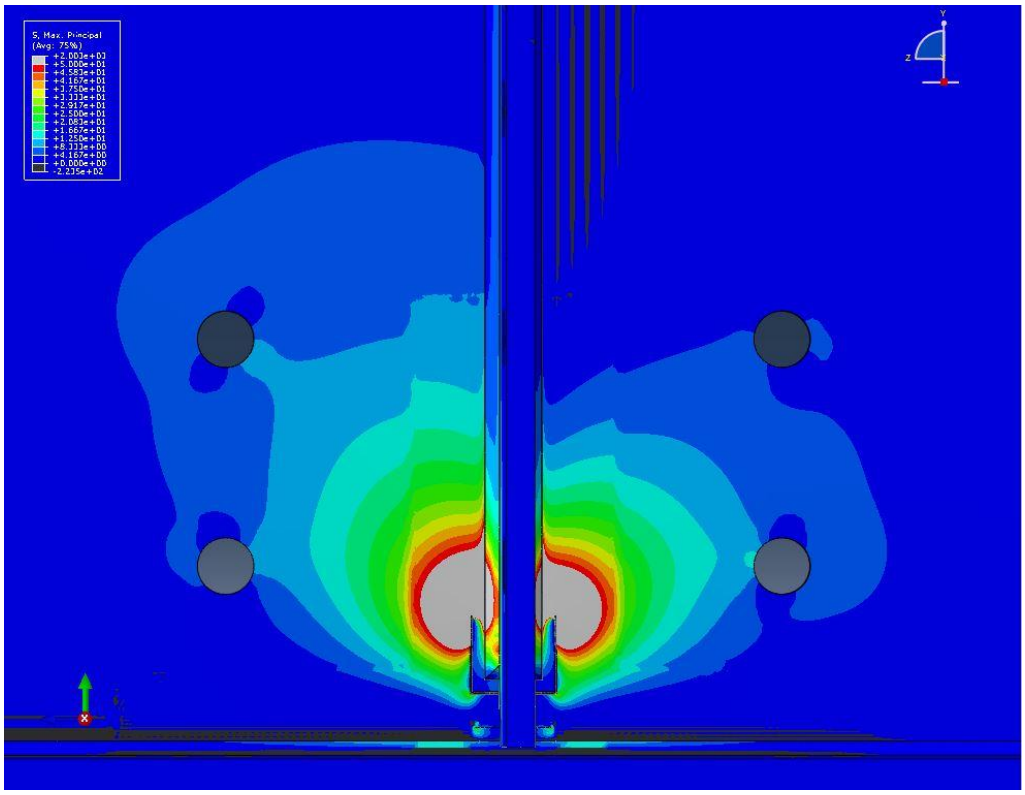

Figure H. 11: 25 mm [1 in.] Type 1 Crack & 25 mm [1 in.] Type 2 Crack with No Retrofit

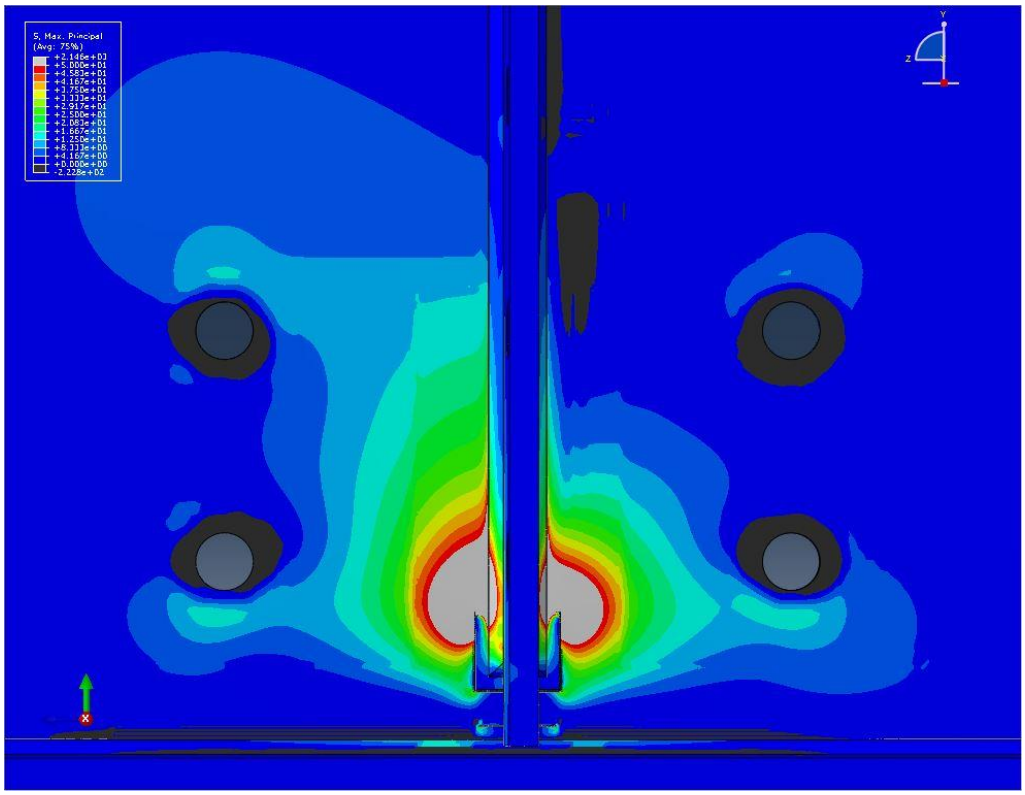

Figure H. 12: 25 mm [1 in.] Type 1 Crack & 25 mm [1 in.] Type 2 Crack with F-F Retrofit

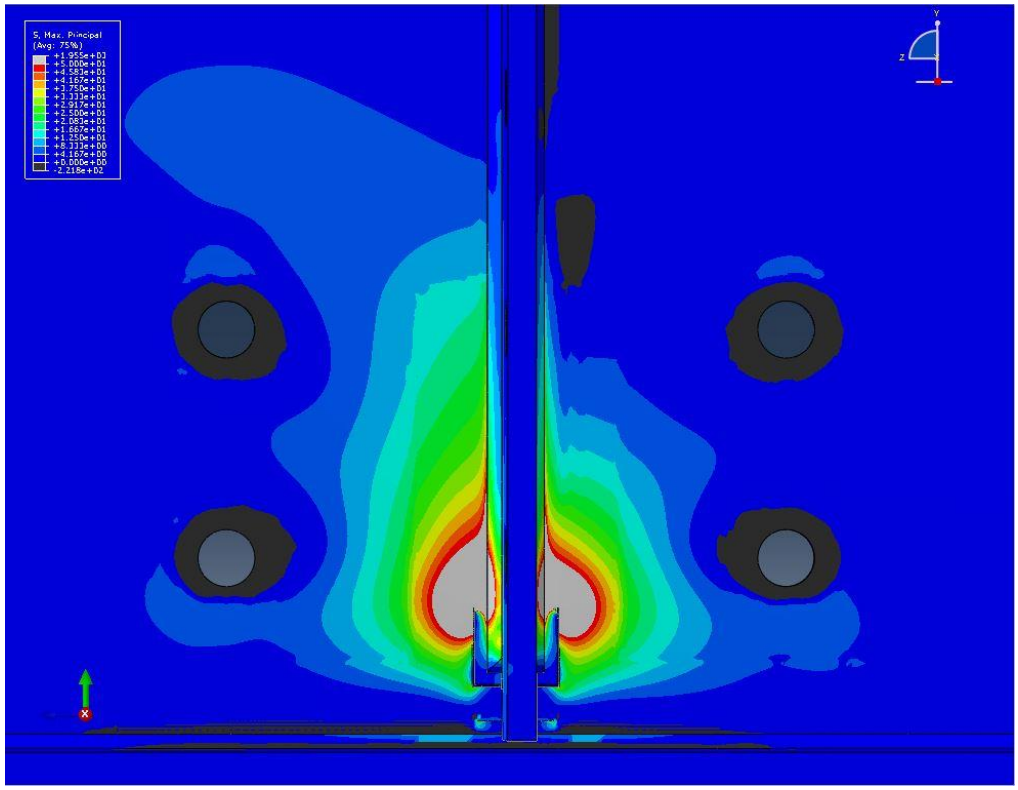

Figure H. 13: 25 mm [1 in.] Type 1 Crack & 25 mm [1 in.] Type 2 Crack with F-M Retrofit

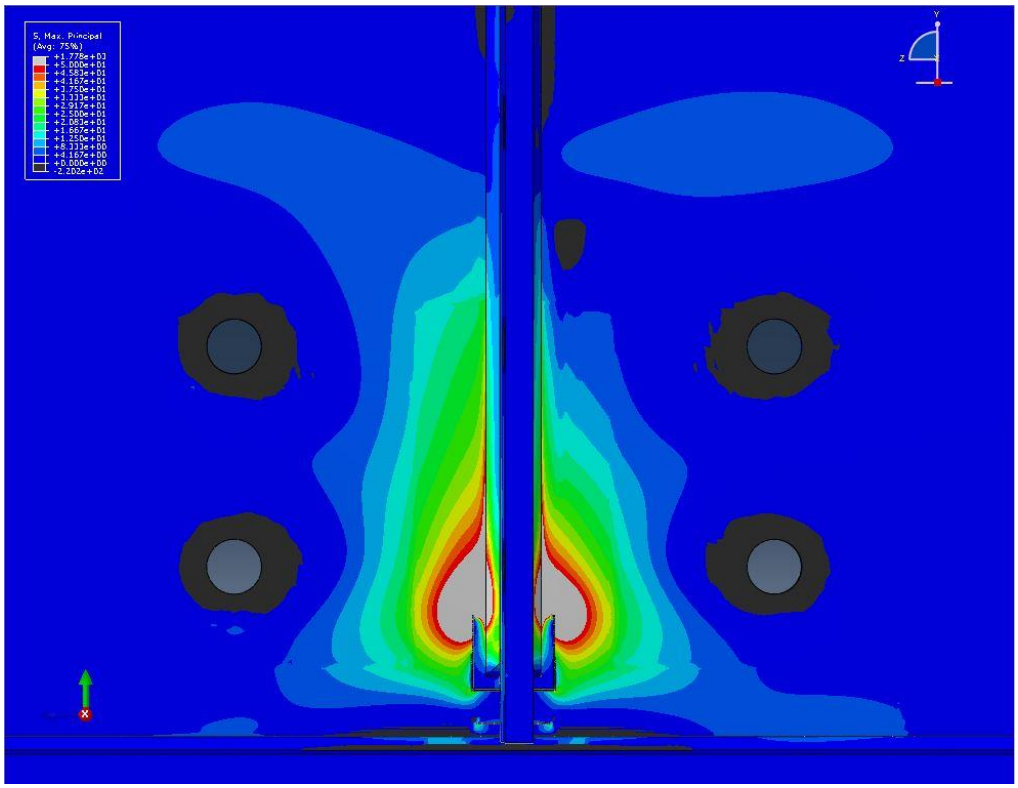

Figure H. 14: 25 mm [1 in.] Type 1 Crack & 25 mm [1 in.] Type 2 Crack with F-S Retrofit

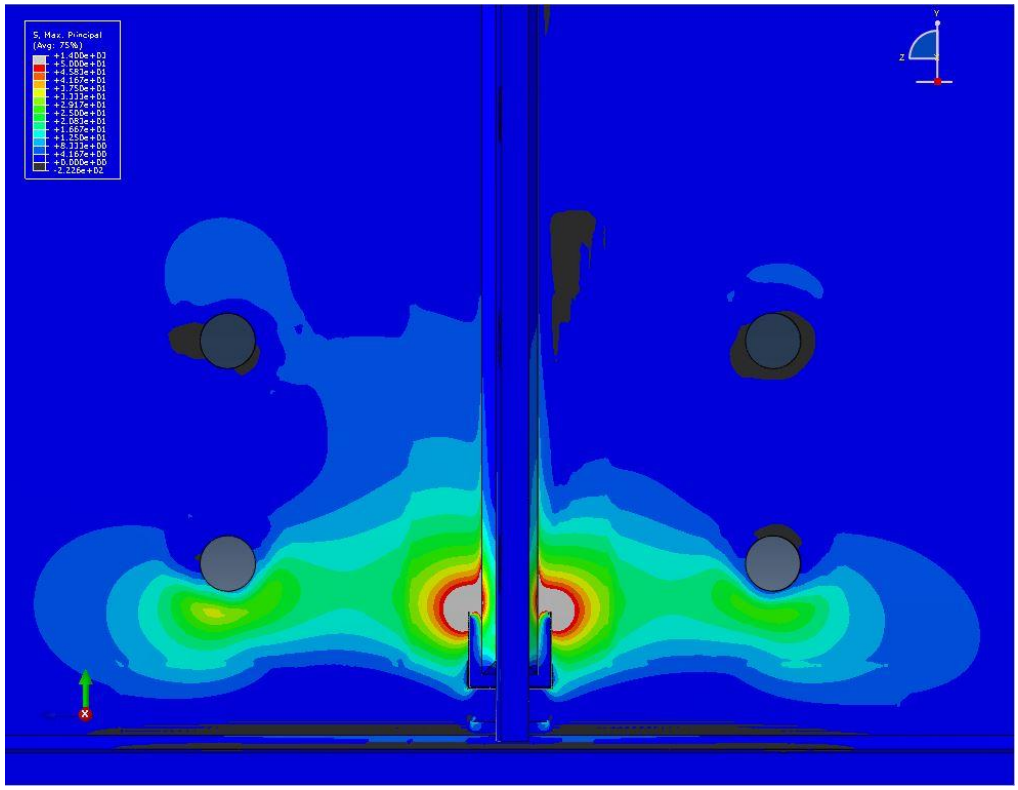

Figure H. 15: 25 mm [1 in.] Type 1 Crack & 25 mm [1 in.] Type 2 Crack with M-F Retrofit

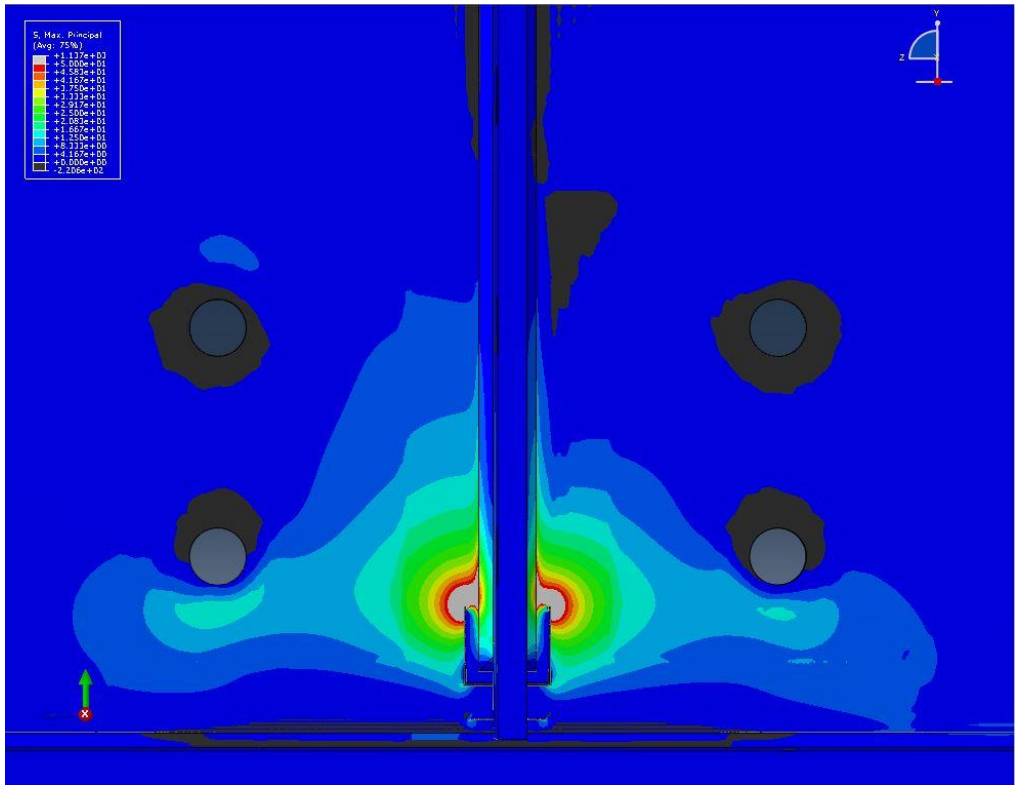

Figure H. 16: 25 mm [1 in.] Type 1 Crack & 25 mm [1 in.] Type 2 Crack with M-M Retrofit

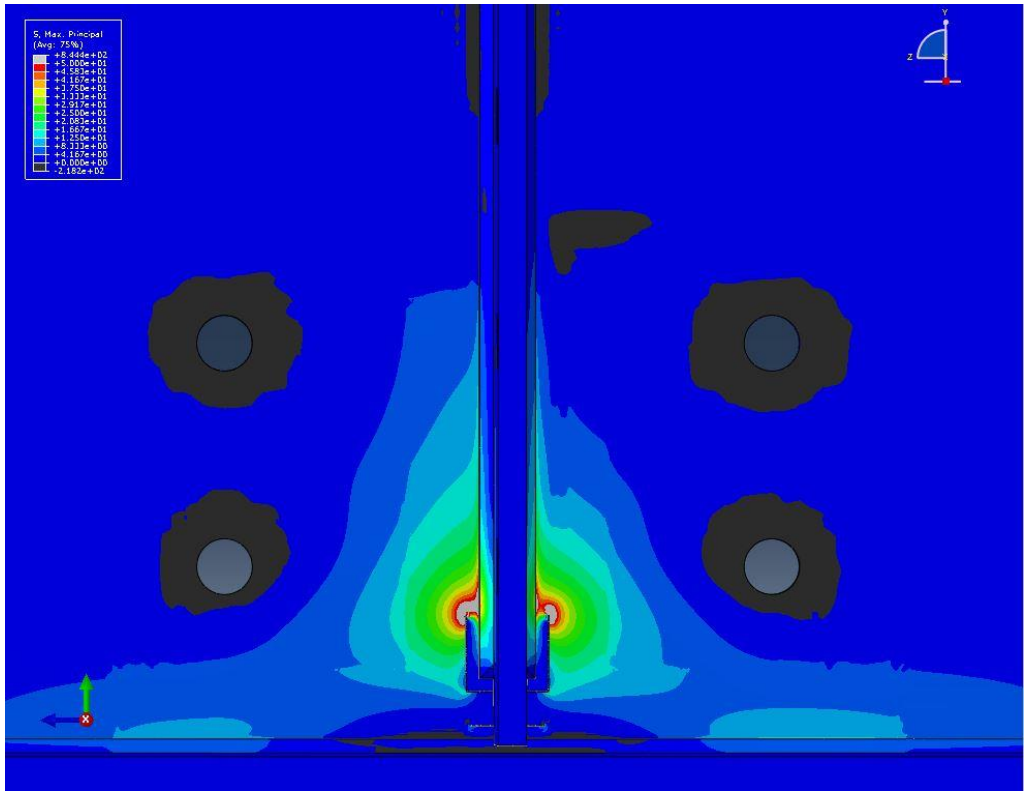

Figure H. 17: 25 mm [1 in.] Type 1 Crack & 25 mm [1 in.] Type 2 Crack with M-S Retrofit

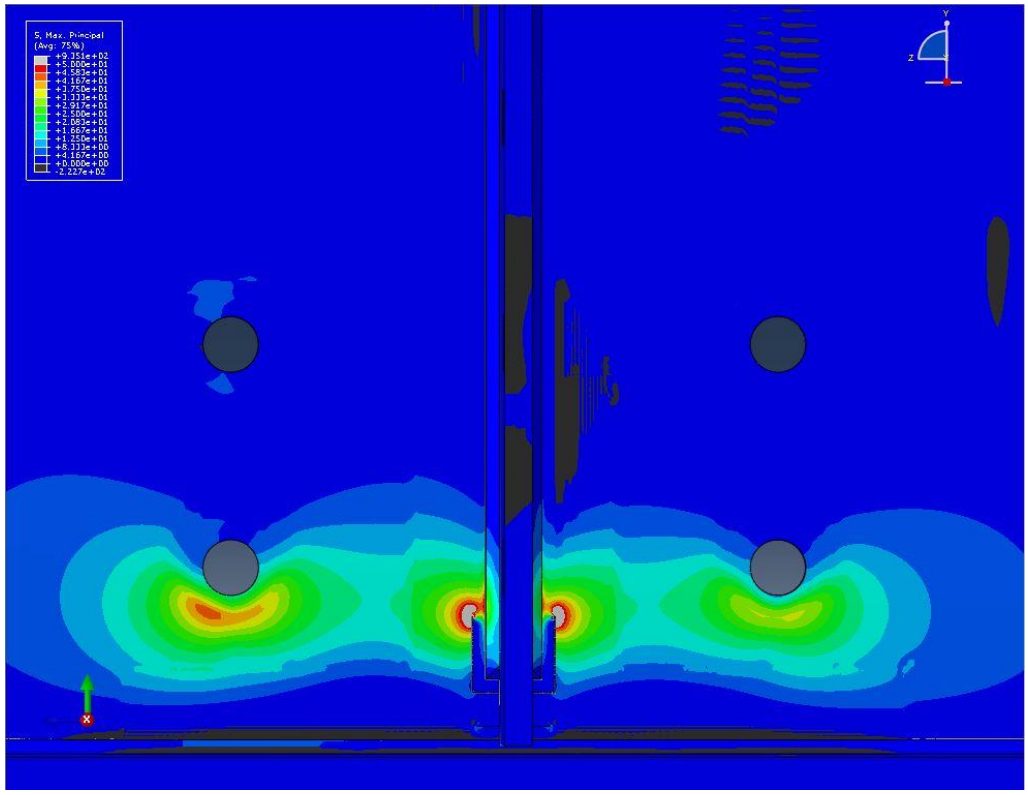

Figure H. 18: 25 mm [1 in.] Type 1 Crack & 25 mm [1 in.] Type 2 Crack with S-F Retrofit

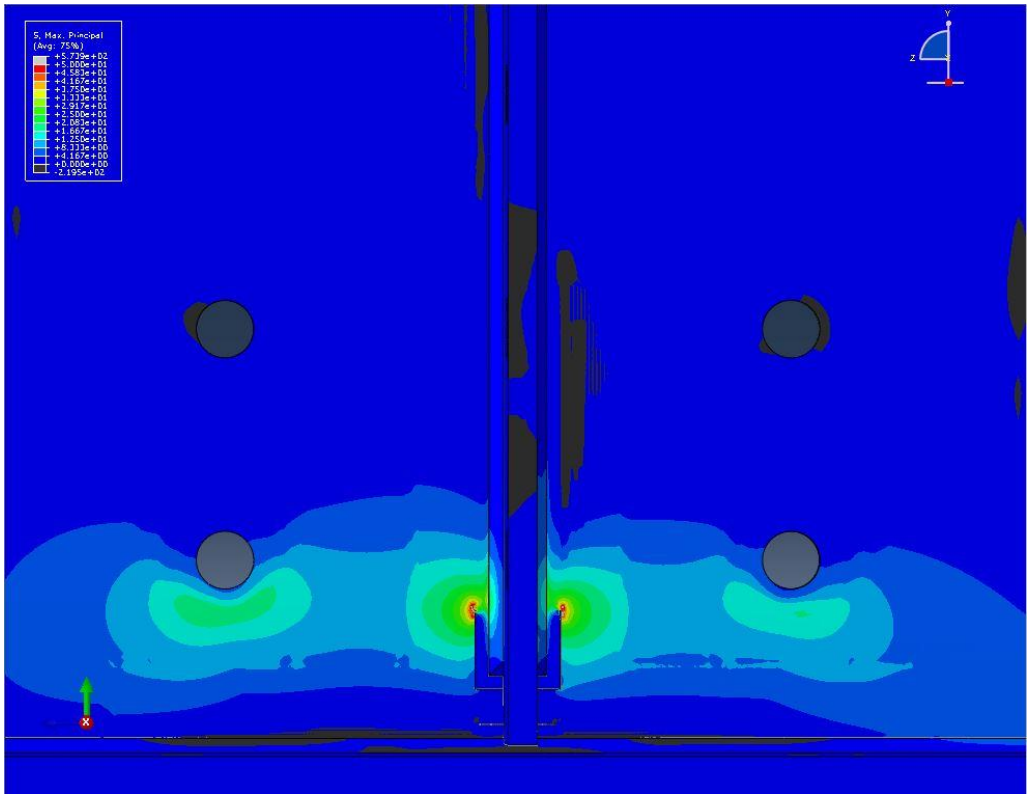

Figure H. 19: 25 mm [1 in.] Type 1 Crack & 25 mm [1 in.] Type 2 Crack with S-M Retrofit

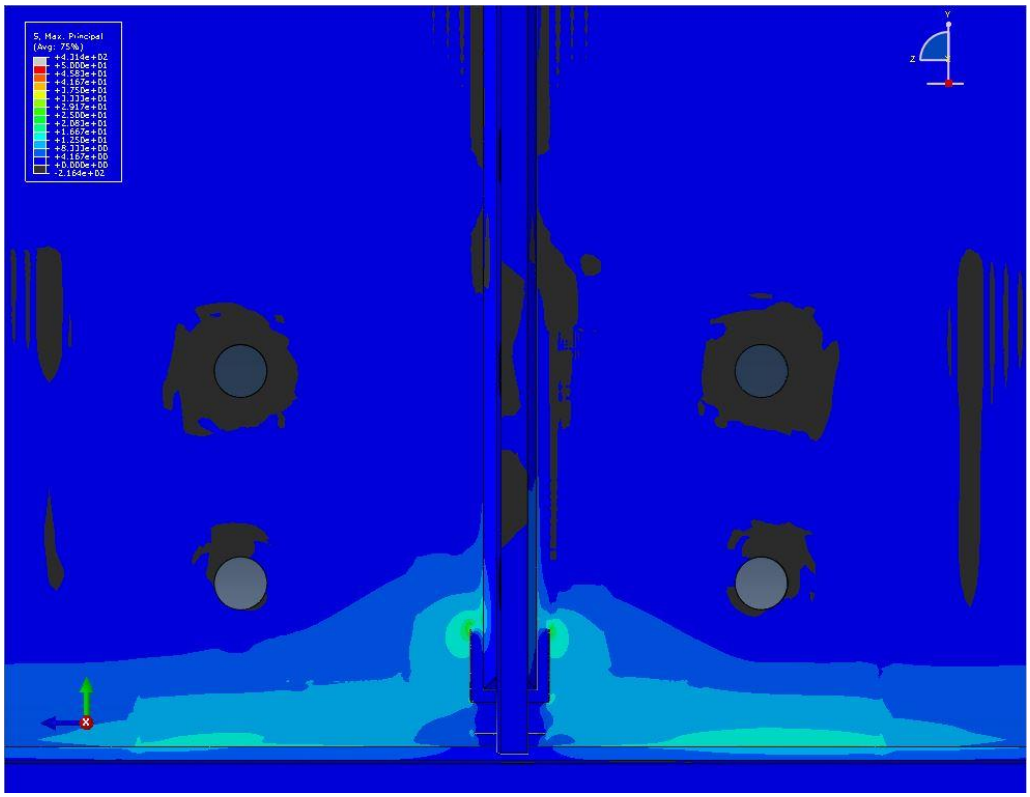

Figure H. 20: 25 mm [1 in.] Type 1 Crack & 25 mm [1 in.] Type 2 Crack with S-S Retrofit

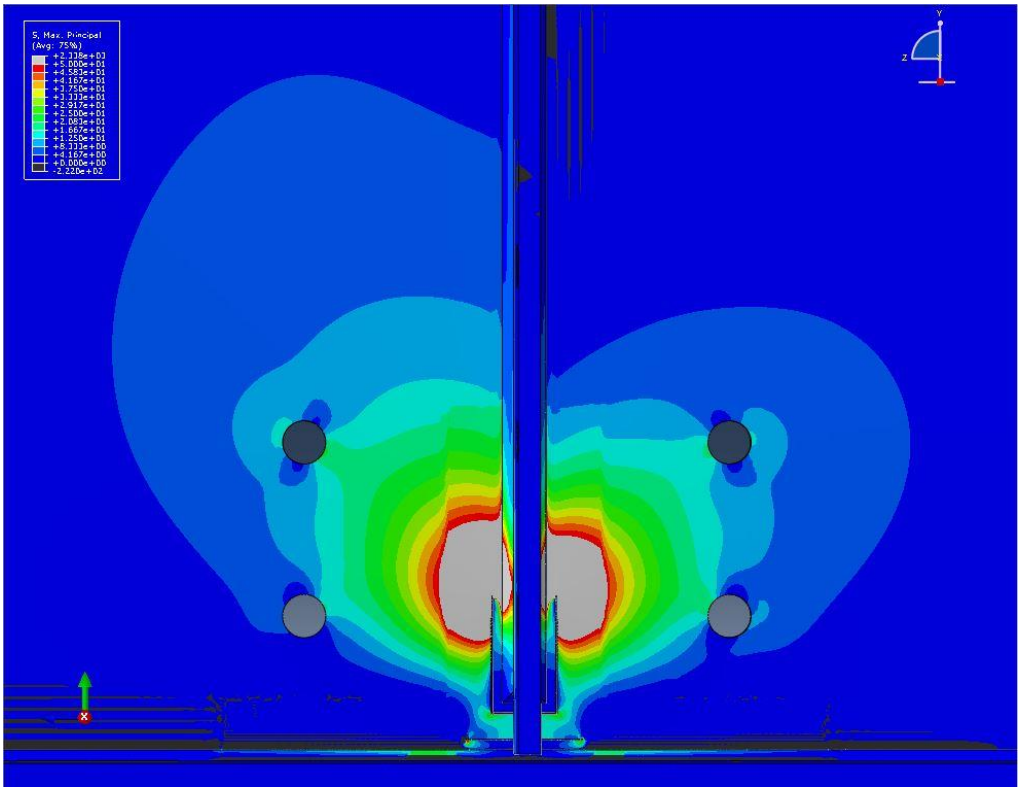

Figure H. 21: 51 mm [2 in.] Type 1 Crack & 51 mm [2 in.] Type 2 Crack with No Retrofit

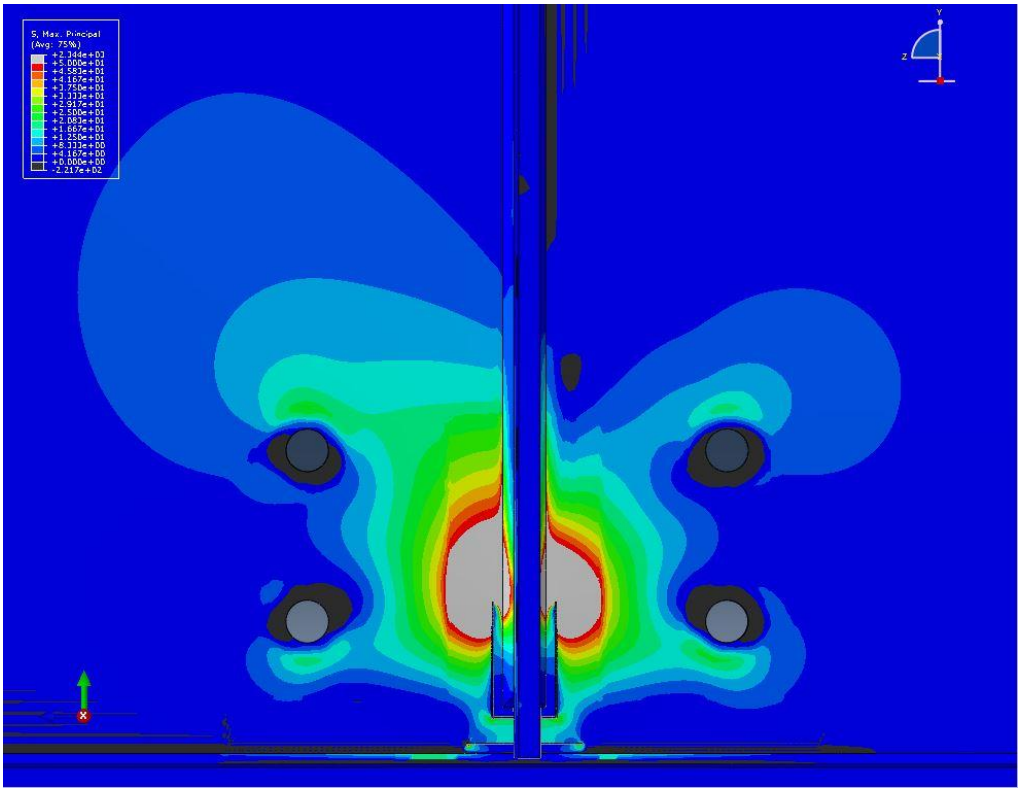

Figure H. 22: 51 mm [2 in.] Type 1 Crack & 51 mm [2 in.] Type 2 Crack with F-F Retrofit

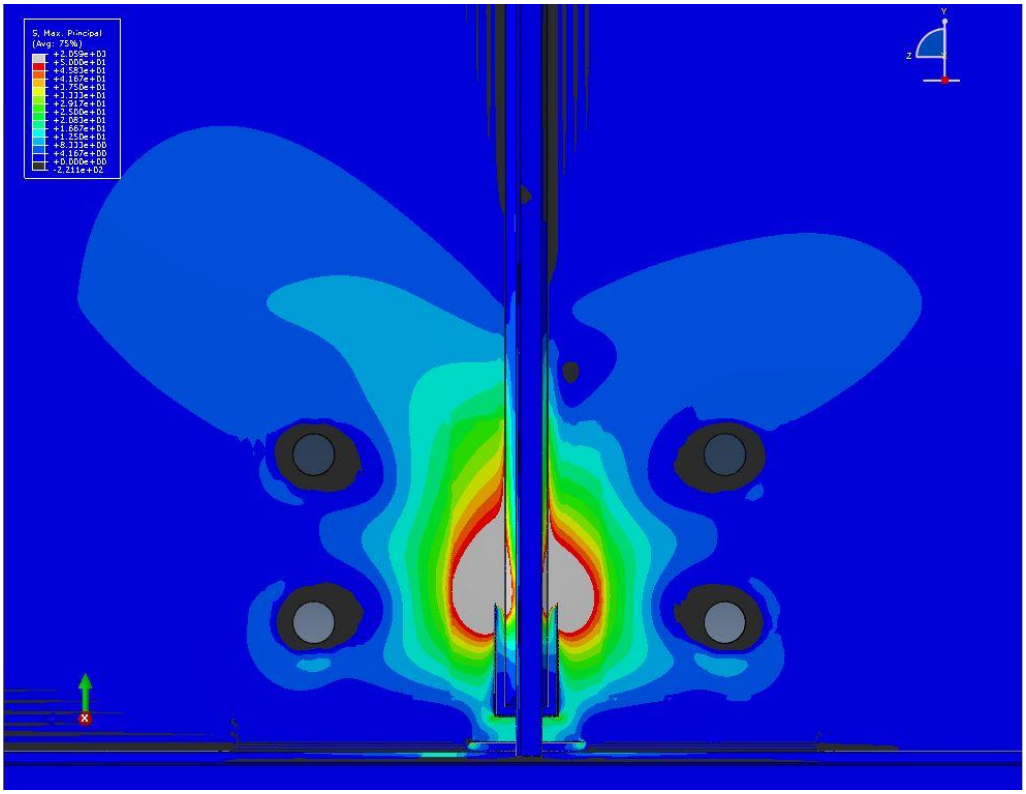

Figure H. 23: 51 mm [2 in.] Type 1 Crack & 51 mm [2 in.] Type 2 Crack with F-M Retrofit

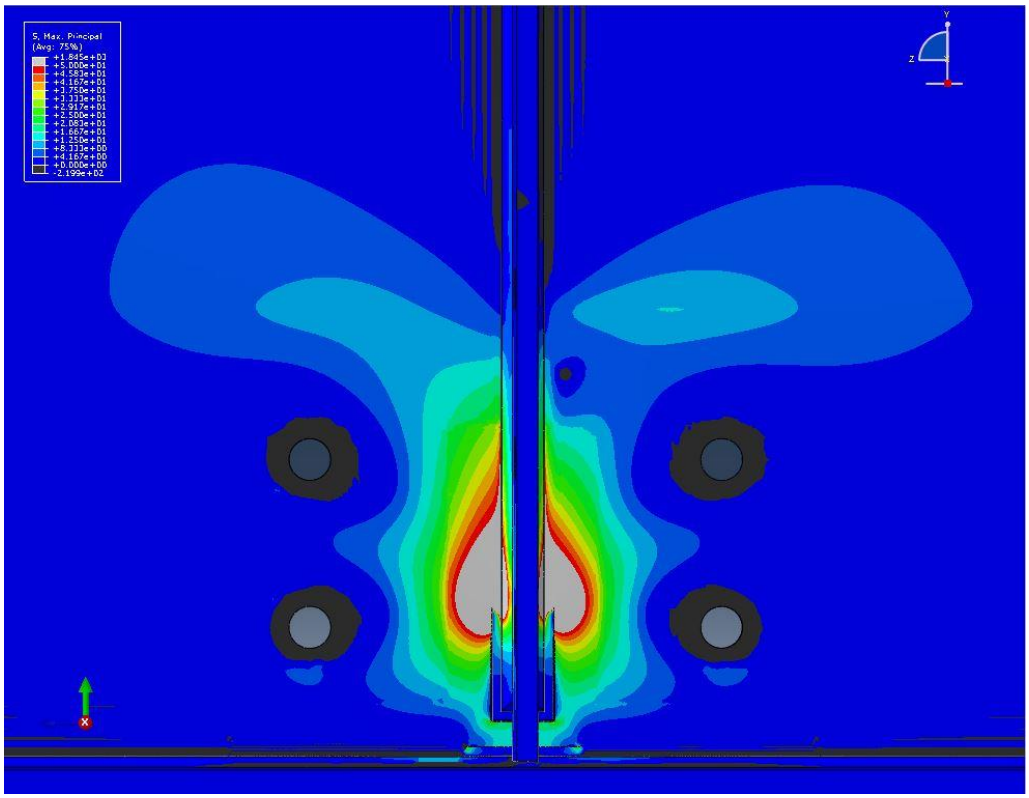

Figure H. 24: 51 mm [2 in.] Type 1 Crack & 51 mm [2 in.] Type 2 Crack with F-S Retrofit

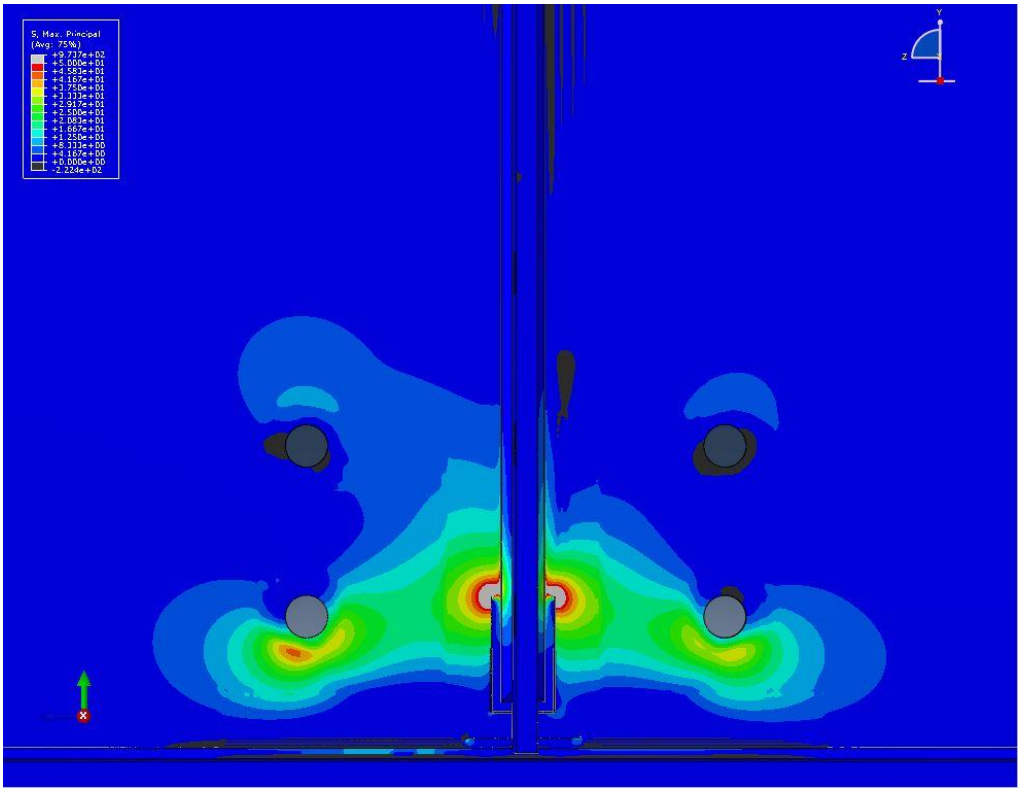

Figure H. 25: 51 mm [2 in.] Type 1 Crack & 51 mm [2 in.] Type 2 Crack with M-F Retrofit

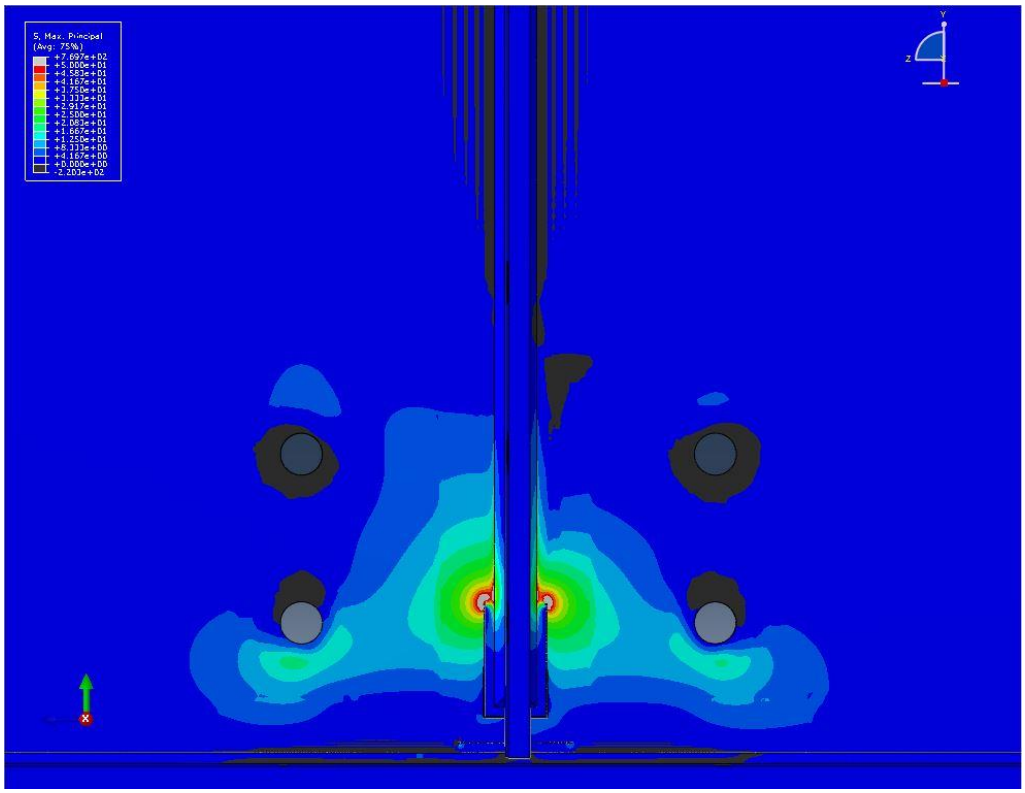

Figure H. 26: 51 mm [2 in.] Type 1 Crack & 51 mm [2 in.] Type 2 Crack with M-M Retrofit

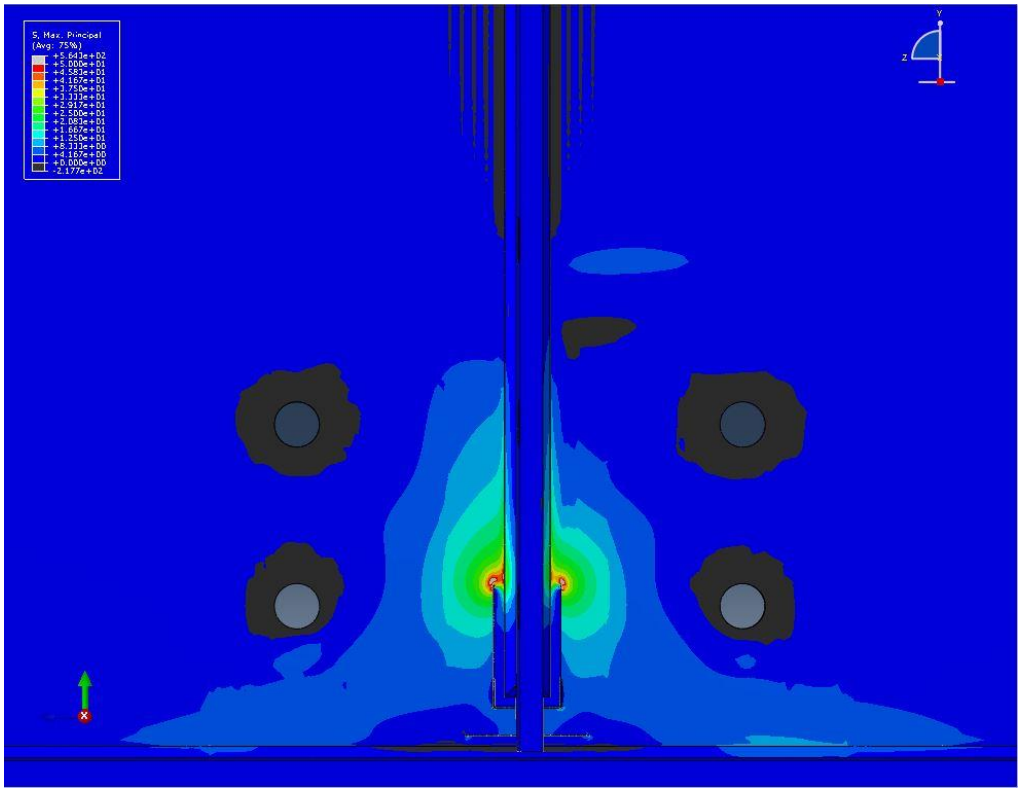

Figure H. 27: 51 mm [2 in.] Type 1 Crack & 51 mm [2 in.] Type 2 Crack with M-S Retrofit

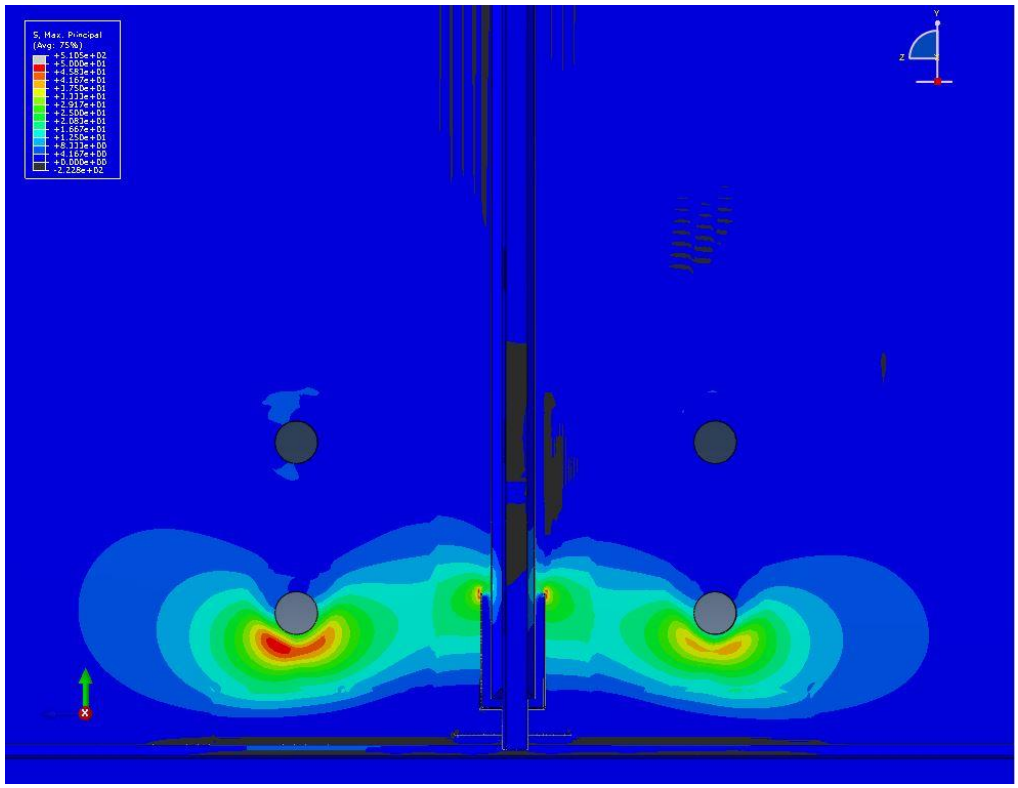

Figure H. 28: 51 mm [2 in.] Type 1 Crack & 51 mm [2 in.] Type 2 Crack with S-F Retrofit

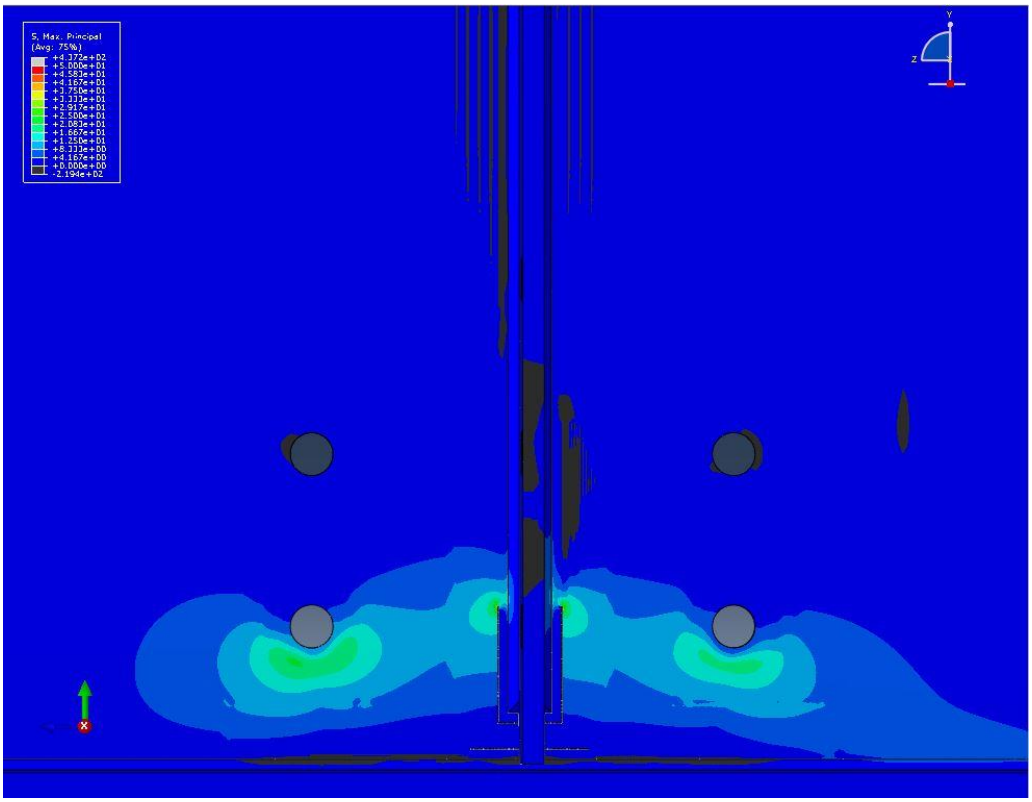

Figure H. 29: 51 mm [2 in.] Type 1 Crack & 51 mm [2 in.] Type 2 Crack with S-M Retrofit

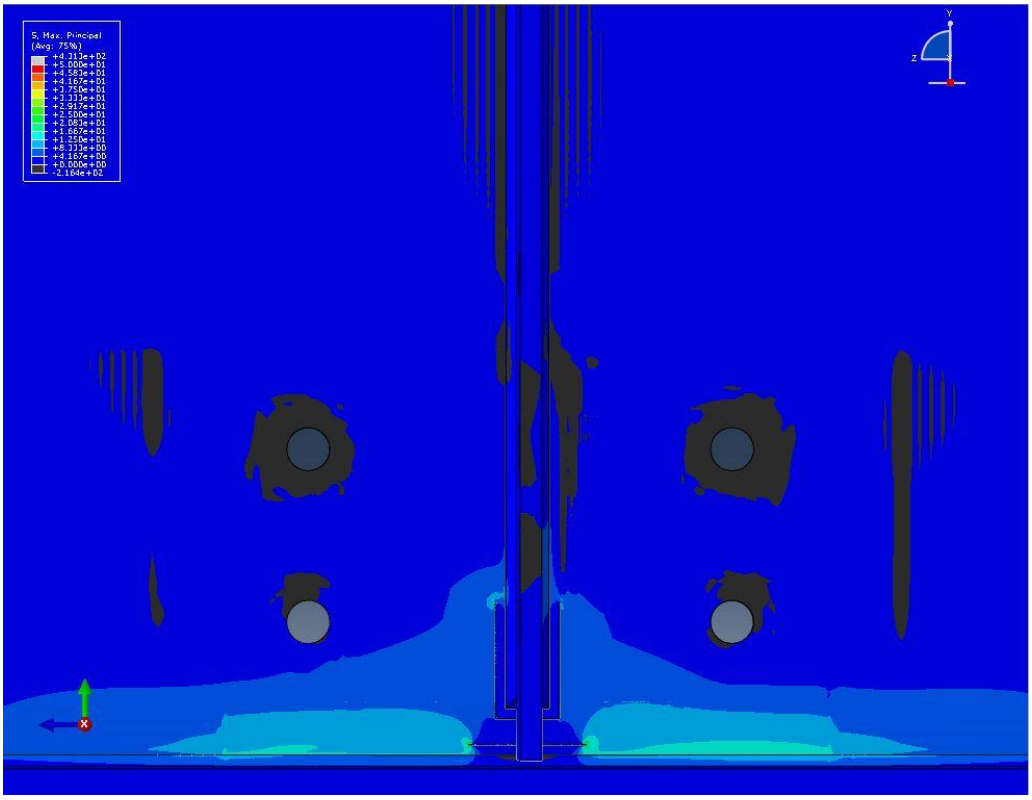

Figure H. 30: 51 mm [2 in.] Type 1 Crack & 51 mm [2 in.] Type 2 Crack with S-S Retrofit

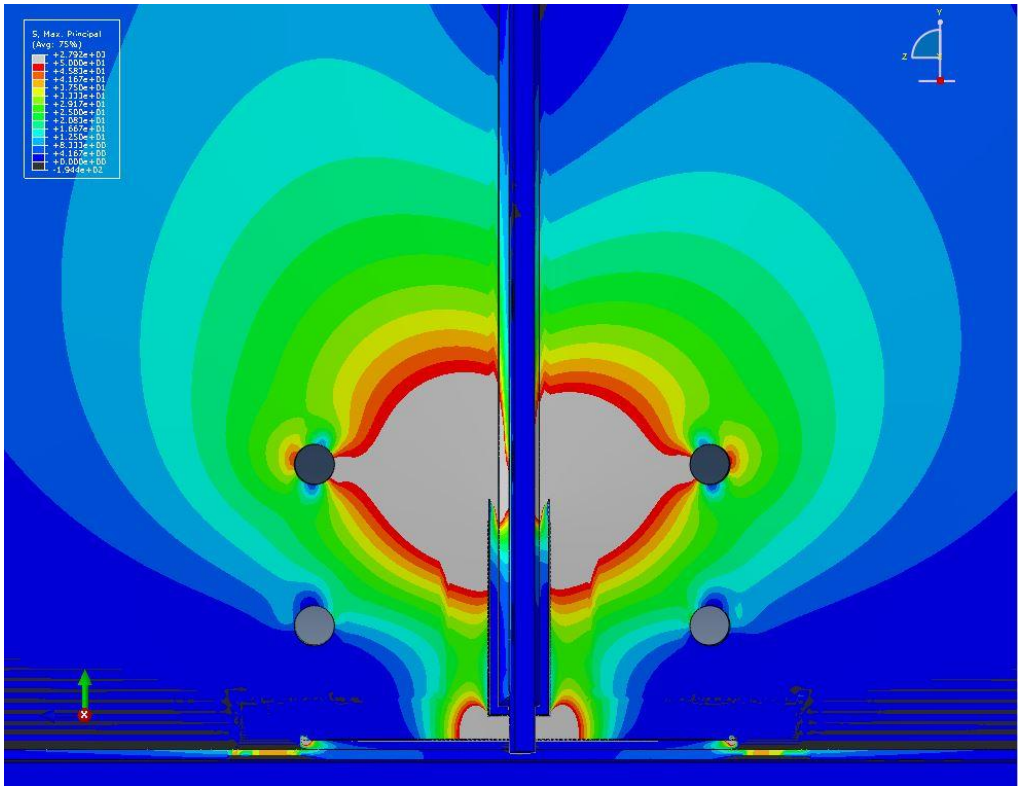

Figure H. 31: 102 mm [4 in.] Type 1 Crack & 203 mm [8 in.] Type 2 Crack with No Retrofit

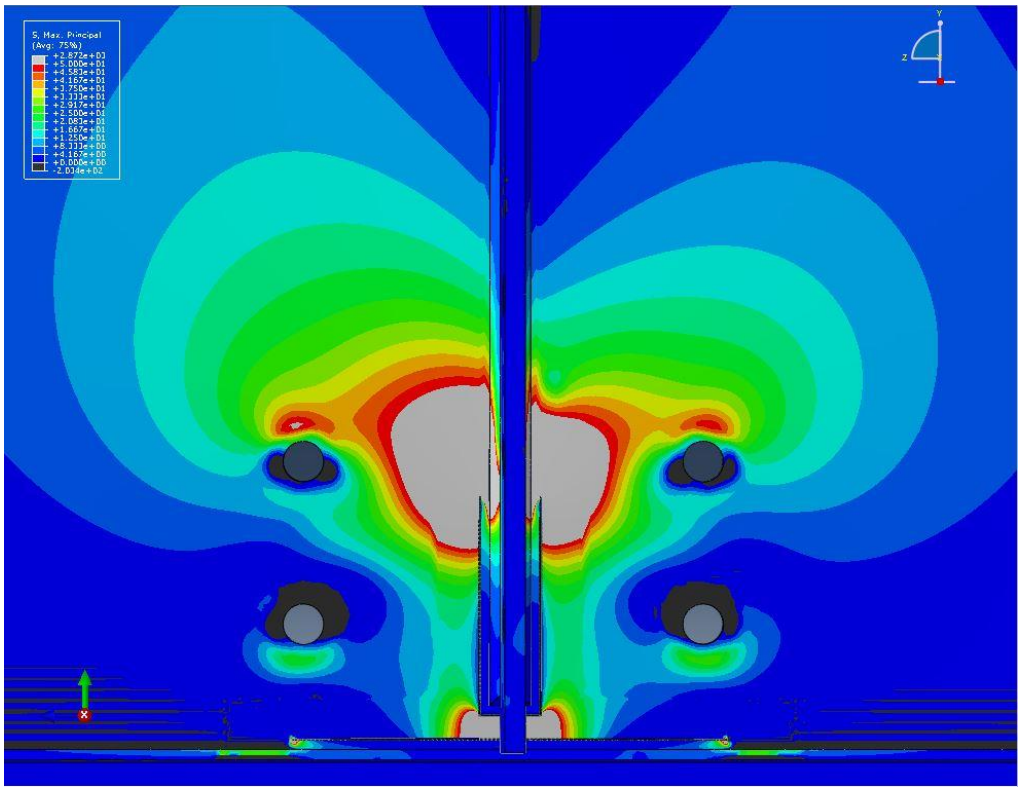

Figure H. 32: 102 mm [4 in.] Type 1 Crack & 203 mm [8 in.] Type 2 Crack with F-F Retrofit

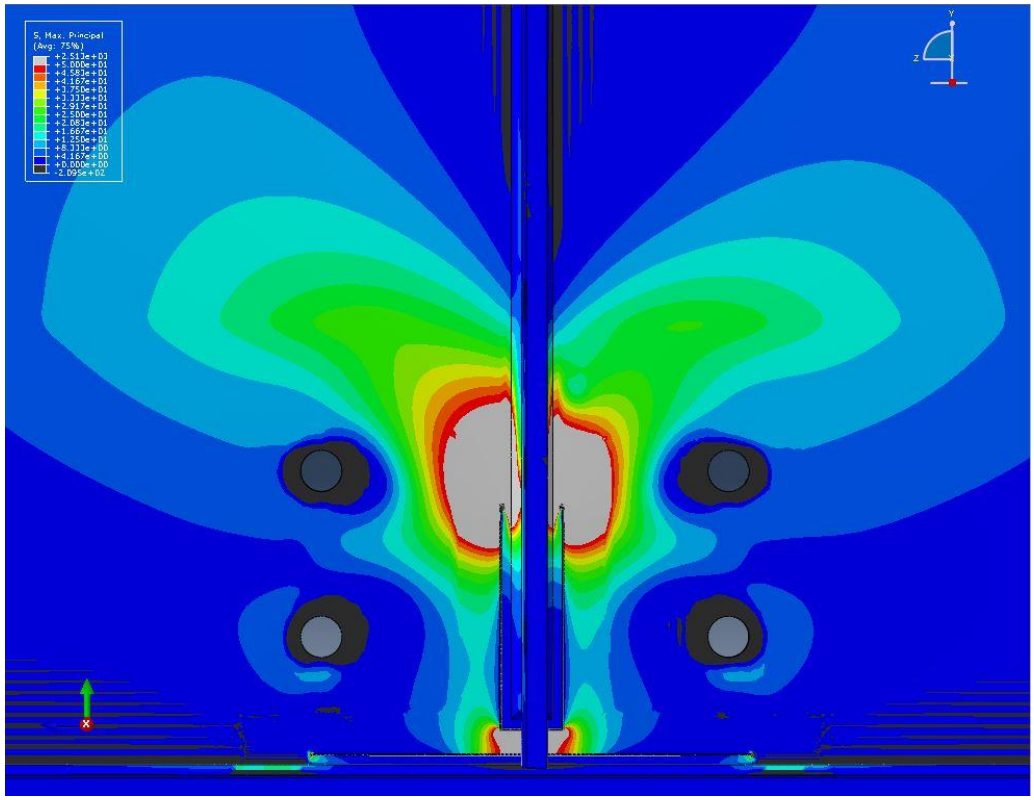

Figure H. 33: 102 mm [4 in.] Type 1 Crack & 203 mm [8 in.] Type 2 Crack with F-M Retrofit

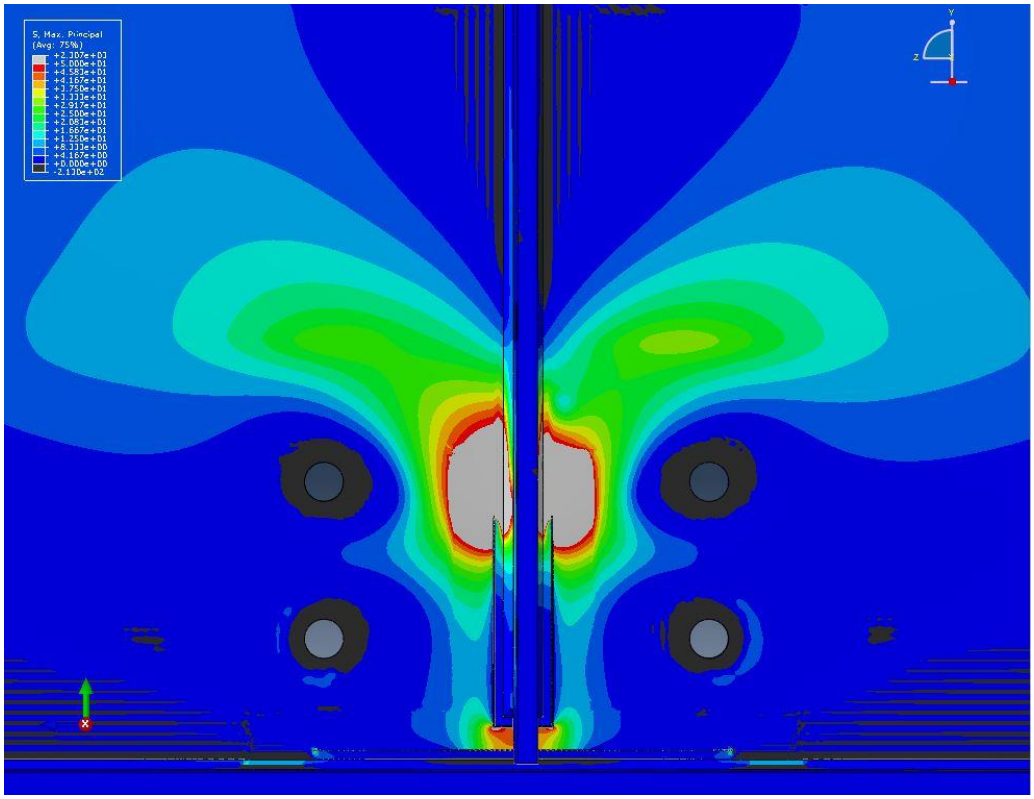

Figure H. 34: 102 mm [4 in.] Type 1 Crack & 203 mm [8 in.] Type 2 Crack with F-S Retrofit

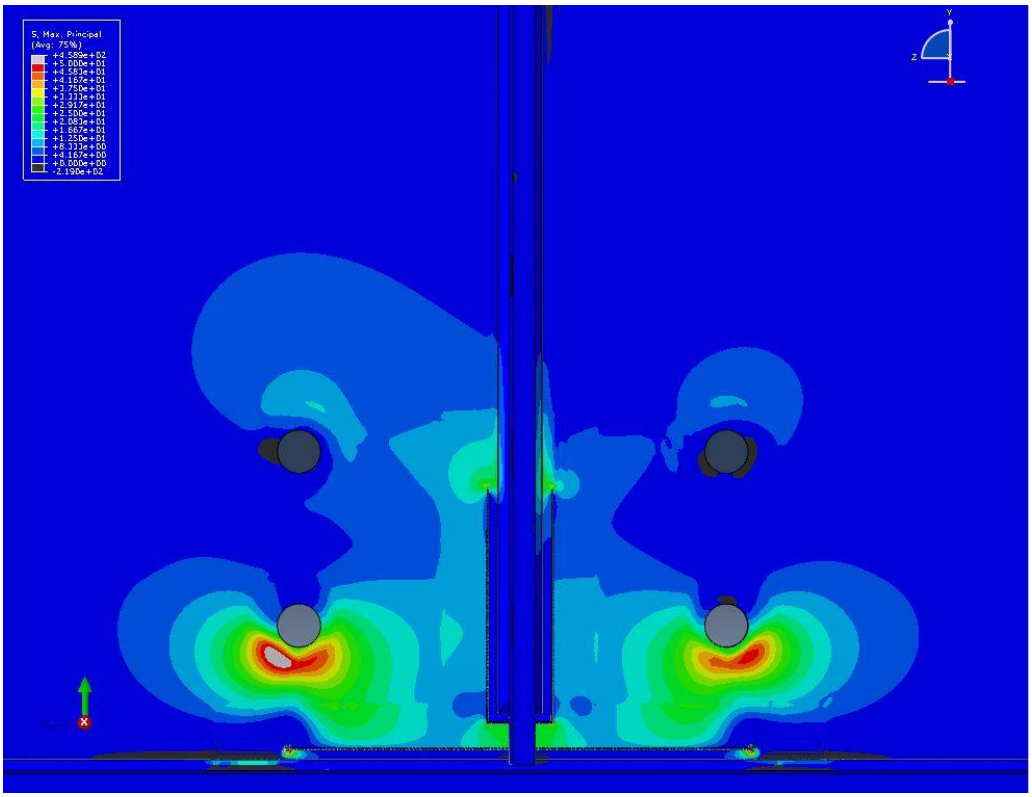

Figure H. 35: 102 mm [4 in.] Type 1 Crack & 203 mm [8 in.] Type 2 Crack with M-F Retrofit

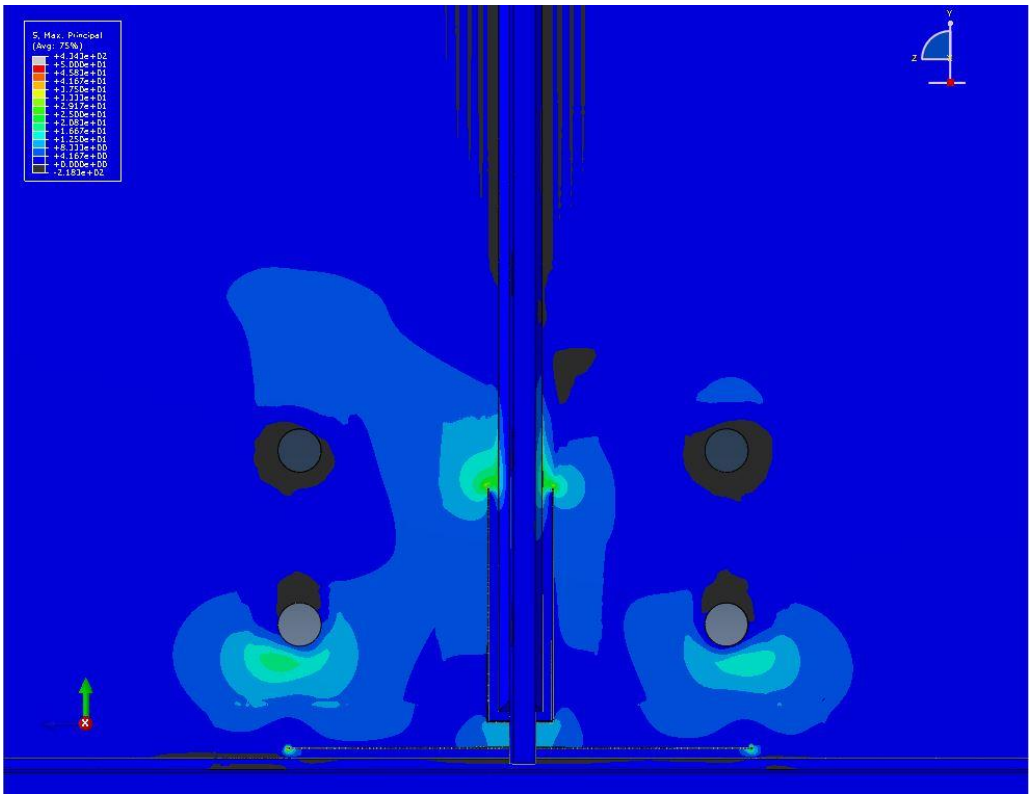

Figure H. 36: 102 mm [4 in.] Type 1 Crack & 203 mm [8 in.] Type 2 Crack with M-M Retrofit

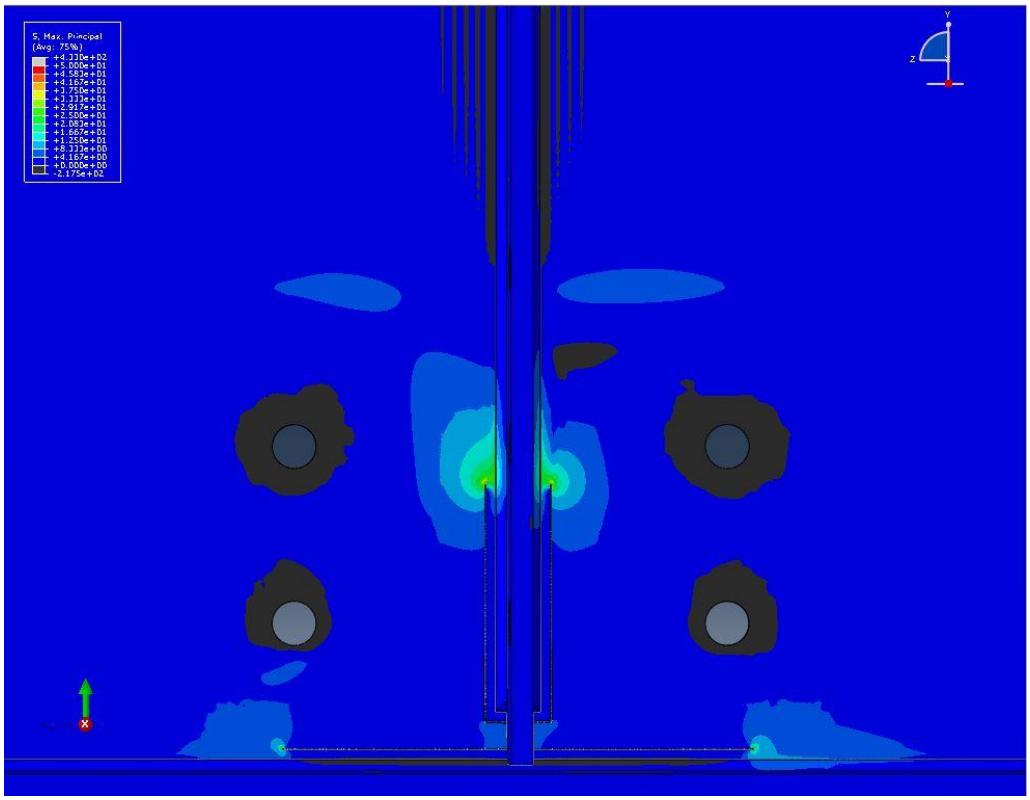

Figure H. 37: 102 mm [4 in.] Type 1 Crack & 203 mm [8 in.] Type 2 Crack with M-S Retrofit

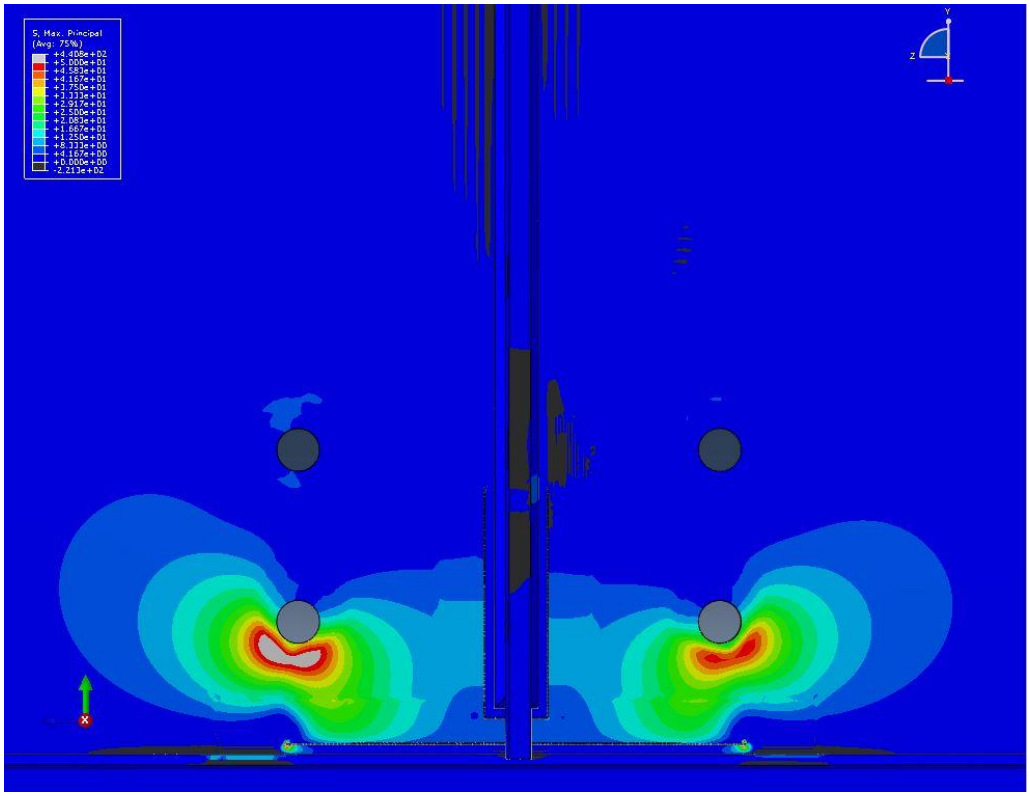

Figure H. 38: 102 mm [4 in.] Type 1 Crack & 203 mm [8 in.] Type 2 Crack with S-F Retrofit

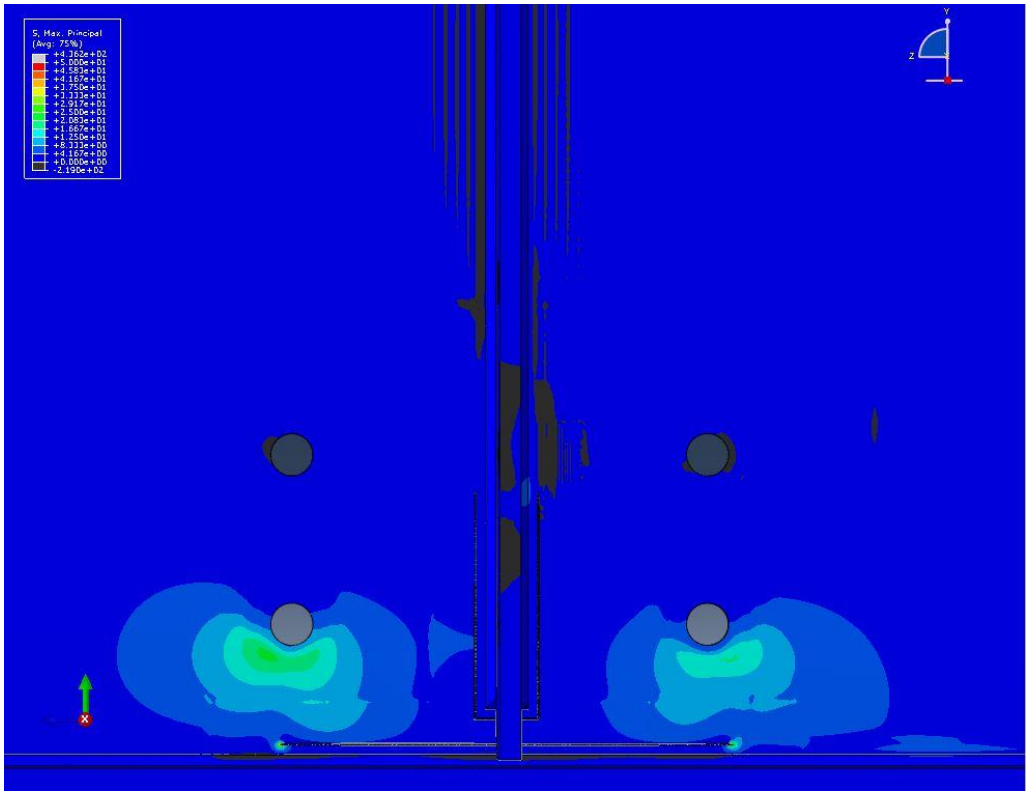

Figure H. 39: 102 mm [4 in.] Type 1 Crack & 203 mm [8 in.] Type 2 Crack with S-M Retrofit

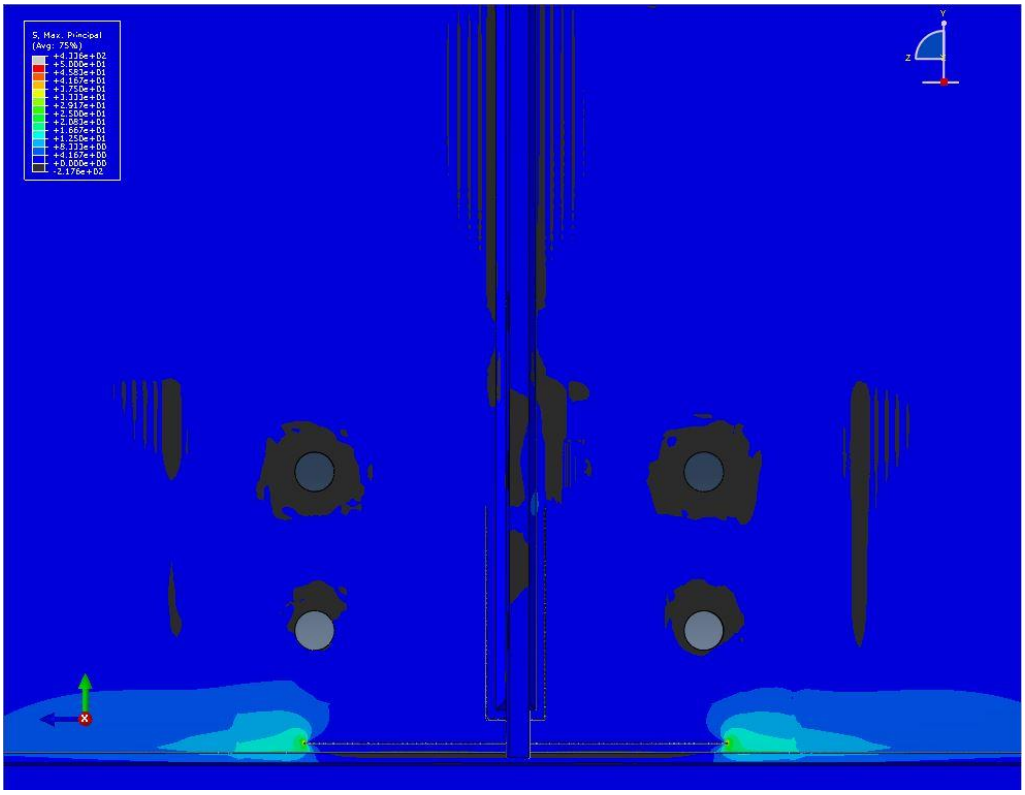

Figure H. 40: 102 mm [4 in.] Type 1 Crack & 203 mm [8 in.] Type 2 Crack with S-S Retrofit

APPENDIX I: DEFORMATION SCREENSHOTS IN THE WEB GAP REGION FOR THE ANGLES-WITH-PLATE RETROFIT MODELS

Stress Range: 0–345 MPa (50 ksi)

Deflection Scale: 10

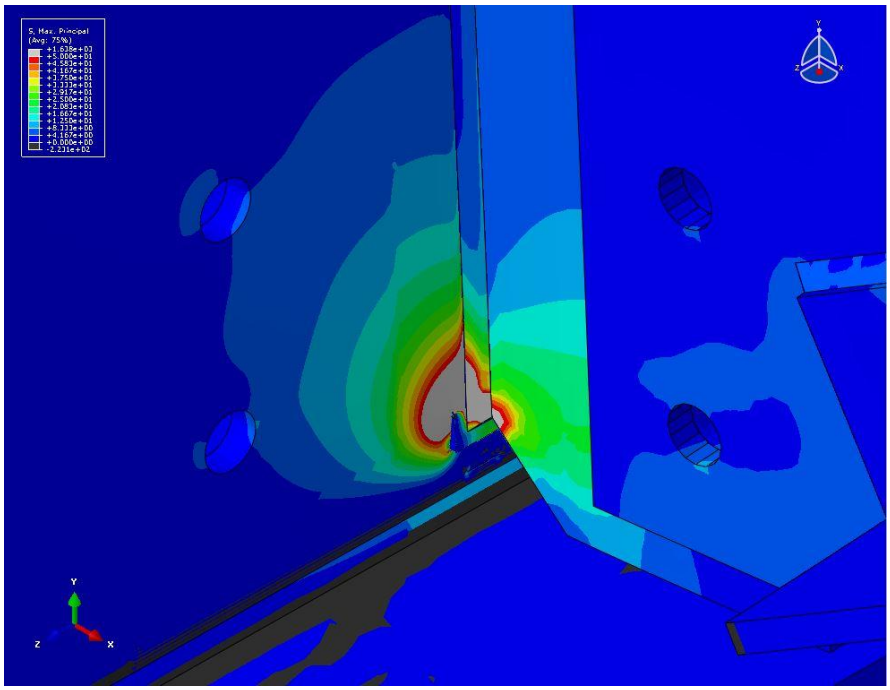

Figure I. 1: 13 mm [1/2 in.] Type 1 Crack & 13 mm [1/2 in.] Type 2 Crack with No Retrofit

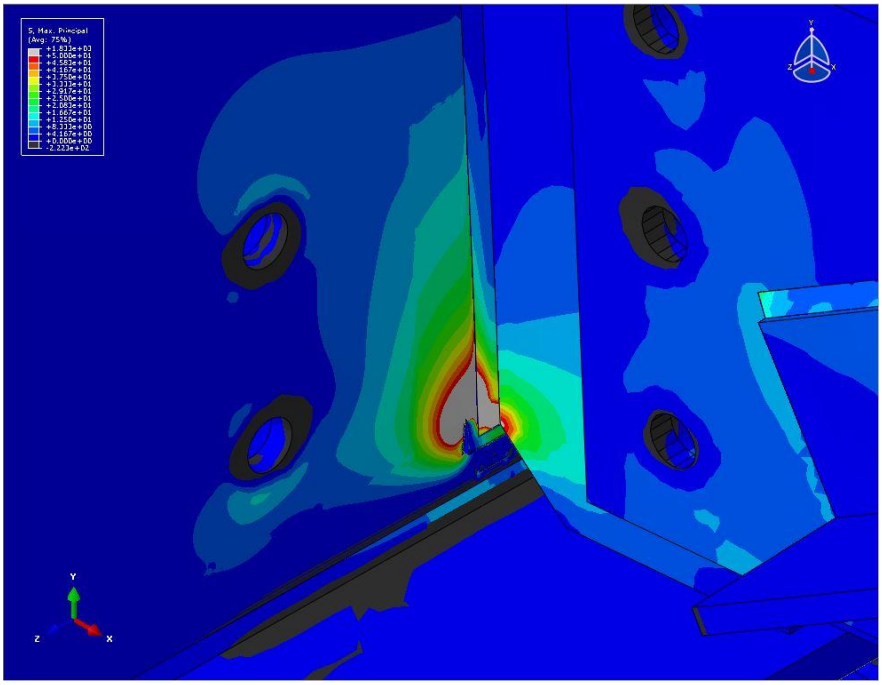

Figure I. 2: 13 mm [1/2 in.] Type 1 Crack & 13 mm [1/2 in.] Type 2 Crack with F-F Retrofit

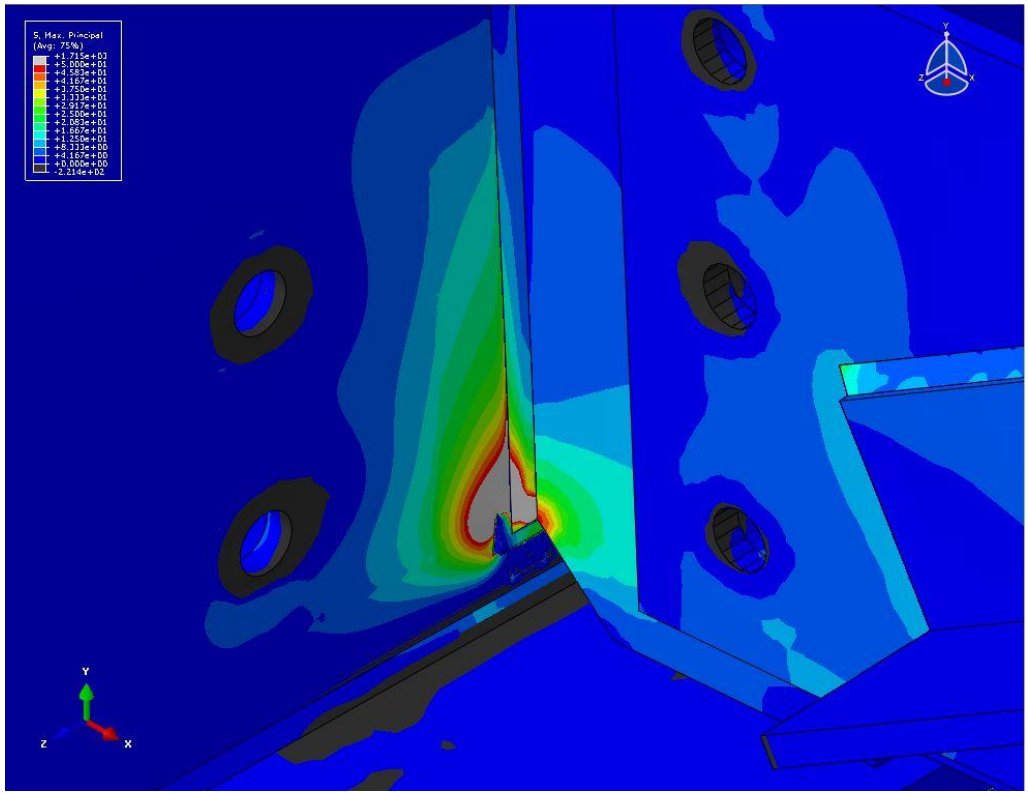

Figure I. 3: 13 mm [1/2 in.] Type 1 Crack & 13 mm [1/2 in.] Type 2 Crack with F-M Retrofit

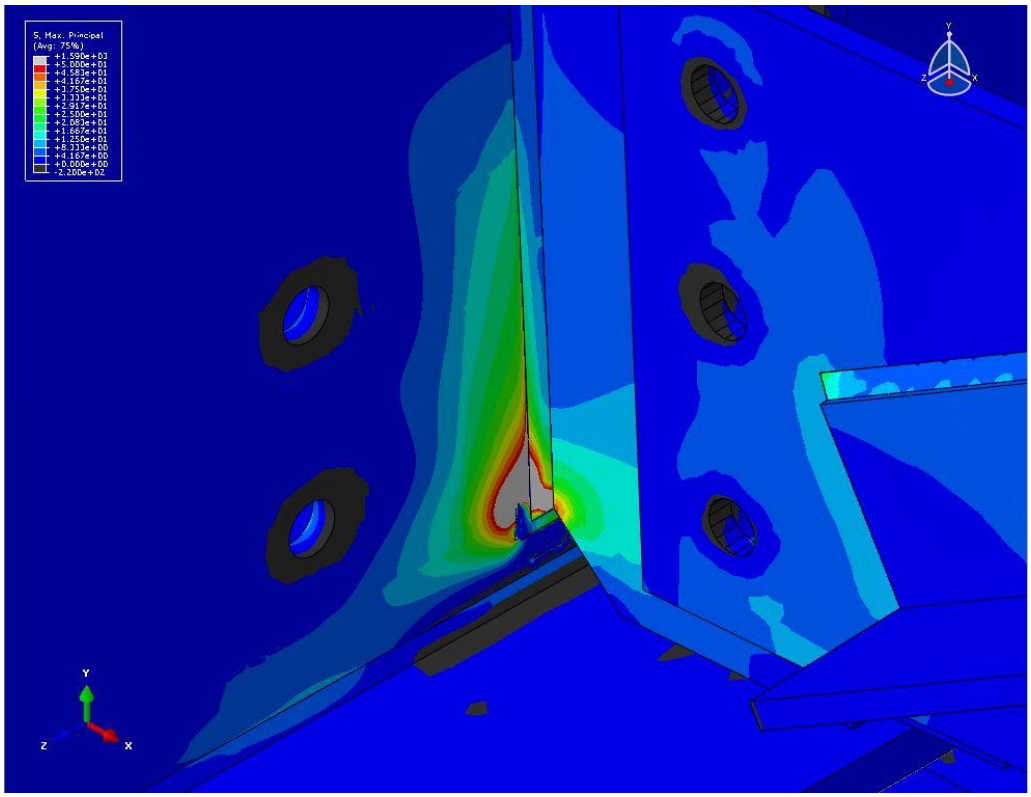

Figure I. 4: 13 mm [1/2 in.] Type 1 Crack & 13 mm [1/2 in.] Type 2 Crack with F-S Retrofit

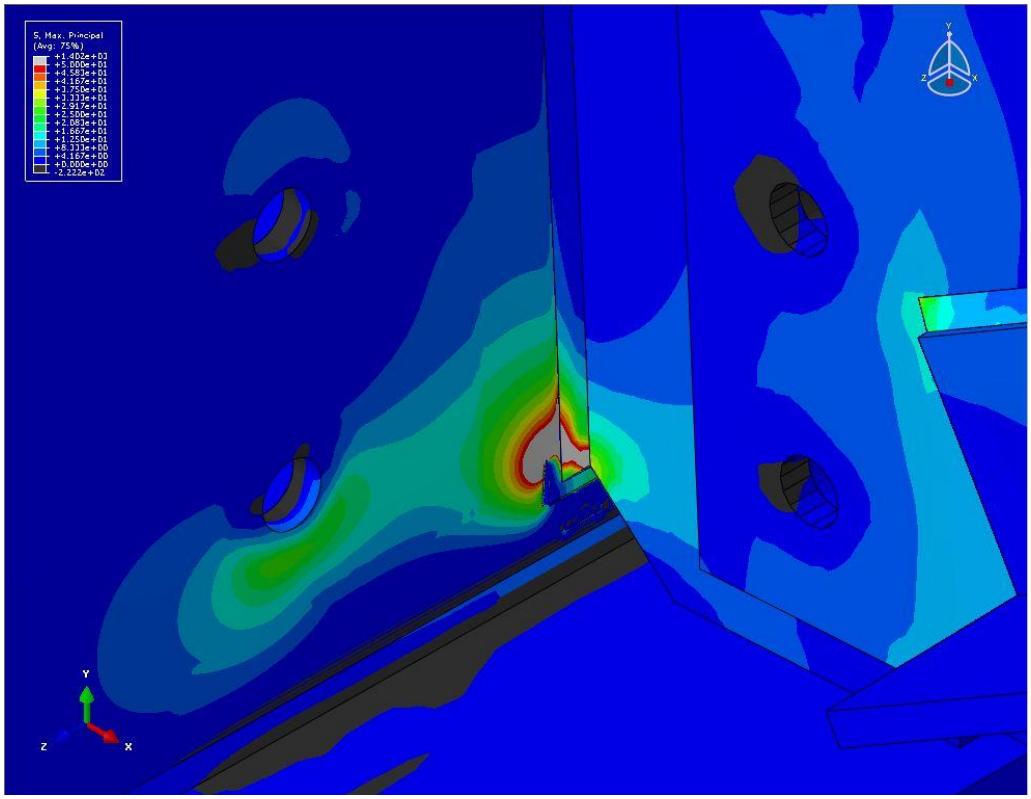

Figure I. 5: 13 mm [1/2 in.] Type 1 Crack & 13 mm [1/2 in.] Type 2 Crack with M-F Retrofit

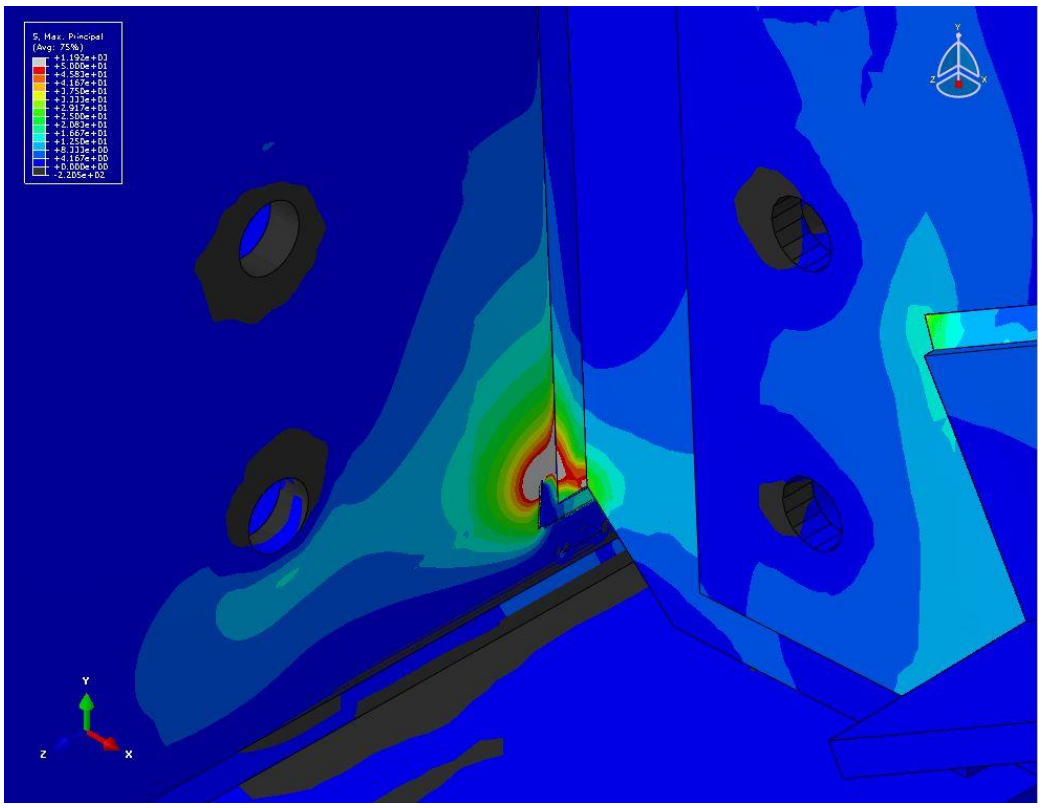

Figure I. 6: 13 mm [1/2 in.] Type 1 Crack & 13 mm [1/2 in.] Type 2 Crack with M-M Retrofit

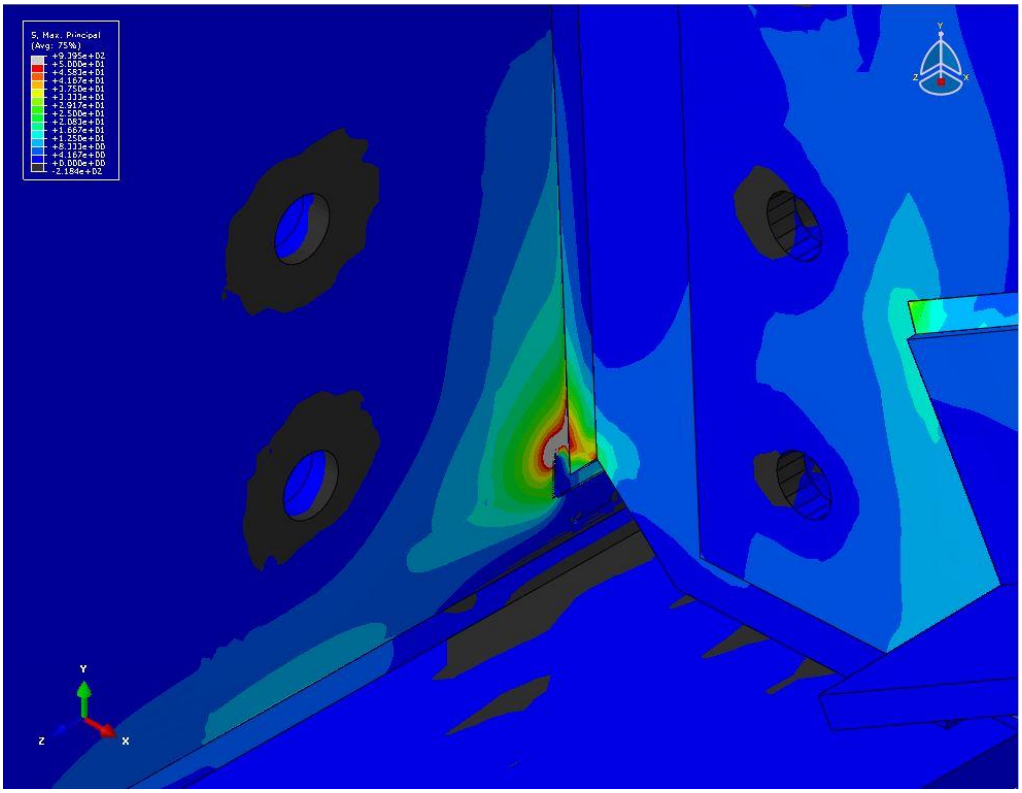

Figure I. 7: 13 mm [1/2 in.] Type 1 Crack & 13 mm [1/2 in.] Type 2 Crack with M-S Retrofit

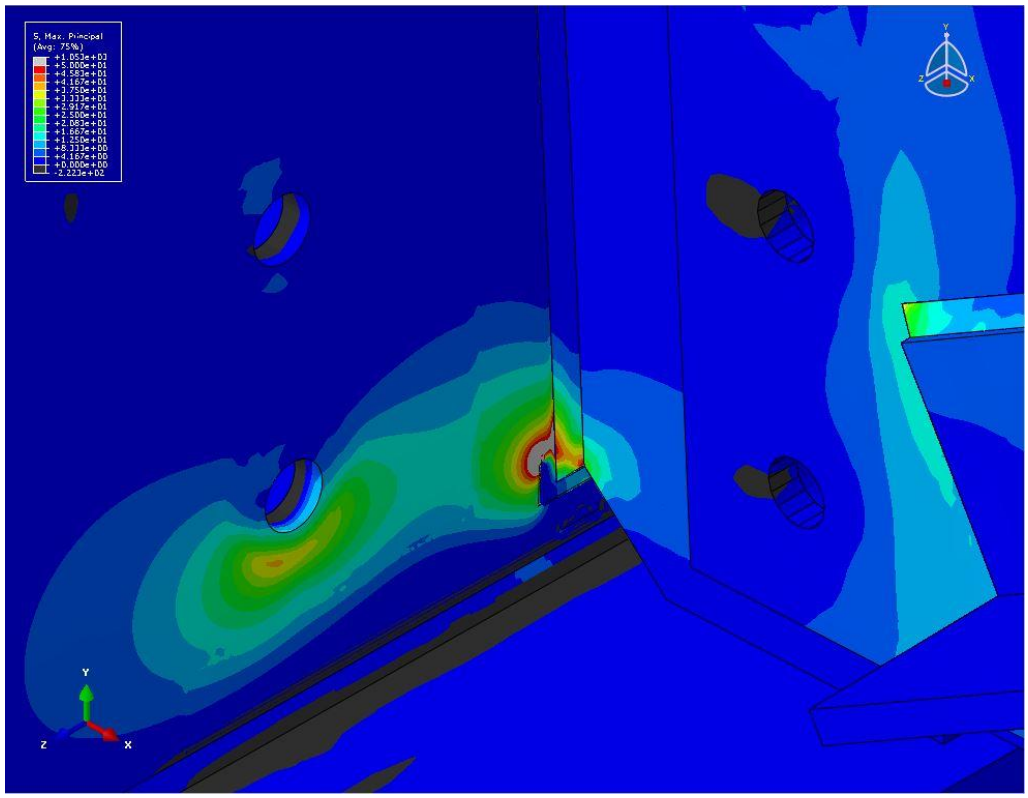

Figure I. 8: 13 mm [1/2 in.] Type 1 Crack & 13 mm [1/2 in.] Type 2 Crack with S-F Retrofit

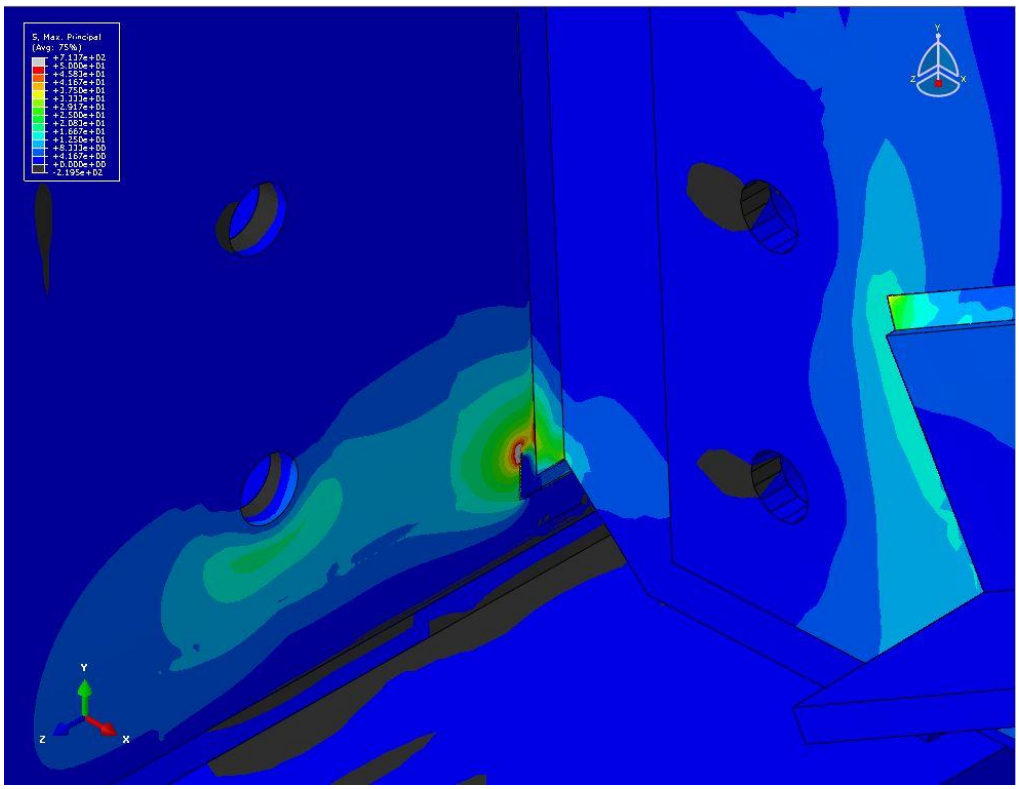

Figure I. 9: 13 mm [1/2 in.] Type 1 Crack & 13 mm [1/2 in.] Type 2 Crack with S-M Retrofit

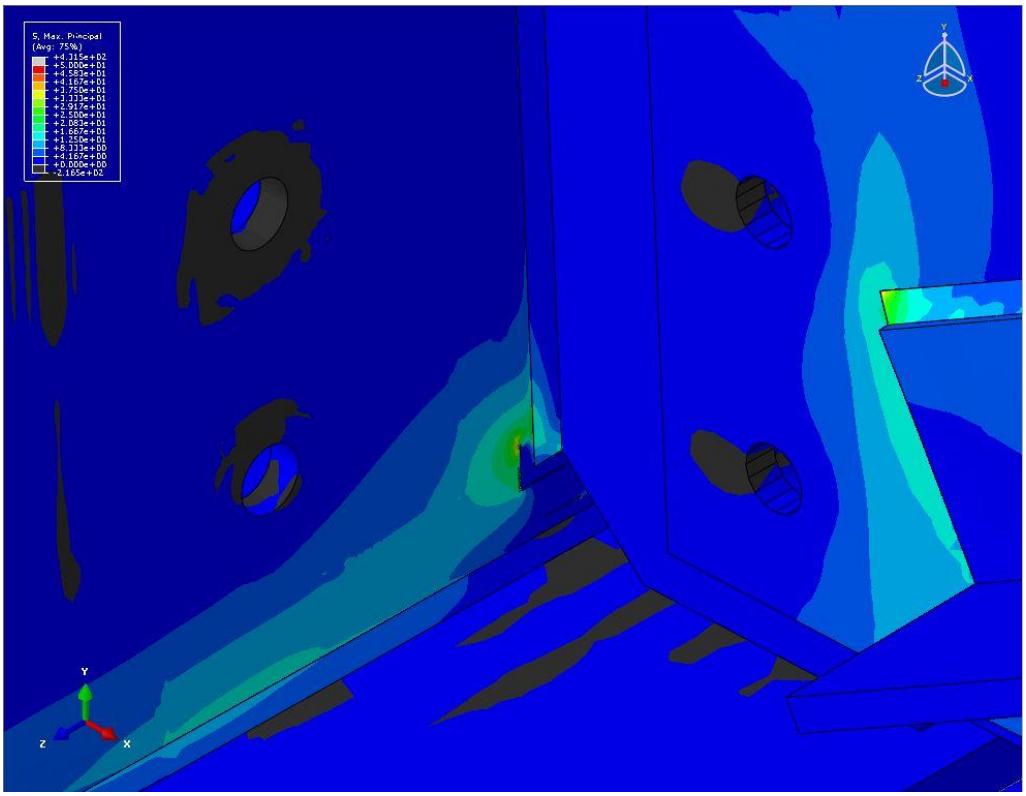

Figure I. 10: 13 mm [1/2 in.] Type 1 Crack & 13 mm [1/2 in.] Type 2 Crack with S-S Retrofit

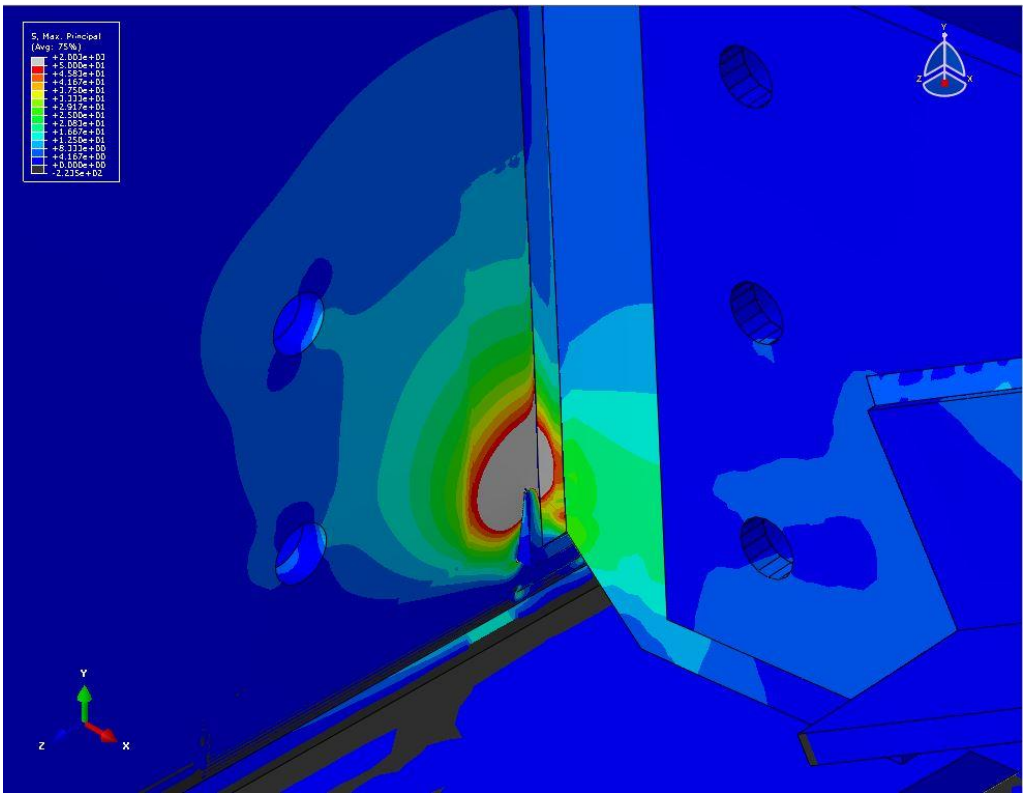

Figure I. 11: 25 mm [1in.] Type 1 Crack &25 mm [1 in.] Type 2 Crack with No Retrofit

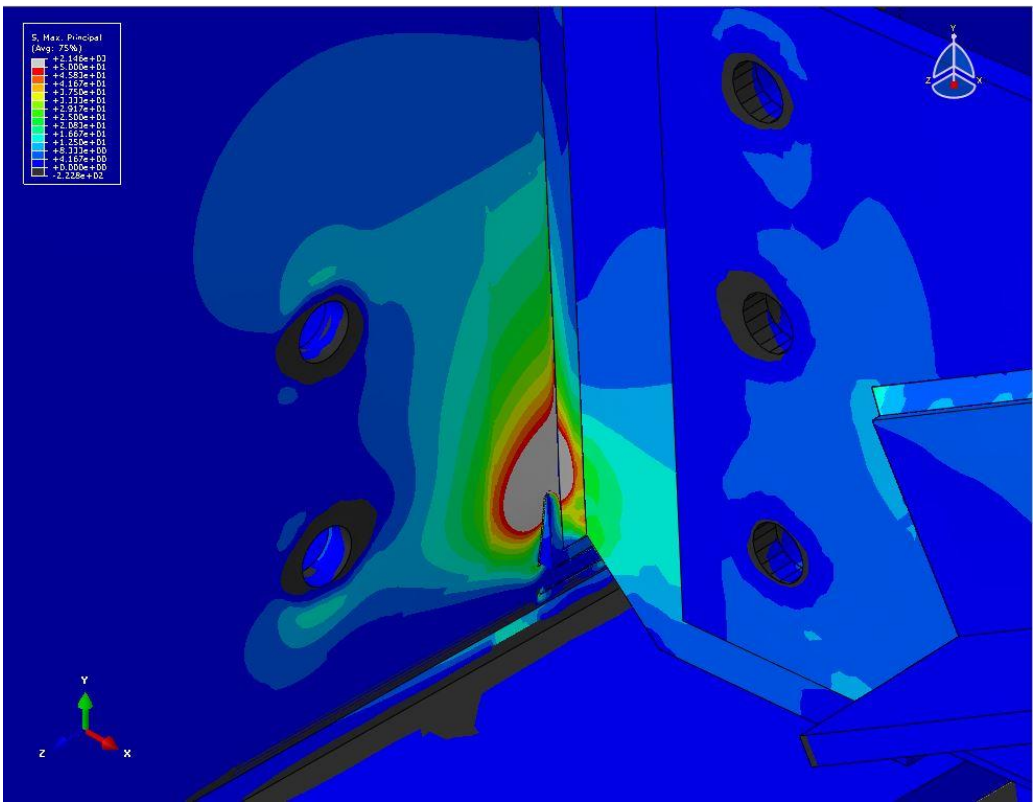

Figure I. 12: 25 mm [1 in.] Type 1 Crack &25 mm [1 in.] Type 2 Crack with F-F Retrofit

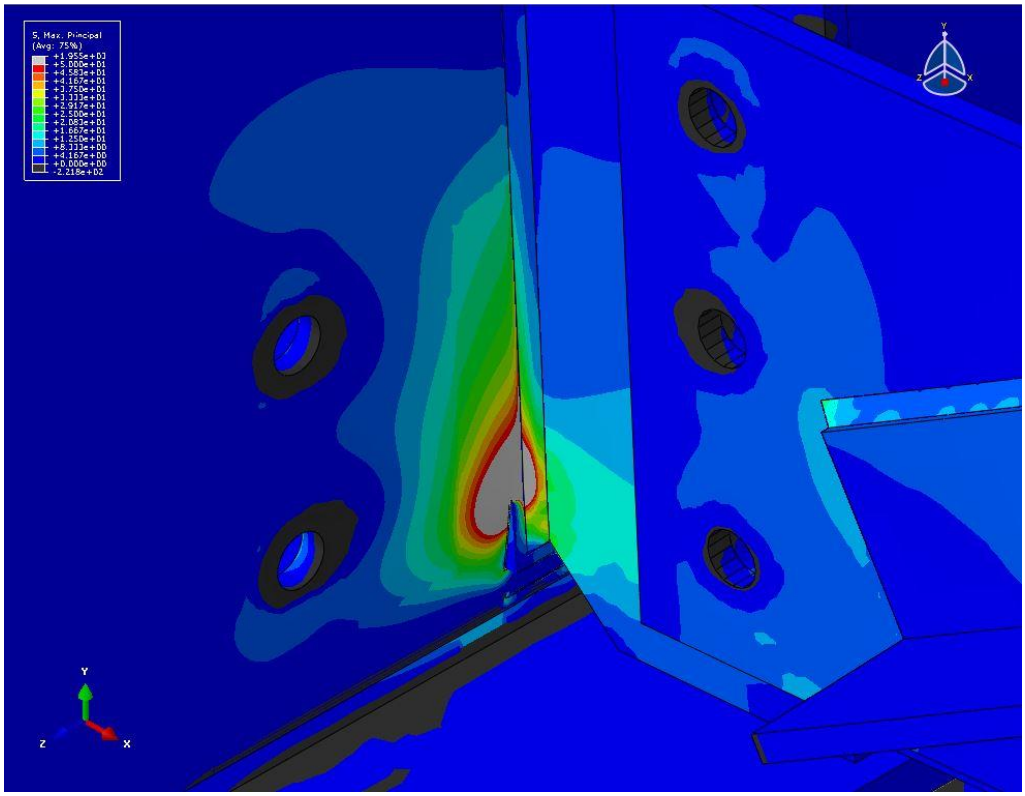

Figure I. 13: 25 mm [1 in.] Type 1 Crack &25 mm [1 in.] Type 2 Crack with F-M Retrofit

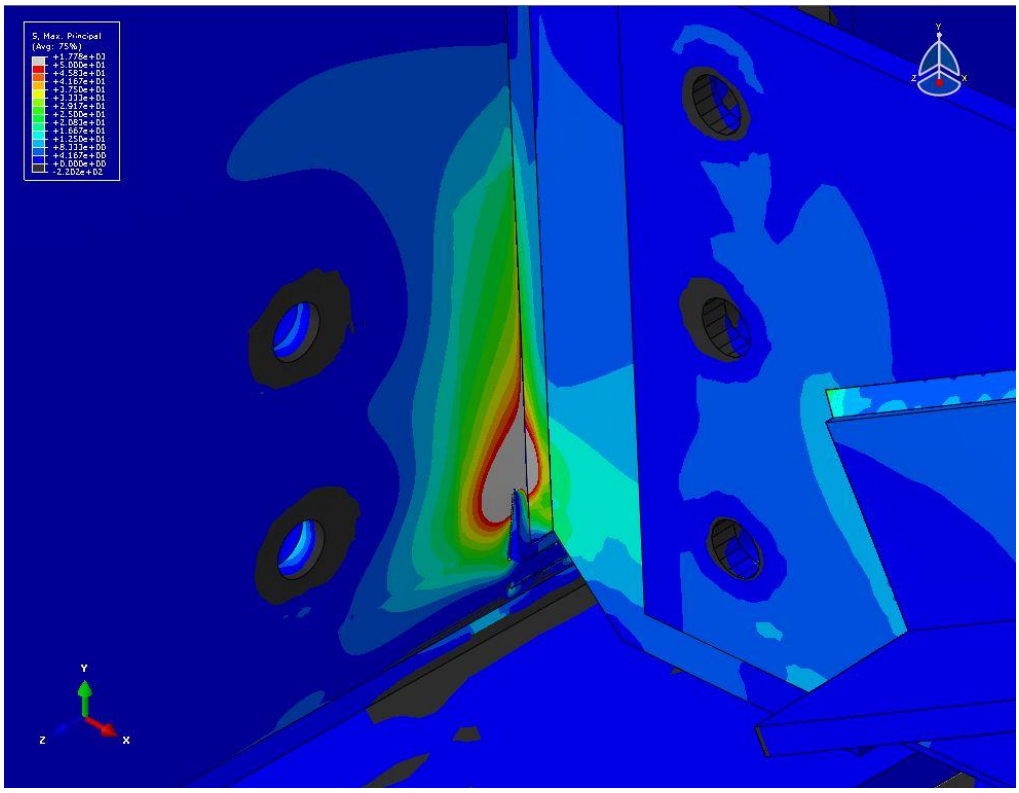

Figure I. 14: 25 mm [1 in.] Type 1 Crack &25 mm [1 in.] Type 2 Crack with F-S Retrofit

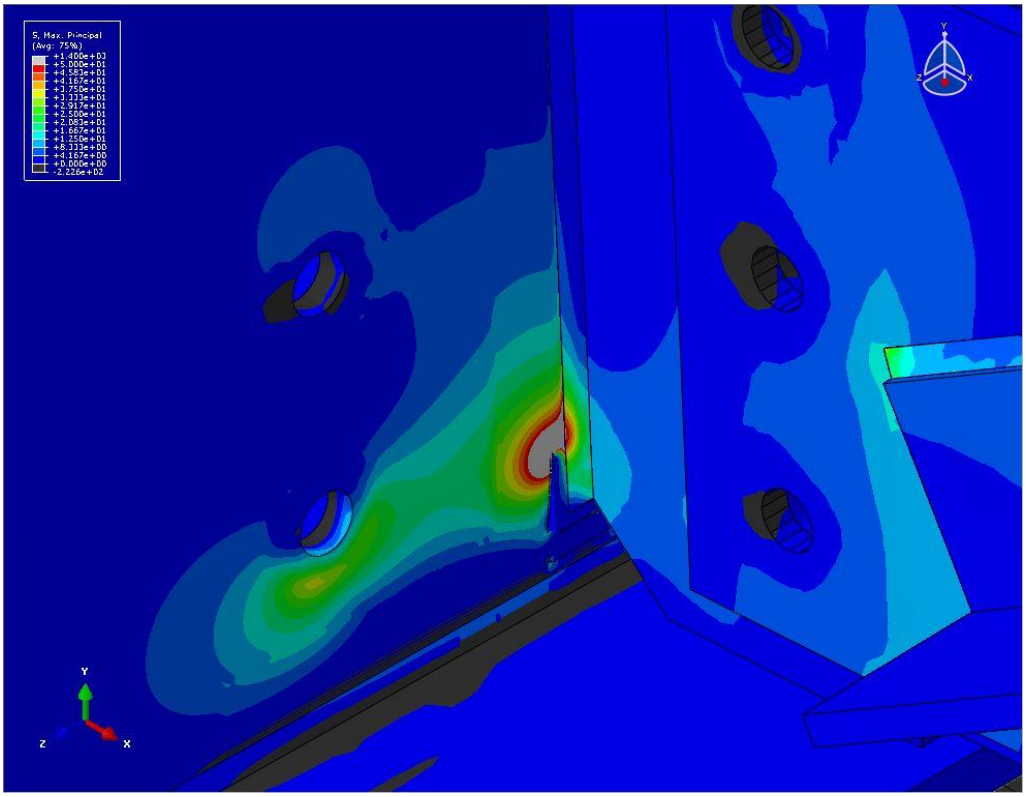

Figure I. 15: 25 mm [1 in.] Type 1 Crack &25 mm [1 in.] Type 2 Crack with M-F Retrofit

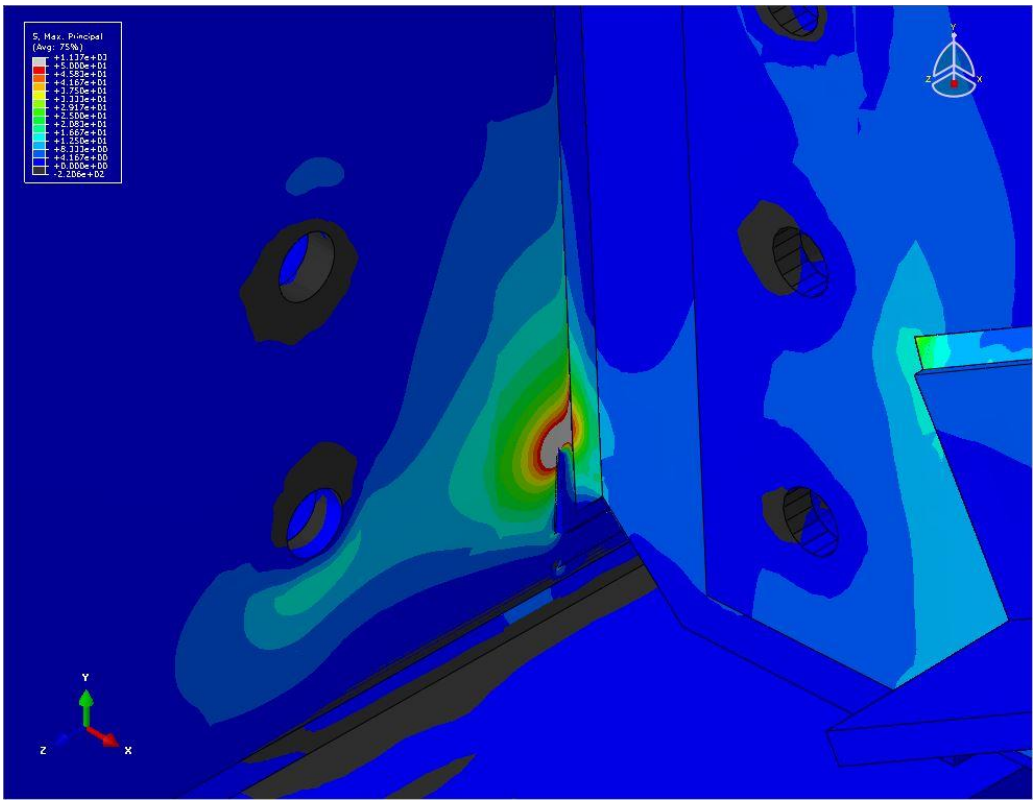

Figure I. 16: 25 mm [1 in.] Type 1 Crack &25 mm [1 in.] Type 2 Crack with M-M Retrofit

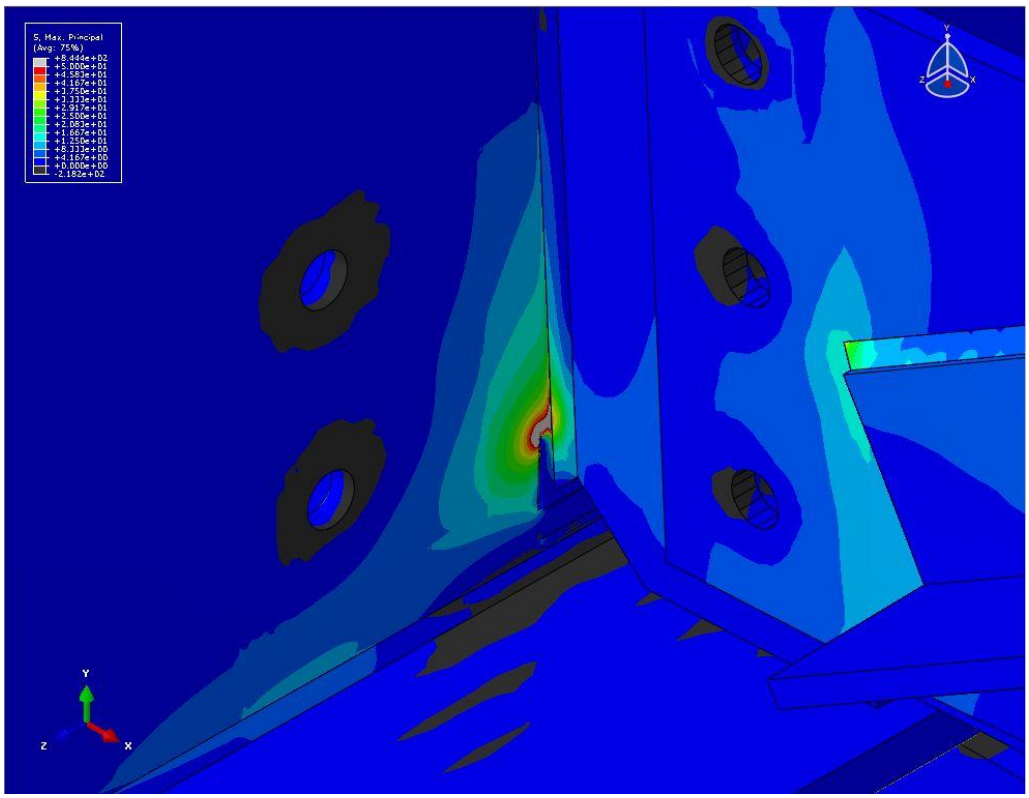

Figure I. 17: 25 mm [1 in.] Type 1 Crack &25 mm [1 in.] Type 2 Crack with M-S Retrofit

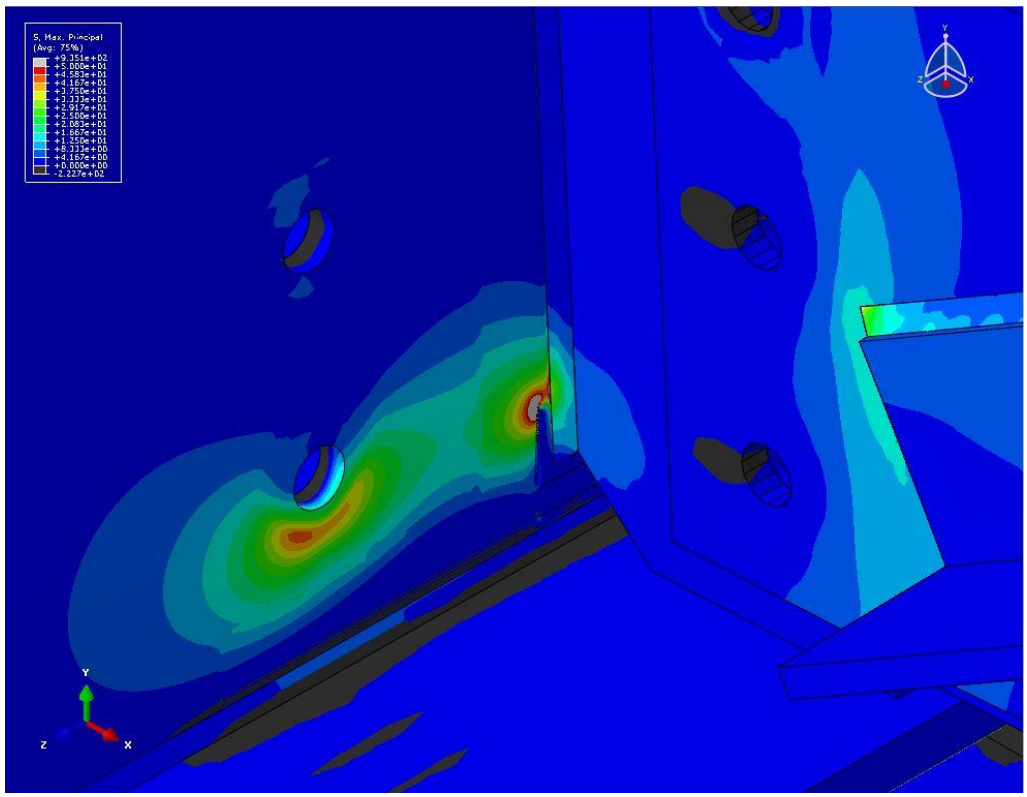

Figure I. 18: 25 mm [1 in.] Type 1 Crack &25 mm [1 in.] Type 2 Crack with S-F Retrofit

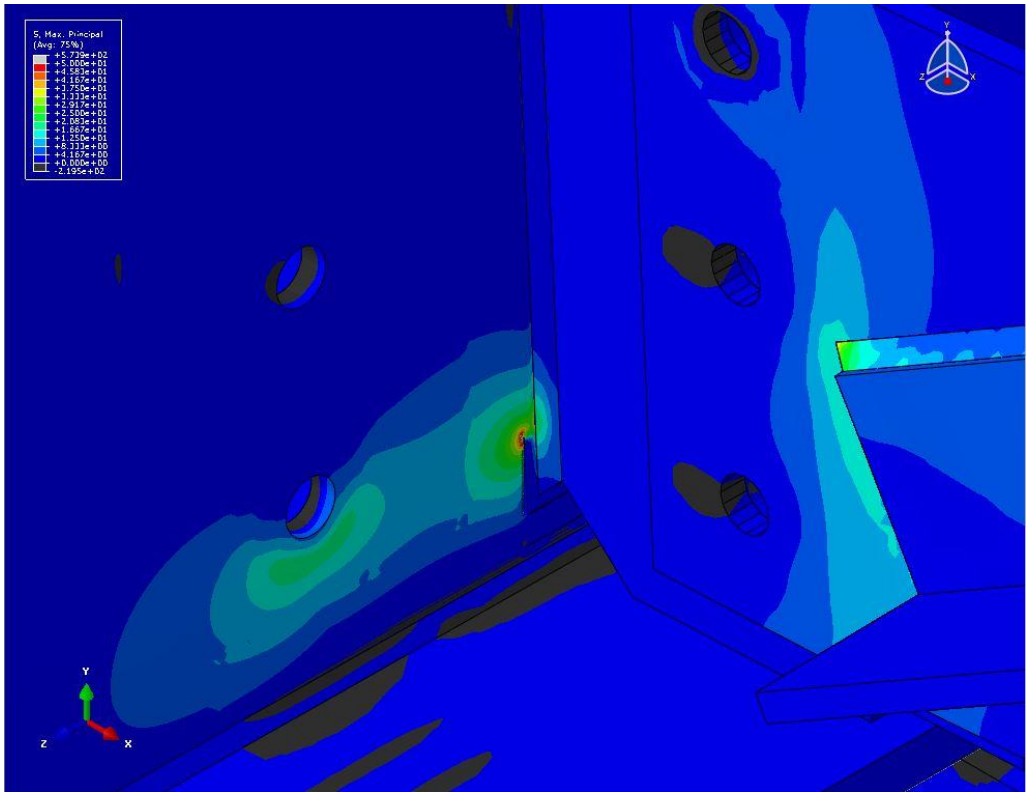

Figure I. 19: 25 mm [1 in.] Type 1 Crack &25 mm [1 in.] Type 2 Crack with S-M Retrofit

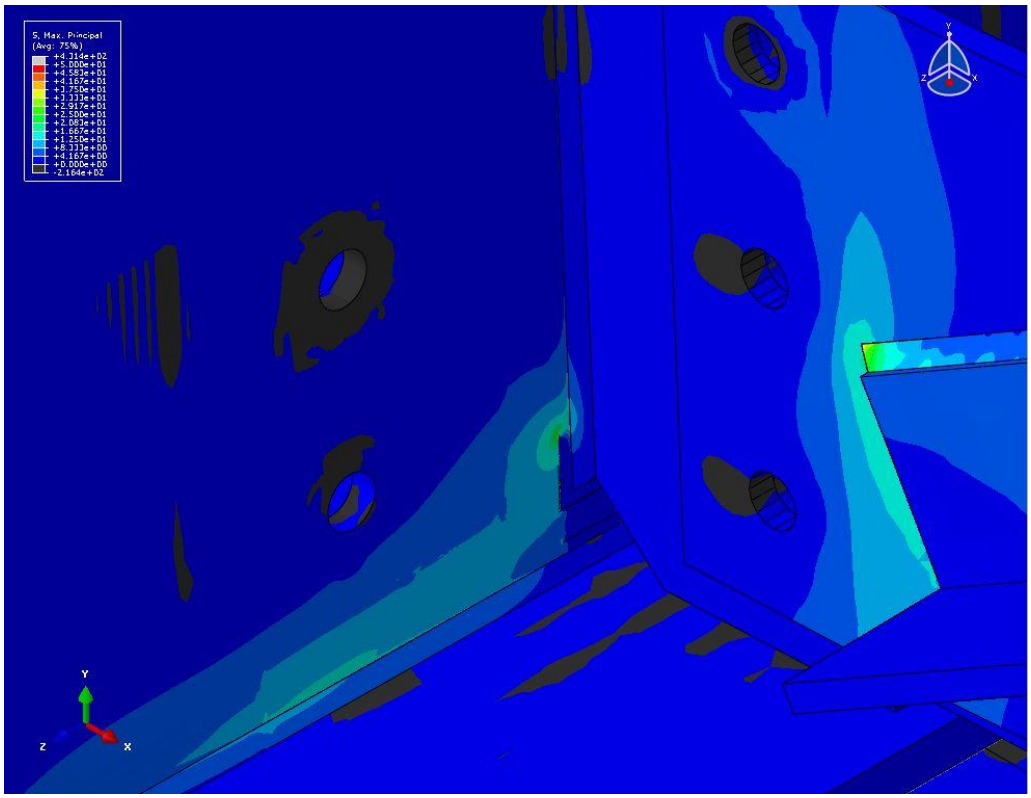

Figure I. 20: 25 mm [1 in.] Type 1 Crack &25 mm [1 in.] Type 2 Crack with S-S Retrofit

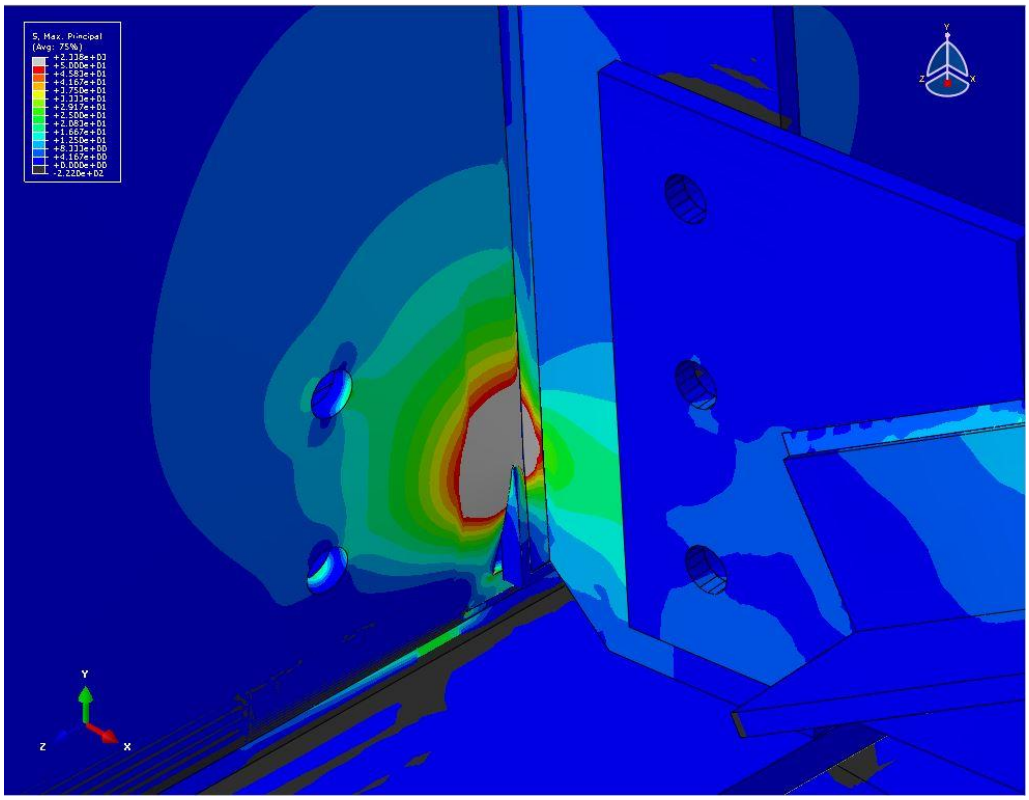

Figure I. 21: 51 mm [2 in.] Type 1 Crack &51 mm [2 in.] Type 2 Crack with No Retrofit

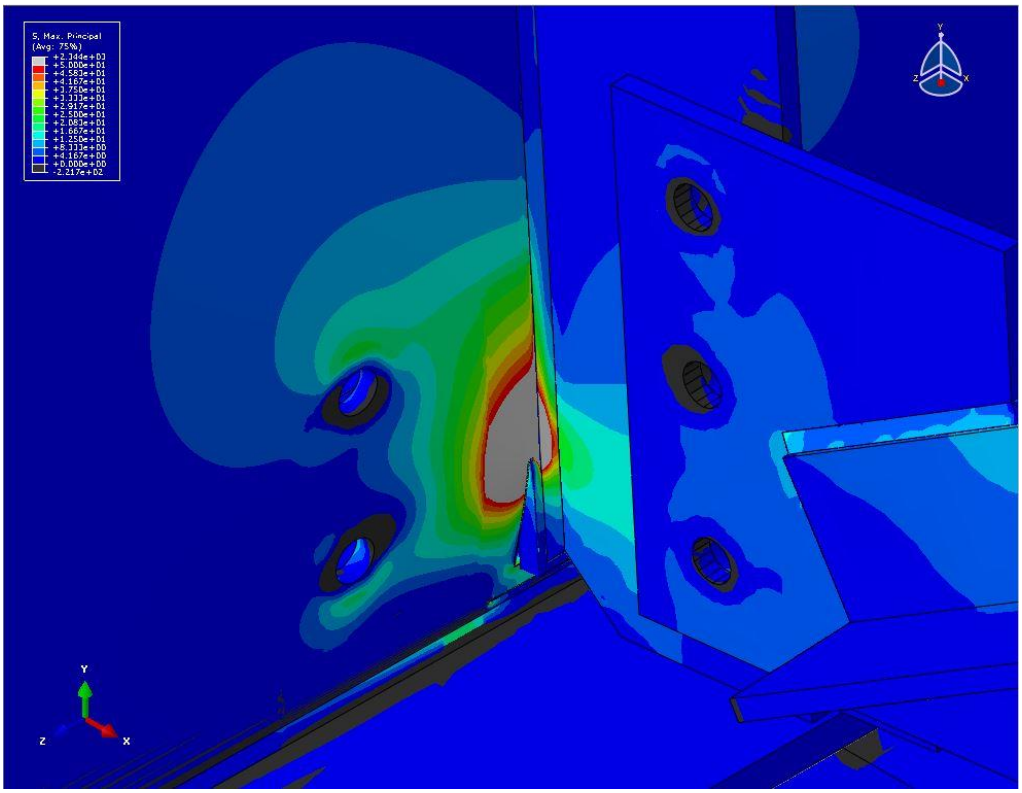

Figure I. 22: 51 mm [2 in.] Type 1 Crack &51 mm [2 in.] Type 2 Crack with F-F Retrofit

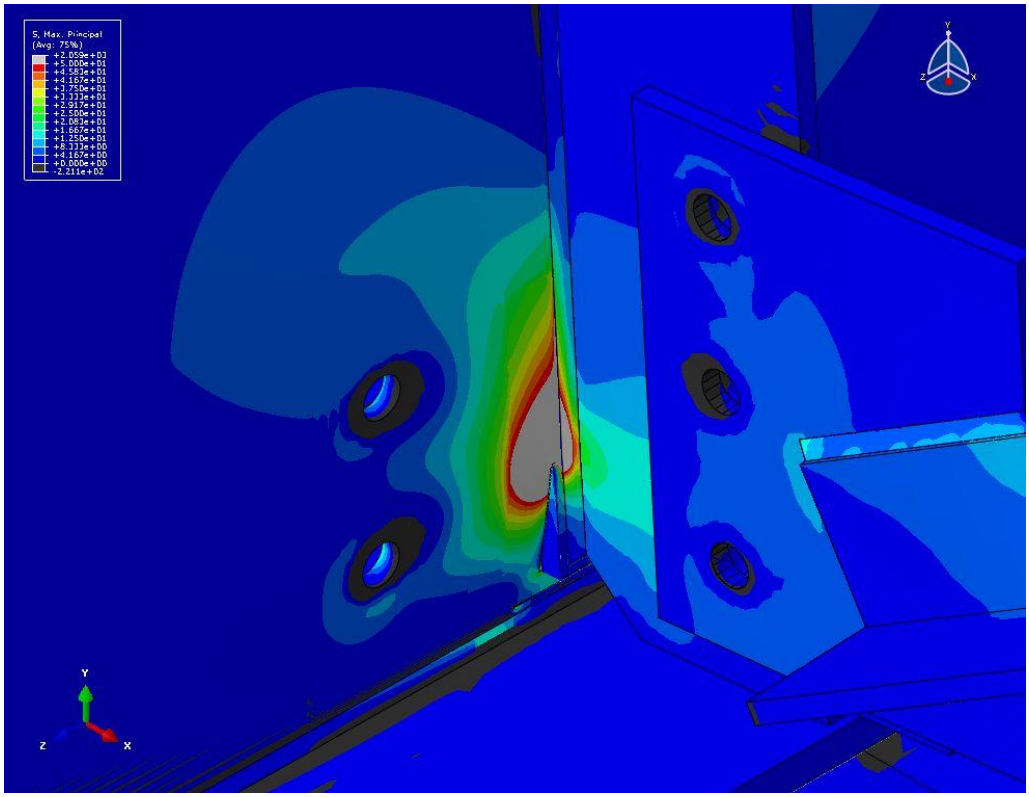

Figure I. 23: 51 mm [2 in.] Type 1 Crack &51 mm [2 in.] Type 2 Crack with F-M Retrofit

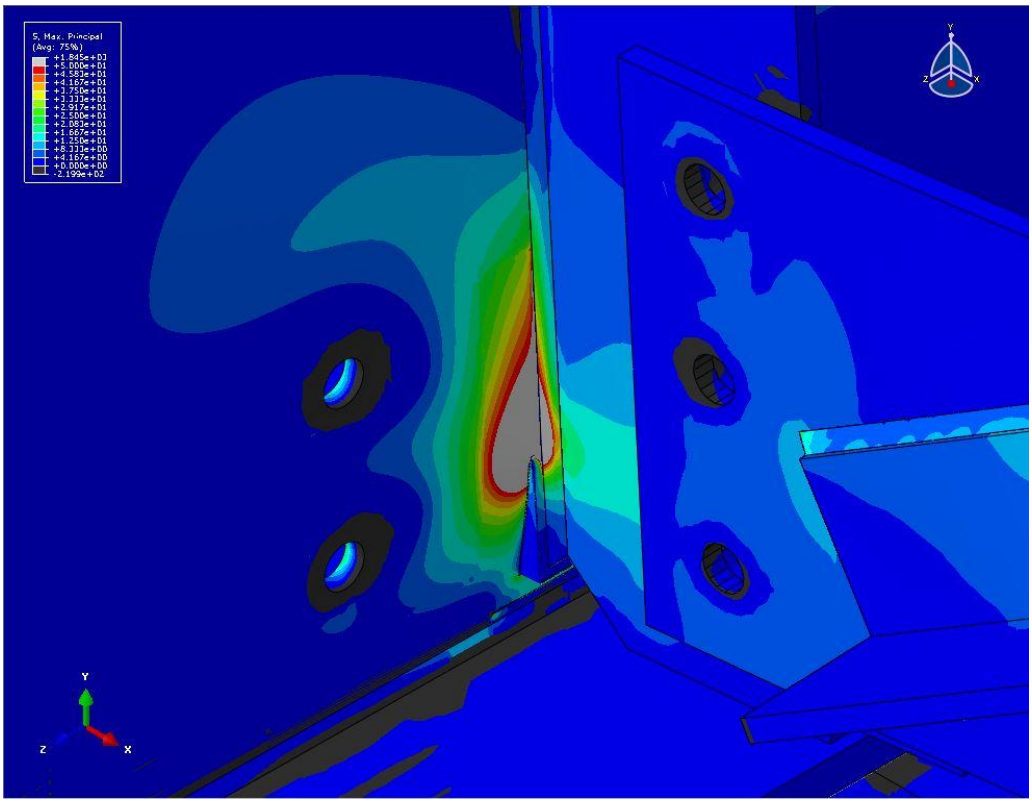

Figure I. 24: 51 mm [2 in.] Type 1 Crack &51 mm [2 in.] Type 2 Crack with F-S Retrofit

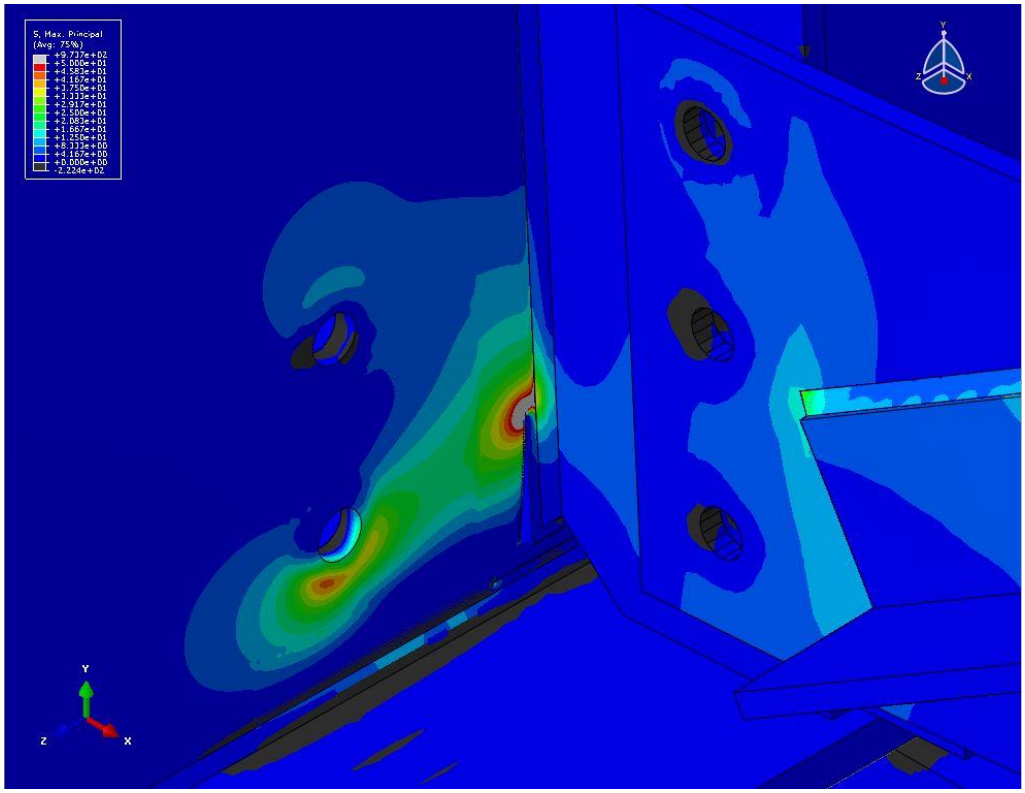

Figure I. 25: 51 mm [2 in.] Type 1 Crack &51 mm [2 in.] Type 2 Crack with M-F Retrofit

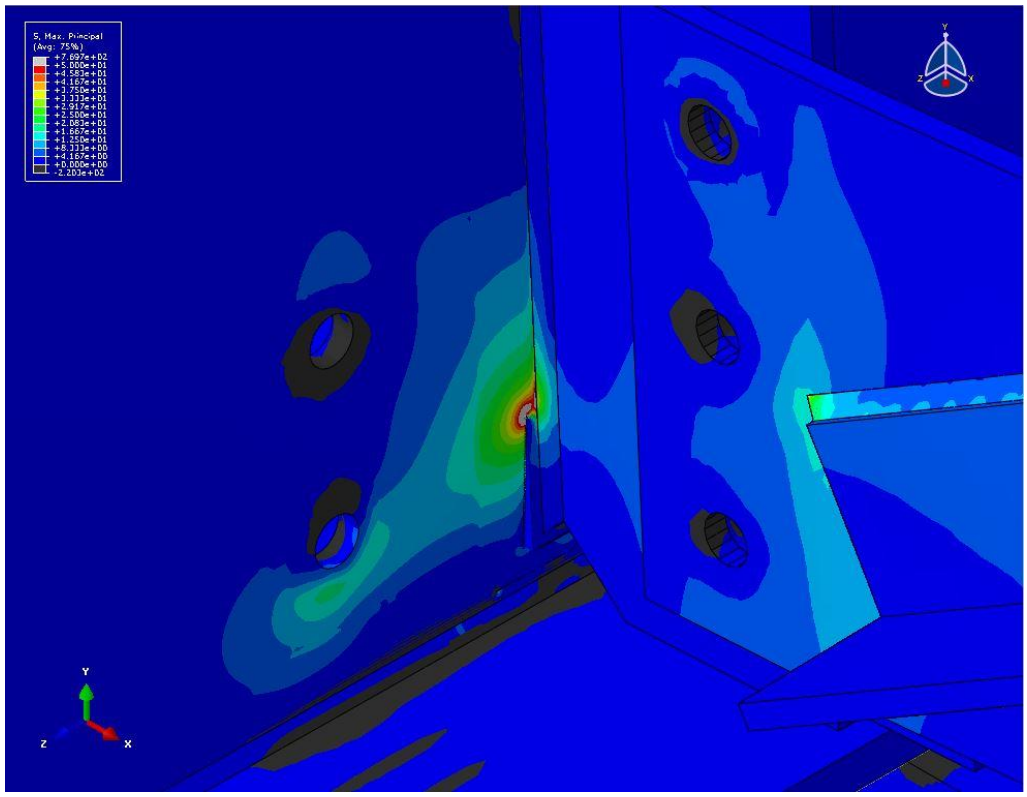

Figure I. 26: 51 mm [2 in.] Type 1 Crack &51 mm [2 in.] Type 2 Crack with M-M Retrofit

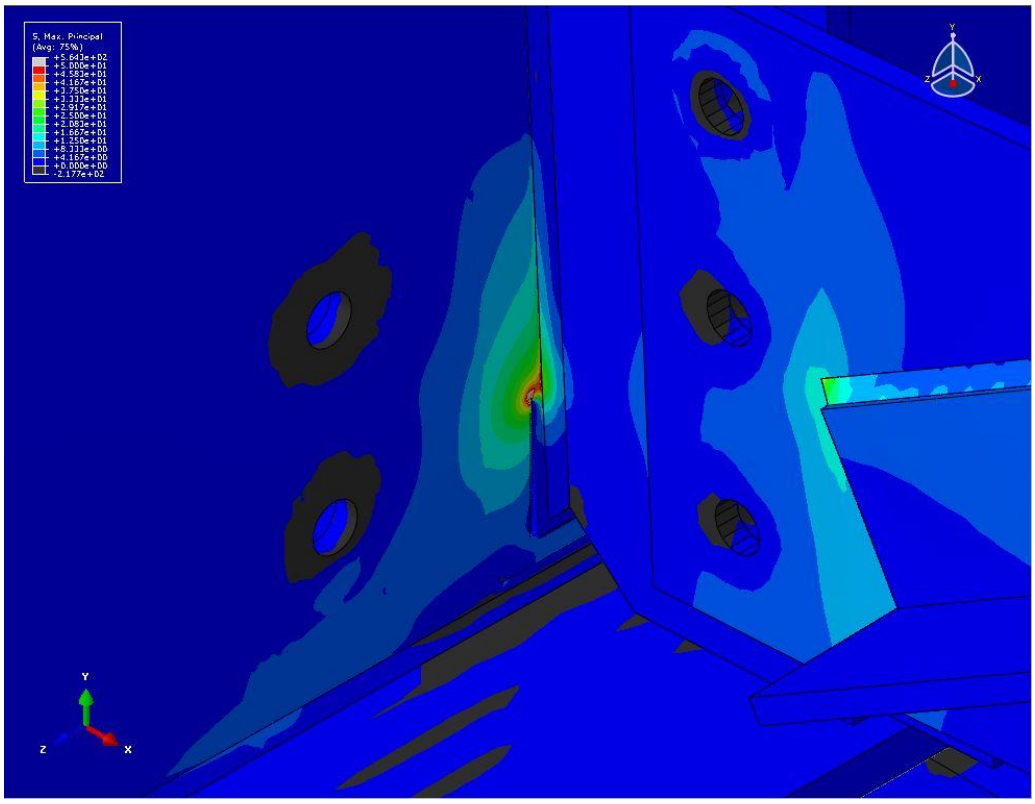

Figure I. 27: 51 mm [2 in.] Type 1 Crack &51 mm [2 in.] Type 2 Crack with M-S Retrofit

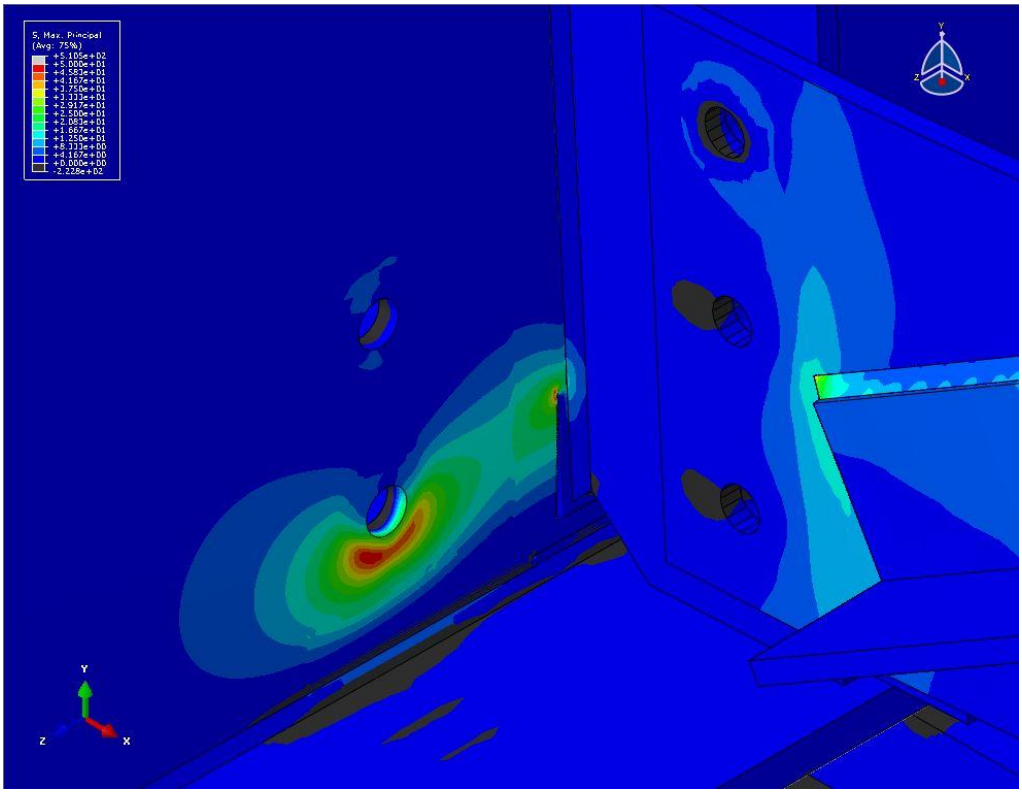

Figure I. 28: 51 mm [2 in.] Type 1 Crack &51 mm [2 in.] Type 2 Crack with S-F Retrofit

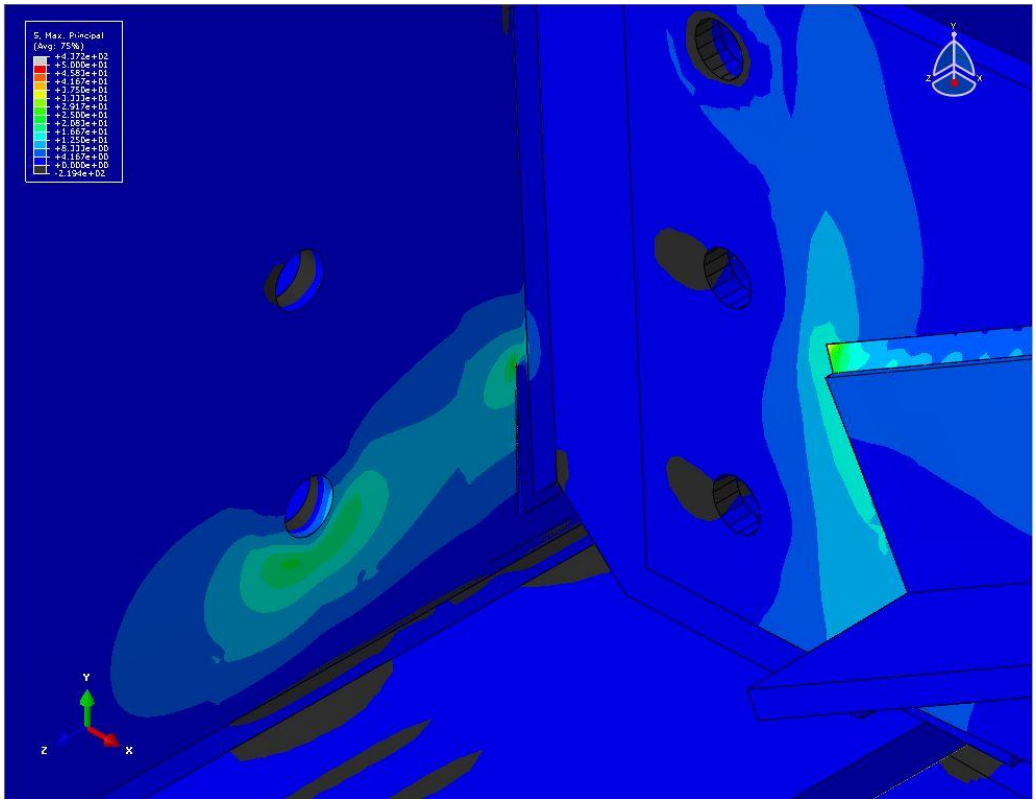

Figure I. 29: 51 mm [2 in.] Type 1 Crack &51 mm [2 in.] Type 2 Crack with S-M Retrofit

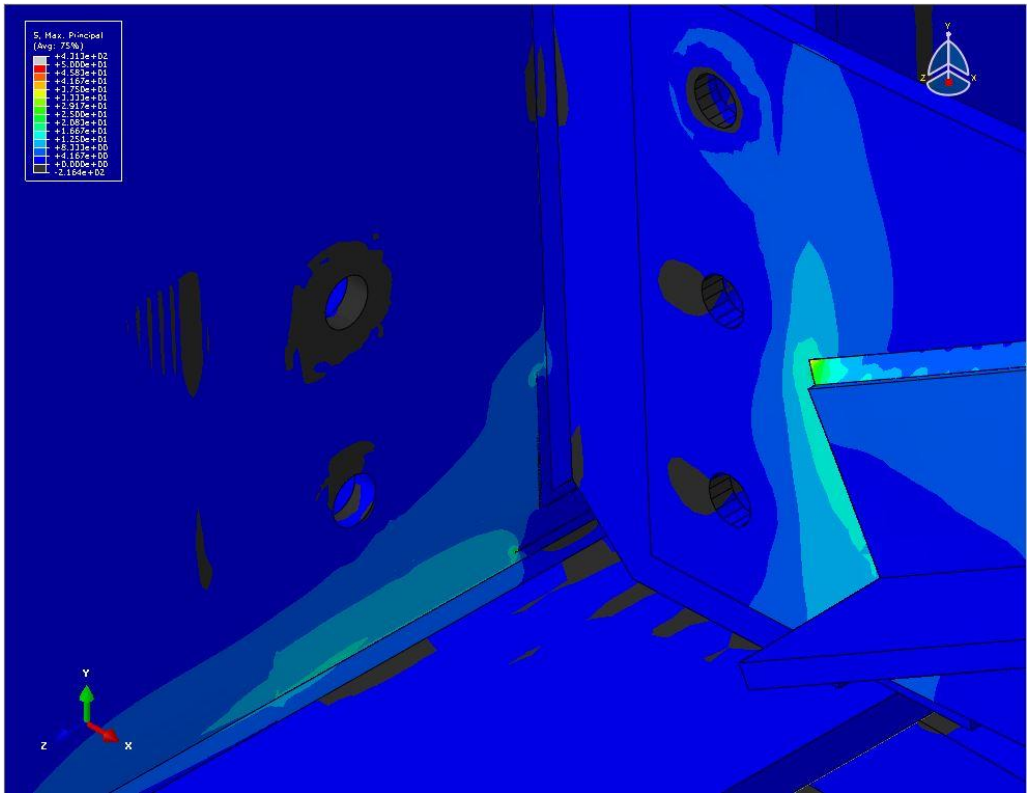

Figure I. 30: 51 mm [2 in.] Type 1 Crack &51 mm [2 in.] Type 2 Crack with S-S Retrofit

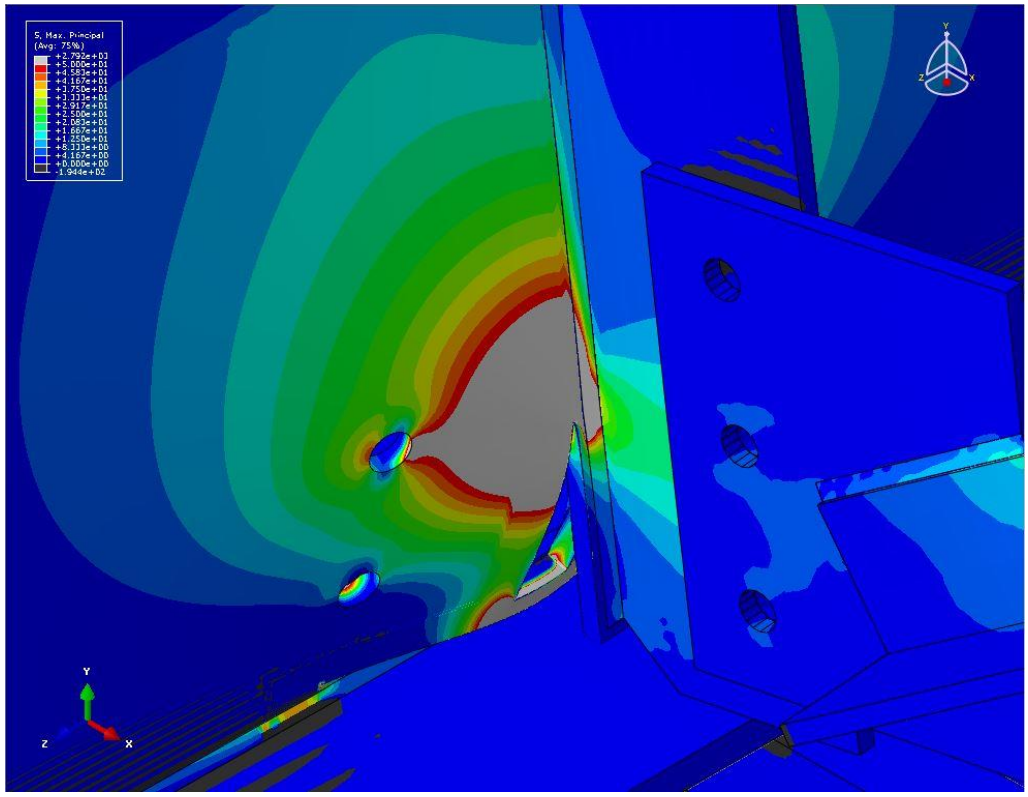

Figure I. 31: 102 mm [4 in.] Type 1 Crack &203 mm [8 in.] Type 2 Crack with No Retrofit

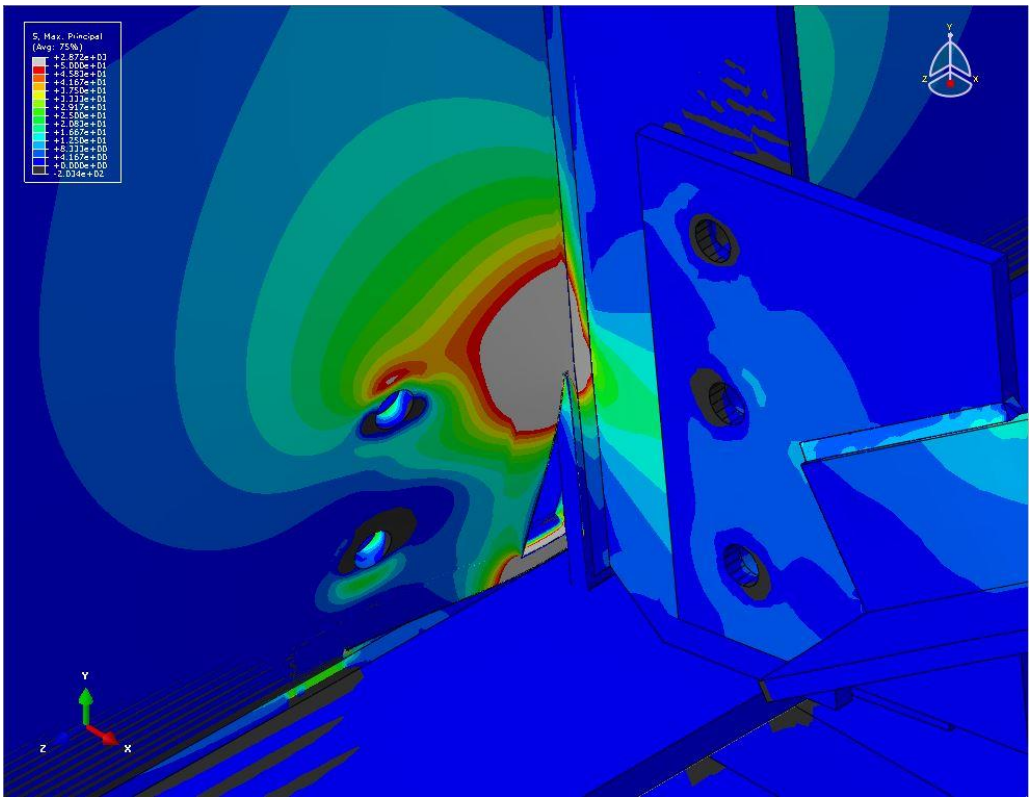

Figure I. 32: 102 mm [4 in.] Type 1 Crack &203 mm [8 in.] Type 2 Crack with F-F Retrofit

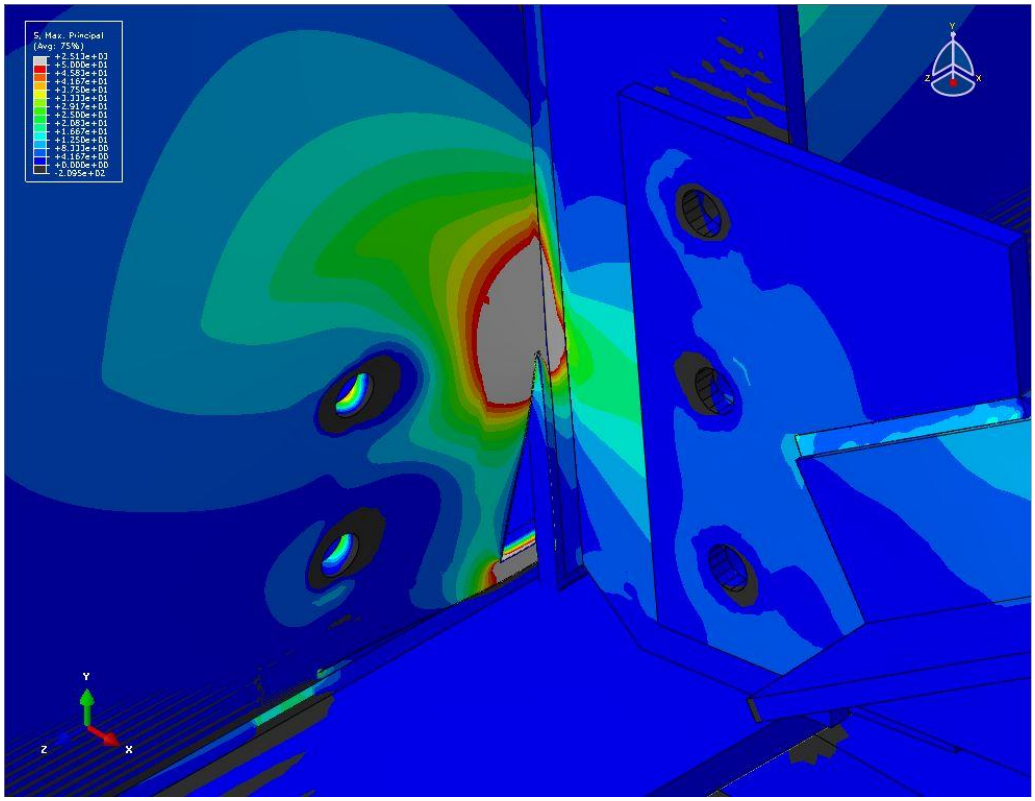

Figure I. 33: 102 mm [4 in.] Type 1 Crack &203 mm [8 in.] Type 2 Crack with F-M Retrofit

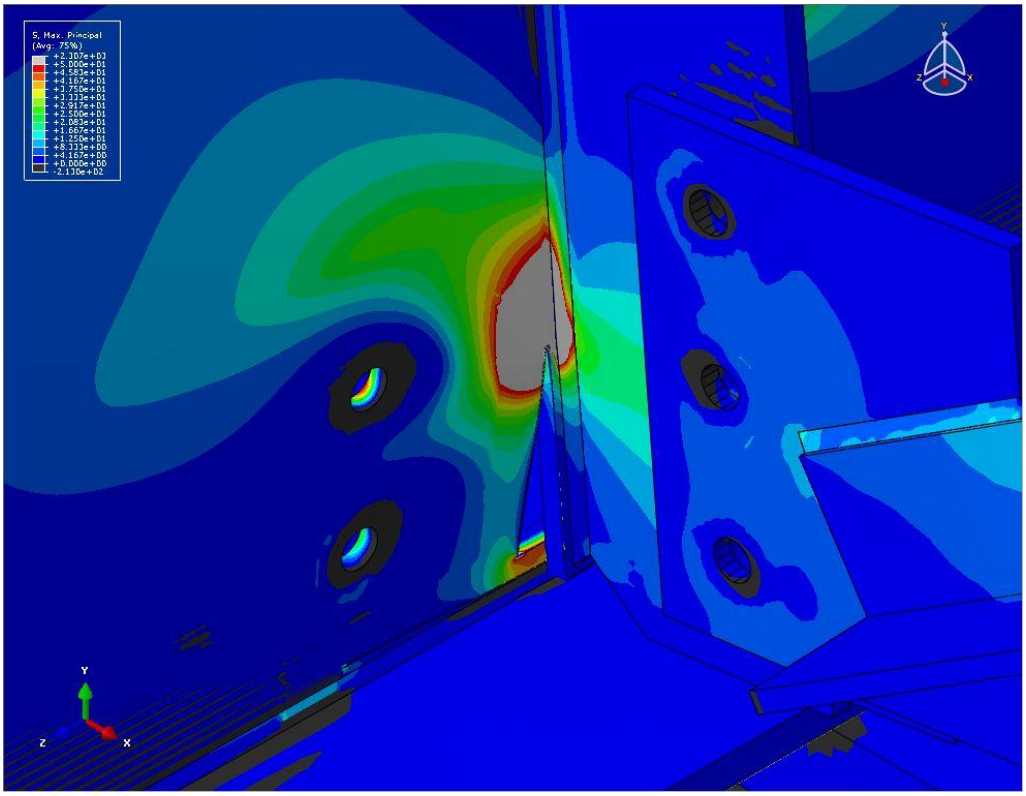

Figure I. 34: 102 mm [4 in.] Type 1 Crack &203 mm [8 in.] Type 2 Crack with F-S Retrofit

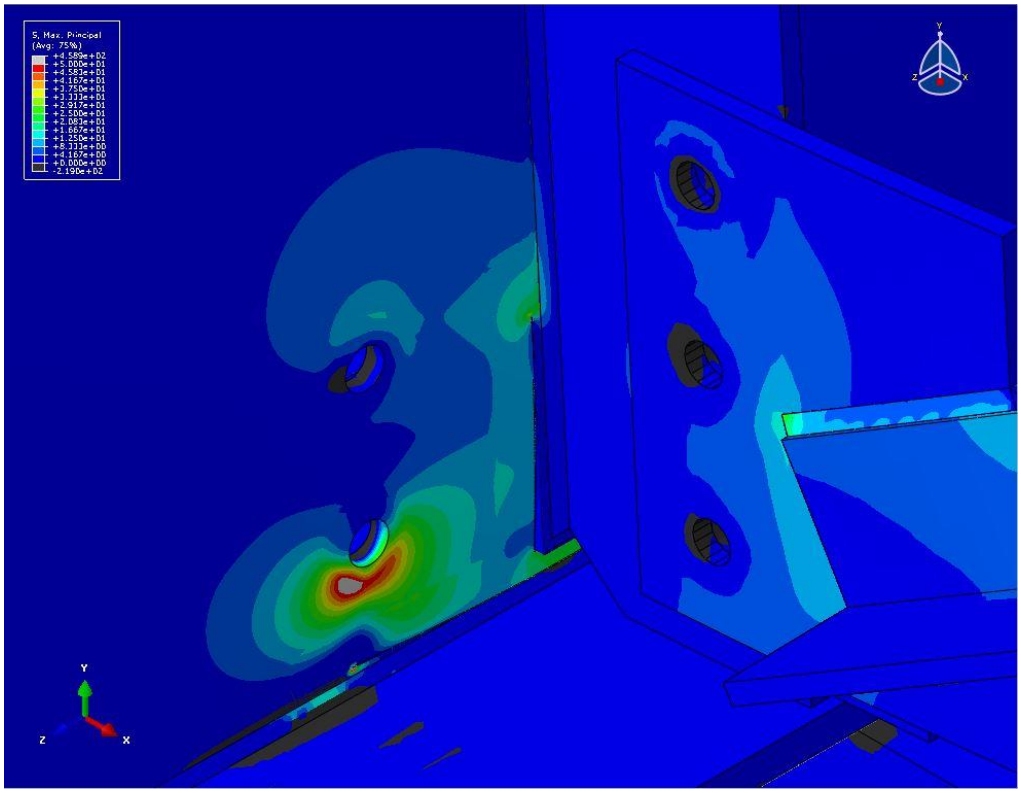

Figure I. 35: 102 mm [4 in.] Type 1 Crack &203 mm [8 in.] Type 2 Crack with M-F Retrofit

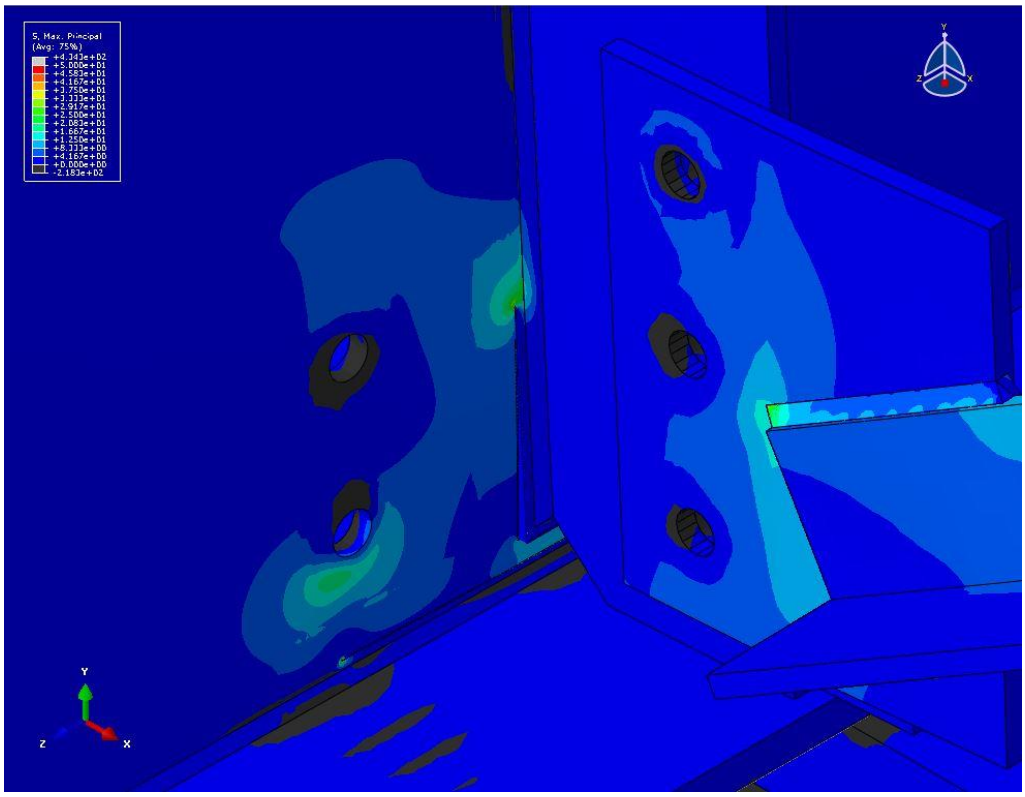

Figure I. 36: 102 mm [4 in.] Type 1 Crack &203 mm [8 in.] Type 2 Crack with M-M Retrofit

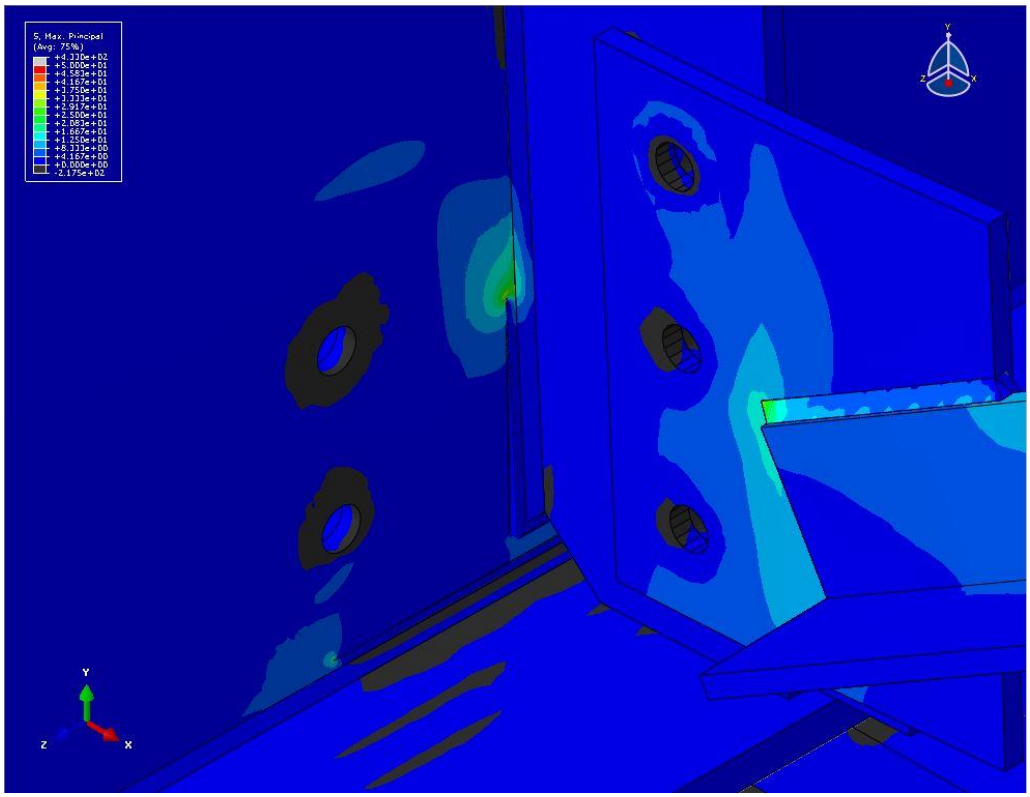

Figure I. 37: 102 mm [4 in.] Type 1 Crack &203 mm [8 in.] Type 2 Crack with M-S Retrofit

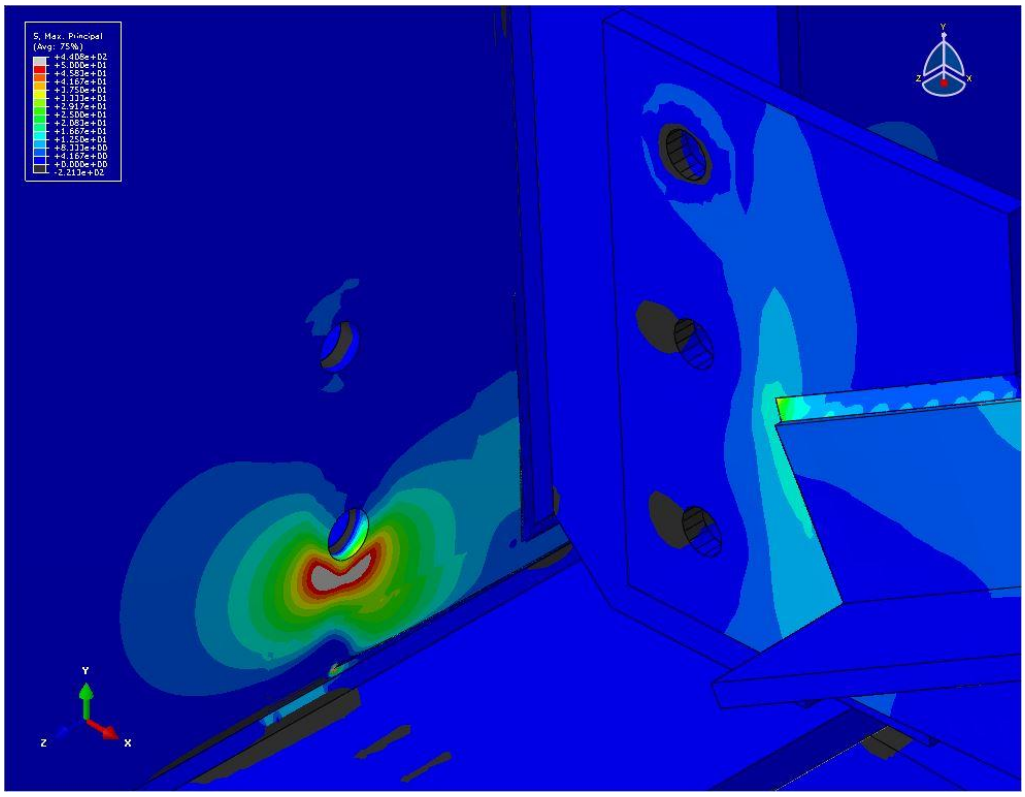

Figure I. 38: 102 mm [4 in.] Type 1 Crack &203 mm [8 in.] Type 2 Crack with S-F Retrofit

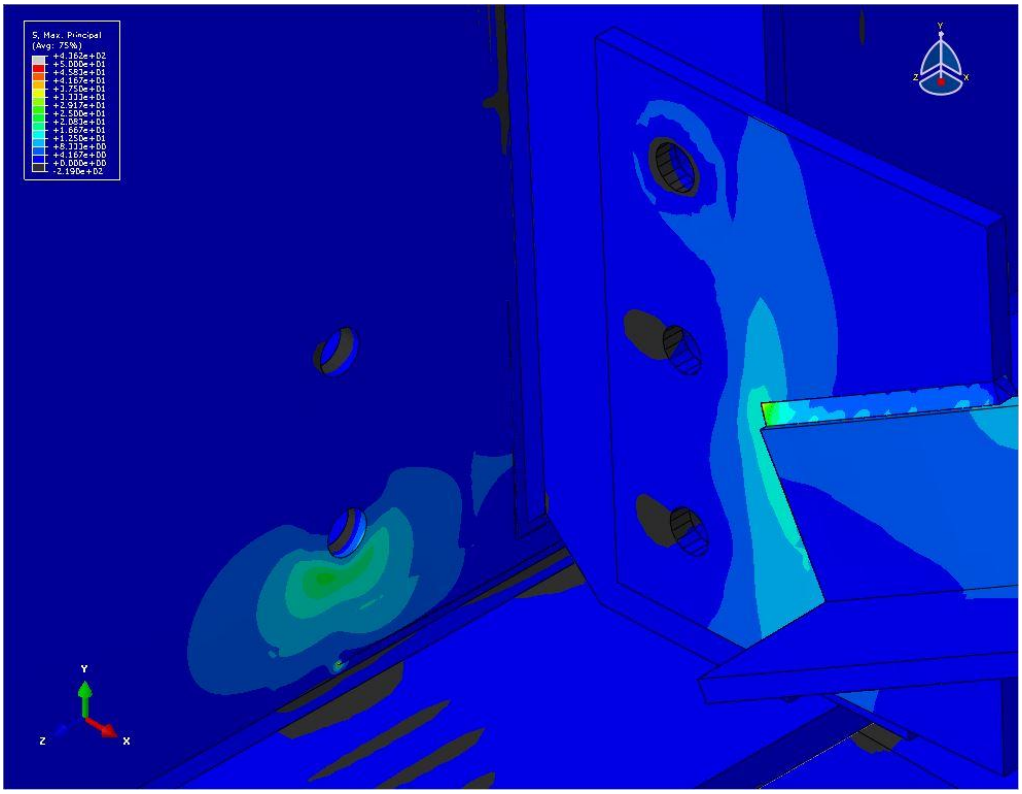

Figure I. 39: 102 mm [4 in.] Type 1 Crack &203 mm [8 in.] Type 2 Crack with S-M Retrofit

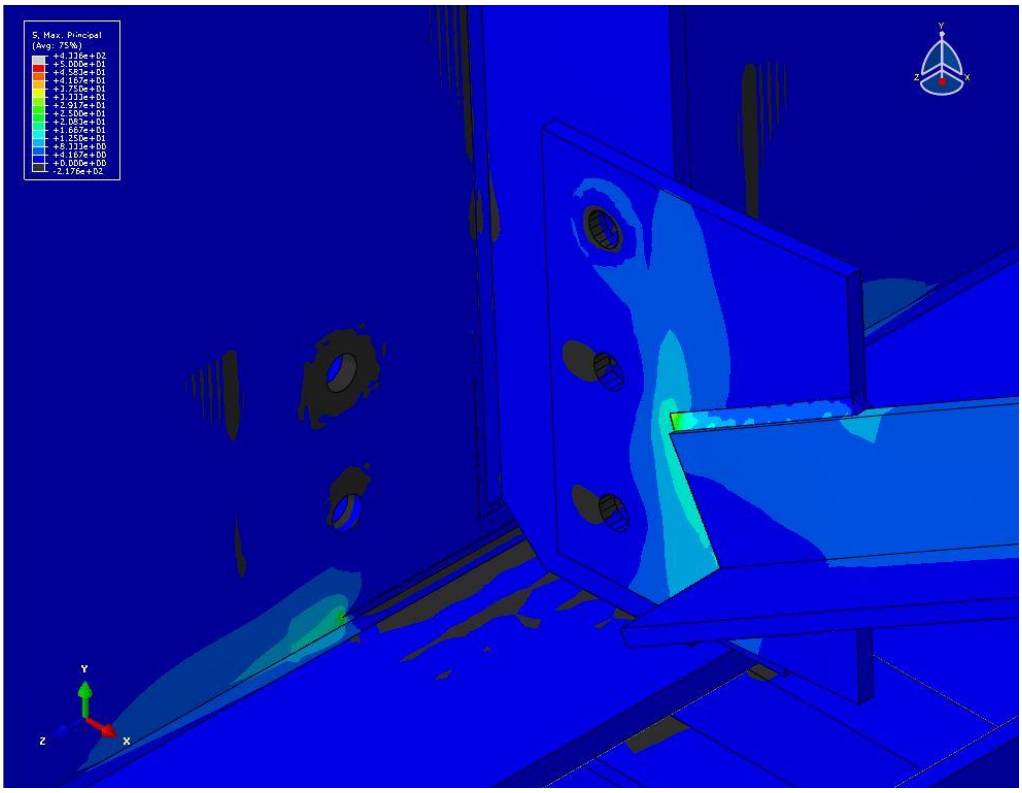

Figure I. 40: 102 mm [4 in.] Type 1 Crack &203 mm [8 in.] Type 2 Crack with S-S Retrofit

APPENDIX J: BOLT MODELING TECHNIQUES

Steps to create a bolt and apply a bolt load

1. The 3-dimentional bolts were modeled as a revolution part, which was then partitioned into three parts: the shank, nut, and headin the *Parts Module* with the diameter needed. The AISC Specification lists all bolts dimensions. The middle of the shank was partitioned in half so the bolt load could be applied to the interior face of the shank.

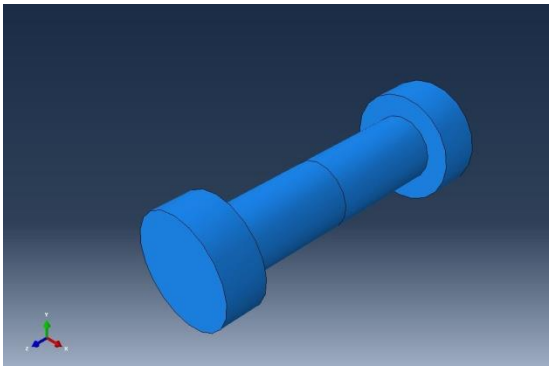

Figure J. 1: Created bolt part.

2. Apply section properties for the bolts.
3. Create a pre-tensioning step after the Initial Step and before the Load Step.
4. Apply a pre-tensioning load to the interior surface of the shank based on the AISC Specification in the Pre-Tensioning Step. In the Loads Module select Create Load, and name the load. Choose the Pre-Tensioning Step, Mechanical under *Category*, select Bolt Load under the section entitled *Types for Selected Step*.

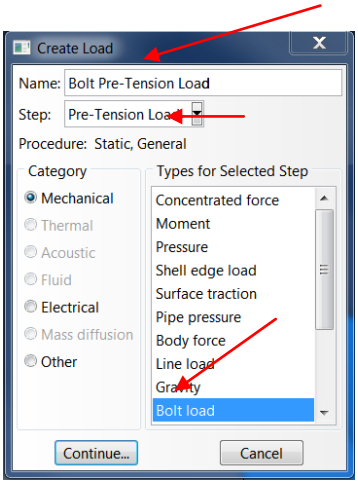

Figure J. 2: The bolt load must be named. The bolt load should be applied in the step before the load is applied.

5. The program will prompt you to select interior surfaces for the bolt load.

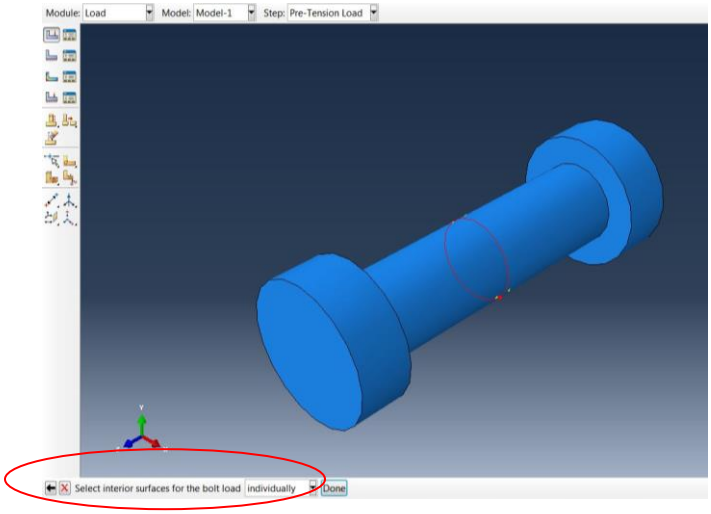

Figure J. 3: Apply bolt load to the interior surface of the shank.

6. Next it will ask you to choose a side for the shell or internal faces- brown or purple. Select the color that appears on the interior surface you selected.

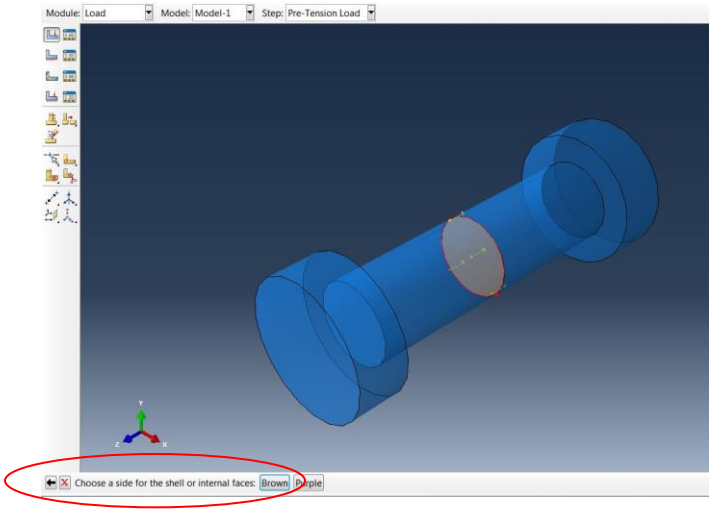

Figure J. 4: Select a side for the internal surface depending on what color is shown. In this figure, the interior surface is highlighted brown, therefore select brown.

7. Select the datum axis that is aligned with the bolt centerline. This specifies in what direction the load will be applied. Frequently you have to display all instances in order to see the datum axis.

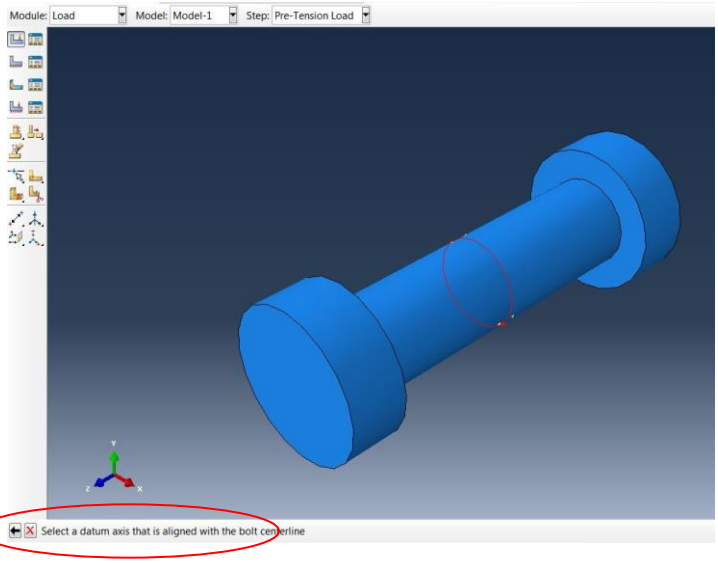

Figure J. 5: Select the datum axis that corresponds to the longitudinal axis of the bolt. In this case, the datum axis should be z.

8. Enter the pre-tensioning load.

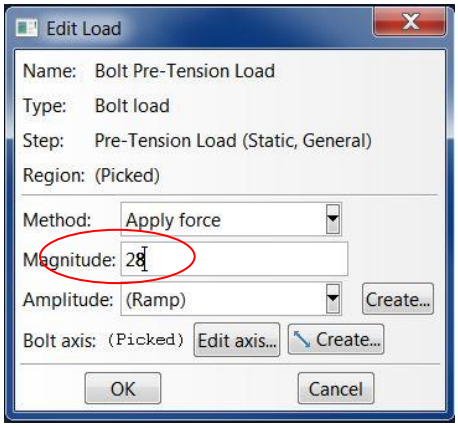

Figure J. 6: Enter the bolt load found in the AISC Specification.

9. Select the loading step next. From the drop down menu to the right of *Menu*, click on *Fix at current length*. This stops the tensioning load during the loading step.

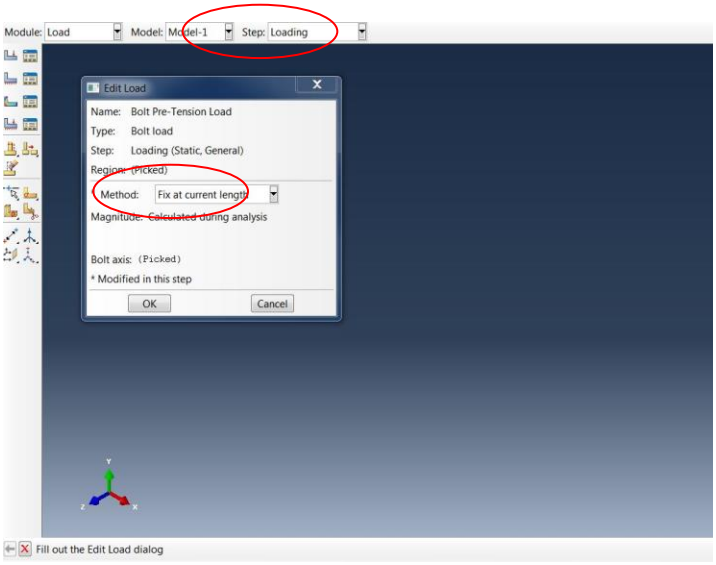

Figure J. 7: Fix the length of the bolt in the step where a global load is applied to the model. This stops the bolt from continuing to have a pre-tension load.

10. Tie the back of the head/nut to the front of the steel surface you are bolting to.
11. Create an interaction between the shank of the bolt and the hole that the bolt will go into to avoid the two surfaces from intersecting each other.

APPENDIX K: FINITE ELEMENT MODELING MESHING TECHNIQUES

Part 2: Use of CFRP Overlays to Repair Fatigue Damage in Steel Plates under Tension Loading

The mesh configuration for the steel specimen part is shown in Figure K. 1(a). The steel specimen was partitioned to allow for an extremely fine mesh to be located in the region around the circular opening, and have a smooth transition region. The mesh was configured using several regions with greater mesh density near the circular opening. The mesh configuration near the opening, presented in Figure K. 1(b), consisted of two concentric circular regions, which allowed gradually increasing element size away from the circular opening. The diameter of the smaller circular region was 6.4 mm (0.25 in.) and the diameter of the larger circular region was 19.1 mm (0.75 in.). Boundaries between the different regions of the mesh are illustrated in Figure K. 1(b).Figure K. 1(c) shows the mesh in the vicinity of the circular opening for an element size at the opening of 0.25 mm (0.01 in.). Figure K. 1(d) shows the mesh in the vicinity of the circular opening for an element size at the opening of 0.13 mm (0.005 in.).

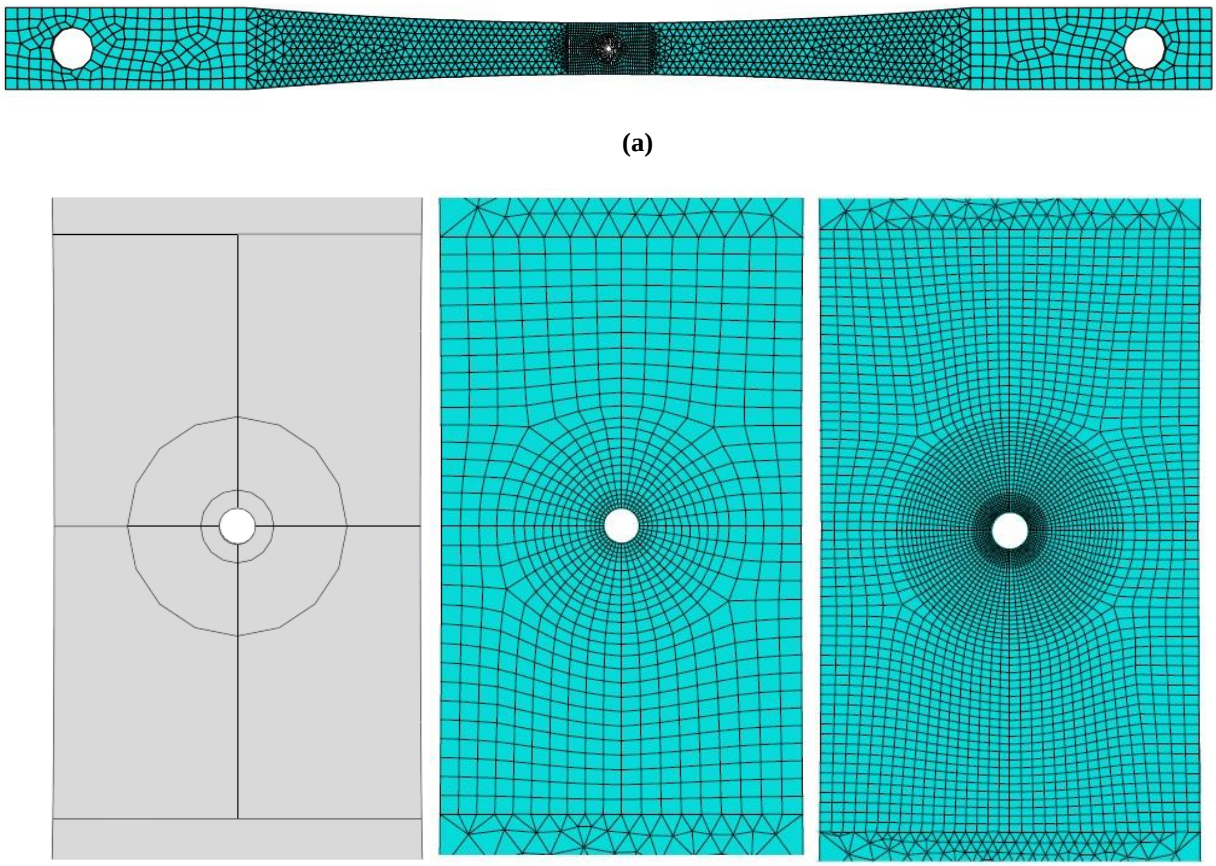

(a)

(b) **(c)** **(d)**

Figure K. 1: (a) Finite element model mesh;(b) Partitioned region around the circular opening;(c) Mesh in the vicinity of the circular opening for an element size at the opening of 0.25 mm (0.01 in.); (d) Mesh in the vicinity of the circular opening for an element size at the opening of 0.13 mm (0.005 in.)

Part 3: Effectiveness of Crack-Arrest Holes under Distortion-Induced Fatigue Loading

The mesh configuration for the girder section is shown in Figure K. 2(a). A large enough area was partitioned such that all crack types with different lengths and varying hole diameters would fit within the partitioned region, as shown in Figure K. 2(b). The mesh configuration near the crack-arrest holes consisted of three concentric circular regions around the holes which allowed gradually increasing element size away from the crack-arrest hole. Rectangular partitions were also created around the crack. The mesh was configured using several regions

with increasing mesh density near the crack-arrest hole. The most coarse and most dense mesh configurations for the region near the crack-arrest holes in the girder web for the diagonal crack model are shown in Figure K. 2(c) and (d). Figure K. 2(c) shows the mesh in the vicinity of the crack-arrest holes for an element size at the path half the thickness of the web away from the edge of crack-arrest hole of 1.80 mm (0.071 in.). Figure K. 2(d) shows the mesh in the vicinity of the crack-arrest holes for an element size at the path half the thickness of the web away from the edge of crack-arrest hole of 0.71 mm (0.028 in.).

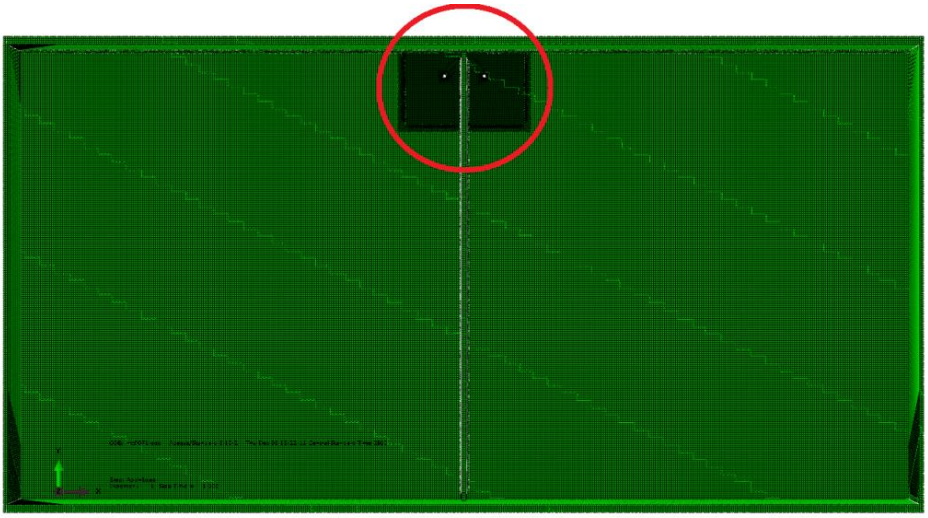

(a)

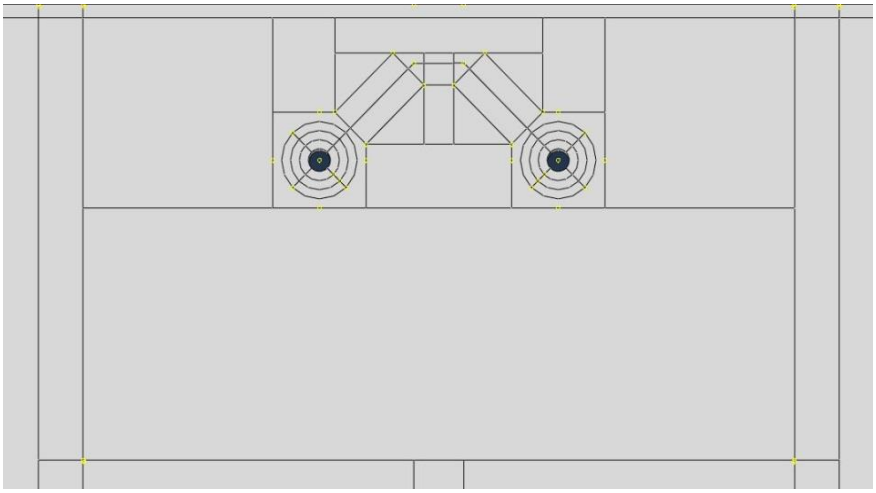

(b)

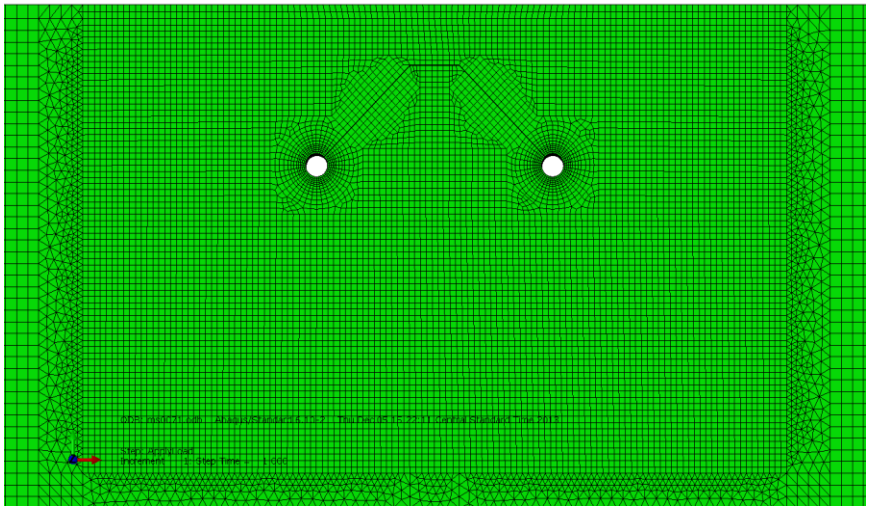

(c)

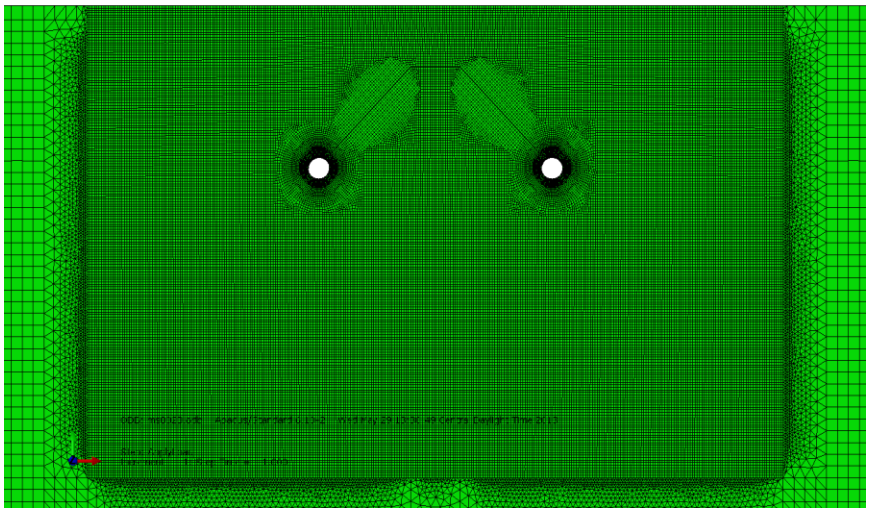

(d)

Figure K. 2: (a) Finite element model mesh;(b) Partitioned region around the crack-arrest hole for the diagonal crack model; (c) Mesh in the vicinity of the crack-arrest holes for an element size of 1.80 mm [0.071 in]; (d) Mesh in the vicinity of the crack-arrest holes for an element size of 0.71 mm [0.028 in]

Figure K. 3(a) shows the partitioned region around the crack-arrest holes for the horseshoe-shaped crack model and Figure K. 3(b) shows the mesh in the vicinity of the crack-arrest holes for the horseshoe-shaped crack model. Figure K. 4(a) shows the partitioned region around the crack-arrest holes for the horseshoe-shaped & web-to-flange crack model and Figure K. 4(b) shows the mesh in the vicinity of the crack-arrest holes for the horseshoe-shaped & web-to-flange crack model. Figure K. 5(a) shows the partitioned region around the crack-arrest holes for

the web-to-flange crack model and Figure K. 5(b) shows the mesh in the vicinity of the crack-arrest holes for the web-to-flange crack model.

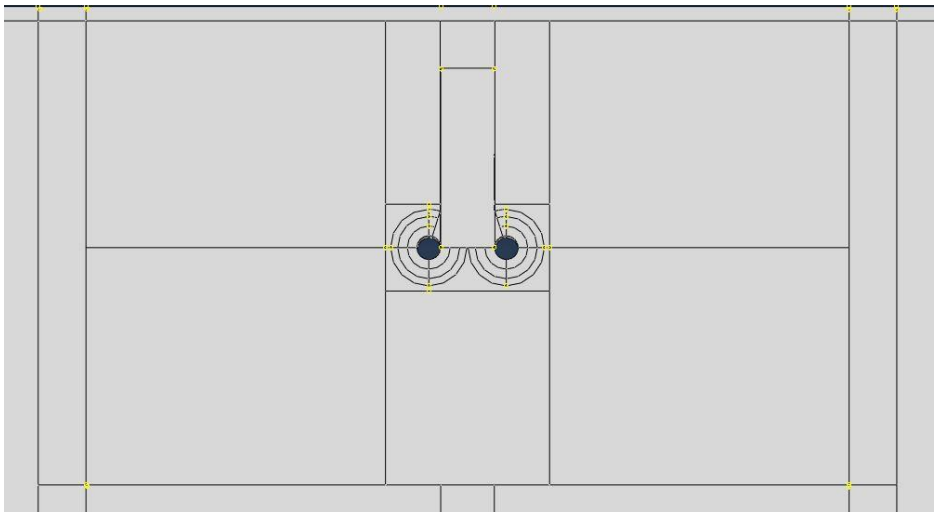

(a)

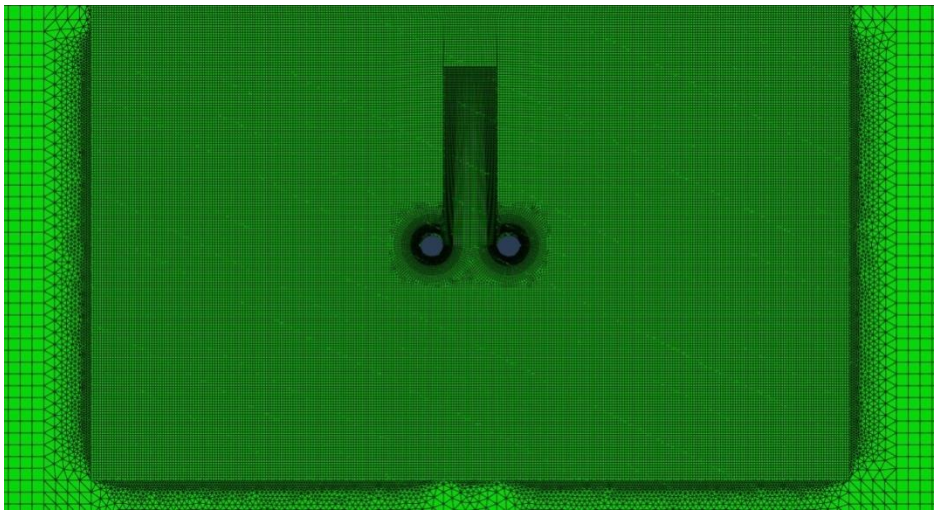

(b)

Figure K. 3: (a) Partitioned region around the crack-arrest holes for the horseshoe-shaped crack model; (b) Mesh in the vicinity of the crack-arrest holes for the horseshoe-shaped crack model

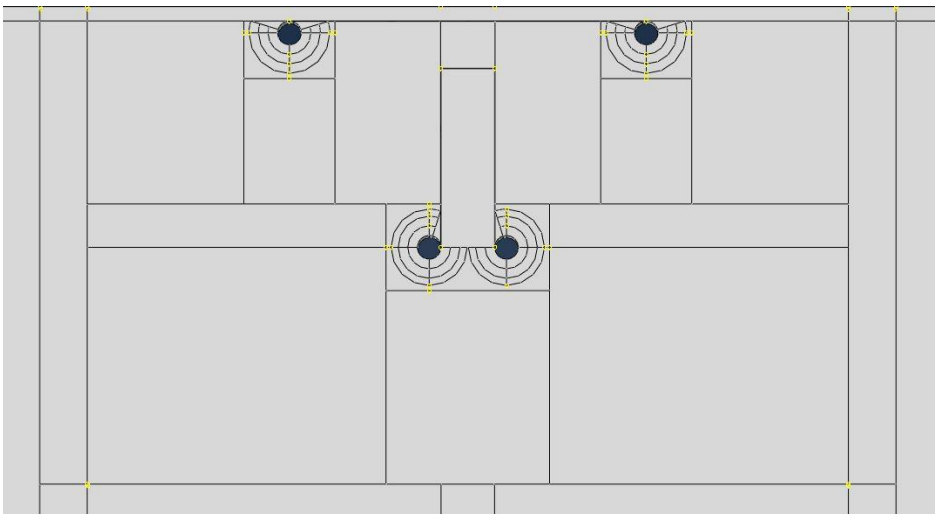

(a)

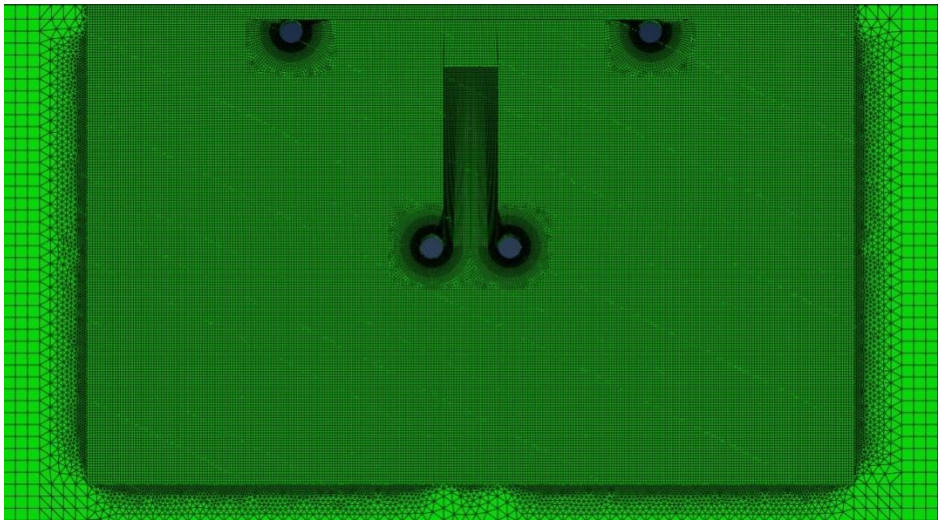

(b)

Figure K. 4: (a) Partitioned region around the crack-arrest holes for the horseshoe-shaped & web-to-flange crack model; (b) Mesh in the vicinity of the crack-arrest holes for the horseshoe-shaped & web-to-flange crack model

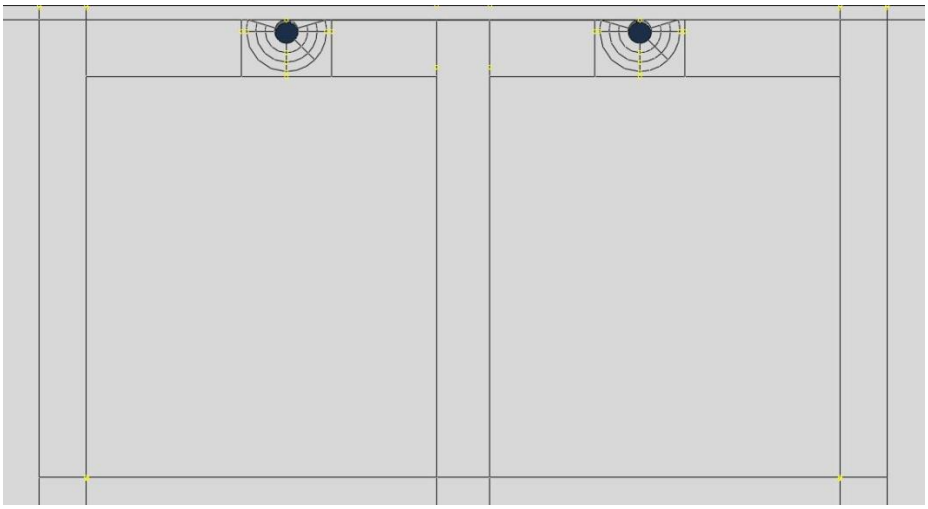

(a)

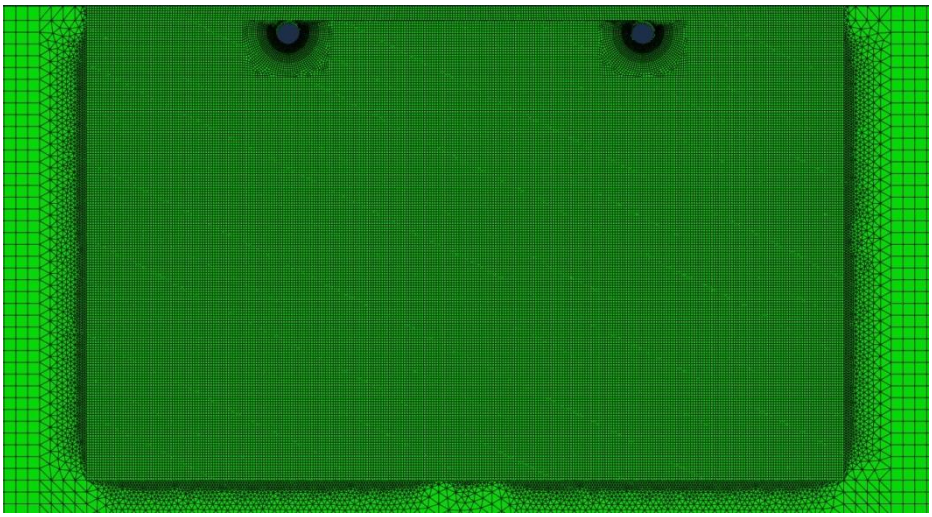

(b)

Figure K. 5: (a) Partitioned region around the crack-arrest holes for the web-to-flange crack model; (b) Mesh in the vicinity of the crack-arrest holes for the web-to-flange crack model